Composite Bone Tissue Engineering Scaffolds Produced by Coaxial Electrospinning

Muna Mustafa Kareem

Submitted in fulfilment of the requirement for the Degree of

Doctor of Philosophy (PhD)

Biomedical Engineering Division

School of Engineering

College of Science and Engineering

University of Glasgow

September 2018

Abstract

Electrospinning of polylactic acid (PLA)/calcium phosphates (CaPs) has been widely investigated for bone tissue engineering, however the significant reduction in mechanical properties and the rapid loss of the structural integrity of the scaffolds upon inclusion of high filler content is still challenging. Coaxial electrospinning has gained attention for tissue engineering applications due to the enhanced quality and the functionality of the resulting fibres compared to the basic electrospinning process. In this study, core and shell polycarpolactone (PCL)-PLA/micro-HA fibrous scaffolds were produced via coaxial electrospinning.

To optimise the shell component, PLA solutions of concentrations ranging from 5 to 25 wt%, and containing 10-40 vol% of either spray dried HA (HA1), sintered HA (HA2) or beta tricalcium phosphate (β-TCP) were electrospun using single-needle electrospinning. However, only 15 and 20 wt% PLA solution with 10 or 20 vol% CaPs produced electrospun scaffolds. Inclusion of all these fillers significantly reduced the mechanical properties of the scaffolds compared to non-filled PLA while increasing fibre diameter and non-homogeneity. TCP-containing scaffolds showed reduced mechanical properties compared to HA1- and HA2-filled scaffolds and increased TCP agglomerations along the fibres. Introduction of HA1 and HA2 into PLA scaffolds decreased the degradation rate of the scaffolds while increasing the bioactivity. However, apatite formation on the fibre surfaces was lower than previously reported due to the lower surface area of micro-HA particles compared to nano-HA in addition to the lack of sufficient HA particles on fibres surface. The higher surface area of HA1 did not significantly affect the rate of bioactivity, however it increased the thermal stability of scaffolds compared to HA2-filled scaffolds and led to further reduction in mechanical properties in vitro than HA2. Scaffolds with either HA lost their mechanical integrity within 28 days of SBF immersion.

As for the core component, changing the solvent system was found to affect the stability of the Taylor cone during electrospinning, and subsequently the morphology of the resultant fibre. Introduction of PCL as the core component in coaxial scaffolds increased both the tensile strength and strain at failure. The mechanical properties were influenced by the flow rate ratio between the core and shell components. Coaxial scaffolds with and without HA exhibited gradual

release of BMP-2 with only 12.8-13.6% released over 96 hours. They also supported cell attachment and spreading over 21 days of culture. However, control scaffolds had improved cell spreading compared to HA-containing scaffolds due to increased fibre uniformity and decreased fibre diameter. Tubular scaffolds made of core and shell structured fibres were also produced using rotating needle collector with G16 and G21 needle producing the internal diameter. Coaxial electrospinning with rotating needle collector produced fibres with improved circumferential alignment compared to stationary collector and increased fibre non-uniformity in HA-containing scaffolds. Bioactivity of tubular coaxial scaffolds was also significantly increased due to partial encapsulation of HA particles, and large areas of coaxial scaffolds were covered with apatite layer after 12 weeks of immersion in SBF. On the other hand, coaxial scaffolds with no HA showed no bioactivity even after 12 weeks of SBF immersion. Tubular control and HA-containing coaxial scaffolds had significantly higher mechanical stability in vitro and showed gradual reduction in their mechanical properties over 12 weeks of immersion in either PBS or SBF.

The results obtained suggest that coaxial electrospinning is a promising technique to produce bone tissue scaffolds with high content of CaPs while preserving the structural and mechanical integrity of the scaffolds. Bioactivity of scaffolds can be significantly increased by incorporating the CaP in the shell layer while mechanical properties of the coaxial scaffolds can be tailored by changing the core composition and diameter. However, further studies should be carried on to enhance the uniformity and alignment of the coaxial fibres in order to improve the mechanical properties of scaffolds.

Acknowledgments

"Allah elevates those among you who believe, and those given knowledge, many steps. Allah is Aware of what you do." **Al-Mujadila 58:11**

First and foremost, I thank Allah, the Almighty, for giving me the strength and patience to carry on this project and for blessing me with many great people who have been my greatest support in both my personal and professional life.

My sincere gratitude and appreciation go to my supervisor, Professor Elizabeth Tanner, for giving me the honour of working with her, and for her unwavering support, encouragement and guidance throughout the course of my work.

I would like to thank my sponsor, The Iraqi Ministry of Higher Education and Scientific Research, for their administrative and financial support during my study period, as well as Professor Manuel Salmeron-Sanchez for providing additional funding for testing.

I am also thankful for all the research, technicians and support staff across the various departments I have worked at in the University of Glasgow who have helped make this work possible. I am especially grateful to Dr Annie Zhe Cheng, Dr Tom Hodgkinson and Mr John Davidson for their respective help with protein release experiment, cell culture studies, and mechanical testing. Dr Margaret Smith, Dr Jafar Alsayednoor and Mrs Margaret Mullin are also thanked for their help and patience in providing me the resources in completing this dissertation.

My very special thanks go to my dearest friend, Omar Adnan, for his ongoing moral support and scientific discussions. This journey would not have been possible without your continuous advice and encouragement.

Last, but not least, no words can express my love and thanks to my beloved family, the greatest treasure in my life, for their unconditional love, support and patience. Mom and Dad, thank you for instilling in me a desire to achieve my goals and a commitment to finish what I start, to the best of my ability, no matter what it takes. Noora and Ahmed, thank you for always being there for me whenever I needed you. You are the best sister and brother one could ever wish for. My brother in law, Imad, many thanks for your useful discussions and valuable

suggestions to improve my work. My sweet nephew, Mahmoud, thank you for brighten up my world with your wonderful smile. I love you so much.

Author Declaration

I declare that, except where explicit reference is made to the contribution of others, that this thesis is the result of my own work and has not been submitted for any other degree at the University of Glasgow or any other institution.

Muna Mustafa Kareem

List of Contents

List of Figures

Chapter 2

Chapter 3

Chapter 4

Chapter 5

Chapter 6

Chapter 7

Chapter 8

List of Tables

Chapter 2

Chapter 3

Chapter 4

Chapter 5

Chapter 6

Chapter 7

List of Abbreviations

A	Cross sectional area
BCP	Biphasic calcium phosphate
BMP-2	Bone morphogenetic protein 2
CaP	calcium phosphate
Co-Cr	cobalt-chromium alloys
D	Pore diameter
E	Young's modulus
E_c	Modulus of the composite
E_f	Modulus of the filler
E_m	Modulus of the matrix
EtO	Ethylene oxide
F	Force
HA	Hydroxyapatite
HA1	Spray dried hydroxyapatite
HA2	Sintered hydroxyapatite
IL-1 and IL-6	Interleukin-1 and-6
L	The original length of the sample
$L_{critical}$	Critical thickness of the polymeric materials
m_{HA}	Mass of HA added to scaffold
m_{PLA}	Mass of PLA in the scaffold
MSC	Mesenchymal stem cells
P	Applied pressure
PBS	Phosphate-buffered saline
PCL	Polycarpolactone
PDGF	Platelet-derived growth factor fibroblast growth factor
PDMS	Poly(dimethylsiloxane)
PE	Poly(ethylene)
PET	Poly(ethylene terphthlate)
PGA	Polyglycolic acid
PHB	polyhydroxybutyrate
PHBV	Polyhydroxybutyrate-valerate
PLA	Polylactic acid
PLGA	Poly(lactic-co-glycolic acid)

PMMA	Poly(methyl methacrylate)
PMTC	Poly(trimethylene carbonate)
PP	Poly(propylene)
PS	Poly(sulfone)
PSZ	Partially stabilized zirconia
PTFE	Poly(tetrafluoroethylene)
SBF	Simulated body fluid
TCP	Tricalcium phosphate
TGF-β	Transforming growth factor-beta
UHMWPE	Ultra-high molecular weight polyethylene
UTS	Ultimate tensile strength
V_f	Volume fraction of the filler
V_m	Volume fraction of the matrix
Vol%	Volume percentage
$W_\circ$	The initial weight of the sample
W_{dry}	Dry weight of the sample
W_r	The residual weight of the sample after degradation
Wt%	Weight percentage
W_{wet}	Wet weight of the sample
γ	The surface tension of mercury
ΔL	Displacement
ε	Strain
θ	The contact angle between mercury and the pore wall
ρ_{HA}	Bulk density of HA
ρ_{PLA}	Bulk density of PLA
$\rho_{scaffold}$	Bulk density of the scaffold
σ	Stress

Chapter 1- Introduction

Since early history mankind has been concerned with the treatment of fractures. Ancient Mesopotamia (2000-1600 BCE) recognised the potential problems associated with bone fractures and described methods for the treatment which included stabilisation of the broken bone and plant medicines to prevent infection (Scurlock and Andersen, 2005). Hippocrates of Kos in approximately 400 BCE have also described a range of methods to treat fractures of various sorts (Gahhos and Ariyan, 1984; Ganz, 2015). However, one of the more complicated problems is when there is a large defect in the bone, which does not allow cell migration to close the space. This is known as "critical size defect". In this case a material is needed to allow the body to track over the defect and repair the space.

Over years, numerous synthetic bone substitutes have been developed to overcome the problems associated with using autografts and allografts which includes the limited supply, donor site complications and the risk of disease transmission and immune rejection. Polymer-based biomaterials have the ability to be fabricated into a variety of structures with an acceptable mechanical properties, topography, geometry and architecture as required for diverse biomedical applications. However, they lack the bioactivity required for bone formation and, consequently, elicit minimal tissue response. The incorporation of bioactive fillers into polymers matrices is therefore required in order to improve their chemical bioactivation (Hannink and Arts, 2011; Raucci et al., 2012). Calcium phosphate ceramics (CaPs), such as hydroxyapatite (HA), tricalcium phosphate (TCP) and biphasic calcium phosphate (BCP), are most commonly added fillers to the polymer matrices due to their resemble to the natural inorganic component of bone and their osteoconductive properties. On the other hand, studies have shown that incorporation of calcium phosphates can both stiffen and strengthen a low modulus and low strength polymer (Tanner, 2010a).

Among various scaffold fabrication techniques, electrospinning has been extensively investigated in last two decades as it is a relatively simple and low-cost method to produce fibrous scaffolds from polymeric solutions with diameters ranging from the nano- to the micro-scale that mimic extracellular matrix of native tissue (Chen et al., 2017). A variety of natural and synthetic polymers have been used to produce electrospun scaffolds for bone tissue engineering and to improve the bioactivity of the scaffolds. They were reinforced with various

amounts of calcium phosphates, bioactive glasses or glass-ceramics. However, one of the major problems associated with filler incorporation is the significant reduction of the mechanical properties upon increasing the filler content due to the brittleness of the ceramic fillers in general, bead formation along the fibres and the lack of interfacial bonding between the polymer matrix and the filler. Therefore, only small amounts of fillers (below 20 wt %) were used in the majority of the previous studies in order to maintain the mechanical integrity of the scaffolds. This in turn would affect the bioactivity of the scaffolds as this generally increases with increasing the calcium phosphate content in the scaffolds. One way to reinforce the fibres and improve the mechanical properties of the scaffold is using coaxial electrospinning where two dissimilar materials are delivered independently through a coaxial needle to form fibres with core and shell configuration. This approach is adopted in this thesis.

In the same time, micro-sized fillers are generally avoided in electrospinning due to their reduced bioactivity compared to nano-sized fillers as nanofillers have higher surface area. However, the high surface area of nanoparticles provides a very high surface energy, i.e. more surface atoms. To minimise their surface energy, nanoparticles tend to bond with adjacent particles which causes aggregate formation. Thus, the probability of nanoparticles agglomeration is higher than for microparticles upon increasing filler content in the scaffold. In this thesis, three micron-sized fillers were investigated for electrospinning with PLA at various contents as the shell component for the coaxial scaffolds, namely spray dried HA, sintered HA and ß-TCP.

The aims of the thesis are to:

1- Optimise electrospinning parameters and CaP contents in PLA scaffolds and investigate the effect of filler type and concentration on the morphology, bioactivity and mechanical properties of scaffolds.

2- Development of bioactive, degradable coaxial electrospun scaffolds in sheet and tube configurations made of PLA/micro-CaP filler as the shell component and PCL as the core of the fibre for bone tissue engineering.

3- Investigate the effect of collector type on the coaxial fibre morphology, alignment and mechanical properties.

4- Study the in vitro degradation and bioactivity of the coaxial scaffolds for up to twelve weeks and their effect on the mechanical properties.

To produce the coaxial scaffolds, the shell component, the core component and coaxial electrospinning parameters will be optimised separately since each of these elements is controlled by several factors, thus carrying out coaxial electrospinning directly would be challenging. The shell layer will be optimised first by electrospinning of PLA at different concentrations with various amounts of either spray dried HA, sintered HA or ß-TCP to investigate the effect of polymer concentration, filler type and filler concentration on the morphology of the scaffolds, in addition to the mechanical properties and bioactivity. Then, the core layer will be optimised via electrospinning of PCL at different concentrations with three solvent systems: chloroform, acetone, and a mixture of chloroform and acetone at 2:1 volume ratio to produce scaffolds with uniform fibres. Coaxial electrospinning will then be carried out using three core: shell flow rate ratios to investigate the effect of core and shell flow rates on the fibre morphology and the dimensions of the two layers within the fibres. Finally, the coaxial scaffolds will be produced in the conventional 2D sheets in addition to 3D tubes to examine the effect of collector on fibre diameter, alignment and mechanical properties.

Chapter 2 of this thesis presents a comprehensive review of the literature which includes the composition, structure and mechanical properties of bone, types of biomaterials used in orthopaedic applications with an overview of tissue engineering and the main techniques used for scaffolds fabrication. This continues with a breakdown of the electrospinning and coaxial electrospinning techniques used and the parameters affecting these two methods. Finally, some of the current techniques to produce 3D electrospun scaffolds are also reviewed. Chapter 3 covers the details of polymers, CaPs and solvents used, electrospinning/coaxial electrospinning configurations and parameters and scaffolds characterisation techniques. Development and characterisation of single fibre PLA/CaP scaffolds, 2D and 3D PCL-PLA/HA2 coaxial scaffolds is then broken down throughout chapters 4 to 7 that each contains their own particular materials and methods, results,

discussion and conclusions. Chapter 8 gives an overall discussion while chapter 9 summarises the conclusions of the project together with future directions.

Chapter 2- Literature Survey

2.1 Bone

2.1.1 Introduction

“Bone” is a term used to describe both bones, the structures, and the tissue of which they are made. The tissue can be defined as a complex, highly specialised connective tissue which plays a major role in critical functions in human physiology, including mechanical support and protection of other critical organs, body movement, blood cells production, mineral storage and homeostasis, blood pH regulation, and multiple progenitor cell (mesenchymal, hemopoietic) housing. Bone tissue is a natural hybrid nanocomposite consisting of an organic matrix that is made predominantly of oriented collagen, reinforced by an inorganic ceramic phase comprising of rod or plate-shaped hydroxyapatite particles. This structure gives bone its balance of stiffness, strength, toughness and vibrational damping properties. In order to maintain the structure–function relationship, bone tissue continuously forms and remodels throughout life to adapt to changes in biomechanical forces, and to remove the old, microdamaged bone and replace it with new, mechanically stronger bone to help maintaining bone strength (Kini and Nandeesh, 2012; Porter et al., 2009; Purbrick et al., 2010).

The adult human skeletal system contains over two hundred bones with a wide range of geometrical and structural architectures (Figure 2.1). These are dependent upon several factors such as skeletal site, physiological function, the age and sex of subjects (Bonucci, 2000).

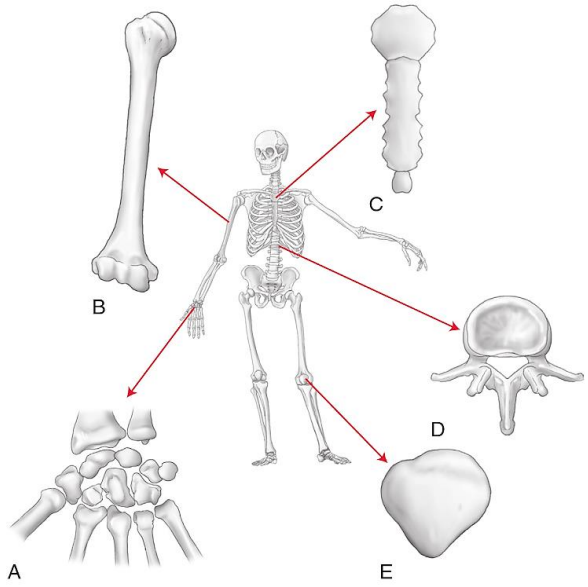

Figure 2.1 Human skeleton with examples of different bone types. (A) short bone (carpals), (B) long bone (humerus), (C) flat bone (sternum), (D) irregular bone (vertebra), and (E) sesamoid bone (patella) (from Mansfield and Neumann, 2013)

2.1.2 Bone composition

As a composite, bone is constituted of inorganic and organic phases in addition to water. By volume, the proportions of these components are approximately 40%, 35% and 25%, respectively. The inorganic phase represents 60-70% of bone's weight consisting mainly of crystalline mineral referred to as non-stoichiometric hydroxyapatite ($Ca_{10}(PO_4)_6(OH)_2$). The size of apatite crystals varies depending on the location of the crystals within the ends of collagen fibrils (smaller) or between collagen fibrils (larger) (Figure 2.2), with thickness ranging over 2–10 nm, length over 20–50 nm, and width over 15–30 nm with a rod-like (or sometimes plate-like) structure (Liu et al., 2016; Morgan et al., 2013).

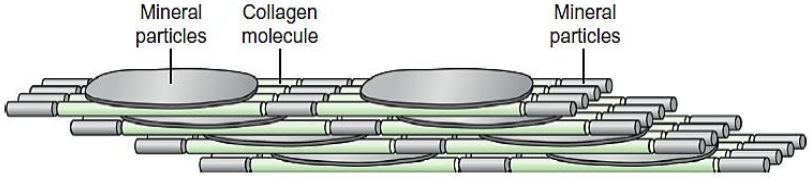

Figure 2.2 Arrangement of the mineral particles (grey coloured) either between the collagen fibrils (plate shaped) or within the ends of collagen fibrils (rod shaped) (from Burr and Akkus, 2013)

The crystal size and crystallinity, that is, the degree of structural order, of bone mineral is also affected by various diseases and therapies. For instance, crystal size was found to be decreased with patients with Paget's disease and diabetes, but increased in osteopetrotic individuals and after bisphosphonate treatment. Changes in the shape and size of the HA crystals affect the bone strength. The hydroxyapatite found in bone is non-stoichiometric because the apatite crystals contain substitutions such as potassium, magnesium, strontium and sodium in place of the calcium ions, chloride and fluoride in place of the hydroxyl groups, and carbonate in place of phosphate groups. The crystal size and/or non-stoichiometry of the apatite crystals is presumed to provide the mineral phase with the solubility required for bone resorption by osteoclasts (Keaveny et al., 2004; Liu et al., 2016; Morgan et al., 2013). The mineral phase of bone tissue stores about 99% of the body's calcium, part of which is released into the bloodstream through bone resorption, while the remaining 1% exists within the extracellular and intracellular fluids. Similarly, the majority of phosphate anions are present in the mineral phase of bone and teeth (85%), with the remaining 15% is distributed between extracellular fluid (1%) and other tissues (14%). The relative content of Ca and P, however, has a decisive influence on preserving mineral homeostasis and bone metabolism, and their co-dependence is evident for bone growth and development. Therefore, it can be considered as a suitable biomarker for the assessment of bone health (Kourkoumelis et al., 2012; Penido and Alon, 2012). Woodard (1962) measured the composition of human cortical bone of subjects aged 5-72 years and found that Ca/P molar ratio ranged from 1.37 to 1.71 depending on the age, with the lowest values being from children and the elderly. However, other studies made by Zaichick and Tzaphlidou in 2002 and 2003 found no correlation between the Ca/P molar ratio in the mineral phase of the bone and the age or sex of individuals (Tzaphlidou and Zaichick, 2003; Zaichick and Tzaphlidou, 2002).

The organic component represents 25-30% of bone's weight and consists of approximately 90% type I collagen, which is a natural polymer, and non-collagenous structural proteins. Type I collagen is made by osteoblasts and deposited in parallel or concentric layers to produce mature (lamellar) bone (Kini and Nandeesh, 2012). The mineral particles provide stiffness to the structure of the composite while the collagen provides ductility and toughness. The non-collagenous proteins regulate collagen formation, control fibril size,

mineralisation, and cell attachment (Burr and Akkus, 2013). Water exists in cells, fluid, collagen and bone mineral-apatite crystals representing the remaining 10% of bone weight (Wang et al., 2010). It help binding the collagen with the mineral phase (Wilson et al., 2006).

Finally, growth factors and cytokines are found in bone matrix, but in very small quantities. They have an effective role in regulating bone cell growth, activation, and differentiation as well as linking the processes of bone formation and resorption (Morgan et al., 2013). Table 2.1 lists the overall composition of bone, although it should be noted that this composition may vary from bone to bone.

Table 2.1 Composition of bone (from Palmero, 2016)

Component	Wt%
Hydroxyapatite	60-70
Collagen	10–20
Water	9–20
Non-collagenous proteins (osteocalcin, osteonectin, osteopontin, thrombospondin, bone morphogenetic proteins, sialoprotein, serum	3–5
Carbonate	4-6
Sodium	~0.7
Magnesium	~0.5
Other inorganic ions (Cl^-, F^-, K^+ Sr^{2+}, Pb^{2+}, Zn^{2+}, Cu^{2+}, Fe^{2+})	Traces
Other organic material (polysaccharides, lipids, cytokines)	Traces
Primary bone cells: osteoblasts, osteocytes, osteoclasts	-

2.1.3 Structure of bone

Bone tissue is organised in a hierarchical manner which contributes to its mechanical role in support and movement of the body as well as its other roles (Burr and Akkus, 2013). The material properties of the tissue change over the different levels of hierarchy. Thus, bone tissue must be studied at various scales to understand its behaviour which is crucial to determine the appropriate design parameters for composite material replacements (Purbrick et al., 2010). Based on the scale, the hierarchical structure of bone can be divided into five levels (Figure 2.3) as follows:

1. Macroscopic: cancellous and cortical bone (>0.5 mm).
2. Microscopic: osteons or Haversian systems and trabeculae (10–500 μm).
3. Submicroscopic: lamellae and mineralised collagen fibres (1–10 μm).
4. Nanostructure: mineralised collagen fibrils (about 100 nm–1 μm).
5. Subnanostructure: molecular and atomic structure of major components (<100 nm) (Mellon and Tanner, 2012).

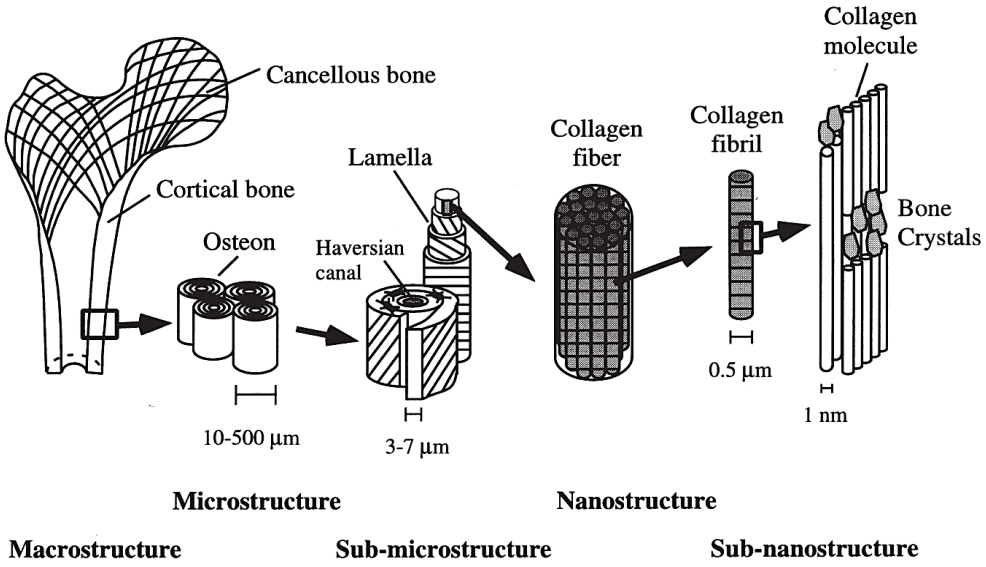

Figure 2.3 The hierarchical organisation of bone from macrostructural to sub-nanostructural level (from Rho et al., 1998)

At the macroscopic level, bone is divided into cortical (compact) bone or cancellous (trabecular or spongy) bone, depending on the specific mechanical or biological needs and its location. Cortical bone is a dense material composed of Harversian systems which are known to resist mechanical shocks, thus they provide both support and protection to the skeleton. It has low porosity over 3-5% in the form of canaliculi, osteocytes and blood vessels, although it increases with age and with osteoporotic changes to the skeleton. Cortical bone makes up approximately 80 wt% of a human's total skeletal mass, and can be mainly found the shafts of the long and short bones (diaphysis) of the extremities, or surrounding the cancellous bone of the vertebral body, at the ends (metaphysis)

of the long bones, in the iliac crest, and in the skull. The thickness of cortical bone shell at the outer surface of each bone can range between several tenths of a millimetre (in vertebra) to several millimetres or even centimetres (in the mid-shaft of long bones) (Figure 2.4), while the thickness of the struts in the cancellous bone is mostly constant, ranging between one and three hundred micrometres.

Cancellous bone, on the other hand, is a highly porous material (50-90%) that is formed of bony struts (trabeculae), each having a thickness in the order of a few hundred micrometres. However these trabeculae comprise only a maximum 25-30% of the total tissue volume, with the remainder being marrow space. It is mainly found in the epiphyses and metaphyses of long bones as well as in flat and irregular shaped bones such as the vertebrae. Cancellous bone is much more active metabolically and undergoes remodelling more often than cortical bone, thus it is generally 'younger' than cortical bone. About 25% of cancellous bone is replaced every year compared only 2–3% of cortical bone. The maturation of the cortical bone material is thought to have an influence on the mechanical properties at the microstructural level (Burr and Akkus, 2013; Fratzl and Weinkamer, 2007; Mellon and Tanner, 2012; Rho et al., 1998).

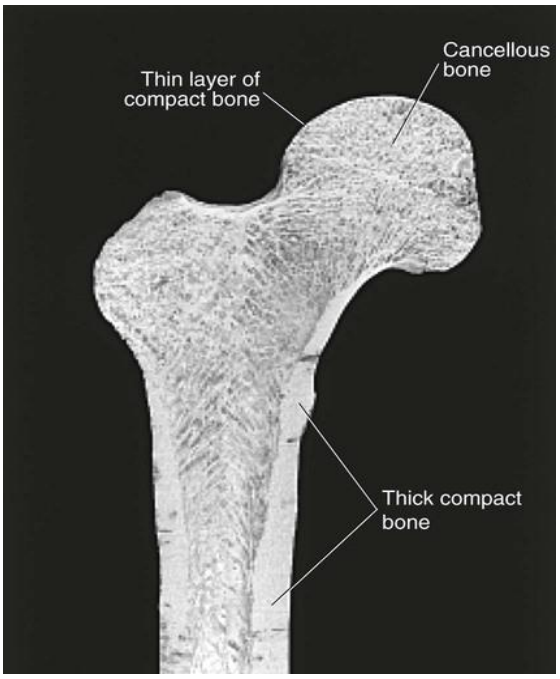

Figure 2.4 Sagittal section of a proximal femur showing the varied thickness of cortical and cancellous bone in the epiphysis (end) and diaphysis (shaft) areas of the bone (from Mansfield and Neumann, 2013)

At the microstructural level, cortical bone is composed of functional units called osteons (also known as Haversian systems), which comprises of concentric layers of bony sheets (lamellae) surrounding a central Haversian canal, containing central blood vessels as well as nerve fibres. The osteons are nearly cylindrical in shape, having diameter between 20–110 μm and length between 2–3 mm, and run roughly parallel to the long axis of the bone or the major loading direction, although they give off cross branches, Volkmann canals, which link the osteons with each other, conducting blood vessels. The small spaces between the lamellae are called lacunae and each hold a type of bone cells called osteocytes. To allow osteocyte communication, each lacuna is branched into fine branches called canaliculi, which contain osteocyte processes. The canaliculi also allow nutrients and oxygen to be delivered to the osteocytes and eliminate metabolism waste products. The outer surface of bones, except at joints (which are protected by articular cartilage), is covered by a thin layer of connective tissue called periosteum.

In contrast, the cancellous bone is composed of a series of interconnecting rods, or occasionally plates, of bone called trabeculae, which form a foam-like network. Similar to the cortical bone, the cancellous bone is lamellar in structure, however the lamellae do not usually run precisely parallel to the surface of the trabeculae so they come out of the surface at different angles, while the trabeculae are aligned closely to the principal stress directions. The trabeculae also contain osteocytes situated in lacunae and branching through canaliculi. However, the trabeculae receive their nourishment directly from the blood circulating through the marrow cavity, therefore Haversian canals are only be found in very thick trabeculae (Belinha, 2014; Currey, 2002; Mellon and Tanner, 2012; Rho et al., 1998). Figure 2.5 shows the microscopic architecture of long bone along with cross sections of the single osteon and trabecula.

At a lower level of bone structure, i.e sub-microstructure, the mineralised collagen fibres are shaped into planar arrangements called lamellae (3–7 μm wide). However the precise arrangement and mechanisms that stimulate fibre orientation between lamella are still controversial. Using polarised light microscopy, Ascenzi and Bonucci (1968) recognised three different types of osteons in cortical bone based on the variation in brightness of the cross section

(Figure 2.6). The alignment of collagen fibre bundles in each lamella were classified either longitudinally (dark), transversely (bright) or intermediately (dark/bright) to the long axis of the Haversian canal. This led Giraud-Guille (1988) to develop the concept of twisted orthogonal plywood of collagen fibres. In the twisted plywood model, collagen fibres in each lamella are running in a continually spiralling manner around the Haversian canal that rotate from plane to plane with fibre orientations alternated between each concentric layer, while in orthogonal model, the fibres on each parallel plane are limited to two orientations that alternate by 90° between each concentric lamella (i.e. longitudinal/transverse) or intermediately composed of both. However, Marotti et al. (1995) suggested that the collagen fibres in each lamella have random orientation, and the variation in polarised light resulted from the changes in collagen fibre density instead of alternate orientations. While the exact fibre arrangement and orientation in lamellae remain a subject of debate, the mechanical testing of individual microstructural components may play a major role in dictating the collagen fibre alignment throughout the bone (Ascenzi and Bonucci, 1967; Burr and Akkus, 2013; Rho et al., 1998).

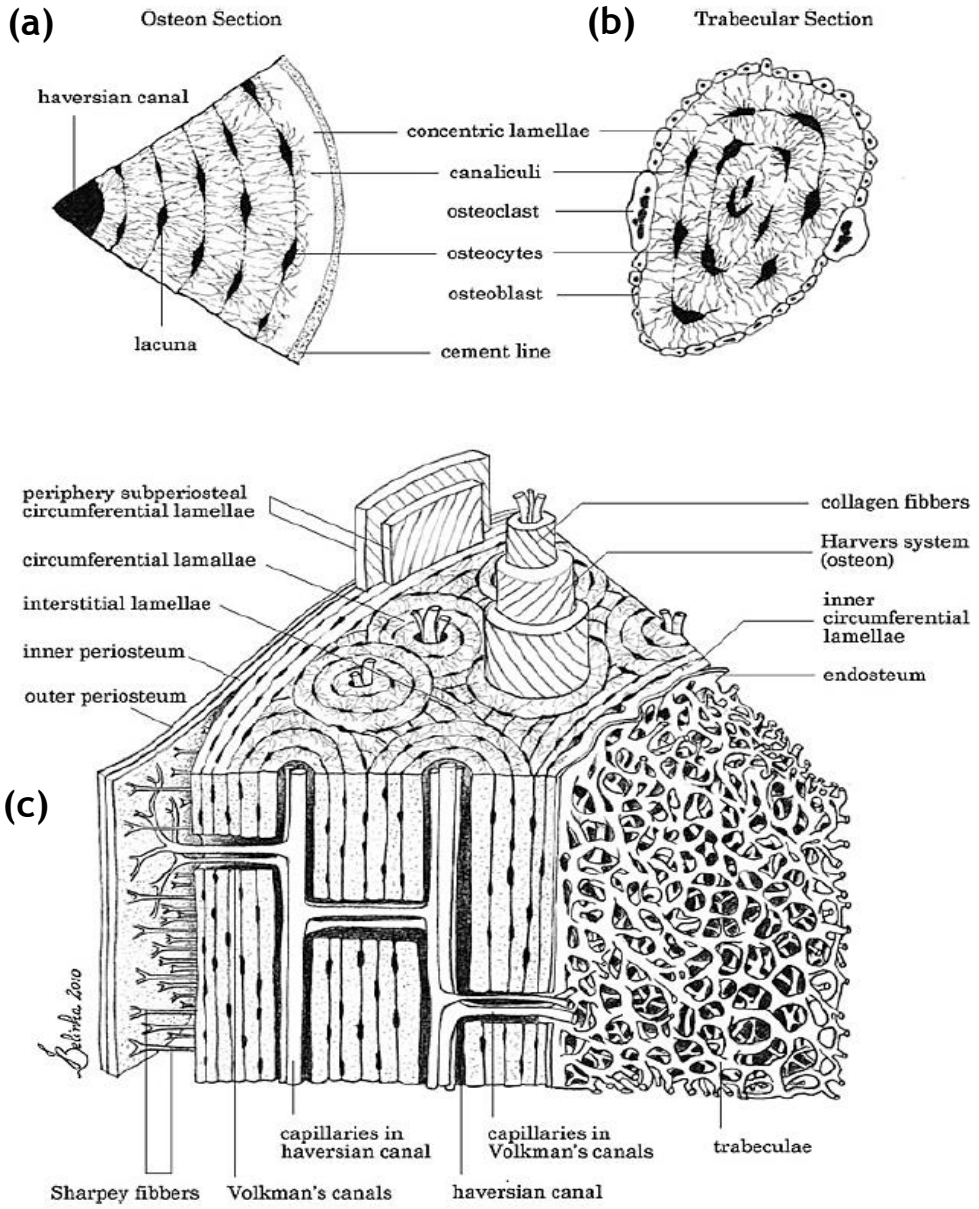

Figure 2.5 (a) transverse cross-section of an osteon, (b) transverse cross-section of a trabecular branch, and (c) internal microscopic structure of the diaphysis from a long bone showing the cortical and cancellous regions (from Belinha, 2014)

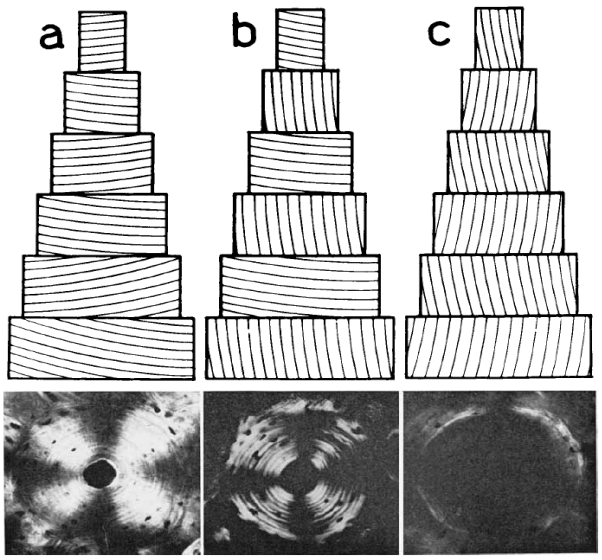

Figure 2.6 From Ascenzi and Bonucci, (1968) classification of osteons as seen in cross sections under the polarised light microscope, with (a) transversely, (b) intermediately, and (c) longitudinally orientated collagen fibres

Finally, at the nano/sub-nanostructural level, bone tissue is composed of collagen fibres which, in turn, are made up of bundles of fibrils interspersed with plates and rods of hydroxyapatite both within and between the fibrils. Type I collagen is the main structural component of the bone matrix, and comprises of three coiled polypeptide chains composed of approximately 1000 amino acids each. These chains take the form of a triple helix of two identical α1 chains and one α2 chain cross-linked by hydrogen bonding. This results in a very rigid linear molecule of about 300 nm in length. The molecules are aligned in parallel to each other and in a quarter-staggered array to form a collagen fibril, which is then grouped with other fibrils to produce the collagen fibre. The gaps between the ends of the molecules within the collagen fibril are known as “hole zones”, which act as a nucleation site for the formation of hydroxyapatite platelets orientated along the fibrils long axis. Pores also exist between the sides of parallel molecules inside the collagen fibril (Figure 2.7). Apatite is initially formed as an amorphous calcium phosphate, along with large amounts of calcium carbonate. As bone tissue matures, the carbonate content is reduced and the apatite crystals grow, becoming more plate-like, and orient themselves parallel to one another and to the collagen fibrils. The long axis of the apatite plate (c-axis) aligns with the

longitudinal axis of the bone (Burr and Akkus, 2013; Liu et al., 2016; Morgan et al., 2013; Rho et al., 1998).

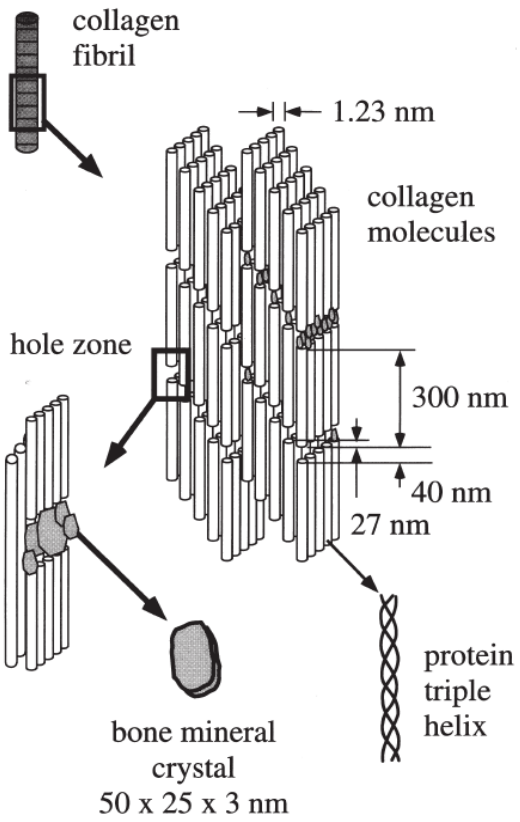

Figure 2.7 Schematic diagram illustrating the assembly of collagen fibrils and fibres and bone mineral crystals (from Rho et al., 1998)

2.1.4 Bone cells

Bone is a dynamic tissue which keeps its balance and strength by regular formation and resorption (Nakamura, 2007). Three types of bone cells are responsible for maintaining bone homeostasis, called osteoblasts, osteocytes and osteoclasts. They derived from two stem cell lineages, the mesenchymal and the hematopoietic lineage (Morgan et al., 2013).

Osteoblasts are responsible for protein matrix synthesis in bone which includes type I collagen in addition to the noncollagenous proteins mentioned earlier (Section 2.1.1). They also help with the initiation of bone resorption by secreting factors that recruit and promote the differentiation of monocyte/macrophage lineage cells into mature osteoclasts and also through producing proteases that degrade the osteoid and prepare the bone surface for osteoclast mediated

remodelling. Osteoblasts are derived from mesenchymal stem cells and can be recognised by their location on the bone surface and their morphological features including round shapes, and single large nuclei close to the membrane of the cell with enlarged Golgi apparatus on its apical surfaces (Bellido et al., 2013). After bone formation, osteoblasts can either go through apoptosis, that is programmed cell death, or become flattened inactive cells and covers bone surface (bone lining cells), or become embedded in bone matrix as osteocytes.

Osteocytes are the most abundant cells in bone tissue, comprising more than 90% of mature bone tissue cells. They are recognised by their cytoplasmic processes that link them with the processes of neighbouring osteocytes. Osteocytes are former mature osteoblasts that become imprisoned during bone deposition and enclosed in a calcified cavity of bone matrix (lacuna). Compared to osteoblasts and osteoclasts, osteocytes are long lived cells with estimates running of about 25 years. They play a key role in bone remodelling process by directing the osteoclasts to the site that is in need of remodelling and controlling the mineralisation of the bone matrix which is produced by the osteoblasts. Osteocytes also maintain mineral haemostasis in conditions where increased calcium is needed such as lactation. Furthermore, recent studies have proved the ability of osteocytes to influence osteoclast formation through the secretion of osteoclastogenic cytokines such as RANKL (Mellon and Tanner, 2012; Oranger et al., 2014).

Finally, the osteoclasts are large, multinucleated cells that are usually found in contact with a calcified bone surface and within pits called Howship's lacunae formed as a results of their own resorptive activity. They are members of the hematopoietic cell lineage and originate from mononuclear-macrophage cells. Unlike osteocytes, Osteoclasts are short lived cells with estimated life span of about two weeks. They play a significant role in bone modelling during growth and bone remodelling which preserves the integrity of the adult skeleton (Nakamura, 2007; Oranger et al., 2014; Ross, 2003).

2.1.5 Bone modelling and remodelling

Biological materials, such as bone, run at much lower safety factors than most engineering materials. However, they can respond to minor or major damages as well as altered loading environments by either initiating repair mechanisms or optimising their performance (Mellon and Tanner, 2012; Taylor, 2011). Bone was recognised as vital and adaptable tissue nearly 200 years ago when surgeons noticed the position and direction of the trabecular bone in the femoral neck and head which seemed to be oriented in engineering way. These observations were summarised and translated into a law by the German surgeon Julius Wolff in 1892. Wolff's law has been summarised as:

"Alterations of the internal architecture clearly observed and following mathematical rules, as well as secondary alterations of the external form of the bones following the same mathematical rules, occur as a consequence of primary changes in shape and stressing or in the stress of the bones." (Robling et al., 2013)

The law suggested that bone is modelled to adapt to different mechanical loads which creates stresses in its structure (Figure 2.8), and those mechanical forces are the most influential factors in bone formation and resorption (Robling et al., 2013). Bone modelling is defined as changing in bone's shape as a result of mechanical loading, and that includes the addition of bone on a particular surface by osteoblasts, and resorption of damaged bone by osteoclasts, while bone remodelling includes continuous removal of old bone and replacement with newly synthesised bone to renew the skeleton over time (Kini and Nandeesh, 2012). Bone modelling and remodelling are achieved by bone cells: osteoblasts, osteocytes, and osteoclasts, and it happens throughout life in both cortical and cancellous bone (Chen et al., 2010). Modelling is initiated by changing local tissue strain. This was first suggested by D'Arcy Thompson in 1917, who stated: *"The origin or causation of the phenomenon would seem to be partly in the tendency of growth to be accelerated under strain. . . accounting therefore for the rearrangement of. . . the trabeculae within the bone"*. According to Thompson's law, formative modelling occurs when local strains exceed a certain threshold while resorptive modelling is stimulated when the strains are low (Robling et al., 2013).

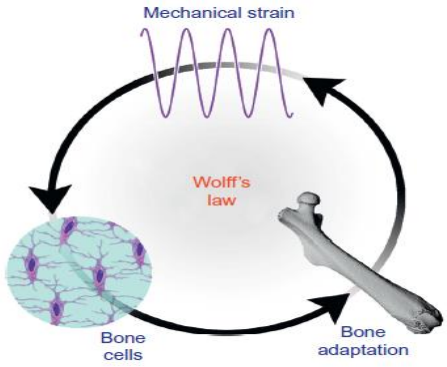

Figure 2.8 Demonstration of Wolff's law (from Robling et al., 2013)

Modelling happens in two phases: an activation phase and either a resorption or a formation phase. Activation process includes stimulation of bone lining cells to differentiate into mature osteoblasts and recruitment of precursor cells to differentiate into mature osteoclasts and osteoblasts. After activation, the activated cells begin to form or resorb bone until the local strains are normalised. Modelling is less frequent in adult skeleton in the absence of pathology or major changes in the dynamic loading.

Remodelling, on the other hand, can be classified into targeted, and stochastic remodelling. Targeted remodelling is mostly initiated by specific signals such as osteocyte apoptosis or micro damage while stochastic remodelling occurs randomly and helps to maintain calcium homeostasis (Allen and Burr, 2013). Both remodelling types, targeted and stochastic, are divided into six phases (Figure 2.9) which are:

1- Activation phase: in this phase the precursors differentiate into mature osteoclasts and migrate to the bone surface where they combine together to initiate bone resorption.

2- Resorption phase: the osteoclasts start dissolving bone matrix and producing Howship's lacunae on the bone surface. During this process, there is continuous recruitment of new osteoclasts to the remodelling site to replace the dead osteoclasts or to support the existing cells.

3- Reversal phase: this is a transition phase characterised by completion of bone resorption and the initiation of bone formation by osteoblasts. The coupling signals that link the end of the bone resorption process

with the formation process are still unknown, but there are several suggestions that have been proposed such as: factors released from bone matrix such as transforming growth factor beta (TGF-ß) and BMPs, and formation of a remodelling canopy by bone lining cells that exist in the remodelling site.

4- Formation phase: in this phase the osteoclasts disengage from the bone surface and are replaced by osteoblasts which produce an non-mineralised organic matrix (osteoid) that fills the resorption cavities and serves as a template for inorganic hydroxyapatite crystals.

5- Mineralisation phase: osteoid mineralisation occurs in two stages: primary mineralization, which takes about 2-3 weeks and includes initial bonding of phosphate and calcium ions inside collagen matrix, and secondary mineralisation which takes more than a year and involves final addition of mineral crystals.

6- Quiescent phase: this is the resting phase of bone and occurs at the end of remodelling cycle (Kini and Nandeesh, 2012).

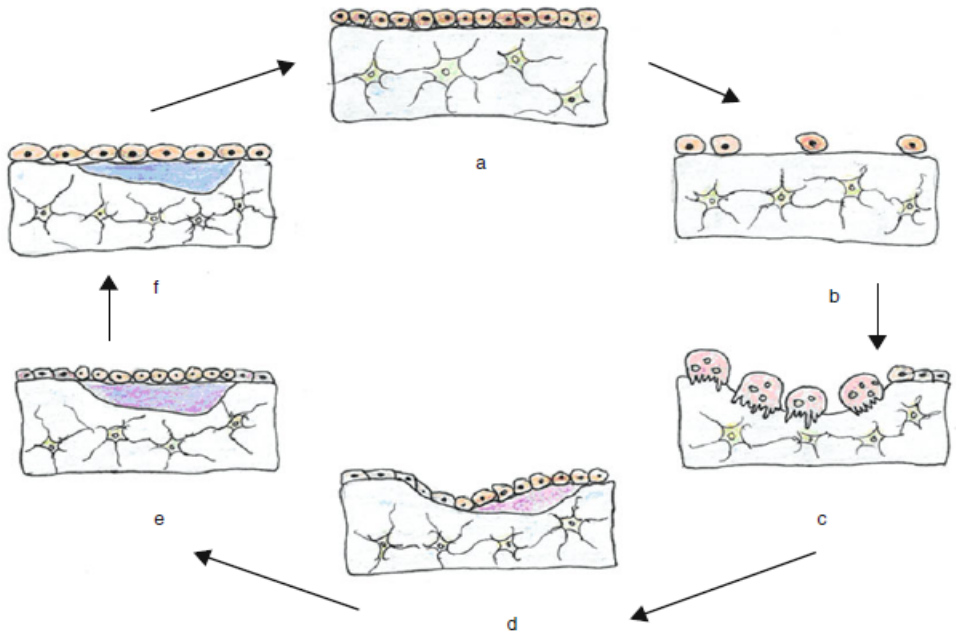

Figure 2.9 The phases of bone remodelling: (a-b)the presence of osteoprogenerator cells on the bone surface, (c) resorption of bone by osteoclasts, and (d-f) the gradual new bone deposition by osteoblasts (from Kini and Nandeesh, 2012)

In cortical bone, the remodelling process occurs by osteoclastic tunnelling (cutting cones) to remove damaged bone, followed by deposition of osteoblasts and deposition of new lamellar layers (closing cone) in new concentric layers, from exterior to interior, until a new osteon is formed. However, they do not completely fill the tunnel as a space is left in the middle for blood vessels, providing the osteocytes with nutrients and oxygen (Figure 2.10a). The group of osteocytes, osteoclasts and osteoblasts involved in remodelling (activation, resorption and formation) of a discrete area of bone is called a basic multicellular unit (BMU). The duration of the remodelling cycle in cortical bone is approximately 120 days. On the other hand, remodelling of cancellous bone occurs on the surface of trabeculae and lasts about 200 days in normal bone. The process is initiated by osteoclastic resorption, which erodes the Howship's lacuna (median duration of 30–40 days), followed by bone formation over a period of 150 days to fill the resorbed lacuna with new bone (Figure 2.10b). In normal bone, the amount of bone resorbed is similar to the amount of bone subsequently formed (i.e. the remodelling balance is close to zero). Thus, only slow changes in bone shape and mass can be achieved with remodelling (Eriksen, 2010; Klein-Nulend et al., 2014; Mellon and Tanner, 2012; Schoenau et al., 2004).

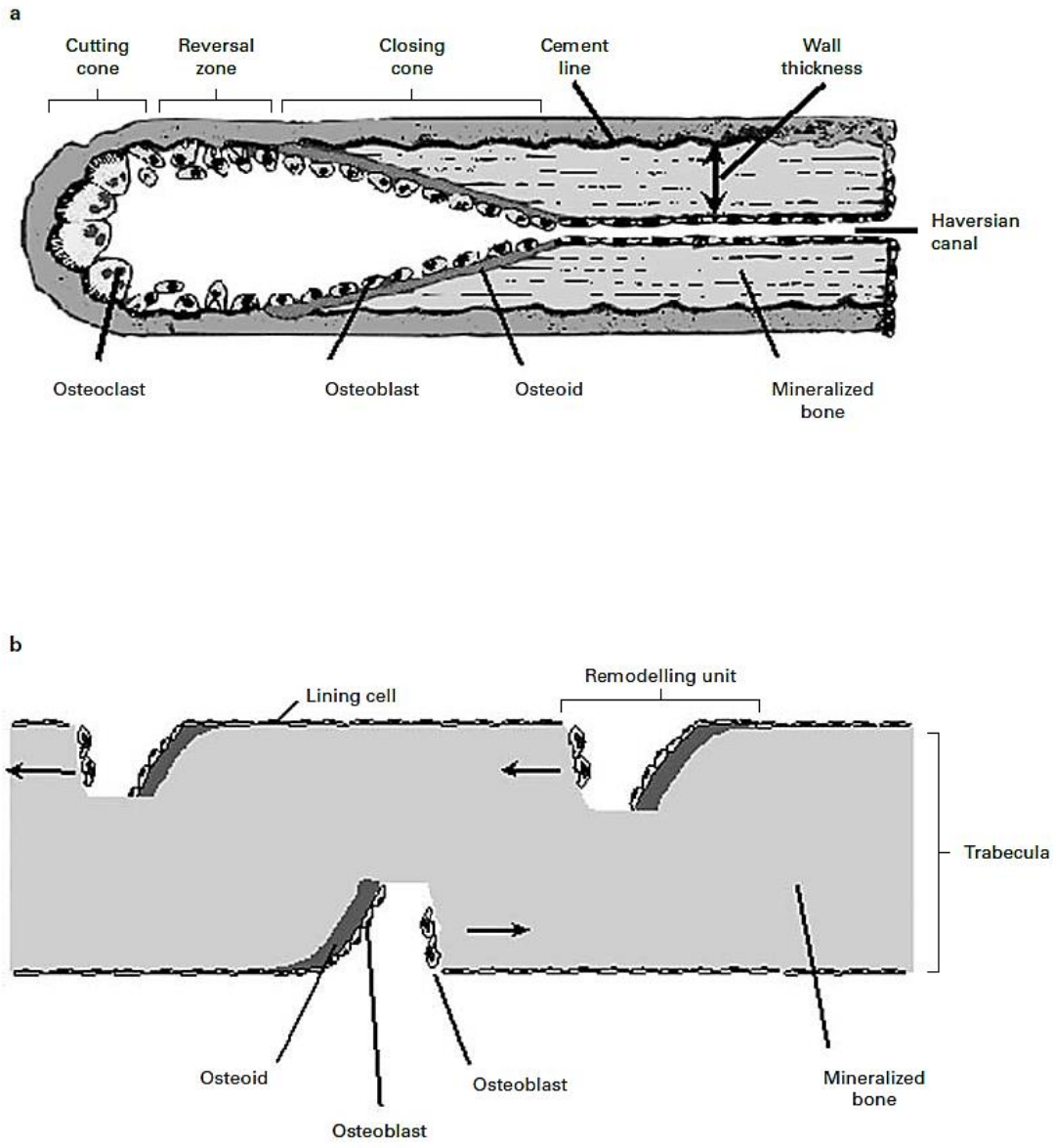

Figure 2.10 Schematic diagram of bone remodelling in (a) cortical bone, and (b) cancellous bone. In cortical bone, remodelling occurs inside the osteons where osteoclasts in the cutting cone create a tunnel which then is filled by osteoblast activity, leaving only a narrow opening for the Haversian canal. In cancellous bone, the cellular activates occur in Howship's lacunae and move parallel to surface of trabeculae as indicated by arrows (from Schoenau et al., 2004)

2.1.6 Mechanical properties of bone

The mechanical properties of bone provide the basic parameters for developing scaffolds with appropriate material properties and sufficient mechanical strength to withstand the different loads acting on bone.

Bone's ability to resist fracture (or whole-bone strength) depends on numerous factors such as the amount of bone (i.e., mass), bone location, the spatial distribution of the bone mass (i.e., shape, ratio of cortical to cancellous bone, and microarchitecture) and the material properties of the bone matrix (i.e., the mineral/collagen ratio, the collagen fibre orientation and the percentage water content). The mechanical properties of bone also depends on the test conditions such as the type of load (compressive or tensile), rate of loading and the direction of the applied load with respect to the orientation of bone microstructure (Johannesdottir and Bouxsein, 2018; Park, 2008).

As discussed earlier in section 2.1.5, the balance between bone formation and resorption during bone remodelling has a strong impact on preserving bone strength. Thus, diseases, conditions and drugs that impact bone remodelling will influence a bone's resistance to fracture (Osterhoff et al., 2016).

Bone, both cortical and cancellous, is generally an anisotropic material, meaning that its mechanical properties are direction-dependent. For example, cortical bone in the femoral diaphysis has a higher elastic modulus and strength when loaded longitudinally than in the transverse or radial directions (Figure 2.11), and cancellous bone from the vertebral body is much stiffer and stronger in the vertical direction than in the transverse direction. However, the degree of anisotropy varies with anatomical site and functional loading. For instance, cancellous bone properties from the iliac crest and central femoral head are nearly isotropic. The anisotropy of bone tissue provides greater resistance to loads applied in the primary loading direction for a given amount of tissue. However, it also results in a lesser load-bearing capacity in directions oblique to the principal loading direction (Karim et al., 2013; Keaveny et al., 2004).

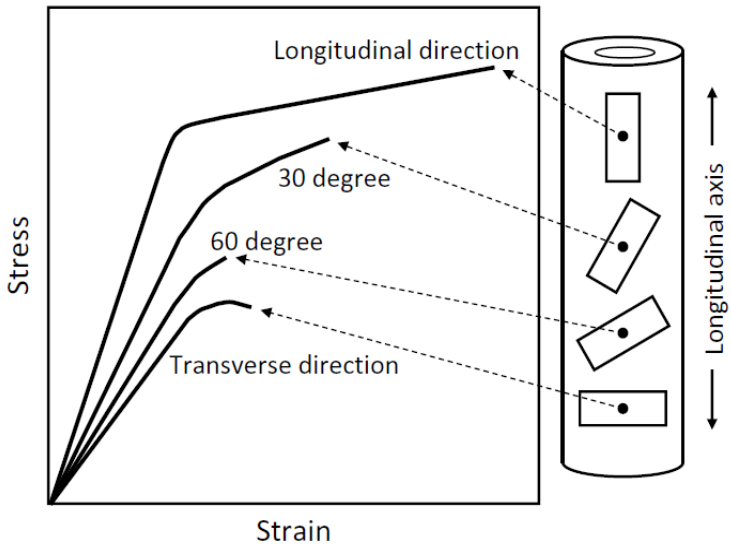

Figure 2.11 Anisotropic behaviour of a long bone. Bone specimens taken in different orientations within the human cortical femur exhibited different stress–strain characteristics (from Nakano, 2015)

Cortical bone is strongest in compression, weaker in bending, and weakest in shear or torsion (Pereira and Thambyah, 2005). Due to its dense nature, cortical bone is stiffer and able to resist higher ultimate stresses than cancellous bone, however it is also more brittle. It fails with tensile strains of only 2% in vitro while cancellous bone can withstand compressive strains up to 30% (Figure 2.12). Cancellous bone shows notable heterogeneity in its elastic and strength properties according to apparent density (or volume fraction) and the trabecular network architecture such as thickness, number and separation of the individual trabecular elements, shape of trabeculae (rod-like vs. plate-like), and the extent of interconnectivity among trabeculae. These in turn are influenced by age, health, and loading direction (Keaveny et al., 2004; Osterhoff et al., 2016). Both cortical and cancellous bone are also viscoelastic materials due to the presence of collagen fibres, meaning that their mechanical properties depend on the rate and frequency of loading. However, the viscoelastic behaviour is more obvious in cancellous bone due to its content of bone marrow, blood and body fluids in its cavities which help absorb high amounts of energy (Keaveny et al., 2004; Pal, 2014; Ramirez et al., 2015). Table 2.2 lists some of the mechanical properties of

cortical and cancellous bone determined under both longitudinal and transverse applied loads.

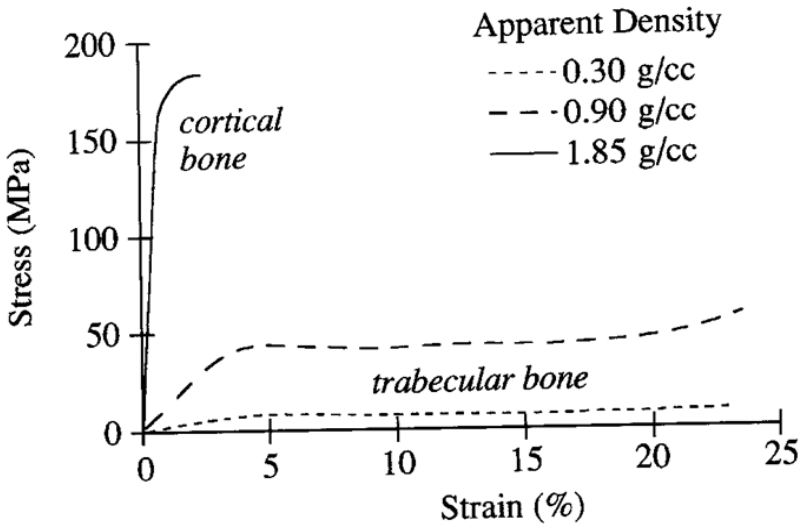

Figure 2.12 Stress-strain characteristics of cortical and cancellous bone under compression as a function of apparent density (from Hart et al., 2017)

Table 2.2 Mechanical properties of cortical and cancellous bone (from Palmero, 2016)

Properties	Cortical bone longitudinal direction	Cortical bone transversal direction	Cancellous bone
Compressive Young's modulus (GPa)	17–20	6–13	0.1–5
Tensile strength (MPa)	79–151	51–56	10–20
Compressive strength (MPa)	170–193	133	7–10
Yield strength in compression (MPa)	131–224	106–131	21.3
Fracture toughness (MPa$\sqrt{m}$)	2–12	2–12	0.1

The location of a bone in the body and the applied forces on it determine its characteristic microstructure and composition, thus influencing its mechanical properties. For instance, vertebral bodies must withstand high and repetitive axial compression loads, but experience much lower shear or tensile loads. If the

cancellous bone is extracted from a vertebral body, this will cause increased cortical shell stresses and a disproportionate decrease in the vertebral bone's ability to resist compression forces. On the other hand, the proximal humerus and femoral neck are mainly subjected to shear forces and bending moments, which, in turn, create a combination of compression, tension, and shear forces. Both show a distinct cortical structure. Any reduction in the cortical bone thickness or shape can increase the risk for sustaining a hip fracture or a proximal humerus fracture, while only small changes in the biomechanical strength occur if the cancellous components are removed from a proximal femur (Osterhoff et al., 2016). Table 2.3 lists the mechanical properties of the mechanical properties of various bones in human body.

Table 2.3 Mechanical properties of bone (from Nakano, 2015)

Type of bone	Direction of test	Modulus of elasticity (GPa)	Tensile strength (MPa)	Compression strength (MPa)
Leg bones				
Femur	Longitudinal	17.2	121	167
Tibia	Longitudinal	18.1	140	159
Fibula	Longitudinal	18.6	146	123
Arm bones				
Humerus	Longitudinal	17.2	130	132
Radius	Longitudinal	18.6	149	114
Ulna	Longitudinal	18.0	148	117
Vertebrae				
Cervical	Longitudinal	0.23	3.1	10
Lumbar	Longitudinal	0.16	3.7	5
Skull				
	Tangential	-	25	-
	Radial	-	-	97

The mechanical properties of the bone results from the combination of its two major components, where the brittle apatite provides the stiffness and compressive strength and the ductile collagen gives toughness and tensile strength

to the bone matrix (Figure 2.13). The mineral content of bone is usually affected by the age and health in both men and women. Studies have shown that the mechanical properties are not only affected by the degree of bone mineralisation, but also the quality of mineral within the bone matrix represented by the degree of crystallinity. At very high mineralisation and crystallinity levels, bone becomes excessively stiff and brittle, leading to micro-crack initiation, propagation and coalescence at reduced levels of deformation. In contrast, low mineralisation and crystallinity increase bone fragility and weakness (Hart et al., 2017; Pal, 2014; Sultana, 2013a).

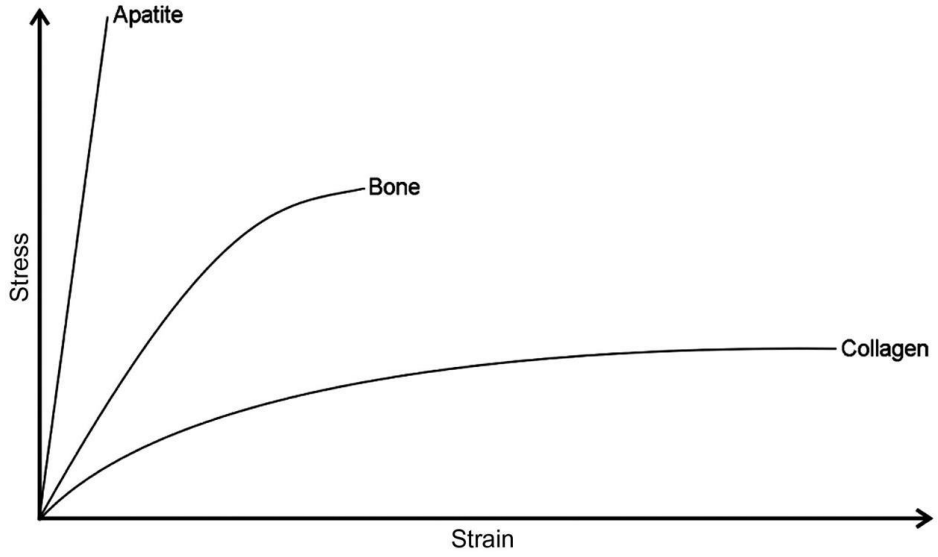

Figure 2.13 The mechanical behaviour of apatite, collagen, and cortical bone (from Sultana 2013a)

It was also noticed that the water content of bone, which constitutes about 10% of its weight, plays an important role in determining bone mechanical properties. Bone drying increases the Young's modulus of bone while decreasing its toughness and strain to fracture. For example, cortical bone's ultimate strain is about 1.2% when it is wet and about 0.4% when dry (Pal, 2014; Rho and Pharr, 1999). Rho and Pharr (1999) suggested that drying leads to contraction of the individual collagen fibrils with the degree of contraction depending on the level of mineralization in the bone, thus the mechanical properties would be altered.

2.1.7 Bone fracture and healing mechanism

Bone fracture is defined as loss of continuity and mechanical stability of bone as a result of trauma such as sport injuries, falls and car accidents, or as the result medical conditions such as osteoporosis and bone cancer (Li and Stocum, 2013). Fractures can be classified into closed or open fractures. Open fractures include skin wounds and soft tissue damage and have a high risk of contamination whereas in closed fractures the skin remains intact and leading to a lower risk of infection (Iyer, 2013). Another classification of fractures depending on the type of force that cause the fracture involves:

1- Simple fracture: in this type bone breaks into two fragments with oblique or transverse edges. It usually results from twisting or bending forces.

2- Comminuted fracture: occurs as a result of high energy trauma, causing the bone to break into multiple fragments. This type of fractures is harder to heal compared to simple fracture and may cause permanent deformation of the injured part.

3- "Stress" fracture: resulted from repetitive low force acting over long period of time causing accumulative microdamage to the bone. It usually heals through normal bone remodelling, but it may also leads to bone failure if the microdamge cannot be repaired or the repetitive loading continues for long time. (Li and Stocum, 2013).

Generally, fracture healing takes about 6-8 weeks to complete and results in full restoration of the function, and anatomy of broken bone. Fracture repair of long bones can be divided into primary (direct) healing and secondary (indirect, spontaneous) healing.

In primary healing, inhibition of callus formation and rigid stabilization of the fractured bone is required. This type of healing is less common than secondary healing since common treatment methods usually involve some degree of movement such as cast immobilisation or external fixation. Primary healing involves gap and contact healing. Gap healing happens in two phases: the first phase includes gap filling by woven bone layer formation followed supportive lamellar bone formation in transverse orientation to the original bone. The second

phase includes remodelling of the fracture site where fracture ends is reconstructed and osteons are formed parallel with the original orientation of the bone. Contact healing, on the other hand, involves osteons growth in the same original bone orientation on the fracture site where the fractured ends are in direct contact. The osteoclasts then form cutting cones around the fracture line penetrated by capillaries leading to the formation of new Harversian systems across the fracture site (Sfeir et al., 2005).

As mentioned earlier, secondary healing is more common than primary healing, involving some controlled motion between the broken ends as in external fixation or plaster cast (Wraighte and Scammell, 2006). It occurs in four overlapping stages (Figure 2.14):

1- Inflammatory phase: this phase lasts about 7 days, resulting from bone matrix, soft tissue and vascular damage which lead to haematoma formation. This reaction immobilizes fracture motion through swelling of injury site (Sfeir et al., 2005). The inflammatory cells then recruit cells to start bone repairing through cytokines releasing such as: transforming growth factor-beta (TGF-ß), platelet-derived growth factor fibroblast growth factor (PDGF), and interleukin-1 and-6 (IL-1 and IL-6) which cause local mesenchymal cells to differentiate into osteoblasts (McKinley, 2003).

2- Soft callus formation (cartilage formation): in this phase, the stimulated cells produce vascularized reparative callus to improve the stability of the bone ends. The peak of this phase occurs 7-10 days after injury.

3- Hard callus formation: it involves calcification of the soft callus tissue into woven bone by endochondral ossification and vessels invasion. This is usually accompanied by intramembranous ossification in the periphery of the fracture site (Li and Stocum, 2013).

4- Remodelling phase: this is the final stage of secondary healing and it involves replacement of woven bone by lamellar bone in addition to excess callus resorption (Sfeir et al., 2005). It begins 3-4 weeks after

injury and may take years to restore the original bone shape (Wraighte and Scammell, 2006).

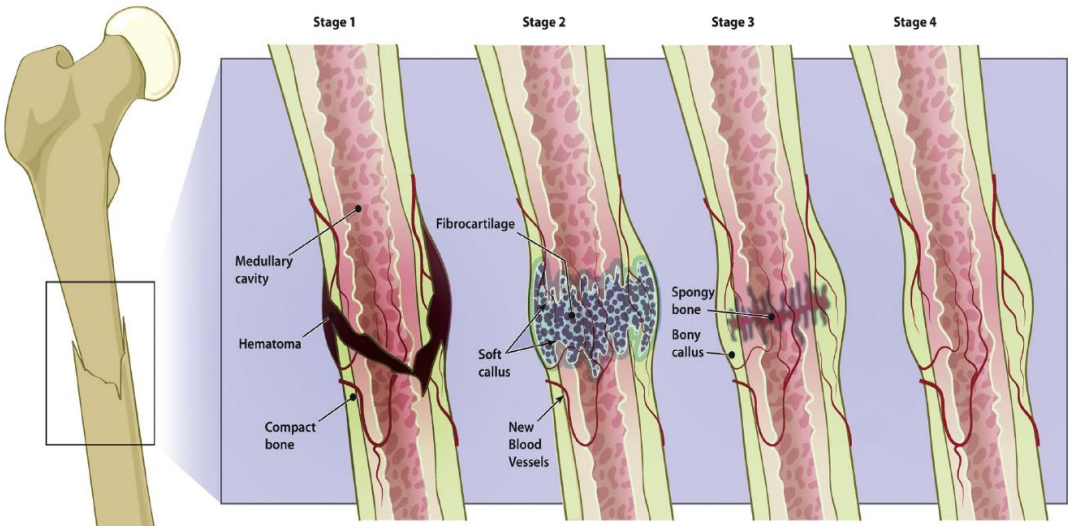

Figure 2.14 Stages of fracture secondary healing (from Li and Stocum, 2013)

2.2 Biomaterials

2.2.1 Introduction

The science of biomaterials developed over the last 60 years with the increasing limitations in the quantity of allografts, the morbidity resulting from during implantations, and the discovery of new materials that can be used as medical implants (Gentleman et al., 2009). There were several attempts to define the word "biomaterial" over the years, but the first real definition came in 1987 by David F. Williams who stated:

"A biomaterial is a nonviable material used in a medical device, intended to interact with biological systems."

Then, in 1999, he modified his definition of biomaterials to become:

"A material intended to interface with biological systems to evaluate, treat, augment or replace any tissue, organ or function of the body."

Another significant definition of biomaterials was made in 2003 by Miller-Keane and O'Toole who said that a biomaterial represents:

"any substance (other than a drug), synthetic or natural, that can be used as a system or part of a system that treats, augments, or replaces any tissue, organ,

or function of the body; especially, material suitable for use in prostheses that will be in contact with living tissue" (Vuluga et al., 2012).

In general, there are a number of important factors for a material in order to be used in human body such as: appropriate mechanical properties, biocompatibility, which was also defined by Williams in 1987 as: *" the ability of a material to perform with an appropriate host response in a specific application"* (Ratner et al., 2013), and biodegradability which means that the material should degrade in the body due to enzymatic or body fluids reactions or be resorbed harmlessly over time by cellular actions (O'Brien, 2011). Biodegradable materials offer advantages in temporary biomedical applications and tissue engineering because of their natural clearance from the body, which will enable the ingrowth of the surrounding tissue over time to restore its normal function after having benefited from the implant (Khan et al., 2014). In addition, biodegradable implants can sometimes prevent or reduce long-term safety problems such as: implant-tissue interface, long-term immune rejection, as well as failure of the device (Treiser et al., 2013).

2.2.2 Types of biomaterials

It has long been accepted that any foreign material, except for autografts, placed within a living body will not be completely compatible and will initiate reactions called host-tissue responses. These reactions occur at the biomaterial/tissue interface and result in time-dependent changes in the surface characteristics of both the implant and the surrounding tissue. Based on the tissue response, biomaterials can be classified into bioinert, bioactive and biodegradable materials. A bioinert material has minimal interaction with the surrounding tissue once implanted in human body. Examples include stainless steel, titanium, alumina, partially stabilized zirconia (PSZ), and ultra-high molecular weight polyethylene (UHMWPE). Generally, the body interacts with bioinert material by producing a thin fibrous capsule around the implant to separate it from the host tissue, thus its biofunctionality relies on tissue integration through the implant.

On the other hand, when a bone bioactive material implanted inside the body, it promotes the creation of a surface layer of biological apatite before interfacing directly with the tissue at the atomic level, leading to formation of direct

chemical bonds to the bone tissue. Examples of bone bioactive materials are synthetic hydroxyapatite, glass ceramics and bioactive glasses.

Finally, a biodegradable material is designed to dissolve over time to allow newly formed tissue to grow into any surface irregularities but may not necessarily interface directly with the material. Common examples of biodegradable materials are polylactic acid (PLA), polylactic–polyglycolic acid copolymers (PLGA), polyhydroxybutyrate (PHB), tricalcium phosphate (TCP) and others (Dorozhkin, 2016; Tur, 2009).

Biomaterials that are currently available to manufacture orthopaedic implants can be divided into metals and alloys, ceramics, polymers and composites.

2.2.3 Metals and alloys

Metals and alloys have been extensively used for load bearing applications such as total joint prostheses (artificial joints) for hips, knees, shoulders and ankles, as well as using them in fracture fixation as plates, pins, and screws. Metallic implants have also been used in maxillofacial surgery, cardiovascular surgery and as dental materials. Metals have strong inter atomic bonds which gives them good tensile strength and fatigue resistance in addition to high ductility, thus they deform under high loads without breaking. However, they have low corrosion resistance under largely variable physiological and mechanical properties of living tissues. With the exception of commercially pure titanium, alloys are more frequently used than pure metals due to their enhanced material properties such as strength and corrosion resistance. Typical examples of metallic orthopaedic materials are: titanium and titanium alloys, 316 and 316L stainless steel, and cobalt-chromium alloys (Gentleman et al., 2009; Patel and Gohil, 2012). Table 2.4 lists the mechanical properties of some of metallic biomaterials compared to human cortical bone.

Table 2.4 Mechanical properties of metallic implants (from Brunski, 2013; Patel and Gohil, 2012)

Material	Modulus of elasticity (GPa)	Yield strength (MPa)	Tensile strength (MPa)
Cortical bone	15-30	30-70	70–150
Stainless steel	190	221–1213	586–1351
Co-Cr alloy	210-253	448–1606	655-1896
Titanium (Ti)	110	485	760
Ti alloy	116	896–1034	965-1103

2.2.4 Ceramics

Ceramic materials, in general, are inorganic, non-metallic solids which comprise crystalline ceramic and amorphous glass compounds. The term “bioceramics” is applied to the ceramics used for the repair and reconstruction of diseased or damaged parts of the musculoskeletal system. Bioceramics, either dense or porous, have been widely used in medical applications such as dental implants, coatings for orthopaedic and maxillofacial prosthetics, bone fillings, bone scaffolds and for alveolar ridge augmentation. Generally, they are hard, stiff and very biocompatible materials, but they are also brittle and weak in tension. According to their biological response, bioceramics can be classified into three types: nearly bioinert such as alumina, pyrolytic carbon and zirconia, bioactive such as HA and the bioactive glasses, and biodegradable such as TCP (Hench, 1991; Huang, 2017).

Bioinert ceramics possess a high chemical stability in vivo as well as high mechanical strength. When they implanted in living bone, they incorporated into the bone tissue in accordance with the pattern of "contact osteogenesis", thus the new tissue is formed on the implant surface, surrounded by non-adhesive connective tissue capsule, without chemically interacting with the implant (Yamamuro, 2004). They are also hard to break, and have good resistance to corrosion. Zirconia is commonly used in the femoral heads of total hip joints because of its high fracture toughness, while alumina is used for dental implants and in hip prostheses for its good biocompatibility, strength and high wear and corrosion resistance. Finally, pyrolytic carbon is known for its good durability and

biocompatibility, but its brittleness and low tensile strength limit its usage in high loads medical applications (Patel and Gohil, 2012).

Bioactive ceramics, including bioactive glasses, glass-ceramics and calcium phosphates, are capable of promoting the formation of bone-like hydroxyapatite layers at their surface and of creating an interface which contributes to the functional longevity of the tissue. The first evidence of direct bone bonding to a silicate-based glass implant was observed by Hench et al. in 1970. Thereafter, some other glasses, glass-ceramics and ceramics had been proved to have bone-bonding capability. (Hannink and Arts, 2011; Hench, 1998; Huang, 2017; Rahaman et al., 2011).

Bioactive glass is an amorphous material that has a random arrangement of atoms due to the rapid cooling of the molten ceramic. The main constituents of most bioactive glasses are SiO_2, Na_2O, CaO and P_2O_5. The specific composition of the bioactive glass determines its bioactivity, osteoconductivity and biodegradability. For instance, Hench et al noticed that for their particular formulation of bioactive glass (45S5 Bioglass), rapid bonding to bone occurred when the silica level was in the range 42–53%, whereas glasses with 54 to 60% of silica required 2–4 weeks for bonding, and with glasses containing more than 60% of silica, there was no direct bonding between the bioactive glasses and bone (Best et al., 2008). 45S5 Bioglass has shown both osteoconductive (able to support bone formation in osseous defect sites) and osteoinductive (stimulates bone growth by osteoprogenitor cell recruitment and activation) properties as it promotes new bone growth along the bone–implant interface as well as within the implant away from the bone–implant interface. A variety of bioactive glasses have been developed over the years, including silicate-based, phosphate-based and borate-based ones. They have been used in bone scaffolds, middle ear replacements and tooth root replacement. However, they have relatively limited use in load-bearing applications due to their amorphous structure which decreases their mechanical strength and lowers their fracture toughness. Bioactive glasses bond to living bone tissue through a sequence of reactions on the material surface followed by cellular reactions. Briefly, ion leaching/exchange occurs at the surface of the implant which leads to dissolution of the glass network and precipitation and growth of a calcium deficient carbonated apatite (HCA) surface. These reactions results in biochemical

adsorption of growth factors, the presence of osteogenic precursors then favors the formation of osteoblasts, and the sequences of cellular events lead to rapid new bone formation (Essien et al., 2016; Hench, 1998; Huang, 2017; Rahaman et al., 2011).

To overcome the limitations of the bioactive glasses, glass-ceramic materials have been developed. Glass–ceramics are crystallised glasses, consisting of a composite of a crystalline phase (crystal sizes ranging from 0.1 to 10 μm) and a residual glassy phase. The production process of glass-ceramics involves the heat treatment of a base glass to induce controlled crystallisation and to convert it into a glass–crystal mixture. The heat treatment promotes the nucleation and growth of various kinds of crystalline phases with fine grain sizes. Thus the crystallisation and formation of the crystal phases can be modulated to achieve a combination of special properties, such as bioactivity, machinability and improved mechanical properties.

Apatite-wollastonite (A-W) glass-ceramic was first introduced by Kokubo and his colleagues in 1982 and became one of the most extensively studied glass ceramics for use as a bone substitute. A-W glass-ceramic is composed of glassy matrix [MgO–CaO–SiO_2] reinforced by crystalline apatite [$Ca_{10}(PO_4)_6(O,F_2)$] and wollastonite [$CaO{\cdot}SiO_2$]. Thus it exhibits not only bioactivity, but also fairly high mechanical strength. Also, its bending strength, fracture toughness and Young's modulus are the highest among bioactive glasses and glass-ceramics, enabling it to be used in some compression load bearing applications such as vertebral prostheses and iliac crest replacement (Best et al., 2008; Huang, 2017; Kokubo, 1993; Palmero, 2016)

Another class of bioactive ceramics are the calcium phosphates. As discussed earlier in Section (2.1.2), calcium phosphates are the major constituent of bone (and teeth) and play as such an essential role in our daily lives. Therefore, over the last few decades, researchers tried to incorporate calcium phosphate based bioceramics to produce implants for clinical application. Nowadays, there are several calcium phosphates that are extensively used for bone replacements (Table 2.5), such as hydroxyapatite (HA), tricalcium phosphate (TCP) and biphasic calcium phosphates (BCP, consisting of HA–TCP mixtures). They can be produced in both dense and porous forms in bulk depending on the application, as well as

in the forms of powders, granules, scaffolds or coatings (Canillas et al., 2017; Habraken et al., 2016; Huang, 2017).

Table 2.5 Summary of calcium phosphate compounds with their corresponding Ca/P molar ratios, abbreviations and formulas (from Canillas et al., 2017; Habraken et al., 2016; Huang, 2017)

Compounds	Typical abbreviations	Ca/P molar ratio	Solubility at 25 °C, –log Ks	Chemical formula
Monocalcium phosphate monohydrate	MCPM	0.5	1.14	$Ca(H_2PO_4)_2{\cdot}H_2O$
Monocalcium phosphate anhydrous	MCPA or MCP	0.5	1.14	$Ca(H_2PO_4)_2$
Dicalcium phosphate dihydrate (brushite)	DCPD	1.0	6.59	$CaHPO_4{\cdot}2H_2O$
Dicalcium phosphate (montite)	DCPA or DCP	1.0	6.90	$CaHPO_4$
Octacalcium phosphate	OCP	1.33	96.6	$Ca_8(HPO_4)_2(PO_4)_4{\cdot}5H_2O$
α-Tricalcium phosphate	α-TCP	1.5	25.5	$\alpha\text{-}Ca_3(PO_4)_2$
β-Tricalcium phosphate	β-TCP	1.5	28.9	$\beta\text{-}Ca_3(PO_4)_2$
Calcium-deficient hydroxyapatite	CDHA or Ca-def HA	1.5–1.67	~85	$Ca_{10-x}(HPO_4)_x(PO_4)_{6-x}(OH)_{2-x}$ $(0 < x < 1)$
Hydroxyapatite	HA, HAp or OHAp	1.67	116.8	$Ca_{10}(PO_4)_6(OH)_2$
Fluorapatite	FA or FAp	1.67	120.0	$Ca_{10}(PO_4)_6F_2$
Oxyapatite	OA, OAp or OXA	1.67	~69	$Ca_{10}(PO_4)_6O$
Tetracalcium phosphate, mineral hilgenstockite	TTCP or TetCP	2.0	38–44	$Ca_4(PO_4)_2O$

Calcium phosphates have an excellent biocompatibility due to their close chemical and crystal resemblance to bone mineral. They are generally osteoconductive but not osteoinductive, with the exception of porous synthetic and coralline HA, α/ß-TCP and calcium phosphate cements, which shown to have the ability to form

bone in ectopic sites in different animals without the addition of osteogenic factors. However, the mechanism of osteoinductivity remains unknown. It has been studied in relation with physicochemical parameters of the bioceramic such as composition, microporosity, the specific surface area, in addition to the surface topography, geometry, and charge (Canillas et al., 2017; Habibovic et al., 2006; Hannink and Arts, 2011; LeGeros, 2008).

It is believed that the bioactivity of calcium phosphates and new bone deposition on their surface is directly linked to their partial dissolution and the release of their ionic products in vivo. The partial dissolution of calcium phosphates results in an increase in the local concentration of calcium and phosphate ions, thus increasing the degree of saturation in their microenvironment, leading to the precipitation of biological apatite microcrystals on the surface of the implant which link between the host tissue and the bioceramic. Consequently, the apatite microcrystals incorporate other ions such carbonate and magnesium in addition to organic macromolecules from biological fluids. The precipitated apatite may also incorporate various proteins and growth factors exist in the microenvironment, which subsequently can promote cell attachment and function (Canillas et al., 2017; Eliaz and Metoki, 2017).

However, the dissolution rate of calcium phosphates is mainly associated with their chemical composition. In general, the Ca/P ratio of calcium phosphates is considered as an indicator for the stability of the ceramic in the body, thus compounds with a Ca/P ratio of less than one are not favourable for biological implantation due to their high solubility. The dissolution rate of calcium phosphates is also influenced several other parameter such as basicity/acidity and solubility of calcium phosphate compounds (Table 2.5), the porosity in the calcium phosphate and its particle size, local acidity, fluid convection and the temperature and pH of media. Porosity of calcium phosphates does not only affect the resorbability of the bioceramic, but it is also important to its mechanical properties and the ingrowth of bone. Porous calcium phosphate permits cell colonisation and vascularisation. Therefore, calcium phosphates with macro- (>100 μm), micro- (<10 μm) and nano- (<100 nm) porosities have been developed to improve cell adhesion, proliferation and differentiation. In addition, studies have demonstrated that increasing the specific surface area and pore volume of

calcium phosphates can greatly accelerate the kinetic process of biological apatite deposition and therefore enhance the bone formation. In vivo biodegradation of calcium phosphates can also occur due to active resorption, mediated by cellular activity of macrophages and osteoclasts or by phagocytosis, which also known as "cell-eating".

Calcium phosphates are brittle in nature, which is attributed to their primary ionic bonds, and have low impact resistance. However, their compressive strength is fairly good, being higher than that of normal bone. Due to their high brittleness, they have been used either as non-load-bearing implants such as middle ear surgery, filling of bone defects in the oral cavity and skeleton, or as coatings on dental and orthopaedic metallic implants. The mechanical properties of calcium phosphate ceramics are strongly dependent on their chemical composition, crystallinity, grain size/shape and porosity. Generally, their mechanical properties decrease with increasing amorphous phase, microporosity and grain size, while compounds with high crystallinity, low porosity and small grain size exhibit higher stiffness, compressive and tensile strength as well as higher fracture toughness (Canillas et al., 2017; Dorozhkin, 2013; Eliaz and Metoki, 2017; Hannink and Arts, 2011; Hench, 1998; Palmero, 2016). The mechanical properties of the common ceramic biomaterials are listed in table 2.6.

Table 2.6 Mechanical properties of bioceramics (from Patel and Gohil, 2012; Prakasam et al., 2015)

Material	Young's modulus (GPa)	Compressive strength (MPa)	Tensile strength (MPa)
Alumina	380	4500	350
Zirconia	150-200	2000	200-500
Pyrolytic carbon	18-28	517	280-560
Bioglass-ceramics	22	500	56-83
Calcium phosphates	40-117	510-896	69-193

2.2.4.1 Tricalcium phosphate

Two major calcium phosphates have been used extensively for synthetic bone scaffolds; tricalcium phosphate (TCP) and hydroxyapatite (HA).

TCP is a biodegradable bioceramic which has a Ca/P ratio of 1.5 and the chemical formula of $Ca_3(PO_4)_2$. It exists in three different polymorphs: ß-TCP stable at low-temperature (<~1125 °C), α-TCP occurring at high-temperature (~1125–1430 °C) and α`-TCP stable at even higher temperature (>~1430 °C). The latter is not of practical interest since it only exists at high temperatures and reverts almost instantaneously to α-TCP upon cooling below the transition temperature. In contrast, both α and ß-TCP have been widely used in several clinical applications in dentistry, maxillo-facial surgery and orthopaedics due to their stability at low temperatures. ß-TCP is stable at room temperature but transforms at ~1125 °C to α-TCP, which can be retained during cooling to room temperature (Carrodeguas and De Aza, 2011; Frasnelli and Sglavo, 2016; Mirhadi et al., 2011). Despite having the same chemical composition, α-TCP and ß-TCP differ in their solubility. α-TCP shows higher solubility (2.5 mg/L) than ß-TCP (0.5 mg/L) at 25 °C due to its crystal structure and higher specific energy, therefore it is considered unsuitable for surgical implants and usually employed as component for bone cements (Eliaz and Metoki, 2017; Frasnelli and Sglavo, 2016; Yin et al., 2003). Both α and ß-TCP are not found in biological systems, Mg-stabilised ß-TCP (Whitlockite) has been detected during pathological calcification, such as dental calculus formation and in renal stones, as well as in arthritic cartilage. However, pure ß-TCP has not been observed in enamel, dentin, or bone (Eliaz and Metoki, 2017; LeGeros and LeGeros, 1984).

When implanted in living tissue, TCP interacts with body fluids and creates HA on exposed surfaces in accordance with equation 2.1 (Mehdikhani and Borhani, 2014; Mirhadi et al., 2011; Oonishi and Oomamiuda, 2016):

$$4Ca_3(PO_4)_2\ (surface) + 2H_2O \rightarrow Ca_{10}(PO_4)_6(OH)_2\ (surface) + 2Ca^{2+} + 2HPO_4^{2-}$$

Equation 2.1

ß-TCP can be produced by different chemical routes, each which have different advantages and disadvantages. One of the preferred methods for ß-TCP synthesis is wet chemical co-precipitation, due to the simplicity of experimental operations,

low operating temperature and high yields of pure products at a reasonable cost. However, it can results in undesirable impurities in the case of incomplete reaction and precipitation. Sol-gel and solution combustion methods have also been used to produce ß-TCP but they are less familiar than the co-percipitation method. Sol-gel method is favoured over other alternatives due to its excellent homogenous molecular mixing and the ability to produce nano-sized particles. However, the starting material is very expensive and the precursor formed is usually extremely moisture sensitive. Finally, solution combustion is a fast exothermic and energy-saving method comprising a self-sustaining chemical reaction between an oxidant and a suitable organic fuel, in an aqueous solution. The exothermic reaction provides the heat required to maintain the combustion and once initiated no external heat source is required. The various synthesis methods have a large effect on the particle size, crystallite size, densification behaviour, shrinkage and morphology (Fathi et al., 2015; Ghosh and Sarkar, 2016; Ghosh et al., 2008; Mirhadi et al., 2011; Sanosh et al., 2010).

As discussed earlier, calcium phosphates are generally brittle and have low tensile strength, thus they provide limited biomechanical support. While TCPs are less brittle compared with HA, their faster degradation rate results in quicker loss of mechanical strength over time (Hannink and Arts, 2011; Watson, 2015).

2.2.4.2 Hydroxyapatite

HA is the second most stable and least soluble calcium phosphate compound after fluorapatite (FA) (Table 2.5). The stoichiometric HA has a Ca/P ratio of 1.67 and the chemical formula $Ca_5(PO_4)_3(OH)$. However, it is frequently written as $Ca_{10}(PO_4)_6(OH)_2$ to indicate that the hexagonal unit cell is composed of two molecules (Dorozhkin, 2009a; Eliaz and Metoki, 2017). Stoichiometric HA never occurs in biological systems. However, it has been extensively used as a bone graft substitute or as a coating for orthopaedic devices (e.g. hip-joint prosthesis) and dental implants due to its chemical and structural similarity with natural bone mineral. The crystal structure of HA can accommodate a variety of cationic and anionic substitutions by various other ions for the Ca^{2+}, PO_4^{3-} and OH^- groups. These ionic substitutions can have a significant effect on the lattice parameters

(i.e. physical dimension of unit cell), crystal morphology, crystallinity, solubility and thermal stability of HA. It can also affect the osteoclastic and osteoblastic response in vitro and degradation and bone regeneration in vivo (Best et al., 2008; Dorozhkin and Epple, 2002; Shepherd et al., 2012). The most abundant apatite found in bone is the carbonate substituted apatite with a carbonate content of 3-8 wt%, thus its Ca/P ratio is less than 1.67 which makes it more soluble than pure HA. Carbonate (CO_3^{2-}) can substitute either hydroxyl (OH^-) groups (Type A), or phosphate (PO_4^{3-}) groups (Type B) (Best et al., 2008; Huang, 2017; LeGeros and LeGeros, 2013). Table 2.7 compares the composition of human enamel and bone and pure HA ceramic.

Table 2.7 Comparison between the composition of human enamel, bone and hydroxyapatite ceramic (from Dorozhkin and Epple, 2002; LeGeros and LeGeros, 2013)

	Enamel	Bone	Stoichiometric HA
Constituents (wt%)			
Calcium	36.0	34.8	39.6
Phosphorous	17.7	15.2	18.5
Sodium	0.5	0.7	-
Potassium	0.08	0.03	-
Magnesium	0.44	0.55	-
Carbonate	3.2	5.8	-
Fluoride	0.01	0.02	-
Chloride	0.30	0.10	-
Ash (total inorganic)	97%	65%	100%
Ca/P molar ratio	1.62	1.71	1.67

HA can be synthesised using different techniques such as dry methods (solid-state reactions), wet methods (precipitation, hydrolysis, sol-gel, emulsion and hydrothermal synthesis) and alternate energy input methods (microwave (MW)-assisted, ball-milling and sonochemical methods). Depending on the preparation technique, HA with various morphology (blades, needles, rods, or equiaxed

particles), particle size (micro or nanoscale), stoichiometry and level of crystallinity can be obtained. Among those techniques, the precipitation method is the most straightforward and commonly used method for the preparation of HA. It comprises a reacting source of PO_4^{3-} ligand with a source of calcium in the presence of other additives such as base or acid. Different sources of these two reagents are used and the process is usually carried out at pH values ranging from 3 to 12 and at temperatures ranging from room temperature to the boiling temperature of water. However, this method can often produce non-stoichiometric HA ($Ca/P \neq 1.67$). On the other hand, solid state reactions are also widely used for HA synthesis and usually yield a stoichiometric and well-crystallised product. However they require relatively high temperatures and long heat-treatment times (Fihri et al., 2017; LeGeros and LeGeros, 2013; Suchanek and Yoshimura, 1998).

HA can also extracted from natural resources such as fish bones, seashells, eggshells, bovine bones and shrimp shells. It can be produced in dense or macroporous form (Szcześ et al., 2017). Dense HA possesses a porosity of less than 5% and can also be described as microporous. The powder is compressed into a mold at a pressure of 60-80 MPa, with or without a binder (e.g. 1 wt% cornstarch and water, stearic acid in alcohol, or hydrocarbons of low molecular weight). Then, the compressed material can sintered at the high temperature, usually 950-1300 °C, at fixed heating rate (~100 °C per hour) and held at this temperature for several hours before cooling at the same rate as the heating rate. Another method for producing dense HA is the hot pressing technique where heat and pressure are applied at the same time in a continuous manner, which allows the densification of HA to occur at a much lower temperature than in conventional sintering, thus producing HA with higher purity and lower grain size. Dense HAs are usually used in unloaded tooth root substitutes due to their poor mechanical properties. On the other hand, porous HA has been widely applied as bone substitute due to its strong bonding to the bone. In addition, the pores provide a mechanical interlock which results in a firmer fixation of the material. Porous HA with pores <10 μm in diameter is required for circulation of body fluids and those >100 μm are required for colonisation of target cells. However, such large pores decrease strength of the implant significantly. Therefore, porous HA implants cannot be heavy loaded and are used to fill only small bone defects. Other applications of porous HA

include drug delivery systems, alveolar ridge augmentation and orthognatic reconstruction (Islam et al., 2017; LeGeros and LeGeros, 2013; Suchanek and Yoshimura, 1998).

The stoichiometry of HA is highly important where thermal processing of the material is needed. A slight decrease in the stoichiometric ratio of calcium and phosphorus in HA can cause the formation of either α- or ß-tricalcium phosphate upon sintering. Existence of TCP phases was shown to improve the mechanical behaviour of HA and increase its biodegradability. In contrast, if the Ca/P ratio of the HA exceeds the value of 1.67, CaO forms during sintering. The presence of CaO is reported to decrease strength of the material and may even lead to decohesion of the whole material because of the build-up of stresses arising from formation of $Ca(OH)_2$ which eventually transforms into $CaCO_3$, and related volume changes (Eliaz and Metoki, 2017; Hench and Best, 2013; Royer et al., 1993; Ślósarczyk et al., 1996; Suchanek and Yoshimura, 1998).

The dissolution rate of HA in vitro depends on the type and concentration of buffered or unbuffered media, pH of the solution, the crystallinity of HA and the amount of non-HA phases, the degree of micro- and macroporosity, and solid/solution ratio. The degree of dissolution decreases in the following order (LeGeros and LeGeros, 2013; Oonishi et al., 1999; Palmero, 2016):

Amorphous HA>> α-TCP>> ß-TCP>> crystalline HA

Similar to other calcium phosphates, the formation of apatite microcrystals on HA-based implants is believed to be a dissolution-precipitation process. However, the partial dissolution of HA arises from the cellular activity, causing the release of Ca^{+}, HPO_4^{2-}, and PO_4^{3-} and increase the supersaturation of the microenvironment, and subsequently results in apatite formation (LeGeros and LeGeros, 2013).

The mechanical properties of HA depends mainly on the form (dense or porous), particle size, sintering condition and the presence of non-HA phases. Table 2.8 summarises the mechanical properties of HA ceramic.

Table 2.8 Mechanical properties of HA bioceramics (from Eliaz and Metoki, 2017; Suchanek and Yoshimura, 1998)

Property	Value	Comments
Tensile strength	38–300 MPa ~3 MPa	Dense HA Porous HA
Compressive strength	120–900 MPa 2-100 MPa	Dense HA Porous HA
Bending strength	38–250 MPa 2–11 MPa	Dense HA Porous HA
Young's modulus	35–120 GPa	Dense HA
Fracture toughness	0.7–1.2 MPa√m	Decreases almost linearly with porosity
Vickers hardness	3–7 GPa	Dense HA
Poisson's ratio	0.27	Synthetic HA (bones ~0.3)

2.2.5 Polymers

Polymers are large organic macromolecules comprising of repeating units called ''mers'' which are covalently bonded chains of atoms. These macromolecules interact with one another by weak secondary bonds such as hydrogen and van der Waals bonds to form entanglement structures. Due to the covalent interatomic bonding within the molecules, polymers exhibit low thermal and electric properties. Their thermal and mechanical behaviour is influenced by a number of factors, including the composition of the backbone, chemical side groups, chain structures and molecular weight.

Polymers are the most versatile class of biomaterials, being widely used in biomedical applications such as contact lenses, drug delivery systems, dental implants and fillings, and bone tissue engineering as well using them in surgical devices. Compared to metals and ceramics biomaterials, polymers are easy to manufacture to the desired shape. They also have good biocompatibility and flexibility, and are available with different physical and mechanical properties (Park and Lakes, 2007a; Yoruç and Cem, 2012). Polymers used in medical applications can be classified into two major categories: degradable and non-degradable polymers.

Non-degradable polymers (also called biostable polymers) were used for various applications in medicine such as dental fillings, heart valves, ocular lenses and drug delivery systems. Their main advantages includes: stability, durability, good

biocompatibility, and excellent mechanical properties, examples of non-degradable polymers are : poly(ethylene) (PE), poly(propylene) (PP), poly(sulfone) (PS), poly(tetrafluoroethylene) (PTFE), poly(methyl methacrylate) (PMMA), poly(dimethylsiloxane) (PDMS), poly(ethylene terphthlate) (PET) and polyurethanes (Subramaniam and Sethuraman, 2014).

Biodegradable polymers, on the other side, degrade non-toxically in the body either enzymatically, or hydrolytically. They include natural and synthetic polymers. Natural polymers can be considered as the first biodegradable biomaterials used clinically. The major natural polymers currently in use are protein-based (e.g. collagen, elastin, gelatin, silk, albumin, fibrin and keratin) and polysaccharide-based polymers (e.g. chitosan, alginic acid, cellulose and hyaluronic acid). Natural polymers are usually bioactive and enzymatically degradable, thus the rate of their in vivo degradation varies significantly with the site of implantation depending on the availability and concentration of the enzymes. Chemical modification of natural polymers can also influence their rate of degradation. Natural polymers have several inherent advantages such as bioactivity, the ability to present receptor-binding ligands to cells, susceptibility to cell-triggered proteolytic degradation and natural remodelling. However, they have some disadvantages such as possible immunogenicity (due to their bioactivity), structural complexity and inferior biomechanical properties (Nair and Laurencin, 2007; Tang et al., 2014).

In contrast, synthetic polymers are commonly bioinert and have more predictable properties and batch-to-batch uniformity than natural polymers. They are generally hydrolytically degradable with the ability to tailor their properties according to the specific application, thus they offer minimal site to-site and patient to-patient variations compared to enzymatically degradable polymers. However, some synthetic polymers are also susceptible to enzymatic degradation. For instance, amorphous poly(l-lactide) can be degraded by proteinase K, while both amorphous and crystalline poly(ε-caprolactone) can be degraded by lipases of various origins. Biodegradable synthetic polymers include polyanhydrides, poly(ortho ester)s, polyurethanes, poly(ester amide)s, polyphosphazenes, polyphosphoesters, poly(ethylene glycol), poly(propylene fumarate) and poly(α-hydroxy ester)s which is the most extensively used in tissue engineering applications (e.g. polycaprolactone (PCL), poly(lactic acid) (PLA), poly(glycolic acid) (PGA), and their copolymer polylactic-co-glycolic acid (PLGA),

poly(trimethylene carbonate) (PTMC), and bacterial polyesters such as polyhydroxybutyrate (PHB) and polyhydroxybutyrate-valerate (PHBV)). Biodegradable polymers are commonly used in soft and hard tissue engineering, drug delivery systems, and gene therapy (Table 2.9) (Karak, 2012; Lin and Anseth, 2013; Nair and Laurencin, 2007; Tang et al., 2014). Figure 2.15 shows the main properties of common natural and synthetic biodegradable polymers.

Table 2.8 Biodegradable polymers and their current major research applications (from Treiser et al., 2013)

Polymer	Applications
Natural degradable polymers	
Collagen	Drug delivery, gene delivery, artificial skin, coatings to improve cellular adhesion, guided tissue regeneration in dental applications, spinal dural repair, orthopaedic applications, soft tissue augmentation, tissue engineering, scaffold for reconstruction of blood vessels, wound closure, haemostatic agents
Fibrinogen and fibrin	Tissue sealant, cell delivery
Elastin	Drug delivery, coating of vascular grafts
Gelatin	Capsule coating for oral drug delivery, haemorrhage arrester
Hyaluronic acid	Wound dressing applications, drug delivery, tissue engineering, synthetic bone grafts, synovial fluid substitutes
Polysaccharides such as chitosan, alginate	Drug/vaccine delivery, encapsulation of cells, sutures, wound dressings/healing
Synthetic degradable polyesters	
Poly(glycolic acid) (PGA), poly(lactic acid) (PLA) and copolymers	Barrier membranes, drug delivery, hormone delivery, guided tissue regeneration (in dental applications), orthopaedic applications, vascular/urological stents, staples, sutures, injectable fillers, dura mater substitutes, skin replacement materials, tissue engineering
Poly(hydroxybutyrate) (PHB), poly(hydroxyvalerate) (PHV) and copolymers	Long-term drug delivery, orthopaedic applications, stents, artificial skin, surgical patching materials for congenital heart defects, sutures
Polycaprolactone (PCL)	Long-term drug delivery, implantable contraceptive drug devices, orthopaedic applications, staples, stents
Polydioxanone (PDS)	Fracture fixation in non-load-bearing bones, sutures, wound clips

Other Synthetic Degradable Polymers	
Polyanhydrides	Drug delivery
Poly(amino acid)s and "pseudo"-poly(amino acid)s	Drug delivery, tissue engineering, orthopaedic applications, stents, anti-adhesion barriers
Poly(ortho ester) (POE)	Drug delivery, and stents
Polyphosphazenes	Blood contacting devices, drug delivery, skeletal reconstruction, vaccine adjuvants
Poly(propylene fumarate) (PPF)	Orthopaedic applications

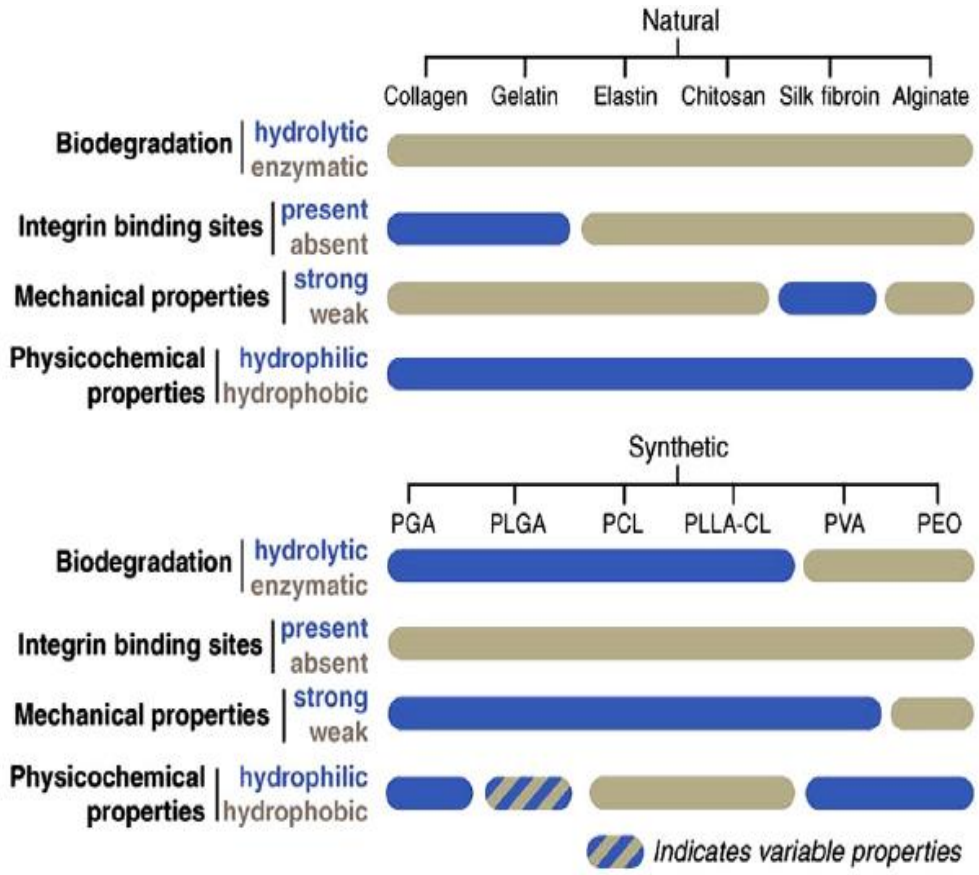

Figure 2.15 Commonly used biodegradable polymers, comparing the of activity levels of different properties (from Kai et al., 2014)

2.2.5.1 Modes of biodegradation

One of the most essential requisites to evaluate the performance of the therapeutic polymeric device is to understand the way it degrades/erodes in the implant site (Treiser et al., 2013). Biodegradable polymers can be classified according to their biodegradation modes into two classes: surface (or heterogeneous) and bulk (or homogeneous) degrading materials (Figure 2.16) (Göpferich, 1996). In surface biodegradation, the erosion of the polymer is restricted to the surface of the material only, hence the material loses its thickness with time while keeping its structural integrity throughout most of the degradation process (Göpferich and Tessmar, 2002; Treiser et al., 2013). Surface erosion take place when the rate of bond cleavage (hydrolysis) is higher than the rate of water diffusion into the polymer (Lin and Anseth, 2013). It occurs in polyanhydrides and poly(ortho esters) polymers due to their hydrophobic nature which excludes water from the bulk of the polymer (Sackett and Narasimhan, 2011). Polymers that undergo surface biodegradation are desirable for drug delivery applications, where the rate of drug release can be directly related to the polymer erosion rate and the system can easily achieve zero-order drug release (Göpferich, 1996; Lin and Anseth, 2013).

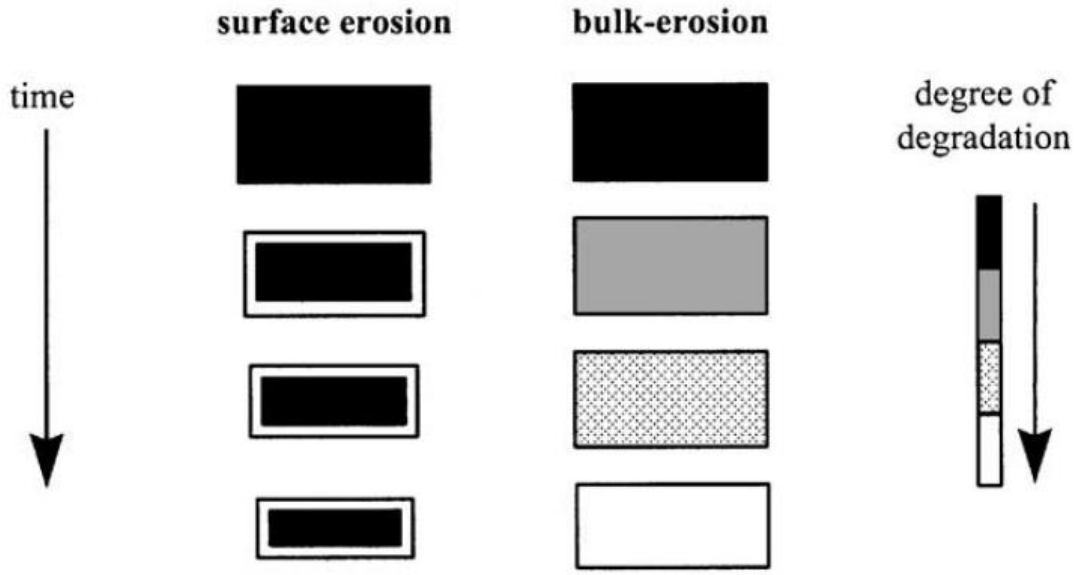

Figure 2.16 Schematic illustration of surface and bulk erosion (from Von Burkersroda et al., 2002)

In contrast to surface erosion, bulk erosion occurs when the rate of water diffusion into the material is faster than rate of polymer hydrolysis. As a result, the erosion happens throughout the material causing sudden and rapid loss of structural integrity and mechanical strength, in addition to molecular weight changing and water content increasing in the polymer followed by soluble monomers and chain fragments release (Gajjar and King, 2014). This type of degradation occurs in poly(α-hydroxy esters) such as PLA, PGA and PLGA (Lin and Anseth, 2013).

The mode of biodegradation for polymeric-based scaffolds not only depends on the rate of hydrolysis of the functional groups in the backbone chain and the rate of diffusion of water inside the matrix, but also on the dimensions of the matrix or "the critical thickness" of the polymeric materials, which was suggested by Von Burkersroda et al. (2002) and has been calculated for a selection of polymers (Table 2.10). If the thickness of the material is higher than the critical thickness, then it will undergo surface erosion, while below this critical thickness will undergo bulk erosion (Gajjar and King, 2014; Von Burkersroda et al., 2002).

Table 2.10 Critical thickness ($L_{critical}$) values for selected biodegradable polymers (from Gajjar and King, 2014)

Polymer	$L_{critical}$
Poly(anhydride)	75 μm
Poly(ketal)	0.4 mm
Poly(ortho esters)	0.6 mm
Poly(ε-caprolactone)	13 mm
Poly(acetal)	24 mm
Poly(α-hydroxy esters)	74 mm
Poly(amides)	13.4 m

2.2.5.2 Factors affecting biodegradation

Biodegradation of synthetic polymers is governed by a large number of factors which can be categorised as follows:

1. Polymer characteristics: which include polymer morphology, the initial molecular weight and molecular weight distribution of the polymer, the type of hydrolytically-susceptible groups in the backbone of the polymer and their chemical stability, the hydrophilic-hydrophobic character of the repeat units, and the type of additives added to the polymer (Shah et al., 2008). The molecular weight has a strong impact on both the chemical and physical properties of a polymer because it determine chain mobility and crystallization as well as determining the number of acidic groups that participate in hydrolysis process. In addition, the polymers remain relatively immune to microbial attack while their molecular weight remain high. So in summary, biodegradation has an inverse relationship with the molecular weight of the polymer (Chandra and Rustgi, 1998; Göpferich, 1996).

   Additionally, the type of chemical bond in the polymer backbone plays a crucial role in determining the rate of biodegradation. Anhydride bonds are the most susceptible to hydrolysis, then comes the carbonate, ester, urethane, ortho ester and finally the amide bonds (Figure 2.17). Therefore, poly(anhydrides) degrade faster than polyesters which in turn, degrade faster than polyamides (Gombotz and Petite, 1995; Treiser et al., 2013).

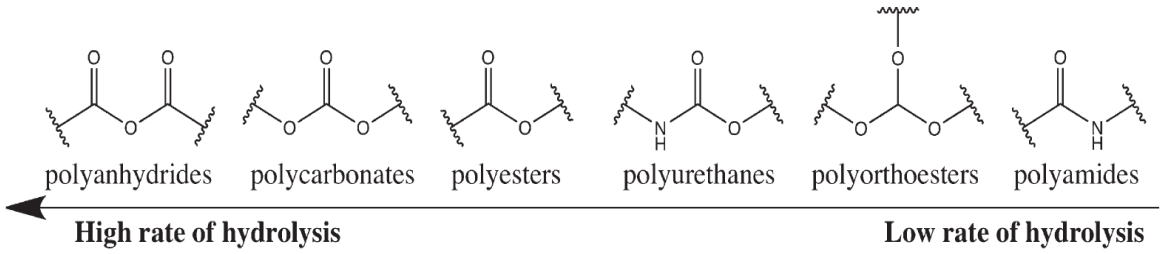

Figure 2.17 Relative hydrolytic susceptibility of degradable bonds (from Treiser et al., 2013)

The hydrophilic- hydrophobic character of the polymer is another key factor in the observed erosion rate because degradation depends strongly on water ability to penetrate into the polymer matrix. This character is mainly dependent on the monomeric starting materials of the polymer. Tamada

and Langer (1993) noted that the degradation rate of poly(anhydrides) is slowed by about three orders of magnitudes when they replaced sebacic acid, which has low hydrophobicity, by bis(carboxy phenoxy) propane (more hydrophobic) as the monomeric starting material.

Moreover, the erosion rate is highly affected by the morphology of the polymer. Polymers can either be semicrystalline, or amorphous. Polymer chains in crystalline state are densely packed and organised in crystalline domains, therefore, they have high resistance to water penetration and enzymes attack leading to slower degradation rate. Amorphous polymers, on the other hand, are loosely packed, thus, they are more susceptible to water ingress and thus degradation (Tokiwa et al., 2009). The impact of polymer morphology on biodegradation could be well noted by comparing poly(L-lactic acid) and poly(D,L-lactic acid) polymers. Though both polymer have the same chemical bonds in their backbone, poly(L-lactic) degrades more slowly than poly(D,L-lactic acid) due to its semicrystallinity, while poly (D,L-lactic acid) is an amorphous polymer so it has faster degradation rate (Lin and Anseth, 2013).

2. Preparation technique: manufacturing technique can have a significant effect on degradation rate as it could affect the morphology and chemical properties of the polymer. For example, Mathiowitz et al. (1990) observed that the erosion rate of densely packed polyanhydride microspheres prepared by melt encapsulation method is slower than that of porous polyanhydride microspheres produced by solvent evaporation. Similarly, Giunchedi et al. (1998) found that PDLA and PLGA particles prepared by spray-drying technique are characterised by a higher monomer release rate than PDLA and PLGA particles obtained by solvent evaporation technique.

3. Sterilisation and packaging: to reduce the risk of infection and associated complications, it is essential to sterilise all medical implants post-fabrication and pre-implantation. There are various techniques for sterilisation, such as: heat, steam, radiation, or some combination of these methods. Choosing the right method for sterilisation can affect the physical and mechanical performance of polymer in vivo. PLA and PGA polymers, for example, are sensitive to heat and moisture, as well as being susceptible

to damage by γ-radiation because it causes chain scission in both polymers leading to increasing degradation rates and decreased tensile strength. Therefore, the chemical sterilisation by gases such as ethylene oxide (EtO) is considered the best method to sterilize those polymers, but it should be noted that the polymers must be subjected to degassing or aeration after sterilisation to remove or reduce the residual EtO concentrations on the surface of the polymer which could be harmful if accumulated in high quantities (Cameron and Kamvari-Moghaddam, 2012). Biodegradable implants are usually packed in air-tight aluminum-backed plastic foil bags, sealed using either inert gas or vacuum. Refrigeration might be required in some cases to prevent backbone degradation of the polymers during storage (Treiser et al., 2013).

4. Environmental conditions: It is also crucial to take into account the medium conditions such as pH and temperature, since they have an impact on both the properties of the polymer and of the enzymes (Azevedo and Reis, 2004). A considerable amount of literature has been published on the effect of medium conditions on the degradation process. According to Göpferich (1996), the breaking strength of PGA and PLA was found to be the highest at neutral pH, while low pH causes faster chain scission due to autocatalysis. Similarly, poly(ortho esters) degrade faster in acidic medium compared to neutral and basic environments. On the other hand, the degradation rate of poly(bis-(p-carboxyphenoxy)propane anhydride) cylinders increased by a factor of 10 when the pH of the degradation medium increased from 7.4 to 10. Li and McCarthy (1999) have investigated the effect of temperature and pH on the hydrolytic degradation of PDLA polymer. They noticed very rapid increase in degradation rate due to increasing the temperature of the media from 37ºC to 60ºC, while decreasing the pH from 7.4 to 3.7 decelerated sharply the degradation rate. Dunne et al. (2000) have also studied the influence of media temperate on the degradation of PLGA particles. The molecular weight loss was found to increase with increasing incubation temperature, which consequently resulted in increasing erosion rate. Finally, Li et al. (2008) examined the effect of pH on the degradation mechanism of Poly(dl-lactide-co-glycolic acid)-methoxypoly(ethyleneglycol) (PLGA-mPEG) micro- particles. By

increasing the pH to 10.08, the particles exhibited surface degradation with slow molecular weight decrease and rapid weight loss. However, at pH 7.4, and pH 1.2, particles showed heterogeneous and homogenous bulk degradation, respectively.

2.2.5.3 Polylactic acid (PLA)

Among the family of biodegradable polyesters, polylactic acid (PLA) is the most extensively researched and used aliphatic polyester as it has high biocompatibility, good mechanical performance compared to other synthetic polymers and can be produced from renewable resources, such as corn starch, tapioca roots, chips or starch, or sugarcane (Ghanbarzadeh and Almasi, 2013; Kariduraganavar et al., 2014). The basic chemical structure of PLA is shown in Figure 2.18.

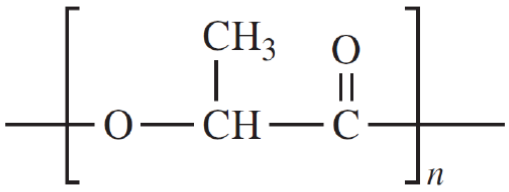

Figure 2.18 Chemical structure of polylactic acid (n= central repeat unit) (from Ghanbarzadeh and Almasi, 2013; Treiser et al., 2013)

The starting compound, lactic acid or lactide (2-hydroxy propionic acid), is a chiral molecule which has the chemical formula of CH_3-CHOHCOOH and exists in two optically active forms or enantiomers; L-lactide and D-lactide (Figure 2.19). The polymerisation of these monomers results in the formation of three PLA stereoisomers; poly(L-lactide) (PLLA), poly(D-lactide) (PDLA), and poly(DL-lactide) (PDLLA). The crystallinity of PLLA is around 37% and it depends on the molecular weight and polymer processing parameters. PLLA has a glass transition temperature in the range 60-65°C, a melting temperature around 173-178°C, and a tensile modulus of 2.7-16 GPa. Modulation of PLLA melting temperature and heat deflection temperature can be achieved by physically blending the polymer with PDLA (poly-D-lactide) as PDLA acts as a nucleating agent, thus increasing the crystallisation rate. In general, PLLA is more frequently used clinically than PDLA,

since the hydrolysis of PLLA yields L(+) lactic acid, which is the naturally occurring stereoisomer of lactic acid. It is also preferred in applications where high mechanical strength and toughness are required, such as sutures and orthopaedic devices. (Kariduraganavar et al., 2014; Lopes et al., 2012; Nair and Laurencin, 2007; Treiser et al., 2013).

Figure 2.19 3D structures of L- and D-lactic acids, noting that ▲ indicates a bond out of the page (toward the viewer) and ≡ is a bond going behind the page (away from the viewer) (from Pretula et al., 2016)

On the other hand, PDLLA is an amorphous polymer due to the random dispersion of L- and D-lactide units and has a glass transition temperature of 55–60 °C. The amorphous nature of PDLLA results in much lower strength (~1.9 GPa) compared to PLLA. It also loses its strength within 1–2 months when hydrolysed and undergoes a loss of mass within 12–16 months. Therefore, it is usually considered for applications such as drug delivery or low strength scaffolding, where it is important to have a homogeneous dispersion of the active species within the carrier matrix (Maurus and Kaeding, 2004; Nair and Laurencin, 2007; Treiser et al., 2013).

In addition to the degree of crystallinity, the mechanical properties of semicrystalline polylactides are also affected by their molar masses and additives. For instance, it has been shown that PLA with molar mass of 100,000 has tensile strength and tensile modulus about 2-times higher than polymer with Mn = 50,000 (Pretula et al., 2016). The mechanical properties of some commercial PLAs are listed in Table 2.11.

Table 2.11 Mechanical properties of some commercial PLAs (differences are due to various molar masses, crystallinity and additives) (from Pretula et al., 2016)

Polymer	Modulus of elasticity GPa	Tensile strength MPa
Biopearls M106	2.6	49
LACEA H-100J	3.7	70
PLA Polymer 2002D	3.5	60
PLA Polymer 3001D	3.8	48
PLA Polymer 3051D	3.8	48

PLA can be synthesised by different polymerisation routes from lactic acid (Figure 2.20) including: polycondensation, ring opening polymerisation and by direct methods like azeotopic dehydration and enzymatic polymerisation. Currently, ring opening polymerisation and direct polymerisation are the most commonly used production techniques (Garlotta, 2002; Lopes et al., 2012).

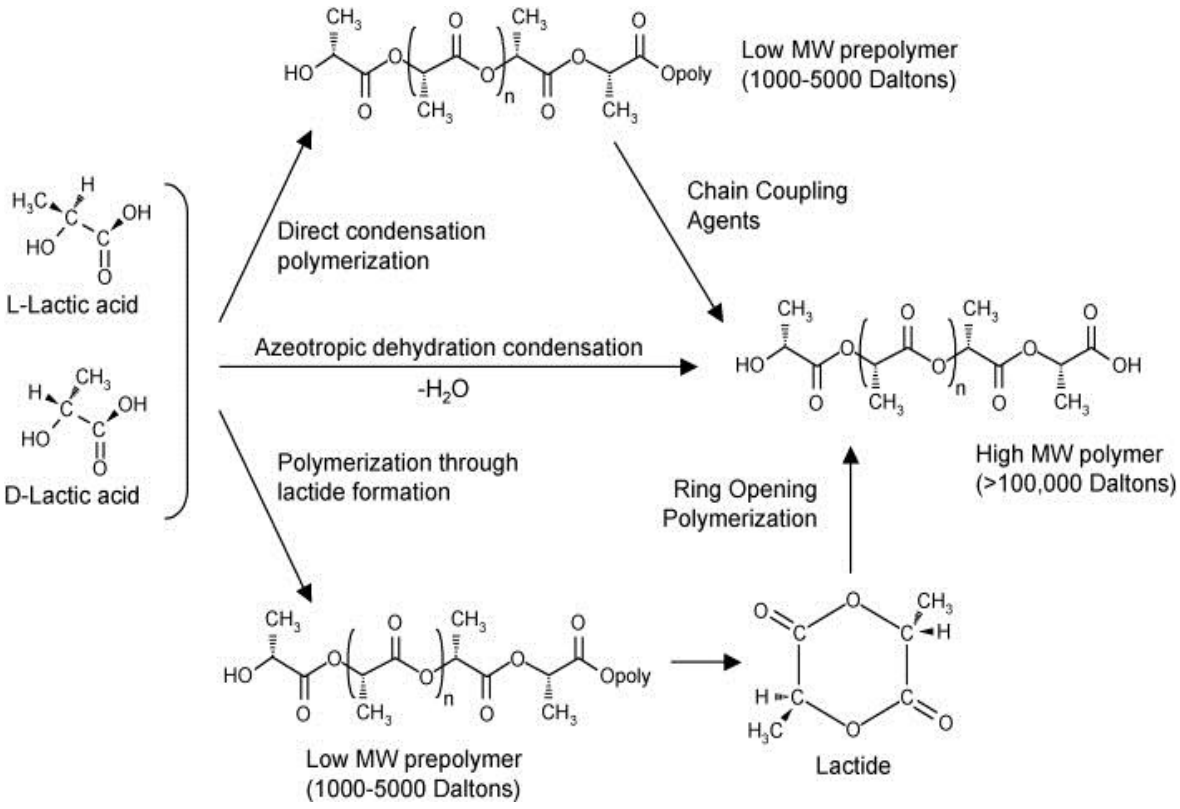

Figure 2.20 Synthesis methods for of polylactic acid (1 Dalton= 1g/mol) (from Garlotta, 2002; Lim et al., 2008)

Condensation polymerisation is the least expensive method for PLA synthesis. However, condensation of lactic acid results in brittle, glassy low molecular weight PLA which unsuitable for any application unless external coupling agents are added to increase the molecular weight and obtain a solvent-free PLA, which consequently leads to increasing costs for the products and complexity of the process. Azeotropic condensation, on the other hand, does not require coupling agents and PLA is produced by a direct condensation while the condensation water is continuously removed by the azeotropic distillation. The process includes reduction of the distillation pressure of lactic acid for 2–3 h at high temperature (130°C) which removes the majority of the condensation water. Catalyst is added along with diphenyl ester. A tube packed with 3Å (0.3nm) molecular sieves is attached to the reaction vessel, and the solvent is returned to the vessel via the molecular sieves for an additional 30–40 h at 130°C. Finally, the polymer is isolated as is or it is dissolved and precipitated for further purification (Castro-Aguirre et al., 2016; Garlotta, 2002).

Ring opening polymerisation of the lactide can be carried out using cationic, anionic and coordination-insertion mechanisms depending on the catalyst, but results in PLA with controlled molecular weight. It is also possible to control the ratio and sequence of D- and L-lactic acid units in the final polymer by modulating the monomer and reaction conditions (Kariduraganavar et al., 2014; Lopes et al., 2012).

Solubility of PLA depends on several factors such as polymer molecular weight, isomeric composition, degree of crystallinity, type of solvent and temperature. Therefore, any list of solvents of polylactides should be treated merely as an indicator as, for some polymer samples, solubility may differ from general expectations. For instance, PDLLA is soluble in xylene, ethyl acetate, tetrahydrofuran, chloroform, methylenedichloride, methylethyl ketone, furan, acetone, 1,4-dioxan, ethyl lactate, 1,3-dioxolane, pyridine, dimethylsulfoxide, N,N-dimethylformamide and acetonitrile. PLLA, on the other hand, is hardly soluble in xylene, ethyl acetate, tetrahydrofuran, methylethyl ketone, acetone, and dimethylsulfoxide as they cause polymer swelling and stable solutions can only be obtained at low polymer concentrations (Pretula et al., 2016).

PLA degrades hydrolytically by random backbone scission of the polymer chains. The ester bond of PLA is cleaved by water to form low molecular weight, water soluble oligomers monomers and ultimately, lactic acid. Equation 2.2 shows the hydrolysis of the ester groups of aliphatic polyesters, as in PLA or PCL, in the presence of water (Castro-Aguirre et al., 2016; Chakaravarthi and Robinson, 2009):

$$R\text{-}COO\text{-}R` + H\text{-}OH \rightarrow R\text{-}COO\text{-}H + R`\text{-}OH \qquad \text{Equation 2.2}$$

The hydrolysis of PLA is autocatalytic in acidic and alkaline media because the degradation produce free acidic carboxyl groups that lowers the pH of the media, thereby accelerating the reaction. PLA hydrolysis occurs in two stages; firstly, the PLA matrix absorbs water and water molecules diffuse into the amorphous regions, which in turn initiates cleavage of the ester bonds and results in formation of low molecular weight polymer products. Polymer degradation starts at the surface of the matrix and then proceeds to the core. The formation of oligomers promotes the second stage of PLA degradation, autocatalysis. However, oligomers formation has another effect on the degradation process, as it also increases the crystallinity of the polymer which decreases hydrolytic degradation. Hence, an exponential increase in the rate of autocatalysis leads to significant loss of the amorphous polymer while the crystalline region is conserved. This in turn causes a loss in the mechanical integrity of the polymer with increased formation of cracks and voids. The remaining crystalline regions of polymer matrix, or “crystalline residues”, have very low hydrolytic degradation, thus they are expected to remain for a long period. The degradation of PLA eventually produces lactic acid, which participates in the tricarboxylic acid cycle and is excreted from the body as CO_2 and H_2O (Castro-Aguirre et al., 2016; Chakaravarthi and Robinson, 2009; Tsuji, 2009).

The hydrolytic degradation of PLA depends on numerous factors which can be classified as polymer-dependant properties, environmental factors and device-related factors (Table 2.12).

Table 2.12 Factors affecting the hydrolytic biodegradation of PLA (from Chakaravarthi and Robinson, 2009; Tsuji, 2009; Vert et al., 1992)

Category	Factors
Polymer properties	Chemical structure and composition Crystallinity and crystalline region thickness Presence of ionic groups Presence of unexpected units or chain defects Molecular weight and distribution (polydispersity) Presence of low molecular weight compounds (monomer, oligomers, solvents, drugs, etc.) Method of polymerisation Morphology (amorphous vs. semicrystalline) Hybridisation (blends and composites)
Environmental factors	Storage history Site of implantation Temperature of the media Ionic strength pH Buffer concentration Adsorbed and absorbed compounds (water, lipids, ions, etc.)
Device properties	Shape and dimension Porosity

PLA can also be degraded enzymatically by various classes of enzymes including proteases, depolymerases and lipases. The degradation occurs when the surface-binding domain of enzyme adsorbs into the polymer and initiates hydrolysis of the ester bond. It has been reported than the PLA-degrading enzymes selectively cleave the α-ester bond of the L-isomer of PLA due to the structural similarity of L-lactic acid unit of PLA with L-alanine of silk fibroin which degrades enzymatically as with other natural polymers (Chakaravarthi and Robinson, 2009). Enzymatic degradation of polymers, in general, is a heterogeneous process which depends on the mode of interaction between the enzymes and the polymer chains. Thus, it is affected by the inherent characteristics of a specific enzyme (activity, stability, local concentration, amino acid composition and 3-D conformation) in addition to the polymer-dependant factors and environment properties previously mentioned in Table 2.12 (Azevedo and Reis, 2004).

2.2.5.4 Poly(ε-caprolactone) (PCL)

Polycaprolactone (PCL) is a biocompatible, semicrystalline aliphatic polyester produced by ring-opening polymerisation of a relatively cheap cyclic monomer called ε-caprolactone (Figure 2.21). A wide variety of catalysts for the ring opening polymerisation of caprolactone has been explored (metal-based, enzymatic and organic systems). Stannous octoate ($SnOct_2$) is the predominantly used catalyst for ring-opening polymerisation of cyclic esters used for biomedical applications due to its low toxicity, while low molecular weight alcohols are used to control the molecular weight of the polymer (Azimi et al., 2014; Labet and Thielemans, 2009; Nair and Laurencin, 2007; Sobczak, 2012). PCL can also be synthesised through polycondensation of 6-hydroxycaproic (6-hydroxyhexanoic) acid under vacuum, thus removing the water produced during the reaction and displacing the equilibrium towards the formation of the polymer. However, open ring polymerisation is the preferred route for PCL synthesis because it gives a polymer with higher molecular weight and lower polydispersity. The number average molecular weight (Mn) of PCL generally range from 3,000 to 80,000 g/mol (Labet and Thielemans, 2009).

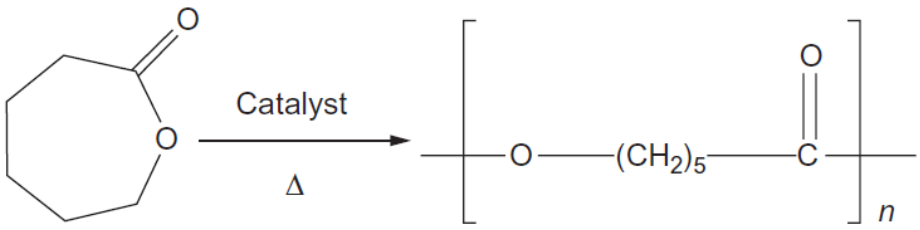

Figure 2.21 Ring opening polymerisation of ε-caprolactone to polycaprolactone (from Kariduraganavar et al., 2014)

PCL has a low melting point (55-60 °C) and glass transition temperature (-60 °C) with the ability to form miscible blends with wide range of polymers. It is also soluble in large range of solvents such as chloroform, dichloromethane, carbon tetrachloride, benzene, toluene, acetone, cyclohexanone and 2-nitropropane at room temperature. PCL is a biodegradable polymer which undergoes hydrolytic degradation due to the presence of hydrolytically labile aliphatic ester linkages. However, the rate of PCL biodegradation is rather slow, ranging from few months to several years depending on the molecular weight, the degree of crystallinity

and the conditions of degradation. The degradation process of PCL in vivo occurs in two stages: the first stage involves the non-enzymatic hydrolytic cleavage of ester groups, resulting in increased polymer crystallinity while decreasing its molecular weight. Once the molecular weight is reduced to below 3000 g/mol, the polymer undergoes intracellular degradation, this was observed experimentally with PCL fragments uptake in phagosomes of macrophages and giant cells and within fibroblasts (Azimi et al., 2014; Nair and Laurencin, 2007; Woodward et al., 1985).

As for the mechanical properties, PCL has low tensile strength (21-42 MPa) and tensile modulus (0.21-0.44 GPa), however it has an extremely high elongation at breakage (300–1000%) which makes it a very good elastic biomaterial when used alone or with polymer blends. It can also serves as an impact modifier to toughen brittle biodegradable polymers such as PLA (Zhang et al., 2017) .

Additionally, PCL has a high drug permeability, thus it was initially investigated as a long-term drug/vaccine delivery vehicle. It has been approved by the Food and Drug Administration (FDA) for specific applications used in the human body such as a drug delivery device and surgical suture. The long-term contraceptive device Capronors is PCL-based and has been developed for the long-term zero order release of levonorgestrel. Due to its high biocompatibility and slow degradation, PCL has also been widely investigated as scaffolds for tissue engineering where long degradation times are required (Nair and Laurencin, 2007; Treiser et al., 2013; Zhang et al., 2017).

2.2.6 Composites

A composite material is composed of two or more materials of different mechanical, chemical or physical properties which remain separate at the macroscopic level in the composite structure. Thus, metal alloys and polymer blends are not composites, based on this definition, because for example, in stainless steel the carbon, chromium, nickel and molybdenum atoms are dispersed throughout the iron atoms so the atoms are interacting together to give the properties of the alloy, while in polymer blends individual polymer chains interact. Composites are made to optimise one or more of the material properties of the

individual phases and to overcome any deficiencies of these phases such as the lack of mechanical strength or bioactivity (Dorozhkin, 2009b; Tanner, 2009). They normally consist of one continuous phase called the matrix, one or multiple discontinuous phases called the reinforcement(s) and in some cases, an interphase between the matrix and reinforcement for the adhesion between the two phases (Yoruç and Cem, 2012). The matrix usually supports the discontinuous reinforcement and distribute the loads over it while the reinforcement(s) work(s) mainly to enhance the composite properties such as: mechanical strength, stiffness, biocompatibility and stability. By controlling the amount, distribution, and the properties of composite components, the design and properties of the composite can be tailored to suit the function it serves (Dorozhkin, 2009b). Therefore, composites have been used in various biomedical applications such as: bone fracture repair, joint replacements, bone grafts, soft tissue repair and dental applications (Figure 2.22) (Ramakrishna et al., 2001).

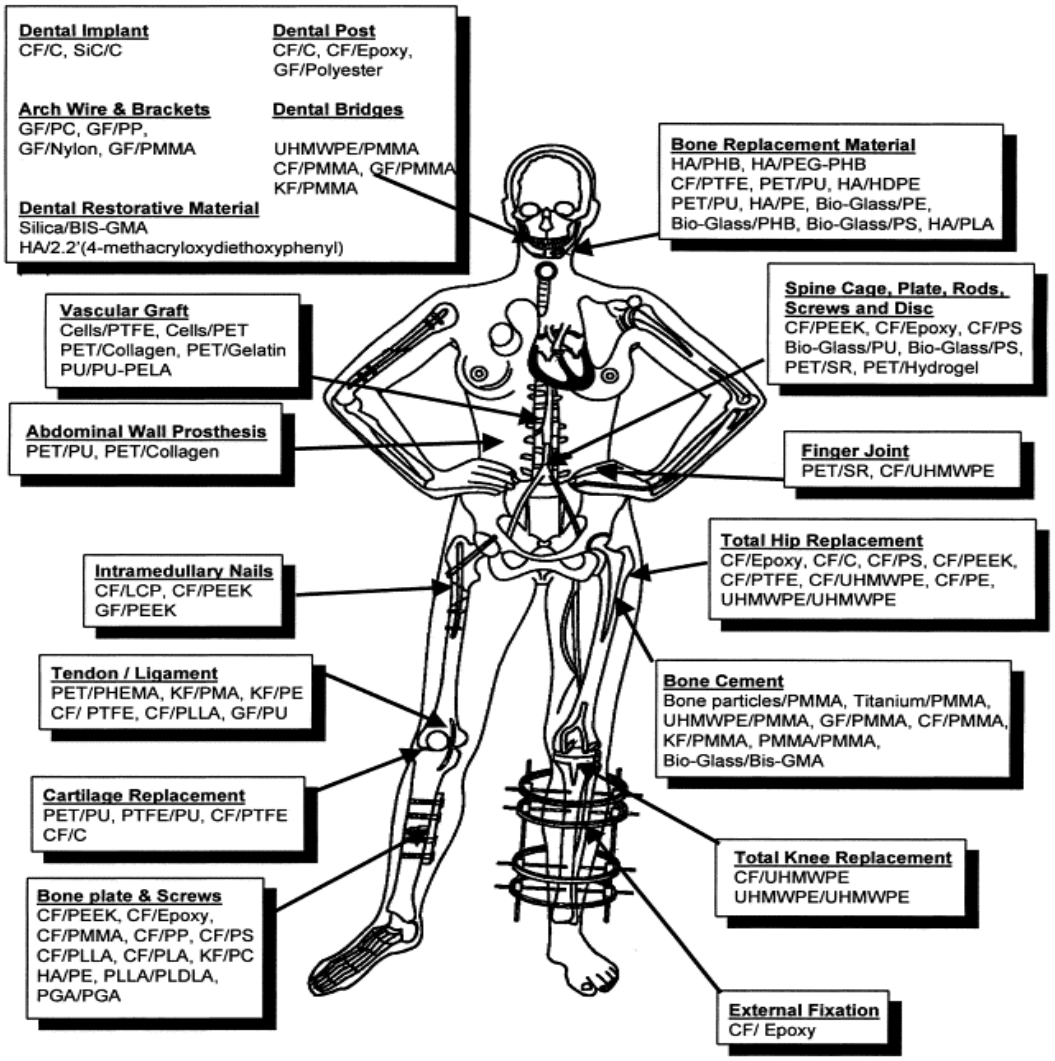

CF: carbon fibers, **C**: carbon, **GF**: glass fibers, **KF**: kevlar fibers, **PMMA**: Polymethylmethacrylate, **PS**: polysulfone, **PP**: Polypropylene, **UHMWPE**: ultra-high-molecular weight polyethylene, **PLDLA**: poly(L-DL-lactide), **PLLA**: poly (L-lactic acid), **PGA**: polglycolic acid, **PC**: polycarbonate, **PEEK**: polyetheretherketone; **HA**: hydroxyapatite, **PMA**: polymethylacrylate, **BIS-GMA**: bis-phenol A glycidyl methacrylate, **PU**: polyurethane, **PTFE**: polytetrafluoroethylene, **PET**: polyethyleneterephthalate, **PEA**: poltethylacrylate, **SR**: silicone rubber, **PELA**: Block co-polymer of lactic acid and polyethylene glycol, **LCP**: liquid crystalline polymer, **PHB**: polyhydroxybutyrate, **PEG**: polyethyleneglycol, **PHEMA**: poly(20hydroxyethyl methacrylate)

Figure 2.22 Applications of composites in human body (from Ramakrishna et al., 2001)

The mechanical properties of the composites depend on several factors such as the type of filler, the matrix, the amount of filler and the interface developed between the filler and matrix which controls the load transfer between the filler and matrix. In considering the effect of filler addition, it is the volume content of filler that is the most relevant, however the easiest way to measure the amount of filler added is by the weight content and conversion from weight to volume content requires calculation using on the densities of the two phases. In the case of polymer/ceramic composites, the ceramic density is normally a factor of 3 to

6 higher than the polymer density, thus the difference in filler content between 20 wt% and 20 vol%, for example, is substantial (Tanner, 2009). Due to the various factors mentioned above, predicting the resultant mechanical properties of the composite is often challenging. However, by assuming that the stress throughout the composite is constant and the composite is composed of layers of filler and matrix aligned perpendicular to the applied load (Figure 2.23), the mechanical properties can be simply predicted using the following equation known as Reuss model:

$$1/E_c = v_f/E_f + v_m/E_m \qquad \text{Equation 2.3}$$

Where E_c is the modulus of the composite, E_f and E_m are the moduli of the filler and the matrix respectively and V_f and V_m are the volume fraction of the filler and the matrix respectively.

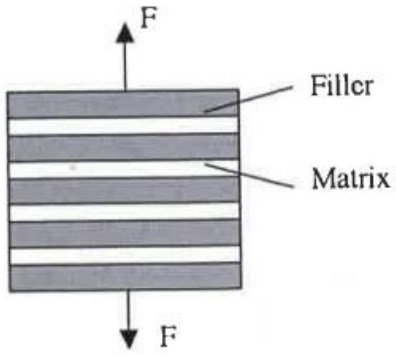

Figure 2.23 Uniform stress model composite (from Tanner, 2009)

On the other hand, by assuming that the strain is constant throughout the composite and the composite is composed of layers of filler and matrix aligned parallel to the load direction (Figure 2.24), the mechanical properties of the composite can be calculated using Equation 2.4 known as Voigt model:

$$E_c = v_f E_f + v_m E_m \qquad \text{Equation 2.4}$$

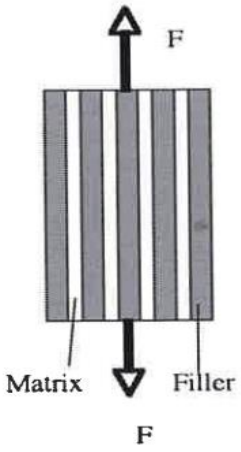

Figure 2.24 Uniform strain model composite (from Tanner, 2009)

While those models represent the simplest composites models, all other models and experimental data give intermediate values to these two (Figure 2.25) (Park and Lakes, 2007b; Tanner, 2009).

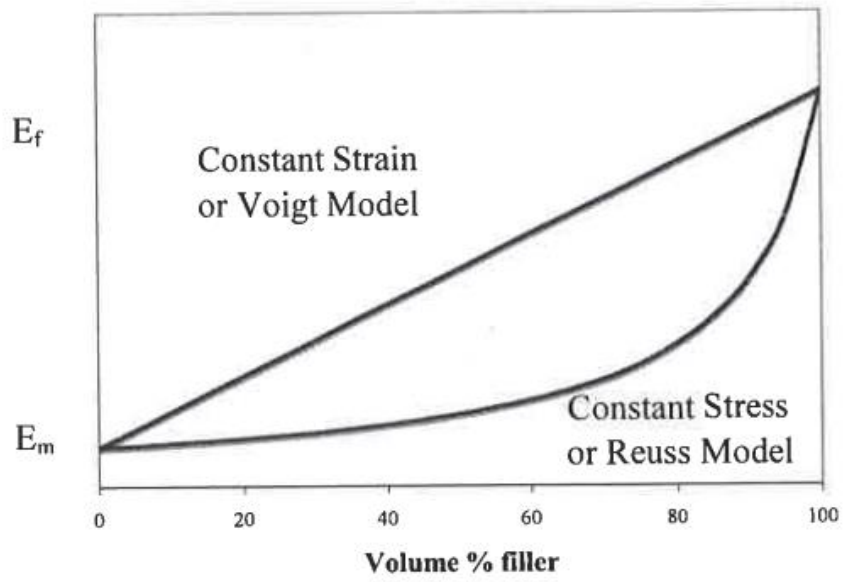

Figure 2.25 Comparison of the constant stress and constant strain models for composites, all composites fit between these two boundaries (from Tanner, 2009)

Biocomposites can either be classified according to the matrix component into ceramic matrix, polymer matrix and metal matrix composites, or classified according to the dispersed phase into particles, fibres and platelet composites, or classified by degradability into degradable and non-degradable composites (Yoruç and Cem, 2012). For hard tissue applications, the composite should be bioactive to encourage bone growth, have similar or greater stiffness and strength than the cortical bone. Bonfield and his colleagues have developed the concept of manufacturing an analogue of bone itself of PE reinforced with hydroxyapatite (HA) at different volumes. The composite with 40 vol% HA was given the trade name HAPEX and was used by Downes and co-workers in orbital floor applications as the first of the bioactive composites implanted into patients (Downes et al., 1991; Tanner et al., 1994). Thereafter HAPEX was used in over 500,000 middle ear implants with successful biological and clinical responses (Goldenberg 1994; Dornhoffer, 1998).

While HAPEX is a non-degradable composite expected to remain in the patient for the rest of their life, for other applications, biocomposites should be degradable with non-toxic products. The degradation property of biocomposites are especially advantageous as their degradation can be controlled and replaced by host tissue once the bone has healed (Tanner, 2010a; Tanner, 2010c).

Biocomposites made of biodegradable polymers with calcium phosphates incorporated as either a filler, coating or both either into or onto the polymer matrix, in the form of particles or fibres, are gaining increased attention for using as scaffolds for bone tissue engineering due to their improved physical, biological and mechanical properties in addition to their resemblance to the natural bone composition (Dorozhkin, 2009b). Synthetic biodegradable polymers such as PLA, PLGA and PCL have been extensively used for bone applications along with HA, TCP and BCP ceramics as reinforcements where the polymers generally provide ductility to the composite while the ceramics enhance the composite bioactivity, osteoconductivity, strength, and stiffness (Grøndahl and Jack, 2010). Many composites have been developed, but few will be described as examples.

Causa et al. (2006) investigated three HA–PCL composites with different volume content of HA (13, 20, and 32%). The structure and mechanical properties of the composites and structure were examined, along with the biocompatibility and

osteoconductivity. Increasing HA contents in the composites significantly increased the mechanical performance. The elastic modulus and tensile strength of composites containing 20 and 32 vol% HA matched well the range of human cortical bone. 3D samples were seeded with human osteoblastic cell line (SaOS-2) cells and osteoblasts from human trabecular bone (hOB) for 1 to 4 weeks. Cell viability, adhesion, proliferation, morphology and ALP release were analysed on non-filled PCL as well as on the HA-loaded polymer. The results showed increased osteoconduction in the filled composite as compared to plain PCL, suggesting that this system is a potential candidate for bone substitution, due to the balance between structural–mechanical properties and biological activities.

Deng et al. (2007) fabricated a hybrid nanocomposite of PLLA and HA using electrospinning. Inclusion of HA particles in electrospun scaffolds reduced inflammation from the acid release by autocatalytical acceleration of PLLA degradation. Human osteosarcoma MG-63 cells were well adhered and proliferated more on the HA-containing scaffolds than pure PLLA scaffolds. However, PLLA/HA scaffolds showed significant reduction on their degradation rate compared to pure PLLA scaffolds due to the dissolution of HA particles which blocked off the entry of water.

Lin et al. (2008) produced PLA/β-TCP microspheres using water/oil/water (w/o/w) emulsion technique. Microspheres containing β-TCP exhibited a slight difference in degradation rates compared with pure PLA microspheres, indicating that β-TCP was entrapped and spread in the whole microsphere, thereby the rate of calcium release from the microspheres depended on the polymer degradation rate. Histological examination of PLA/β-TCP microspheres in a rabbit condyle model showed excellent repairing and recover of the osteocyte tissues within 1 month of application.

Furthermore, Shuai et al. (2013) developed PLGA/nano-HA composite porous scaffolds, with well-controlled pore architectures as well as high exposure of the bioactive ceramics to the scaffold surface, using selective laser sintering technique. Mechanical testing showed that the compressive strength and modulus of the scaffolds were increased when the nano-HA content was increased for up to 20% (w/w), however thereafter the mechanical properties decreased dramatically.

2.3 Bone tissue engineering

2.3.1 Introduction

There are many clinical conditions that require bone regeneration in large quantity, such as bone defects created by trauma, infection, tumour resection and skeletal abnormalities, as well as cases such as avascular necrosis, atrophic non-union and osteoporosis in which the regenerative process is compromised. Worldwide, there are roughly 2.2 million bone graft procedures performed annually. Although autografts are considered as 'the gold standard' treatment of bone defects because they are histocompatible, non-immunogenic and can induce bone growth, they have significant limitations such as donor site morbidity and limited supply. On the other hand, allografts which can be obtained from living donors or cadavers can overcome harvesting and quantity problems associated with autografts, but they are expensive, and can cause host immune response in addition to the possibility of transmitting diseases from donor to recipient. Bone tissue engineering is an emerging field that work towards providing a suitable alternatives to conventional treatments of bone disease and combat their limitations (Akter and Ibanez, 2016; Romagnoli et al., 2013). It is based on understanding bone structure, formation and mechanics, and aims to develop artificially designed biological substitutes that restore, preserve, or improve tissue function by using synergistic combination of biomaterials, cells and factor therapy (Amini et al., 2012; Langer and Vacanti, 1993; Salgado et al., 2004).

The field of bone tissue engineering was initiated nearly four decades ago when W.T. Green, an orthopaedic surgeon, attempted in early 1970's to generate new cartilage via implanting chondrocyte cells into a spicule of bone and then transplant it in a nude mice. In the mid-1980's the Vacanti brothers and Langer made extensive studies to design a method to create scaffoldings for cell delivery using a branching network of synthetic biocompatible and biodegradable polymers instead of using naturally occurring scaffoldings that could not be replicated (Vacanti and Vacanti, 2013). In 1991, Caplan assumed that autologous stem cell isolation, mitotic expansion and site-directed delivery can control the rapid and specific repair of skeletal tissues. The first clinical paper reporting the repair of large bone defects with the use of autologous bone marrow stromal cells was published by Quarto et al. in 2001. Thereafter, Schimming and Schmelzeisen reported the first study in humans in 2004 showing that osteoblasts derived from

periosteum can form lamellar bone within three months after transplantation. Although much progress has been made, there still many crucial obstacles remain to be cleared on the way to bone tissue engineering becoming a true clinical reality (Amini et al., 2012; Meijer et al., 2007).

Tissue engineering technologies are mainly based on the successful interaction between the following three components (also known as the tissue engineering triad) (Figure 2.26): (1) a scaffold or matrix that closely mimics the natural extracellular matrix and has the ability to hold the cells together; (2) implanted and cultured cells to create new tissue; and (3) biological signalling molecules, such as growth factors, differentiation factors and adhesion molecules that guide cells to form the desired tissue (Bartold et al., 2006; Garg et al., 2012; Smith and Grande, 2015).

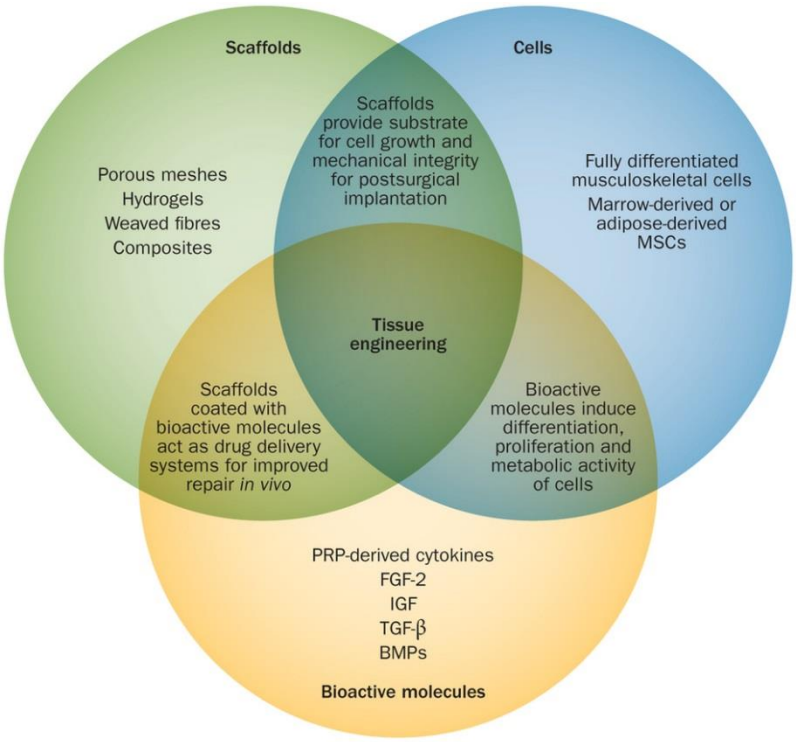

Figure 2.26 The tissue engineering triad (from Smith and Grande, 2015)

In general, the process of creating an engineered tissue requires some or all of the following stages (Figure 2.27):

1- Scaffold fabrication.
2- Removal or isolation of cells (biopsy).

3- Expansion of number of culture through cell cultivation and proliferation.
4- Seeding into appropriate scaffolds with growth factors.
5- Tissue culture in vitro.
6- Surgical implantation of the scaffold into the body.
7- Implant assimilation/remodelling (Bambole and Yakhmi, 2016; Velasco et al., 2015).

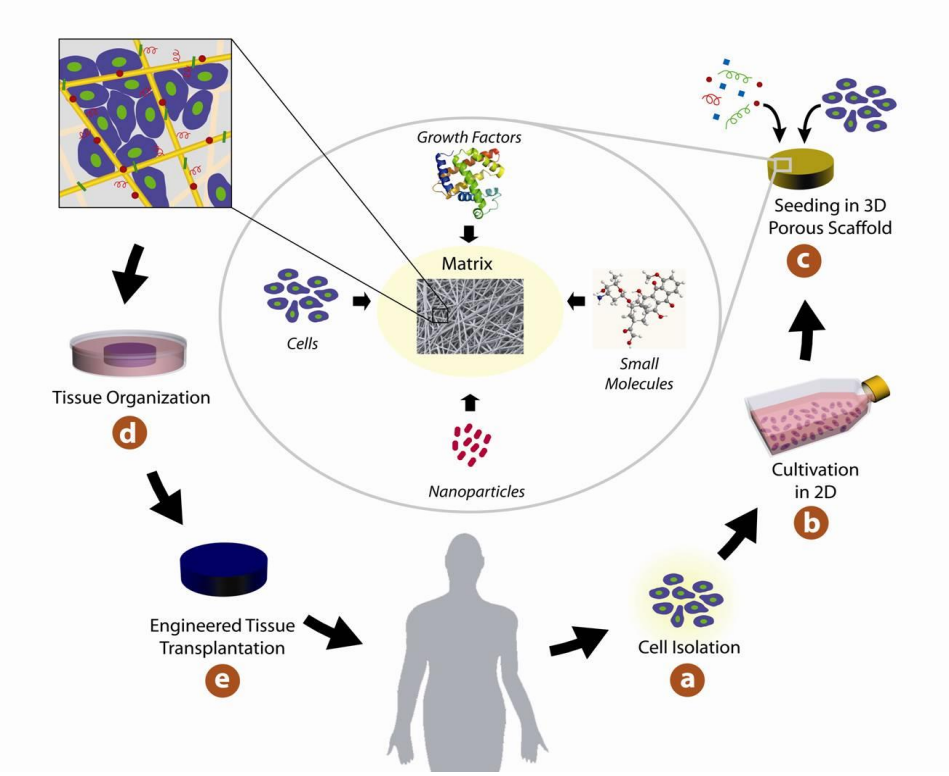

Figure 2.27 Schematic representation of the typical tissue engineering pathway followed from (a) cell isolation through (e) the return of the expanded and seeded cells in a scaffold to the patient (from Cools et al., 2016)

2.3.2 Bone scaffold characteristics

Bone tissue scaffolds must satisfy various macro and micro structural properties to ensure proper growth of the new tissue. The following properties are essential for scaffolds in bone tissue engineering:

1- Biocompatibility and bioactivity: The materials chosen for bone scaffolds should be well integrated with the host's tissue without causing any immunological responses. Biocompatibility gives tissue engineering superiority over the allograft and autograft techniques where host rejection due to immunological responses is frequently encountered (Mallick et al.,

2015). Biocompatibility of the scaffold depends on polymer (and filler) synthesis in addition to scaffold fabrication technique. For instance, residual chemicals involved in polymer processes, such as organic solvents, initiators, stabilizers, cross-linking agents, or unreacted monomers, may leach out of the scaffold once implanted. Thus, in addition to the intact biomaterial, any leachable components or degradation products from the scaffold must be biocompatible to prevent tissue inflammation (Liu and Webster, 2007). While biocompatibility is an essential requirement for bone tissue scaffolds, bioactivity is an optional, but preferred, property since it allows direct bonding of the implant with the host tissue and the formation of bone-like apatite on its surface in the living body, thus promoting faster bone healing (Oyane et al., 2003).

2- Porosity and pore size: During the design of bone scaffolds, porosity, as well as pore structure and pore size play a significant role, because they affect cell distribution throughout the porous structure and they are also responsible for the nutrient supply to transplanted and regenerated cells. Scaffolds must be permeable, with open and fully interconnected pores and pore size ranging from 100 to 400 μm to allow bone tissue ingrowth. Porous scaffolds facilitate the migration and proliferation of cells, allow high mass transfer rates of nutrients, oxygen and metabolic waste products within the structure, and promote better vascularisation. However, increasing the porosity will reduce the mechanical stability of the scaffold, therefore, it is important to maintain the balance between porosity and mechanical strength of the scaffolds (Bose et al., 2012; Salgado et al., 2004; Velasco et al., 2015).

3- Surface properties: The surface area of a scaffold represents the space where pivotal interactions between scaffold's materials and host tissue take place. Scaffold’s surface properties, both chemical and topographical, should support cell adhesion and proliferation, and facilitate cell-to-cell contact as well as cell migration. Surface roughness has also a direct influence on cellular morphology in vitro as well as in vivo and on cell phenotype expression. Sometimes, modifying the surface of the scaffold is required to increase cellular attachment or to provide a selection for the

desired cell types. Modification of surface properties can be achieved by either using gas plasma (modifying polymer surface covalently), or by attachment of growth factors and biologically active compounds (Mallick et al., 2015; Salgado et al., 2004).

4- Mechanical properties: Bone development in vivo requires dynamic stresses, therefore, bone scaffolds must possess sufficient strength and stiffness to ensure the mechanical integrity and protection to the developing tissues. The material composition of the scaffold has a major influence on its mechanical properties. Biodegradable polymeric scaffolds can display cancellous bone compatible mechanics and tunable degradation rates. On the other hand, dense ceramics such as HA and TCP exhibit compressive strength and elastic moduli similar to human cortical bone, however, they are brittle and have slow degradation rates. As mentioned before, mechanical properties of bone vary widely from cancellous to cortical bone. Therefore, using polymer-ceramic composites in bone tissue engineering is becoming increasingly attractive because the mechanical properties of the scaffolds can be tailored by controlling the morphology, volume fraction and arrangement of the inorganic fillers in the polymer matrix (Amini et al., 2012; Mallick et al., 2015; Tanner, 2010b; Velasco et al., 2015).

5- Biodegradability: Biodegradability is another crucial factor for scaffolds in bone tissue regeneration. An ideal scaffold should degrade in vivo at a controlled degradation rate in order to create space for new tissue to grow, so that the degradation rate is similar to the new bone formation. Degradation behaviour of the scaffolds should vary according to their applications. For example, scaffolds used in spinal fusion should take 9 months or more to degrade while scaffolds used for cranio-maxillofacial applications should degrade within 3 to 6 months (Bose et al., 2012). Degradation rate can usually be tailored by varying either the monomer composition or scaffold fabrication technique (Sill and von Recum, 2008). Further discussion on the degradation behaviour of polymers can be found in sections 2.2.5.1 and 2.2.5.2.

2.3.3 Cells for bone tissue engineering

One goal of bone tissue engineering is to design a delivery system for skeletal stem/progenitor cells in order to repair or replace damaged bone. Although the materials used to retain cells play a major role in the quality of the scaffolds, a reliable cell source is key for bone regeneration (Colnot, 2011). Using autologous cells, i.e. isolation of osteoblasts from biopsies taken from the patient followed by limited expansion in vitro, is usually the first and most obvious choice due to their non-immunogenicity. However, this methodology has many restrictions such as: it is time consuming and can only provide few cells after the dissociation of the tissue. Also, the isolated cells have relatively low expansion rates which affect the number of cells available to be seeded on the scaffolds. Alternatively, the use of non-human donor cells (xenogeneic cells) can solve the problem of low cells number, but the immunogenicity of these cells, the possibility of infectious agent transmission, in addition to the ethical and social problems related with this case have limited the enthusiasm for this approach.

Using stem cells in tissue engineering appears the most valid and promising solution because of their self-renewal ability, high proliferation capability, and multilineage differentiation which lead to regeneration of tissues (Salgado et al., 2004). Additionally, stem cells are responsible for regulating bone remodelling by balancing the osteoblast-osteoclast ratio. So far, several stem cell types have been investigated for their abilities to promote bone repair and regeneration such as: adult stem cells, embryonic stem cells (ESCs), stem cells from human exfoliated deciduous teeth (SHED), induced pluripotent stem cells (iPSCs), and umbilical cord blood mesenchymal stem cells (CB-MSCs). Furthermore, adipose-derived stromal vascular fraction (SVF) has been found to be an efficient and abundant source for vascularization purposes, where regenerating vascularized bone tissues is desired (Yousefi et al., 2016). Table 2.13 summarises some of stem cell types that have been used so far for clinical bone defect repair along with their advantages and disadvantages.

Table 2.13 Stem cell sources for bone tissue engineering (from Yousefi et al., 2016)

Cell Source	Advantages	Disadvantages
Bone marrow-derived mesenchymal stem cells (BM-MSCs)	- High osteogenic potential - Studied extensively	-Low abundance; requires extensive in vitro expansion
Embryonic stem cells (ESCs)	- Pluripotency - Capable of differentiating into all cell types in bone	- Ethical and regulatory constraints - Can produce teratomas when transplanted in vivo
Adipose-derived stem cells (ASCs)	- Similar osteogenic characteristics as BM-MCSs - Highly abundant; easy to harvest surgically	- More studies are needed to test their use in bone repair
Umbilical cord blood mesenchymal stem cells (CB-MSCs)	- High availability - Broad differentiation and proliferation potential - Higher in vivo safety than embryonic stem cells	- More difficult to isolate than MSCs from the marrow - More studies are needed to test their use in bone repair
Induced pluripotent stem cells (iPSCs)	- Pluripotency - Capable of differentiating into all bone cell types	- Reprogramming efficiency is low - Require extensive expansion - Safety concerns; limited clinical application
Adipose-derived stromal vascular fraction (SVF)	- Abundant; easily harvested via liposuction - Able to form vascularized bone	- Cell population varies among donors - 2-3 hours multistep isolation process

Stem cell homing is a term that describes the recruitment of stem cell populations to the injury site. In the natural healing process, mesenchymal stem cells are mobilized into circulation and then migrate to the injured tissue to participate in the regenerative process. This process occurs through a combination of regulating growth factors and cytokine release by activated platelets and vascular endothelium which provide a signal gradient for bone marrow stem cells to start mobilization and homing (Rennert et al., 2013). For tissue engineering, two main methods have been investigated to achieve enhanced cell homing to defect sites:

cell-based approaches, in which stem cells are engineered to express markers useful for guiding them to the regeneration site, and scaffold-based approaches where implanted scaffold release chemokines and growth factors responsible for MSC homing. Both "engineered cell homing" methods have gained wide interest and may play a significant role for effective bone regeneration in vivo (Amini et al., 2012).

2.3.4 Growth factors

Growth factors represent a family of proteins controlling different cellular processes involved in tissue healing; such as cell growth, differentiation, migration, metabolism and apoptosis. They play a crucial role in tissue regeneration process as they act as signalling molecules between cells, transferring information between cell populations and their micro-environment resulting in accelerated functional restoration of the damaged tissues (Taraballi et al., 2015). A variety of growth factors has been proposed for bone tissue engineering applications (Table 2.14) such as: bone morphogenetic proteins (BMPs), platelet derived growth factor (PDGF), fibroblast growth factors (FGFs), insulin-like growth factor I and II (IGF I/II), and transforming growth factor beta (TGFb). BMPs, in particular, have been the most extensive studied as they induce the mitogenesis of mesenchymal stem cells and other osteoprogenitors, and their differentiation towards osteoblasts. More than 15 different BMPs have been identified in humans to date and, among these, BMP-2 has been shown to be one of the most effective inducers of bone formation in vivo, even in critical size defects (Romagnoli et al., 2013).

Table 2.14 Growth factors employed in bone tissue engineering applications (from Tozzi et al., 2016)

Growth Factor	Mechanism of Action	Limitations
BMP-2 (Bone morphogenic protein)	- Induces osteoblasts proliferation and mesenchymal cells (MSCs) differentiation - Induces VEGF-A secretion therefore has a role in angiogenesis	- Needs to be delivered in a controlled manner - Variable outcomes have been seen in humans - Limited capacity to initiate vascular proliferation
VEGF (Vascular endothelial growth factor)	- Induces endothelial cells mitogenesis - Attracts MSCs and induces their differentiation	Delivered alone they lead to an inability to produce organized bone regeneration
PDGF (Platelet derived growth factor)	- Attracts cells that stabilise growing vasculature - Recruits MSCs - Upregulates VEGF production	
FGF (Fibrobast growth factor)	Involved in the formation of new capillaries	
TGF-β (Transforming growth factor-β)	Extracellular matrix (ECM) production	
IGF (insulin like growth factor)	Involved in adult neo angiogenesis	

The incorporation of growth factors into bone tissue scaffolds has considerable potential to enhance healing outcomes. However, their current use has shown very limited success because they are used at high doses due to their short half-life and ability to diffuse to other tissues which makes the treatment costly and unsafe. Complications like ectopic bone formation, surgery site swelling, as well as neurological side effects have all been reported in spinal fusion application of BMP. Therefore, a considerable scientific effort has been directed towards developing new strategies for growth factors formulation and delivery in order to make them available for clinical treatment of extensive skeletal defects (Tozzi et al., 2016). The current strategies for the fabrication of growth factors-loaded scaffolds can be divided into two main categories: chemical immobilization of the

growth factor into or onto the matrix, and physical encapsulation of growth factors in the delivery system. In the former approach, growth factors can be covalently bound or linked through biomimetic interactions to the polymers that make up the hydrogel matrix to precisely control their loading, distribution, stability, and delivery. This method can minimise burst release and prolong growth factor delivery, but linkage strategy must be designed carefully in order to preserve the bioactivity of the growth factors. On the other hand, bulk incorporation of growth factors is one of the simplest approaches for producing inductive tissue engineering systems, where growth factors to be delivered are blended directly into hydrogels or within solid scaffold polymers and physically entrapped. The release kinetics of proteins and/or DNA from this type of system is characterised by an initial burst followed by slower release which is controlled by the diffusion and degradation rates of the scaffold, and that in turn depend on the scaffold properties such as porosity, polymer chemistry (i.e., molecular weight, hydrophobicity/hydrophilicity and charge density), and swelling behaviour. The current trend for growth factors incorporation into 3D polymeric and composite scaffolds is moving towards finding hybrid approaches to produce tissue engineering systems capable of multi-agent delivery and/or stimuli-responsive release (Lee et al., 2011; Nyberg et al., 2016).

2.3.5 Scaffold fabrication techniques

Cells and tissues in human body are organized into three-dimensional architecture. Thus, to engineer these functional tissue and organs, scaffolds have to be fabricated into three-dimensional space which mimics the architecture of the native extracellular matrix to facilitate the cell distribution and guide their growth for regeneration of new tissue. Over years, various methods to design and fabricate 3D biomimetic scaffolds have been developed for tissue engineering and regenerative medicine, and choosing the appropriate technique depends on several factors including: the required shape and properties of the scaffold, types of materials used in the scaffold, shape and size of pores as well as their interconnectivity, and the distribution of the materials in the scaffold (Cardon et al., 2010; Subia et al., 2010).

Examples for scaffold manufacturing techniques include:

1- Solvent casting: this is an easy method to fabricate 3D porous polymer scaffolds because it does not require any specialised equipment or high temperatures. The polymer is dissolved in solvent and cast into a glass or Teflon container, then the solvent is allowed to evaporate. The concentration used of the polymer-solvent solution depends on the required properties of the solvent cast film. Evaporation of the solvent can be enhanced using vacuum drying. Once the solvent has evaporated, the film is removed from the container and is ready to use. Solvent casting has been used in biomedical scaffolds by using dissolving biodegradable polymers such as PLLA and PLGA in chloroform or methylene chloride. Porous scaffolds can be made by adding particles that does not dissolve in the solvent to the polymer-solvent mixture, typically salt or sugars (called a porogen) and then immerse the composite in water to leach out the salt or sugar after the solvent is evaporated (salt or particulate leaching). The pore size is controlled by the size and shape of the porogen particles used while the total porosity of the scaffold can be controlled by the progen/polymer composite ratio (Liu and Webster, 2007; Loh and Choong, 2013; Sultana, 2013b). Figure 2.28 illustrates the steps of solvent casting process.

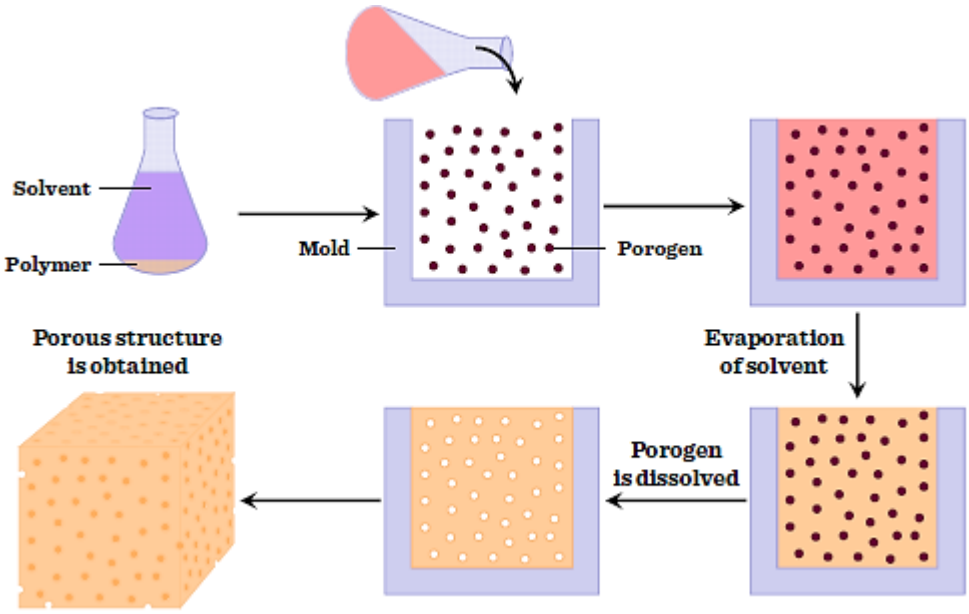

Figure 2.28 Schematic diagram of solvent casting/salt leaching technique (from Revati et al., 2015)

2- Phase separation: this method can be applied to polymer-ceramic mixtures or polymer solutions alone to produce high porosity scaffolds with interconnected pore morphology. This technique uses thermal energy as a driving force to induce phase separation in the polymeric solution. The polymer is dissolved in a solvent with a high boiling point and low molecular weight at elevated temperature to form a homogeneous solution and then cast onto a mould and placed in the freezer. As the temperature drops, the homogeneous multi-component solution becomes thermodynamically unstable and separates into more than one phase in order to lower the system free energy. Based on this principle, two types of thermally induced phase separation have been developed for the fabrication of 3D porous scaffolds: solid-liquid and liquid–liquid phase separation. The main difference between the two types is the miscibility of the system. Strong polymer–solvent interaction results in solid–liquid phase separation, whereas weak polymer–solvent interaction leads to liquid–liquid phase separation. In solid-liquid phase separation, also known as emulsion freeze drying, the low temperature will freeze and crystallise the solvent leading to solid-liquid phase separation. Then, the solvent is removed by applying vacuum in a freeze dryer leaving a porous structure. On the other hand, the addition of water or a non-solvent, such as salt particles, to the solution will increase the crystallinity of the polymer and lower the degree of polymer-solvent interaction to induce liquid–liquid phase separation where polymer-rich and polymer-poor phases are created within a polymer solution. The polymer-poor phase is then removed, leaving a highly porous polymer network. Various porous structures can be obtained with phase separation technique by varying process conditions, such as types of polymer and solvent, polymer concentration, solvent/non-solvent ratio, and thermal quenching strategy (Akbarzadeh and Yousefi, 2014; Budyanto et al., 2009; Cardon et al., 2010).

3- Gas foaming: this method was developed to avoid using cytotoxic organic solvents. Instead, this technique uses high-pressure CO_2, usually 800 psi (5.52 MPa), to saturate the polymer in an isolated chamber for a certain period of time. Once polymer is saturated with CO_2, intermolecular interactions between CO_2 and the polymer molecules become higher which

leads to reduction of glass transition temperature of the polymer. By bringing the CO_2 pressure back to atmospheric level, the solubility of the gas in the polymer decreases rapidly, and as the CO_2 tries to escape from the polymer, it causes the nucleation and growth of bubbles, resulting in a porous microstructure. Nitrogen gas can also be used instead of carbon dioxide. Gas foaming method typically creates sponge-like structures with an average pore size in the range of 30–700 μm and a porosity up to 85%. However, the main drawback of this technique is that it mostly yields a nonporous skin layer and closed pore structure. To overcome this issue, an additional soluble porogen, such as salt particles (NaCl), is added to the polymer solution before gas foaming, thus by leaching those particles, interconnecting open pore structures are formed within the polymer matrix (Sampath et al., 2016; Subia et al., 2010).

4- Rapid prototyping (RP): this method, which also known as solid freeform fabrication, is more advanced technique for designing and fabricating 3D scaffolds with 100% interconnected pores and high porosities. In this technique, the design of scaffold model is generated by computer added design (CAD) software and then expressed as a series of cross sections. Based on these cross sections, the RP machine starts to lay down a layer of material starting from the bottom and moving up a layer at a time to create the scaffolds. The main advantage of this method is the ability of controlling the architecture of the scaffold in terms of size, shape, inter-connectivity, branching, geometry and orientation by varying the design and material composition of the scaffold. It can also be integrated with an imaging technique in order to produce customised scaffolds for particular applications or for individual patients. However, this method has several drawbacks such as high machine cost, high processing temperatures which limits the ability to process temperature-sensitive polymers, and the low resolutions achieved by current systems. Various RP technologies have been developed within the last few years including: Stereolithography (SL), Fused Deposition Modeling (FDM), Selective Laser Sintering (SLS), 3D Printing (3DP) and Bioprinting (Roseti et al., 2017; Subia et al., 2010).

5- Electrospinning: this process has been recognized as a simple and efficient technique for the fabrication of ultrafine fibres with diameters ranging from few nanometres to several micrometres using polymer solutions of both natural and synthetic polymers and high electric potentials. It also offers unique capabilities for producing fibrous membranes with high surface area to volume ratio and large number of inter/intra fibrous pores (Bhardwaj and Kundu, 2010; Haider et al., 2015). The original idea of applying high electric forces to induce the formation of liquid drops can be traced back more than 100 years (Cooley, 1902; Morton, 1902). Between 1934 and 1944, Formhals attempted to produce electrospun fibres and published a series of patents illustrating an experimental setup for the fabrication of polymer filaments using an electrostatic force. Despite these early discoveries, the real interest of this technique begin in the 1990s when a group of researchers, Reneker and co-workers, experienced electrospinning to produce thin fibres from different organic polymers. In recent years, the number of publications on electrospinning has grown exponentially due to a number of factors such as improvements in imaging techniques, the ability to fabricate complex scaffolds and the convergence of nanotechnology and biotechnology for the application of tissue engineering (Mirjalili and Zohoori, 2016; Teo and Ramakrishna, 2006).

The basic setup needed for electrospinning on the laboratory scale is relatively simple and comprised of the following components: a polymer solution, a syringe that holds the polymer solution and acts as the spinneret, syringe pump, high DC voltage power supply (usually 5-50 kV) and an earthed collector. The process is usually carried out at room temperature and atmospheric pressure, with either vertical or horizontal setup (Figure 2.29) (Bhardwaj and Kundu, 2010; Rogina, 2014).

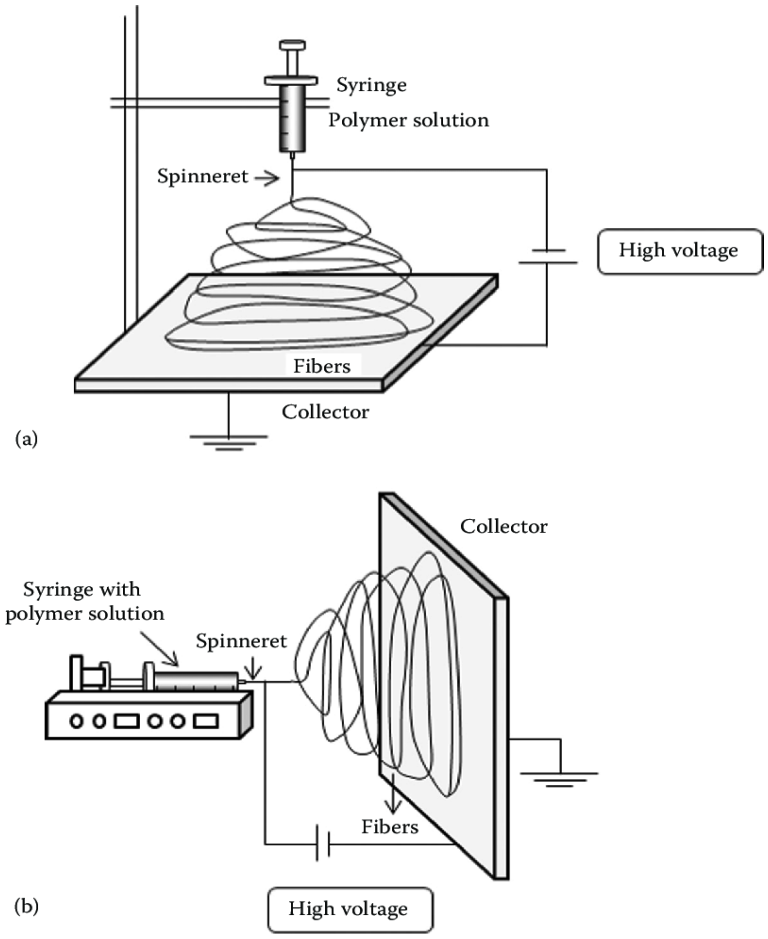

Figure 2.29 Schematic diagram of the electrospinning equipment: (a) vertical setup and (b) horizontal setup (from Bhardwaj and Kundu, 2010)

After loading the syringe with polymer solution and connecting it to the high voltage, the pendant polymer droplet at the syringe nozzle becomes statically charged and the induced charges are evenly distributed over the droplet surface. As a result of charges accumulation, the normal spherical shape of the droplet, created by surface tension, starts to distort and the tip of the polymer droplet becomes conical in shape forming what is known as a "Taylor cone". As field strength increases beyond the critical value, the repulsive electrostatic force overcomes the surface tension and a jet of charged polymer solution is ejected from Taylor cone and pass through stretching and whipping process due to electrical instabilities to form a series of discharged loops. These whipping or bending instabilities, shown in Figure 2.30, results in long thread formation. At this stage, the solvent starts to evaporate from the polymer solution leaving solid polymer fibres

that settle in layers on the electrically ground collector (Davis et al., 2015; Wang and Ryan, 2011).

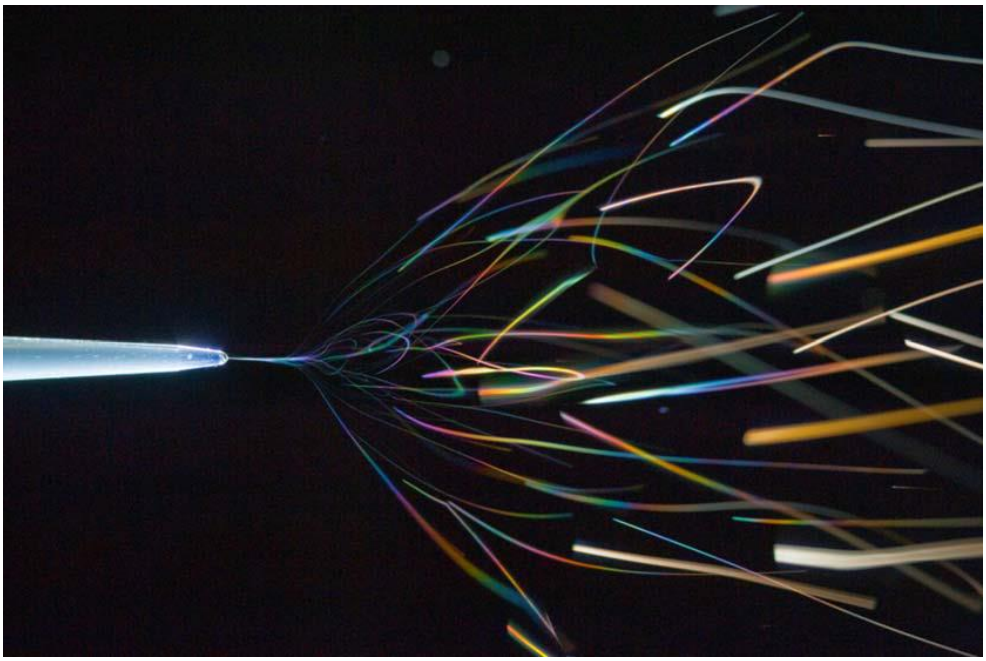

Figure 2.30 Path of jet formed by electrical instabilities during electrospinning (from Davis et al., 2015)

2.3.6 Parameters of electrospinning process

Although electrospinning is relatively straightforward to set up, there are numerous parameters that can be manipulated to produce electrospun fibres with different architectures. These parameters may affect the fibre morphology individually in some way, or they may all work in harmony with one another, and can be broadly classified into three categories: polymer solution parameters, process parameters and ambient parameters (Coles and Wooldridge, 2015; Davis et al., 2015).

The choice of electrospinning solution is usually dictated by the necessity to form fibres from a given material. However, the following parameters must be considered when preparing the solution:

1- Solution concentration and/or viscosity: the viscosity of the polymeric solution, which is controlled by changing the polymer concentration and the amount of any filler, play an important role in determining the fibre size and morphology during electrospinning, thus it has been widely studied

for different synthetic and natural polymer-solvent systems. If the viscosity is too low, electrospraying occurs instead of electrospinning and nano/micro particles are obtained instead of fibres. If the viscosity is little higher, a mixture of fibres and beads will be formed, and as the viscosity increases, spherical beads become spindle shaped and finally turn into uniform fibres. Fibres with increased diameters are formed when using solutions with higher viscosity (Robb and Lennox, 2011; Unnithan et al., 2015). Eda and Shivkumar (2007) examined the morphological transition of electrospun polymer with varying the concentration of polystyrene in tetrahydrofuran. Only beads were obtained at 5.1 wt% polystyrene concentration (Figure 2.31a) while at both 7.5 and 11.9 wt% concentrations, thin fibres connecting the beads were also visible (Figure 2.31b-d). A transition to a 'beads-on-string' structure was observed when the polymer concentration was increased to 13.9 and 18.9 wt% respectively (Figure 2.31e), and at 21.2 wt% polystyrene concentration, smooth fibres with no beading were produced (Figure 2.31f). However, the formation of continuous fibres are prohibited at very high viscosity because of the inability to maintain the flow of the solution at the tip of the needle. It should also be noted that the viscosity of polymeric solution is also dependent on the molecular weight of the polymer as it reflects the number of entanglements of polymer chains in a solution, thus increasing the polymer molecular weight, resulting in higher solution viscosity (Bhardwaj and Kundu, 2010; Eda and Shivkumar, 2007; Unnithan et al., 2015).

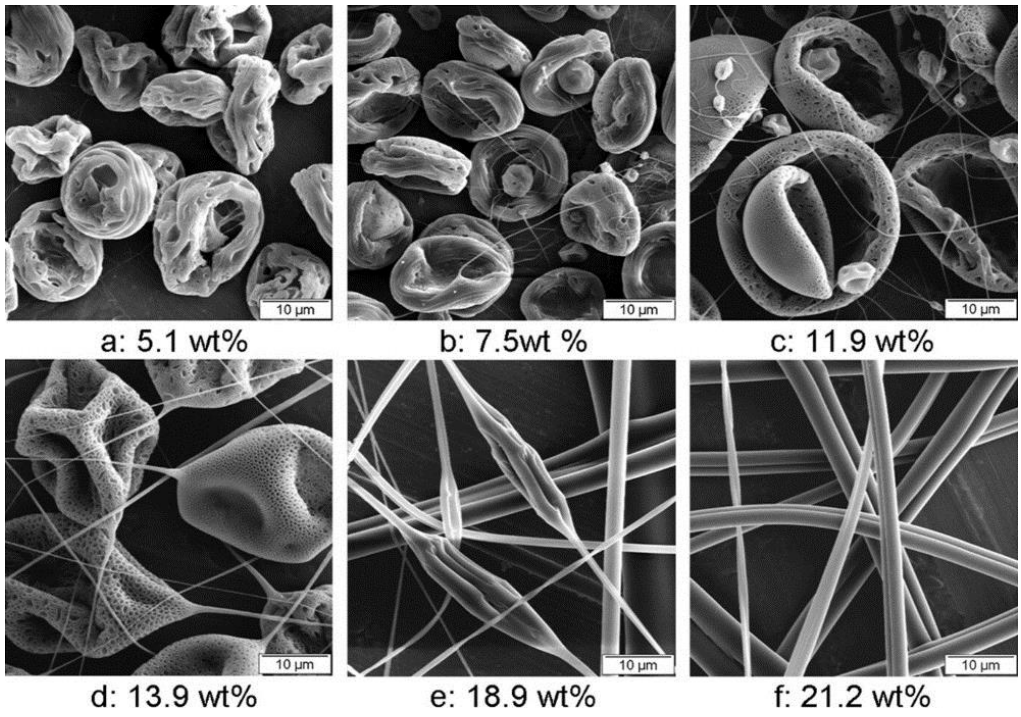

Figure 2.31 SEM images of electrospun polystyrene in tetrahydrofuran at various concentrations showing different structural regimes during bead-fibre transition. As the concentration is increased, the morphology consists of (a) beads only, (b,c) beads with incipient fibres, (d,e) bead-on-string, and (f) bead-free smooth fibres (from Eda and Shivkumar, 2007)

2- Surface tension: As a stand-alone parameter, surface tension can be very critical because the electric field needs to overcome surface tension in terms of energy to generate the solution jet. The surface tension of the solution is more related to the solvent rather than to the polymer, thus different solvents may generate different surface tensions. It also depends on the solvent amount as well as the interaction between the solvent and the polymer. The high surface tension of the polymeric solution inhibits the electrospinning process due to jet instability which results in droplet formation, while a lower surface tension helps electrospinning to occur at a lower electric field. Therefore, the surface tension can define the upper and lower boundaries of the electrospinning window if all other conditions are held constant (Bhardwaj and Kundu, 2010; Rogina, 2014; Unnithan et al., 2015).

3- Conductivity: the polymeric solution used for electrospinning must be ionic in nature so that the electric charge can be transferred from the electrode to the spinning droplet at the tip of the needle and then to the collector through the solution jet. Therefore, increasing the solution conductivity will cause more ions to be formed on the polymer molecules and subsequently leads to thinner fibre formation as greater jet elongation occurs during electrospinning. Solution with low conductivity, on the other hand, may not produce fibres due to insufficient elongation of the jet by the electrical force, thus beads are formed instead. Solution conductivity can be modulated to produce beadles fibres with smaller diameter by changing the type of polymer or solvent, the concentration of the solution, or by the addition ionic salts such as KH_2PO_4, NaH_2PO_4 and NaCl (Coles and Wooldridge, 2015; Robb and Lennox, 2011; Zong et al., 2002).

4- Dielectric constant (ε): this is another solvent dependent factor which at the simplest measures the effectiveness of a solvent to concentrate the electrostatic lines of flux when placed in an electric field. In other words, it is a measure of how much electrical charge the solvent is capable of holding (Andrady, 2007). Wannatong et al. (2004) demonstrated that the productivity of polystyrene fibres (the number of webs per unit area per time) increased with increasing dielectric constant of the solvent, while other studies have found that the bending instability of the electrospinning jet increases with higher dielectric constant which causes jet splitting, thus inducing the formation of smaller diameter fibres (Du et al., 2016; Gu et al., 2014; Hsu and Shivkumar, 2004a).

5- Solvent volatility: the formation of solid polymer fibres at the collector during electrospinning depends on the evaporation of solvent from the solution jet, meaning that the solvent must evaporate completely by the time the fibres reaches the collector, otherwise flat ribbon-like fibres might be produced or the wet fibres might fuse together to form a reticular mat (Figure 2.32) (Andrady, 2007; Haider et al., 2015; Hsu and Shivkumar, 2004b). The deposition of solvent-containing fibres on the collector might also encourage the formation of beaded fibres. Volatile solvents are therefore used to ensure a complete evaporation of the solvent from the

solution jet during ejection from the needle tip to collector. However, highly volatile solvents are usually avoided due to their high evaporation rates which cause the drying of the jet at the needle tip and blocking the jet flow (Megelski et al., 2002). Using highly volatile solvents might also hinder the formation of smaller diameter fibres as the relaxation time for the polymer chains in the solution during jet ejection needs to match the rate of extensional deformation due to bending instability (Andrady, 2007; Wannatong et al., 2004).

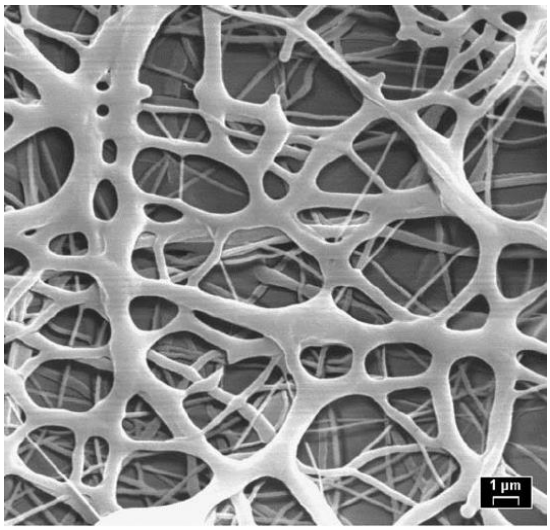

Figure 2.32 SEM image of reticular mesh resulted from fused "wet" fibres reaching the collector (from Hsu and Shivkumar, 2004b)

The processing parameters when producing fibres include:

1- Applied voltage: this is a crucial element for the electrospinning process as the electric voltage must have a higher potential than the surface tension of the solution in order to eject the charged jet from the Taylor cone and initiate electrospinning (Robb and Lennox, 2011; Unnithan et al., 2015). In addition, the applied voltage must be high enough to maintain a stable jet ejection during electrospinning. However, at very high voltages, the jet can became unstable and multiple jets will be ejected (Doshi and Reneker, 1995). Deitzel et al. (2001) and Jalili et al. (2005) also demonstrated that a higher voltage offers greater probability of bead formation in electrospun poly(ethylene oxide) (PEO) and polyacrilonitrile (PAN) fibres, respectively.

2- Flow rate: polymer flow rate plays a major role on solvent evaporation. The polymeric solution must be pumped with sufficient pressure to maintain a stable droplet at the end of the needle that can be deformed when the high voltage is applied. To ensure the stability of the jet, the polymer droplet size needs to remain constant, which means that the polymer flow rate must hold the droplet on the tip without generating an excess of supply causing the droplet to become unstable to ensure the fabrication of consistent fibres. Using high flow rates does not give enough time for solvent to evaporate and can cause bead formation, while too slow flow rate may cause solution solidification on the syringe tip as well as preventing Taylor cone formation due to insufficient polymer solution at the end of spinneret (Coles and Wooldridge, 2015; Robb and Lennox, 2011).

3- Tip-to-collector distance: The distance between the tip of the syringe and the collector has also major influence on the morphology and diameter of electrospun fibres as it determines the strength of the electric field in addition to the time available for the solvent to evaporate from the jet before reaching the collector. It should be far enough to cause solvent evaporation and prevent wet fibres or bead formation and short enough to prevent weakening of the electric field (Andrady, 2007; Martins et al., 2008).

4- Collector geometry: the collector serves as a conductive substrate to collect the charged fibres during the electrospinning process and, since it is grounded, the residual charges on the fibres will be removed rapidly which allow the fibres to solidify into a mat of high areal density. The geometry of the collectors affects the physical properties of the fibres (such as crystal morphology and molecular orientation) as well as the fibre packing and orientation. The simplest and most commonly used collector in laboratory electrospinning is the stationary collector comprises a metal plate and/or an aluminium foil. This type of collector allows the formation of a nonwoven mat of fibres in a random orientation, while using other specifically designed collectors such as rotating disks, drums and mandrels allows the collection of aligned fibres. For these rotating collectors, the speed of rotation is a further crucial factor as it influences the degree of

fibre alignment in addition to rate of fibre deposition. The crystal orientation of fibres can also be improved with increasing the collector speed due to drawing and thus alignment of polymer molecular chains in the direction of fibre axis which results from the collector rotational speed. Researchers have also used other kinds of collectors such as wire meshes, pins, grids, parallel or gridded bars and liquid baths depending on the type of application. On the other hand, studies have shown that composition of collector has an important effect on the packing density of fibrous mats. For example, Liu and Hsieh (2002) examined the effect of collector nature using on fibres structure using four different target materials including copper mesh, aluminium foil, water and paper. They found that the fibres collected on paper had more uniform sizes, smooth surfaces and fewer defects than other collectors, while fibres collected on water had a large size variation. Aluminium foil and water, both of which are electrically conductive, produced more tightly packed and less porous scaffolds because they dissipated the electric charges and reduced the repulsion among fibres, while for non-conductive collectors, electrostatic charges caused fibres to repel each other, giving a more loosely packed fibrous network (Andrady, 2007; Kongkhlang et al., 2008; Liu and Hsieh, 2002; Mirjalili and Zohoori, 2016; Unnithan et al., 2015).

Finally, ambient parameters such as the surrounding temperature and humidity can also affect electrospinning process. Increasing the ambient temperature results in two main effects: the solvent evaporation rate increases and the viscosity of the solution decreases. In a warmer environment, individual molecules of the solvent will have more energy to transform from liquid to gaseous form, thus the polymeric solution will dry faster, leaving less time for elongation and thinning during electrospinning. Also, studies have shown that decreasing solution viscosity usually results in fibres with small diameters (Bhardwaj and Kundu, 2010). However, it increases the tendency of bead formation as discussed earlier. Varying the humidity, on the other hand, affects solvent evaporation time and may also leads to the formation of small circular pores on the surface of the fibres (Coles and Wooldridge, 2015; Robb and Lennox, 2011).

2.4 Core and shell fibres

Tissue engineering involves the preparation of biomimetic scaffolds that deliver therapeutic molecules and cells, with the goal of repairing and reconstructing diseased and damaged tissues and then degrade away. However, the key challenge is how to safely incorporate those cells and molecules into scaffolds without adversely affecting their activity or the scaffold's properties. Conventional scaffolds used for tissue engineering are typically composed of single biodegradable fibres that form porous structures, with the loaded bioactive molecules situated in pores between the fibres. This structure gives rise to burst release of the encapsulated drug which reduces the effective lifetime of the device and may have toxicological ramifications. Recent efforts are focused on producing scaffolds with modified fibres such as core and shell, hollow, and triaxial-channel fibres for use in various biomedical applications. The core-and-shell design has emerged as a promising approach for delivering therapeutic molecules and stem cells. Typically, cells and bioactive molecules can be secured and partitioned within the layered core and shell structure and can be delivered to target defects with more controlled release profiles. The release mode and kinetics of the core compounds can be adjusted by controlling shell properties such as thickness and biodegradability. In addition, using core-shell fibres can improve biocompatibility, biodegradability, hydrophilicity and mechanical properties of the scaffolds. Core-shell fibres can be produced by two methods: emulsion electrospinning and coaxial electrospinning (Khalf and Madihally, 2017; Perez and Kim, 2015).

2.4.1 Emulsion electrospinning

Emulsion electrospinning is a widely adopted technique for producing nanofibres with a core-shell structure and encapsulation of drugs and cells into the fibre matrix with the advantage of having a simpler set-up than coaxial electrospinning. The technique was originally used to incorporate water-soluble drugs into hydrophobic or amphiphilic polymers. It depends mainly on the immiscible nature of water or water-like solvents and oil or organic solvents. There are two common types of emulsions: water-in-oil (W/O) or oil-in-water (O/W). Immiscibility occurs due to the polar nature of water and the nonpolar nature of the organic solvent. The immiscible solutions are vigorously mixed into an emulsion and then

electrospun. In the case of water-in-oil, as the emulsion passes through the needle, the water droplets containing drug molecules or water-soluble polymer will be forced to the inner core of the stream while the organic phase containing the polymer will form an outer shell for the stream (Manoukian et al., 2016). Besides producing core-shell structured fibres, emulsion electrospinning can be used to fabricate bead-on-a-string fibres, or produce a dispersion of the separated phase within the polymer fibres. Emulsion electrospinning have the advantages of fabricating nanofibres from less concentrated polymer solutions compared to conventional electrospinning. Additionally, it does not require a specific type of spinneret/set-up to produce core-shell nanofibres. Therefore, it is considered as a user-friendly and economically applicable technique. However, the major drawbacks of this method include the need for maintaining stable emulsified solution throughout the electrospinning process. Vigorous mixing of the polymer and drug solutions and using ultrasound sonication, in addition to the incorporation of an emulsifying agent is also necessary to avoid phase separation, all which can cause damage to certain drugs, particularly proteins and DNA (Mohammadzadehmoghadam et al., 2016; Xu et al., 2008; Yang et al., 2008).

2.4.2 Coaxial electrospinning

Coaxial or co-electrospinning electrospinning has emerged as a branch of electrospinning and an effective alternative to the emulsion electrospinning for producing core and-shell and hollow structured fibres. This innovative technique was first demonstrated by Loscertales et al. in 2002, where two different liquids were delivered independently through coaxial spinneret and electrosprayed to encapsulate the liquid droplets (Mohammadzadehmoghadam et al., 2016; Zhang et al., 2010). The method was then further developed by Sun et al. in 2003 who used the setup to produce core and shell nanofibers. On the other hand, the first biomedical application of coaxial electrospinning was reported by Zhang et al. in 2004, who prepared core–shell PCL-gelatin nanofibers for controlled drug release. Since then, coaxial electrospinning has attracted a significant amount of attention in medical and pharmaceutical fields. The technique has been used for producing antibacterial nanofibres, wound dressings, drug delivery materials and tissue engineering scaffolds (Khodkar and Golshan Ebrahimi, 2017).

The basic set up of coaxial electrospinning is largely similar to the conventional electrospinning, but the spinneret is modified to have two capillaries, inner and outer, that fit concentrically inside each other resulting in a coaxial configuration (Elahi et al., 2013). The outer capillary is connected to the shell solution reservoir while the inner capillary is attached to the core solution reservoir as shown in Figure 2.33. When high voltage is applied, a charge accumulation develops on the surface of the shell solution. Due to charge-charge repulsion, the meniscus of the shell solution on the tip of the spinneret elongates and stretches to form a Taylor cone, and when the charge accumulation reaches a certain threshold value due to the increased applied voltage, a fine jet extends from the cone. Meanwhile, the stresses generated in the shell solution create shearing of the core solution via "viscous dragging" and "contact friction." The core solution is then deforms into conical shape with the shell solution to create a compound Taylor cone with a core-shell jet initiating from the tip of the spinneret (Figure 2.34). Under the whipping force of electrostatic repulsion, the core-shell fibres are formed and ultimately deposited on the grounded collector (Wei and Xia, 2012).

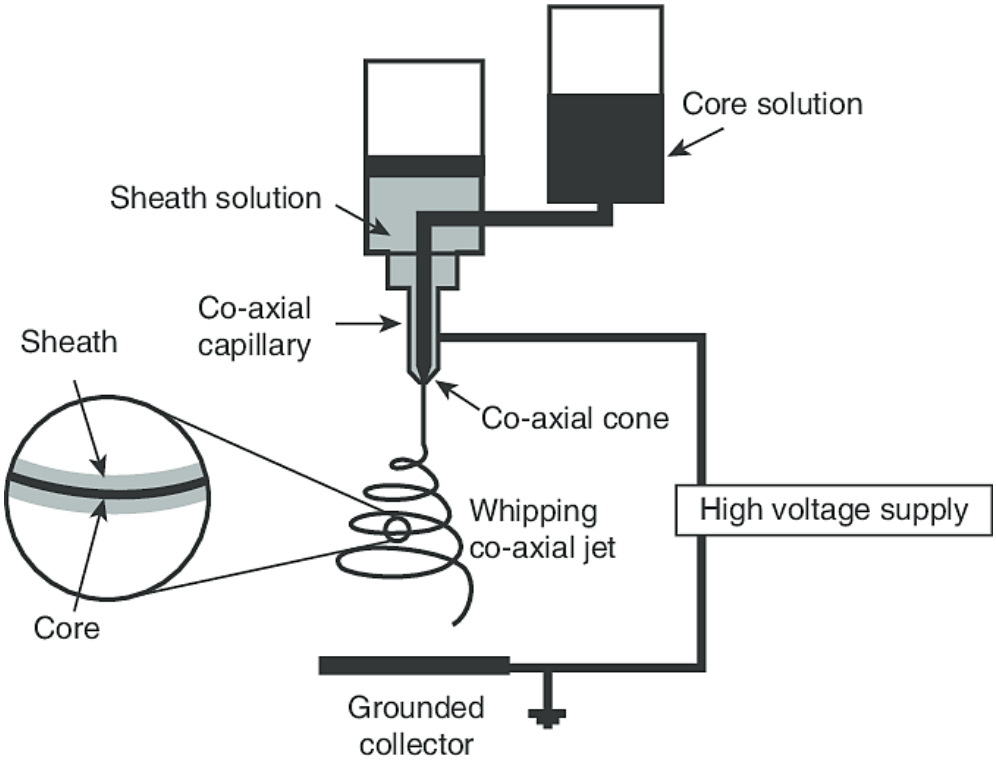

Figure 2.33 Schematic diagram of coaxial electrospinning (from Elahi et al., 2013)

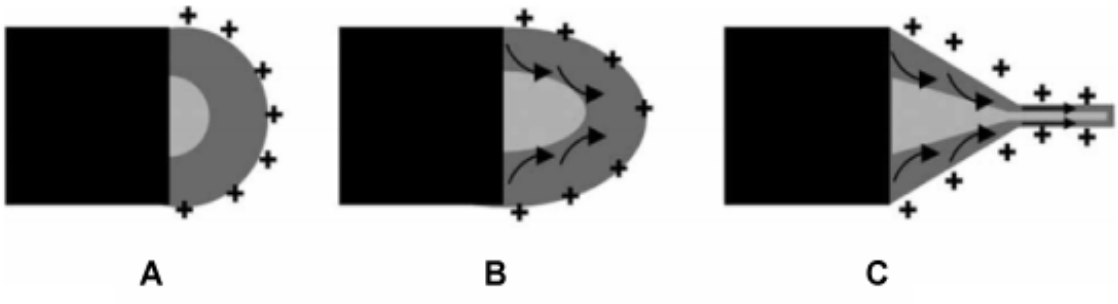

Figure 2.34 Schematic illustration of compound Taylor cone formation. (A) Surface charges on the shell solution, (B) viscous drag exerted on the core by the deformed shell droplet, and (C) core-shell compound Taylor cone formed due to continuous viscous drag (from Moghe and Gupta, 2008)

Coaxial electrospinning has been used extensively because it is a one-step process which is simple to use. In addition, it allows the use of a number of core materials which are cannot form electrospun fibres alone, to be electrospun through the protection and guidance of the sheath solution. Unstable compounds, such as antibiotics, growth factors and living cells, can be isolated from harsh environment and electric charges via the shell layer. The mechanical properties and degradation rate of coaxial fibres can be tailored by choosing the suitable components for the core and shell solutions, while the size of fibres can be controlled by adjusting the solution and processing parameters (Lu et al., 2016).

2.4.3 Parameters affecting coaxial electrospinning

Since the process of coaxial electrospinning is similar to that of conventional electrospinning, all conventional electrospinning parameters that control the morphology of the fibres produced and the quality of the process also affects the behaviour in the coaxial electrospinning. Those parameters can be mainly divided into solution parameters and processing parameters (Chan and Kotaki, 2009).

2.4.3.1 Solution parameters

Various organic and inorganic materials have been used successfully to produce ultrafine coaxial fibres. Choosing the appropriate materials and solvents to prepare core-and-shell solutions is essential for steady generation of coaxial fibres especially those for biomedical applications. Solution parameters includes:

1- Solution viscosities: Since the shell solution acts as a guide that surrounds and drives the core solution and dominate the fibre formation process in coaxial electrospinning, the viscosity of shell solution needs to be sufficient to overcome the interfacial tension between the core-sheath solutions and allows a stable compound Taylor cone to be formed. Shell solutions with low viscoelasticity can lead to beads on string fibres or core-shell particles instead of uniform coaxial fibres. However, if the viscosity is too high, clogs frequently will be formed on the tip of the spinneret, preventing fibres from being drawn. Studies have shown that the requirements for the spinnability of the core solution by itself are not as critical as they are for the shell material, however, a minimum viscosity is still required for the core solution to prevent the jet breakup of during the stretching and whipping stages (Moghe and Gupta, 2008).

2- Solution concentration: The concentration of polymer solution has a direct effect on its viscosity. With increasing concentration of polymer, the viscosity of the solution increases as well. While Sun et al. (2006) reported that increasing core concentration does not affect the fibre morphology but can result in a broad distribution of fibre diameters, Zhang et al. (2004) reported that increasing core concentration while keeping the shell concentration constant leads to producing core-shell fibres with increased fibre diameters and thinner shell layer. The inverse occurs with higher concentrations for the shell solution.

3- Solution conductivity: Another factor affecting the quality of fibres produced by electrospinning is the solution conductivity. Solutions with high conductivity produce smaller diameter fibres due to the enhancement of the whipping action on the jet during electrospinning. In coaxial electrospinning, the conductivity of the core is not important. Nonconductive core solutions can be used in coaxial electrospinning as long as the shell solution is conductive. In fact, Yu et al. (2004) have found that high conductivity of the core solution can cause discontinuity in the core-shell structure due to the strong pulling force acting on the core.

Higher shell solution conductivity, on the other hand, results in producing thinner fibres with thin cores due to increasing shear stress on the core material and the strong electrostatic force and bending instability of the whipping jet (Elahi et al., 2013; Yu et al., 2004).

4- Solvent vapour pressure: The type of solvent used to prepare core-and-shell solutions can strongly influence the resulting morphology of the core shell structure. Li et al. (2004a) have reported that using high vapour pressure solvents (i.e. solvents that evaporate rapidly) in the core solution leads to the formation of a thin layer of the core material at the interface of the shell and the core due to rapid evaporation of core solvent, which traps and slows down the diffusion of the core solvent. Eventually, when the core solvent fully evaporates, it creates a vacuum inside the core, leading to the structural collapse under atmospheric pressure to give ribbon-like fibres. Using high vapour pressure solvents in the shell solution may also affect coaxial electrospinning, as they may produce unstable Taylor cones and lead to multiple jets due to fast evaporation. This in turn can cause the formation of non-uniform core-sheath structures as well and result in separate fibres from the two solutions (Larsen et al., 2004; Li et al., 2004a).

5- Miscibility of core and shell solutions: The interaction between the core and shell solutions controls the resultant fibres structure, the interfacial tension between the shell and core solution should be as low as possible to generate a stabilized compound Taylor cone (Díaz et al., 2006). Sun et al. (2003) and Yu et al. (2004) demonstrated that using miscible or same solvents for core and shell can also help reduce the interfacial tension between the two solutions, which should further favour the development of a uniform core-shell fibres. Li and Xia (2004) on the other hand, showed that immiscible core-shell solvents produce defined core-shell boundary interfaces resulting from phase separation during the spinning process, whereas miscible core-shell solvents yield less defined interfaces due to mixing between the solutions occurring during the electrospinning process (Elahi et al., 2013; Qin, 2017; Zhang et al., 2010).

2.4.3.2 Process parameters

Processing parameters can also have significant effect on the formation and structure of coaxial fibres. They include the following:

1- Applied voltage: The influence of applied voltage on coaxial electrospinning was not reported widely in the literature except in Li and Xia's (2004) study, where they showed that the inner and the outer diameters of the hollow fibres both decreased by increasing the strength of the electric field. All other studies only used one voltage for each specific compound Taylor cone stabilization. Moghe and Gupta (2008) have found that for a given pair of polymer systems and flow rates, there exists a narrow range of applied voltages (critical voltage) within which a stable compound Taylor cone can be formed. If the applied voltage is too low, dripping of the two solutions will occur followed by discontinuous jet from the shell solution with an occasional incorporation of the core. In addition, the increased size of Taylor cone will lead to mixing of the two solutions, especially if miscible solutions were used. On the contrary, if the applied voltage is higher than the critical voltage, separate jets from the shell and core solutions will be formed instead of a coaxial jet. Very high voltages can also result in broad fibre diameter distributions (Lu et al., 2016; Moghe and Gupta, 2008).

2- Flow rate: The flow rates of the two solutions are crucial for controlling the thickness of the shell and the core layers in coaxial electrospinning. If the flow rate of the core solution is too high, the shell solution may fail to appropriately encapsulate the inner liquid, and cause a disrupted process. In addition, high flow rate of core solutions can cause the core jet to break-up into droplets within the fibre. Based on experimental investigations, it has been suggested that the core flow rate should generally be lower than the shell flow rate, however, inadequate delivery of core material may result in non-continuous core segments within the fibre (Díaz et al., 2006; Gonçalves et al., 2015; Lu et al., 2016).

2.5 3D electrospun scaffolds for Tissue engineering applications

Electrospun polymeric scaffolds have significant potential in the field of tissue engineering due to their extracellular matrix mimicking topographical features that allows the control of a variety of key cellular activities. However, the main limitation associated with conventional electrospinning is that the scaffolds produced are usually two dimensional (2D) dense mats rather than three dimensional (3D) porous structures, which limit their applications in tissue engineering that ideally require 3D constructs. In addition, the small pore sizes of densely packed 2D fibrous mats restrict the access of cells to the interior of electrospun scaffolds. Thus, the cultured cells would mainly spread and distribute within a limited depth below the surface (Cai et al., 2013; Chen et al., 2016). Recently, several techniques have been explored to fabricate 3D electrospun scaffolds for various applications in tissue engineering. These techniques mostly include manual stacking, twisting, or rolling of scaffolds into 3D structures, redesigning the electrospinning collector, modifying the electrospinning process, or combining electrospinning with other scaffolds fabrication methods. For instance, Bosworth et al. (2013) created 3D electrospun PCL scaffolds that mimic the parallel arrangement of collagen fibres in natural tendon by manually twisting sheets of aligned fibres into 3D bundles to be used for tendon repair.

Jakobsson et al. (2017) designed a novel collector comprising a concave semi-spherical array of metal needles mounted on a non-conductive base to produce 3D electrospun scaffolds for neural tissue applications with high porosity and low fibre density while maintaining interconnecting pores. The resulted uncompressed 3D scaffold allowed for formation of highly intermingled glial–neuronal complexes.

For dermal tissue engineering applications, Leong et al. (2016) used a needle collector to produce 3D electrospun PCL scaffolds with multiscale fibre dimensions and 4 times larger pore size than conventional 2D electrospun scaffolds. Scaffolds were then surface modified by grafting with gelatine molecules which significantly improved human dermal fibroblasts (HDFs) cell infiltration throughout the 3D scaffolds.

Using coaxial electrospinning and a rotating rod collector, Duan et al. (2016) fabricated tubular scaffolds with core and shell structure made of PCL (core) and collagen (shell) for vascular tissue applications. The collagen shell was

subsequently crosslinked by genipin and further bound with heparin. Cytotoxicity, cell adhesion and smooth muscle cells (SMCs) infiltration tests indicated that the tubular scaffolds had good biocompatibility and cell affinity. Vascular cells included were not only attached and proliferate on the scaffold surface, but also infiltrate into its interior.

On the other hand, Rivet et al. (2015) created a 3D hybrid scaffold made of PLLA/fibronectin electrospun fibres and agarose/methylcellulose hydrogel to treat brain tissue injuries. Electrospun PLLA fibres were created and dispersed throughout the hydrogel matrix to provide a good control over the fibre density. By implanting the scaffold into the rat striatum, infiltrating macrophages/microglia and resident astrocytes were able to locate the fibres and utilize their cues for migration into the hybrid matrix.

For bone tissue engineering, electrospun 3D bone-like structures have been created in various methods, including stacking, rolling, or directly electrospinning a 3D structure. These methods have been proven to be successful in inducing bone tissue formation in vivo, especially when combined with other biomimetic stimulation methods such as growth factor delivery. The most common approach to create a 3D bone scaffolds is to stack seeded electrospun scaffolds on top of each other in a layer-by-layer manner. Li et al. (2004) were the first to introduce this approach, where they stacked electrospun uniaxially aligned nanofibers into multi-layered structures with controllable hierarchical for bone regeneration. However, they did not conduct any in vitro or in vivo studies using the scaffolds (Li et al., 2004c). Srouji et al. (2008) and Paşcu et al. (2016) also used the stacking method to produce functional 3D-stacked electrospun scaffolds, but they used randomly oriented fibres instead of aligned fibres, thus, they could not create patterned structures. In vivo results of the Srouji et al. study indicated that the 3D scaffolds support cell infiltration and neovascularisation.

Wet electrospinning is an effective technique for manufacturing electrospun 3D nanofibrous scaffolds without using sophisticated devices or chemical additives. Instead of the traditional metal plate used in conventional electrospinning, nanofibers are collected in a liquid collector, usually a metallic one, to produce 3D sponge-like structures (Kostakova et al., 2014). Wet electrospinning was first

introduced by Yokoyama et al. (2009) where they fabricated spongiform PGA nanofiber with controlled fibre density using novel wet electrospinning system. They used wet spinning stainless bath filled with three different solvents (pure water, 50% tertiary-butyl alcohol (t-BuOH), and 99% t-BuOH) as a grounded fibre collector in order to decrease the bulk density of the nanofibres fabric. Ki et al. (2008) have also used this method and collected 3D nanofibrous scaffolds in a grounded metal bath containing methanol for bone tissue regeneration. Physically, the resultant 3D scaffolds were 10 times thicker than the 2D scaffolds and contained higher pore size and increased porosity as well, while cell studies showed significantly higher proliferation of cells on the 3D scaffolds than on 2D scaffolds after 5 and 7 days of culture.

Rolling scaffolds into cylinders is also popular method for creating 3D electrospun bone scaffolds. For instance, Pişkin et al. (2009) manufactured 3D spiral-wound PCL structures for reconstruction of cranial bone defects by simply rolling 2D electrospun simvastatin-loaded PCL scaffolds. The technique showed improved bone formation and mineralisation in vivo as compared to the control, in which the defect did not contain a scaffold. To mimic the complex hierarchical structures of bone tissue, Deng et al. (2011) constructed a 3D biomimetic scaffold by rolling electrospun nanofiber matrices in a concentric manner with an open central cavity to imitate native bone structurally and mechanically. They found that this biomimicry resulted in stress–strain curve similar to that of native bone with a compressive modulus in the mid-range of values for human trabecular bone. The 3D scaffolds have also encouraged osteoblast infiltration and ECM secretion, bridging the gaps of scaffold concentric walls during in vitro culture. Moreover, Hejazi and Mirzadeh (2016) prepared 3D PCL/gelatin scaffolds with natural coral microparticles for load bearing bone defects by cutting the 2D mats into strands with desired width and length, and then rolling them into cylinders. In vitro cytotoxicity evaluation showed no release of cytotoxic materials from the scaffolds and coral particles. Furthermore, the fabricated 3D scaffolds exhibited comparable mechanical properties to those of natural cortical bone.

Finally, some studies have combined electrospinning scaffolds with other techniques in order to create 3D bone-like scaffolds for bone regeneration. Martins et al. (2009), for example, combined electrospinning and rapid prototyping in

order to create a 3D bone-like scaffold. The technique is very similar to the stacking method discussed earlier, but it incorporates the layers of electrospun nanofiber scaffolds within the microfiber meshes produced by rapid prototyping. The resulted scaffolds exhibited significantly higher proliferation and ALP activity after 7 days in culture compared to the scaffolds produced by rapid prototyping alone (Katsanevakis et al., 2012; Martins et al., 2009). Yao et al. (2017), on the other hand, developed 3D PCL and PCL/PLA scaffolds through combination of electrospinning, freeze drying and the innovative technique of thermally induced nanofiber self-agglomeration. PCL/PLA 3D scaffolds exhibited higher mechanical properties and in vitro bioactivity compared to neat PCL-3D scaffolds, while in vivo studies revealed that PCL/PLA 3D scaffolds supported new bone formation in a critical-sized cranial bone defect in a mouse model.

2.6 Conclusions

As a result of this literature survey, it was decided that a slow degrading core with high ductility was essential for the coaxial fibres to maintain the structural and mechanical integrity of the scaffolds and therefore, PCL was chosen. The outer layer of the fibre should also be slowly degradable, have a good compatibility with core layer and can be combined with a calcium phosphate, therefore PLA was chosen. For the degradable calcium phosphate, hydroxyapatite, in both sintered and non-sintered forms, and ß-tricalcium phosphate were selected to be electrospun with PLA for the shell layer. The coaxial scaffolds will be electrospun into tubular shape in addition to the conventional 2D sheets because within another group in the University of Glasgow, there is a mouse repair model which uses fracture of the mouse radius and places a narrow tube over defect, thus by making a tubular electrospun scaffolds, this would give a potential for in vivo test methodology.

Chapter 3- General Materials and Methods

3.1 Materials

3.1.1 Polymers

To prepare single electrospinning solutions as well as shell solutions for coaxial electrospinning, polylactic acid (Ingeo Biopolymer 3001D PLA) with an average molecular weight (Mw) of 136 000 g mol^{-1} (Yang et al., 2015), 1.5% D-lactide content, and density of 1.24 g cm^{-3} was supplied by NatureWorks LLC (Minnetonka, USA) in the form of small white granules. The core solutions for coaxial electrospinning was prepared using polycaprolactone (PCL) with average number molecular weight of 80,000 and density of 1.145 g cm^{-3} (Sigma-Aldrich, UK).

3.1.2 Calcium phosphates

Three types of calcium phosphates fillers were used in this study: spray dried hydroxyapatite (HA P218R, d_{50}= 4.02μm), sintered hydroxyapatite (HA P220S, d_{50}= 3.59μm) and tricalcium phosphate (β-TCP, d_{50}=3.44μm) (all obtained from Plasma Biotal Ltd, UK). Both types of hydroxyapatite have the same density of 3.162 g cm^{-3}, however, HA1 (P218R) has specific surface area of 13.536 $m^2 g^{-1}$ while HA2 (P220S) has specific surface area of 0.965 $m^2 g^{-1}$ (Zhang and Tanner, 2008). The particle surface morphology of HA1 and HA2 powders are shown in Figure 3.1. Lastly, β-TCP has a specific surface area of 2.30 $m^2 g^{-1}$, and theoretical density of 3.14 g cm^{-3}.

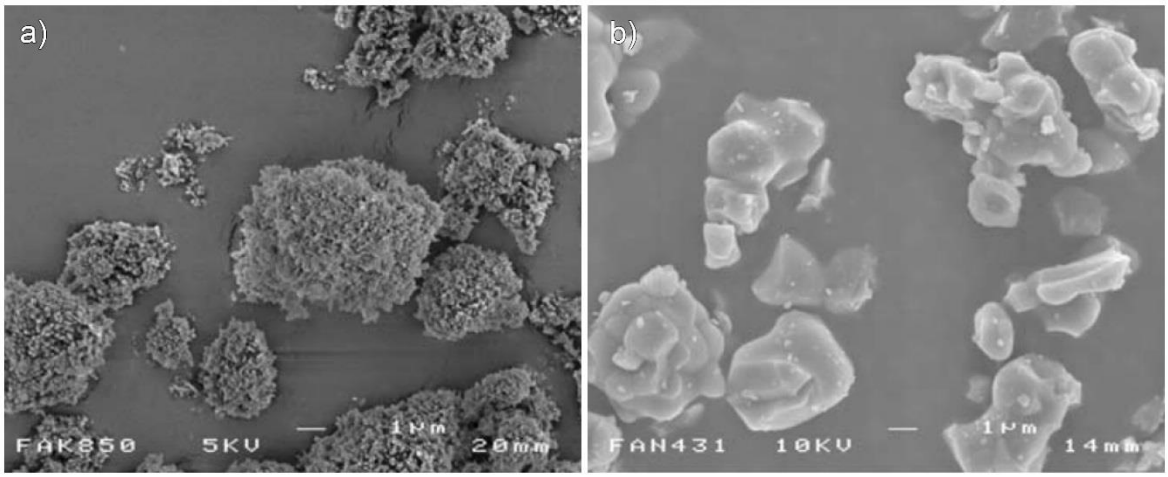

Figure 3.1 Particle morphologies of HA powders: a) HA1 and b) HA2 (marker bars=1μm) (from Zhang and Tanner, 2008)

3.1.3 Solvents

Solvents used to prepare polymeric solutions were as follows: chloroform, 99.8+%, certified AR for analysis and stabilized with amylene, and acetone, 99.5+%, for analysis (both supplied by Fisher Scientific, UK).

3.2 Methods

3.2.1 Single electrospinning

3.2.1.1 Solutions preparation

PLA solutions were prepared by dissolving PLA in chloroform (the weights and volumes are listed in Table 3.1) in a glass container with a magnetic stirrer inside. The container was then sealed to prevent solvent evaporation and left to stir overnight at room temperature to obtain homogenous mixtures. Once the PLA solutions appeared to have dissolved completely, the calcium phosphate fillers (HA1, HA2 or TCP) were added to the solutions to form the range of the desired volume ratios (Table 3.2). The PLA/filler solutions were then mixed for 30 minutes, followed by ultrasonic bath for at least 15 minutes to ensure that the filler was well distributed throughout the solution.

Table 3.1 Weights and volumes used to prepare PLA solutions

PLA percentage in sample (w/v)	PLA weight (g)	Chloroform volume (ml)
5%	2.5	50
10%	5	50
15%	7.5	50
20%	10	50
25%	12.5	50

Table 3.2 Percentages and weight of the calcium phosphate fillers used prepare 50 ml of PLA/filler mixture

Filler Percentage in sample (v/v)	Filler weight in 5% PLA solution (g)	Filler weight in 10% PLA solution (g)	Filler weight in 15% PLA solution (g)	Filler weight in 20% PLA solution (g)	Filler weight in 25% PLA solution (g)
0%	-	-	-	-	-
10% HA1/HA2	0.71	1.42	2.13	2.83	3.54
20% HA1/HA2	1.59	3.19	4.78	6.38	7.97
30% HA1/HA2	2.73	5.46	8.20	10.93	13.66
40% HA1/HA2	4.25	8.50	12.75	17.00	21.25
10% TCP	0.70	1.41	2.11	2.81	3.52
20% TCP	1.58	3.17	4.75	6.33	7.91
30% TCP	2.71	5.43	8.14	10.85	13.57
40% TCP	4.22	8.44	12.66	16.88	21.10

3.2.1.2 Electrospinning setup and parameters

Electrospinning experiments were performed using a horizontally placed electrospinning setup. PLA/filler solutions were loaded into a 10 mL luer-lock glass syringe with a straight blunt end metal needle (gauge 16, 30 mm long). The rate of solution flow was controlled by a syringe pump, and the tip of the needle was connected to a high voltage power supply (Figure 3.2). For safety purposes, the electrospinning setup is placed in a designated cupboard that contains a safety magnetic circuit breaker to turn the voltage off if the cupboard shield is opened. The samples were electrospun onto 75 x 25 mm microscope slides at a feeding rate of 1mL/h. After studies of voltages between 0 and 19 kV, 13.7 kV was chosen, and the distance between the needle tip to the collector was set at 20 cm. After electrospinning, scaffolds were left at least 3 hours to ensure complete solvent evaporation.

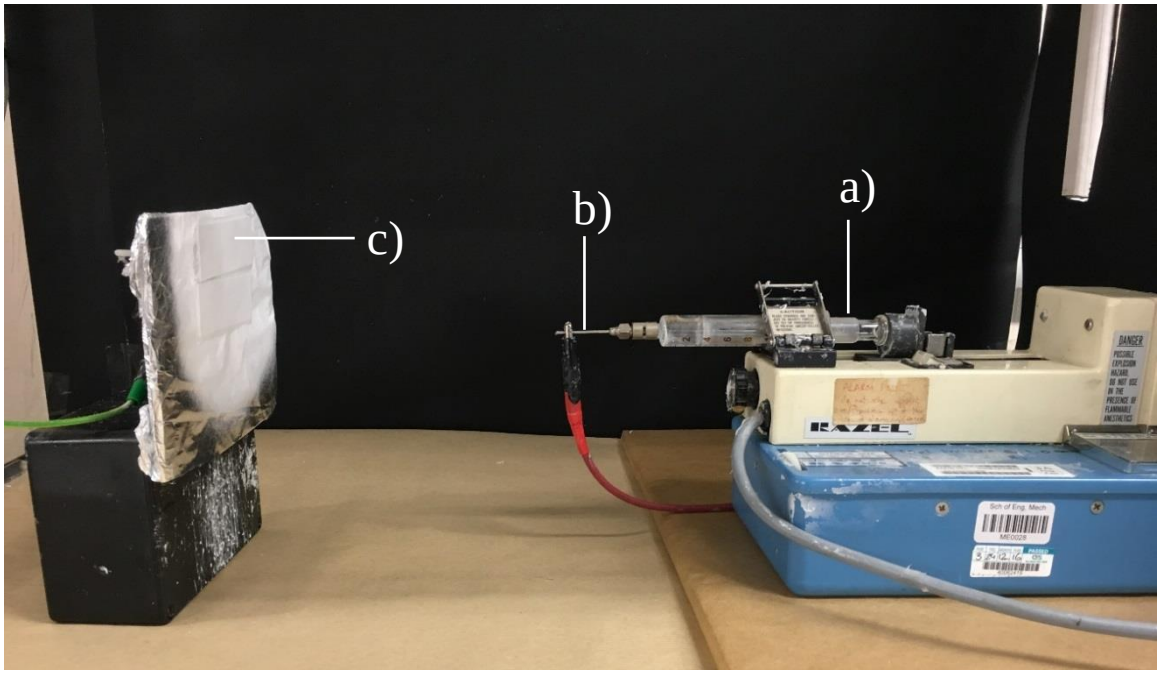

Figure 3.2 Single electrospinning setup showing (a) the syringe in the pump, (b) the needle attached to the voltage supply, and (c) the collector

3.2.2 Coaxial electrospinning

3.2.2.1 Solutions preparation

To optimize the core solution, PCL was dissolved in chloroform at room temperature, acetone, or a mixture of chloroform/acetone (2:1) at 40°C at concentrations of 10, 15, and 20% (w/v). The shell solution was prepared by dissolving PLA in chloroform/acetone (2:1) at room temperature to make 15% (w/v) PLA solution. HA2 was then added to the PLA solution to give 20% (v/v) in the final composite. PLA/HA2 solution was then mixed for 30 minutes, followed by 15 minutes in an ultrasonic bath at room temperature.

3.2.2.2 Setup and parameters

The coaxial electrospinning setup was similar to that of the single needle electrospinning system, except that in this setup, two programmable syringe pump modules (Spraybase, Ireland) were used separately to deliver shell and core solutions (Figure 3.2). The solutions were fed into two 5 mL plastic syringes and connected to a coaxial needle (16 G inner diameter, 11 G outer diameter) via 1m long PTFE tubes with an internal diameter of 1 mm (Spraybase, Ireland) (Figure 3.3). The flow rate of the shell solution was fixed at 3 ml/h, while the

core flow rate was varied between 1-3ml/hr. Samples were electrospun on microscope slides using 13.7 kV voltage and tip-to-collector distance of 20 cm.

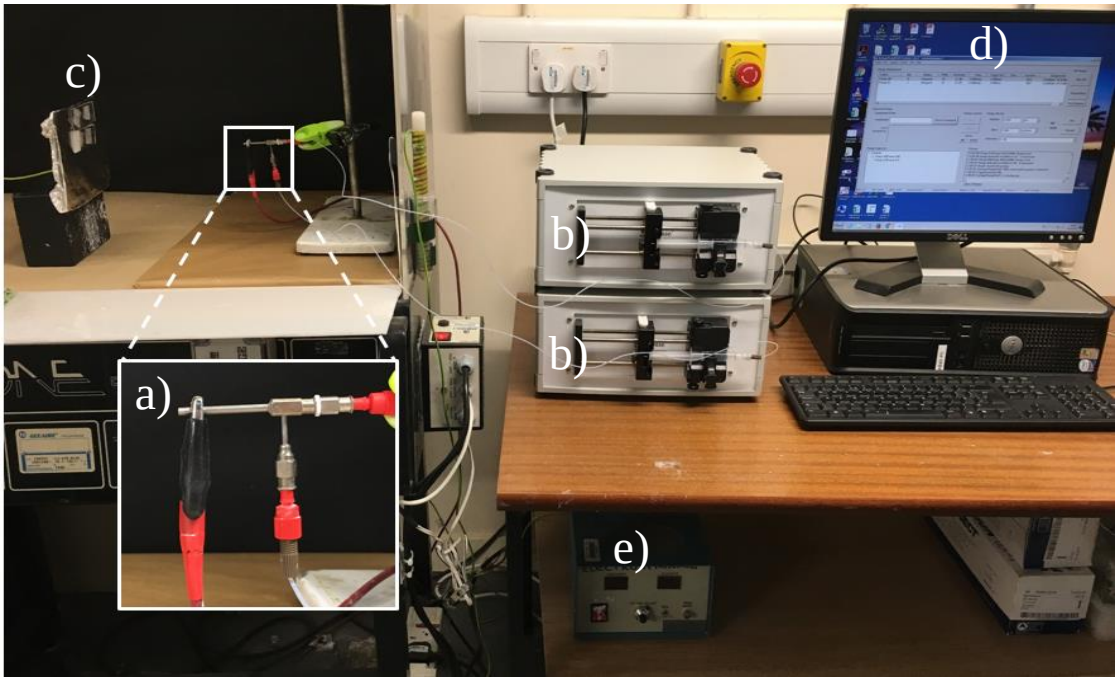

Figure 3.3 Coaxial electrospinning setup showing a) the coaxial needle, b) the two syringes mounted in their pumps, c) the collector, d) the computer used to control the syringe pumps, and e) the voltage supply

3.2.3 3D electrospinning

Core and shell solutions for 3D scaffolds were prepared following the method described in Section 3.2.2.1. To produce tubular co-electrospun scaffolds, a custom built needle collector were made using LEGO power functions XL-motor (rotation speed 220 rpm) and stainless steel needles of various diameters as shown in Figure 3.4. Prior to electrospinning, collector needles were sprayed with anti-adhesive PTFE spray in order to facilitate tubes extraction from the needles and left to dry for 10-15 minutes before electrospinning. Solutions were electrospun into the needle collectors using the working parameters described in Section 3.2.2.2. Electrospun tubes were left to dry for 15-20 minutes after electrospinning before extracting them gently from the collector.

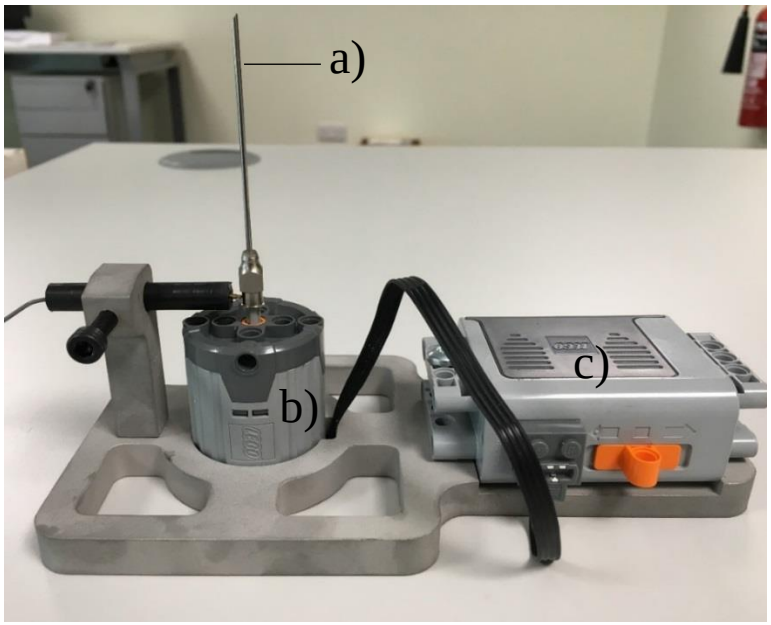

Figure 3.4 Needle collector for 3D electrospinning showing a) the needle, b) the motor, and c) the LEGO battery box

3.3 Characterisation

3.3.1 Optical microscope

The morphology of electrospun fibres were observed at different magnifications using Nomarski microscope (Nikon Eclipse ME600) with Nikon digital Camera DXM 1200. Images were taken and saved via ACT-1 software, and the average fibre diameter were measured by using ImageJ software (NIH, USA).

3.3.2 Scanning electron microscopy (SEM)

SEM was used to examine surfaces with high depth of focus or to identify the material composition of the samples. It uses a fine electron beam to scan the surface of the sample in a raster pattern. This beam is focused by electromagnetic lenses on a small spot on the surface. Depending on the material and the required magnification, the electron beam energy may vary from as low as 100 V to 30 kV. When the beam hits the surface, secondary electrons, backscattered electrons, and X-ray cathodoluminescence beams are emitted as a result of the interaction between the electron beam and the sample. These emitted beams are detected and counted and the resulted signals for each point are converted to grey values. Finally, by synchronizing the scanning movement with a display, a grey value

image of the topography is obtained, which is similar to black and white television images (Schmitt, 2014).

The morphology of the electrospun scaffolds was observed using scanning electron microscope (JOEL JSM-6400 SEM) at an accelerated voltage of 10 kV at the School of Chemistry, University of Glasgow. Specimens were cut from each PLA and PLA/HA combination and mounted on aluminium stubs using double sided carbon conductive adhesive tape. The specimens were sputter coated with a thin layer of gold-palladium using a Quorum Q150T ES sputter coater. Coating was carried out at a current of 25 mA for 4 minutes maximum (stopping at 20 nm thickness). The average fibre diameter of each sample was calculated by analysing at least 50 fibres from three different SEM images using ImageJ software. In addition, SEM was also used to observe if there was an apatite layer formed on the surface layer of the fibres after immersion in SBF (section 3.3.7.1).

3.3.3 Transmission electron microscopy (TEM)

Transmission electron microscopy (TEM) has been extensively used to investigate the morphology, crystalline structure and composition of membrane materials at the nanometre level. Similar to SEM microscope, TEM generates highly focused beam of electrons, which impact the specimen inside a vacuum chamber. However SEM microscope is primarily used to examine the surfaces of the materials (like reflection light microscopes), while the TEM is designed to characterise the internal structure of specimens (like transmission light microscopes). The other main difference between SEM and TEM is that SEM imaging is based on reflected electrons from the specimen, whereas in TEM the electrons through the specimen are collected and used for imaging. In addition, TEM microscope uses much higher electron beam energy than SEM, typically 80–300 kV, to enable penetration through the material, thus providing higher spatial resolution to allow easier analysis of features as small as few nanometres. The key components of TEM microscope include the electron gun which accelerates electrons through the high accelerating voltage to give them sufficient energy to pass through up to 1 μm of material, electromagnetic lenses (condenser, objective, and projector lenses) located before and after the specimen to focus the electrons into a beam of controlled diameter and convergence and then form and magnify the diffraction

pattern (image), and a digital transmitted electron detection system, usually charged coupled devices (CCD), which convert incoming electrons into an electronic pulse per pixel. The thickness of a TEM specimen should usually be less than 100nm to allow electrons to pass through the material and achieve good signal-to-noise ratio (Inkson, 2016; Kogure, 2013; Tang and Yang, 2017; Walther, 2017).

TEM microscopy was used to identify the core and shell structure of the control and HA-containing coaxial fibres. Samples were cut into small square pieces and embedded in Epon resin before slicing them into thin (~70nm thick) sections using a Leica ultracut UCT ultramicrotome (Leica, Austria) equipped with an ultrafine diamond knife. TEM copper grids were used to collect the thin sections, which were then imaged using a JOEL 1200 EX II transmission electron microscope at an accelerated voltage of 80 kV. TEM imaging was performed at the School of Chemistry, University of Glasgow.

3.3.4 Laser Scanning Confocal Microscopy (LSCM)

Laser scanning confocal microscopy (LSCM) is a powerful light imaging technique used for creating high-quality images of samples that would otherwise appear hazy when observed under a conventional microscope. This is accomplished by actively suppressing any signal coming from out-of-focus planes, which is achieved by placing a pinhole in front of the photomultiplier detector. When light is arises from an in-focus plane, it can freely passes through the pinhole and imaged by the microscope objective, while light coming from out-of-focus planes is largely blocked by the pinhole. Thus, the obtained image would have less blur and better contrast than that of a traditional optical microscope (Müller, 2006). In addition, LSCM offers other distinct features such as: the ability to control depth of field, and the capability of producing a series of thin optical sections (0.5 to 1.5 micrometre) from thick specimens (Claxton et al., 2006). Although LSCM can be used to view unstained samples by using the light reflected back from it, samples are mostly labelled with one or more fluorescent probes.

To optically determine the presence of the core/shell morphology within the fibres, fluorescent dyes were added to each of the polymer solutions, which allowed their visualization with confocal microscopy. About 10 mg of rhodamine

B (red fluorescence) was mixed with 15ml of PCL core solution, while 10 mg of fluorescein isothiocyanate (FITC) (green fluorescence) was mixed with 15ml of PLA-HA sheath solution (Figure 3.5). The dyes were added immediately before electrospinning and mixed for about 1 hour to ensure homogeneity. Aluminium foil was wrapped around the solution containers to protect them from light. Samples were observed using a LSM880 inverted confocal microscope with Airyscan (Carl Zeiss, Germany) with 20×, 40×, and 63× objectives. A 488nm laser was used to excite the FITC labelled shell and collect the resulting fluorescence, while a 561nm laser was used to excite the rhodamine B labelled core. ZEN Black software (Carl Zeiss) was used to acquire and analyse the images while Imaris software (version 7.6.5.) was used to generate 3D model from the z stacks.

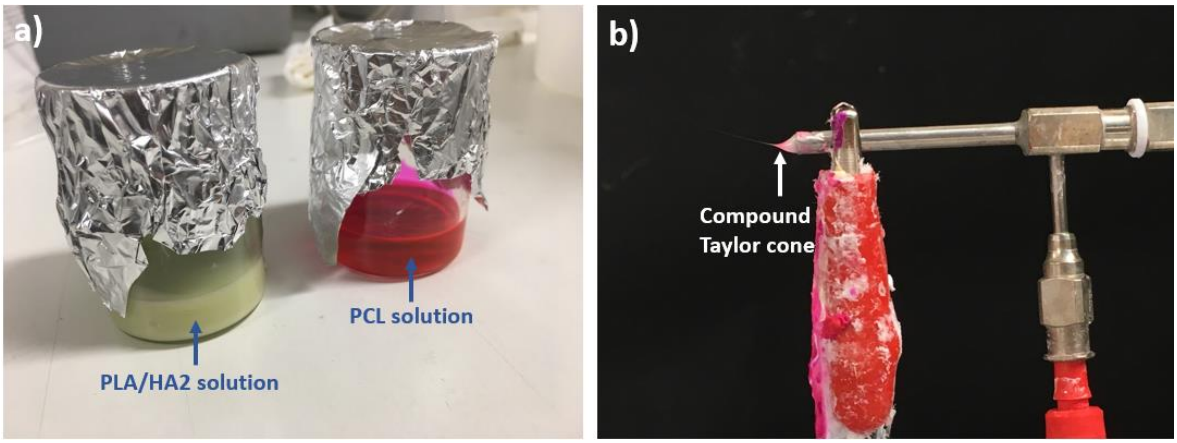

Figure 3.5 (a) PLA/HA2 and PCL solutions labelled with green (FITC) and red (rhodamine B) fluorescence dyes respectively right before electrospinning. (b) The compound Taylor cone generated during the coaxial electrospinning of polymeric solutions labelled with fluorescence dyes

3.3.5 Porosity

Porosity is an important property of scaffolds and is defined as the ratio of void space to the total volume. In this study, porosity of electrospun scaffolds were measured using one or more of the following methods: gravimetric method, mercury porosimetry and DiameterJ (ImageJ plugin).

In the gravimetric method, the apparent density and porosity of the electrospun scaffolds were calculated using the following equations (Guarino et al., 2008; He et al., 2005; Ma et al., 2005):

$$\text{Apparent density (g cm}^{-3}\text{)} = \frac{\text{scaffold mass (g)}}{\text{scaffold thickness (cm)} \times scaffold\ area\ (cm^2)} \quad \text{Equation 3.1}$$

$$\text{Scaffold porosity (\%)} = \left(1 - \frac{Scaffold\ apparent\ density\ (g\ cm^{-3})}{\text{Scaffold bulk density}\ \ (g\ cm^{-3})}\right) \times 100\% \quad \text{Equation 3.2}$$

The thickness of the scaffolds were measure by a micrometre (Mitutoyo 102-217, Japan) with an accuracy of ±0.002 mm. The bulk density for neat PLA scaffolds were taken as 1.24 g cm^{-3}, while the bulk density of PLA/HA scaffolds were calculated using the following equation (Whelan, 1994):

$$\rho_{scaffold} = (m_{PLA} + m_{HA})/(m_{PLA}/\rho_{PLA} + m_{HA}/\rho_{HA}) \quad \text{Equation 3.3}$$

Where $\rho_{scaffold}$= bulk density of electrospun PLA/HA scaffold, m_{HA}= mass of HA added to scaffold, m_{PLA}= mass of PLA in the scaffold, ρ_{PLA}= bulk density of PLA, and ρ_{HA}= bulk density of HA (3.162 g cm^{-3}). For coaxial electrospinning, the bulk density of the scaffolds were roughly estimated to be 1.30 g cm^{-3}. Five samples (n=5) were measured for each composition and the results were expressed as the average ± standard deviation.

The mercury porosimetry technique allows the determination of the average pore diameter and pore size distribution in addition to the total porosity of the samples. Scaffolds are placed in the sample cell and subsequently infused with mercury under progressive pressures to force the mercury into the pores of the scaffolds. Mercury is a non-wetting material which makes it the best choice for pore investigation because its high surface tension does not wet the samples and no pore penetration occurs by capillary action (Hekmati et al., 2014; Loh and Choong, 2013). Assuming that the pores are entirely cylindrical and equally accessible to mercury, the applied pressure can then be converted into the pore diameter by using the Washburn equation:

$$D = \frac{-4\,\gamma \cos\theta}{P} \quad \text{Equation 3.4}$$

Where D is the pore diameter, P is the applied pressure, γ is the surface tension of mercury (480 erg cm^{-2}, 0.48 N m^{-1}) and θ is the contact angle between mercury and the pore wall, taken as 140° (Hekmati et al., 2014; Keun Kwon et al., 2005; Pham et al., 2006).

Mercury porosimetry measurements were performed at The Advanced Materials Research Laboratory (AMRL), University of Strathclyde using a Quantachrome Poremaster 60 porosimeter. Measurements were made on one sample, approximately 200mg mass, of each scaffold type.

The total porosity and pore size were also determined using DiameterJ which is an ImageJ plugin that measures pore areas and porosities based on a thresholding technique. This technique relies on separating the pixels which fall in defined range from those which do not. Thus, by defining a grayscale cut-off point (defined by the segmentation algorithms in the program), the grayscale SEM image is converted into a binary image, and any grayscale values below the cut-off become black (background) and those above become white (object). Porosity and pore size were determined for five SEM images (n=5) per scaffold type.

3.3.6 Mechanical testing

The mechanical properties of the electrospun mats were measured using uniaxial tensile testing. The experiment was carried out using a Zwick/Roell Z2.0 (Zwick Roell, USA) tensile test machine with a 5N load cell operating at displacement rate of 1 mm min^{-1}. The thickness of the samples were varied according to sample composition, hence, it was measured individually for each sample using a micrometer. Samples were cut in a rectangular shape with dimensions of 60 x 10 mm using a custom built cutting device. Prior to testing, all specimens were mounted on rectangular cardboard frames with outer dimensions of 60 x 40 mm and an inner rectangular cut out at 40 x 20mm and fixed by adhesive tape. Frames were then loaded into the test machine and secured in place before cutting the sidewalls of the frame to ensure that only the sample is loaded during the test (Figure 3.6). Tensile testing was thus performed to a reduced size version of BS ISO 13934-1 standard for fabric textiles (British Standards Institution, 1999). The

force-displacement data was collected for all the samples using Zwick/Roell TestXpert® software.

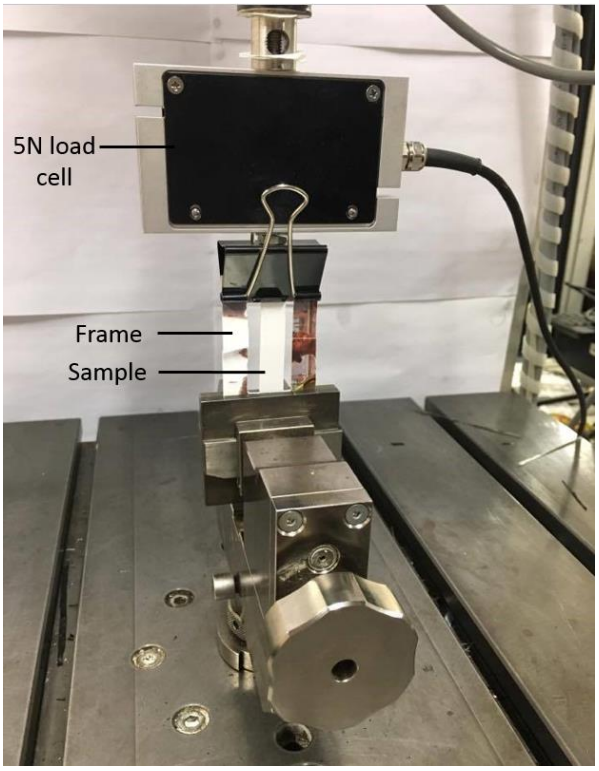

Figure 3.6 Sample cut mounted on the tensile testing machine showing both the mounting frame and the sample

From the force-displacement data, the stress and strain were calculated using equations 3.5 and 3.6

Stress: $\sigma = F/A$ Equation 3.5

Strain: $\varepsilon = \Delta L/L$ Equation 3.6

Where *F* is the force, *A* is the cross sectional area of the sample, *ΔL* is the displacement, and *L* is the original length of the sample.

From obtained stress-strain curve (a typical curve is shown in Figure 3.7), Young's modulus was calculated over the linear region of the graph by using equation 3.7

Young's modulus: $E = \sigma/\varepsilon$ Equation 3.7

The ultimate tensile strength (UTS) was also calculated for each sample. The final results for each PLA/filler composition were averaged to get the average values of UTS and Young's modulus.

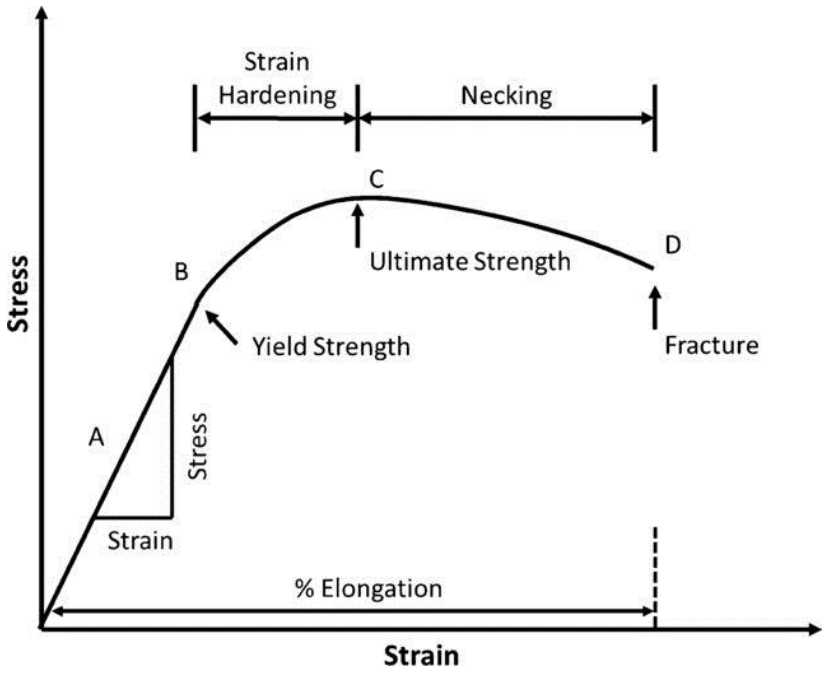

Figure 3.7 A typical stress–strain curve obtained from tensile testing (from Lim and Hoag, 2013)

3.3.7 Degradation studies

3.3.7.1 SBF preparation

Bioactivity and degradation studies were carried out using corrected Simulated Body Fluid (c-SBF) (Kokubo, 1991), distilled water and PBS, respectively. Simulated body fluids have an equal ion concentrations to those of blood plasma, except for Cl^- and HCO_3^- ions, where the concentration of Cl^- in c-SBF is higher, and the concentration of HCO_3^- which in c-SBF is lower than those of blood plasma. It should mentioned that c-SBF differs from the original SBF (SBF-K9) prepared by Kokubo et al. (1990) in the level of SO_4^{2-} ions; the SBF-K9 lacks SO_4^{2-} ions contained in human blood plasma. Ionic concentrations of SBF-K9 and c-SBF compared to those of human blood plasma are shown in Table 3.3 (Kokubo and Takadama, 2006; Oyane et al., 2003).

Table 3.3 Ion concentrations of the original SBF-K9, c-SBF and PBS in comparison with human blood plasma (Kokubo and Takadama, 2006; Oyane et al., 2003)

Ion	Human Blood Plasma (mM)	SBF-K9 (mM)	c-SBF (mM)	PBS
Na^+	142.0	142.0	142.0	156.4
K^+	5.0	5.0	5.0	4.5
Mg^{2+}	1.5	1.5	1.5	-
Ca^{2+}	2.5	2.5	2.5	-
Cl^-	103.0	148.8	147.8	139.7
HCO_3^-	27.0	4.2	4.2	-
HPO_4^{2-}	1.0	1.0	1.0	10
$H_2PO_4^-$	-	-	-	1.8
SO_4^{2-}	0.5	-	0.5	-

Prior to c-SBF preparation, all the apparatus used (glassware, spatulas, bottles, etc.) were washed with 1.0 M HCl, neutral detergent and distilled water. First, approximately 1.4 litres of distilled water were poured into a 2 litre polypropylene (PP) beaker and this was stirred using a magnetic bar and heated to 36.5°C. The chemicals shown in Table 3.4 (all supplied from Sigma-Aldrich, UK) were added in order while stirring, making sure that each reagent was completely dissolved before adding the next. After the addition of the final reagent, the final pH of the fluid was adjusted to 7.40 at 36.5°C using 1.0 M HCl and further distilled water was added to create a final solution volume of 2 litres. PP bottles were rinsed with a small amount of the solution before using to store SBF. The prepared SBF was refrigerated at 5ºC for up to a week before use.

Table 3.4 Chemical reagents used to prepare 2 litres of c-SBF (Oyane et al., 2003)

Order	Reagent	Amount
1	NaCl	16.072 g
2	$NaHCO_3$	0.704 g
3	KCl	0.45 g
4	$K_2HPO_3 \cdot 3H_2O$	0.46 g
5	$MgCl_2 \cdot 6H_2O$	0.622 g
6	1.0 M HCl	80 ml
7	$CaCl_2$	0.586 g
8	Na_2SO_4	0.144 g
9	$(CH_2OH)_3CNH_2$	12.126 g
10	1.0 M HCl	Titrate to pH 7.40

3.3.7.2 Water uptake and weight loss measurements

Degradation samples were cut into the same dimensions used for tensile test (60mm x 10 mm) and their initial weight were recorded before testing (±0.1mg Pioneer™ analytical balance, Ohaus, USA). Thereafter, they were immersed in SBF solution in rinsed polypropylene bottles. The volume of solution used for sample evaluation is calculated using equation 3.8

$$V_s = S_a/10 \qquad \text{Equation 3.8}$$

Where V_s is the volume of SBF and S_a is the apparent surface area of the sample (mm^2) (Marques et al., 2011).

After each degradation period, samples were taken out of the solution, washed thoroughly with distilled water, and then blotted gently with a paper towel to remove excess water after which they were immediately weighed with analytical balance. Water uptake percentage was calculated using equation 3.9 (Augustine et al., 2014; Choi et al., 2011; Huang et al., 2013):

$$\text{Percentage of water uptake} = \frac{W_{wet} - W_{dry}}{W_{dry}} \times 100 \qquad \text{Equation 3.9}$$

Where W_{wet} is the wet weight of the sample, and W_{dry} is the dry weight of the sample.

After measuring the wet weights, samples were dried for 48h in a desiccator and weighed again. Weight loss percentage was then calculated using equation 3.10 (Augustine et al., 2014; Huang et al., 2013):

$$\text{Weight loss percentage} = \frac{W_{\circ} - W_r}{W_{\circ}} \times 100 \qquad \text{Equation 3.10}$$

Where $W_{\circ}$ is the initial weight of the sample, and W_r is the residual weight of the sample after degradation.

3.3.8 Thermogravimetric analysis (TGA)

TGA analysis was used to characterise the thermal stability and decomposition mechanism of polymers and fibres, as well as explaining the effect of additives and chemical modifications on fibres and the thermal behaviour of polymer blends and copolymers.

A typical TGA instrument is consist of three major components: a sensitive recording balance, a controlled furnace with atmosphere management system, and a data recorder or plotter. The analysis is conducted by heating the sample to a certain temperature and monitoring its weight with time. This alteration might results from the removal of residual solvent or due to polymer degradation. TGA results are usually displayed as a TGA curve in which weight (mg) or weight percent (%) (Y-axis) is plotted against time or temperature (X-axis), while the first order derivative curve of TGA refers to the temperatures at which the maximum decrease of weight occurs (Hatakeyama and Quinn, 1999; Price et al., 2000).

TGA measurements were performed for PLA particles, dissolved PLA and electrospun PLA, PLA/HA scaffolds before and after 28 days of degradation using TGA Q500 TA Instrument under nitrogen atmosphere. Samples were heated from room temperature to 500 C° at heating rate of 10 C° min^{-1}. Two samples of each combination (n=2) were tested and then averaged. All the results were plotted as temperature (C°) versus weight loss (%) and curves were then analysed using Universal Analysis 2000 software (TA Instruments-Waters LLC, USA). TGA was

performed at the School of Chemistry, University of Glasgow by Mr Andrew Monaghan.

3.3.9 Fourier Transform Infrared (FTIR) spectroscopy

Fourier transform infrared (FTIR) spectroscopy is a physico-chemical technique used for analysing the molecular structure of organic and non-organic materials by measuring the vibration of molecules excited by IR radiation at specific wavelength range. FITR measurements can also be used to confirm the presence of fillers inside the composites and determine if any chemical bonding occurs with the host materials.

The IR region (10-14000 cm^{-1}) of the electromagnetic spectrum is commonly divided into three smaller areas: near-IR (10-400 cm^{-1}), mid-IR (400-4000 cm^{-1}), and far-IR (4000–14000 cm^{-1}). The mid-IR is the most commonly used region for analysis as all molecules possess characteristic absorbance frequencies and primary molecular vibrations in this range. Therefore, IR spectroscopy methods are mainly based on examining the interaction of mid-IR radiation with samples. As the radiation passes through the sample, specific wavelengths are absorbed causing the chemical bonds in the material to undergo vibrations such as stretching, contraction, and bending. The spectrum is then plotted where Y-axis represents absorbance or transmittance and the X- axis represents wavenumber (cm^{-1}). FTIR spectra follow the Beer-Lambert law which shows that the absorbance is directly proportional to the concentration of the material as shown in the equation 3.11:

$$A = l \varepsilon c \qquad \text{Equation 3.11}$$

Where A = absorbance, l = Path length, ε = absorptivity, and c = concentration.

Transmittance, on the other hand, depends on measuring the intensity of the IR radiation before and after it passes through the sample as shown in equation 3.12:

$$\%T = I_S / I_R \qquad \text{Equation 3.12}$$

Where T= transmittance, I_S = Intensity of IR beam after passing through the sample, and I_R = Intensity of IR beam before passing through the sample (Davis and Mauer, 2010).

Once measurements are made, the resulted FTIR spectrum is considered as a "fingerprint" of the sample where absorption peaks positions indicate the frequencies of vibrations between the bonds of the atoms forming the materials and the size of those peaks indicate the amount the materials present in the sample (Singh et al., 2011). The FTIR technique became significant analytical method for biomedical applications because it offers the following advantages:

1- FTIR is non-destructive and only small amount of materials are required for the measurement. Additionally, minimal tissue preparation is needed.

2- It can provide an indirect evaluation for the synthesized implant materials obtained from TCP and HA bioceramics because it identifies peaks location, intensity, width, and shape (Berzina-Cimdina and Borodajenko, 2012; Rehman et al., 1995).

FTIR spectra were recorded using a Spectrum One FTIR Spectrometer (PerkinElmer, USA). Samples were tested directly without the need to prepare KBr disks typically used in the preparation of FTIR samples due to the Attenuated Total Reflectance (ATR) accessory attached to the FTIR equipment. The ATR crystal used was a diamond/thallium-bromoiodide (C/KRS-5) with a penetration depth up to 2 μm. Scans were obtained in absorbance mode across the 4000–400 cm^{-1} wavenumber range at a resolution of 8 cm^{-1} with 32 scans performed per spectrum and analysed using the equipment's Spectrum® software (PerkinElmer, USA). Five samples were tested for each type of scaffolds and then spectrums were averaged and analysed using KnowItAll® Academic Edition Spectroscopy Software (Bio-Rad Laboratories, Inc., USA). FTIR was performed at the Centre for Textile Conservation, University of Glasgow.

3.3.10 Energy Dispersive X-ray spectroscopy (EDX)

EDX spectroscopy is a non-destructive analytical tool used to detect the elemental composition of substance by using scanning electron microscope. When the high energy electron beam of an SEM hits the sample, elements within the sample interact with the beam and emit characteristic X-rays based on the energy of the incident beam. EDX detects the emitted X-rays and measures the energy and intensity of each element's X-rays. The elements can be identified and measured for their concentration in the sample due to the principle that no elements have the same X-ray emission spectrum. The resulted information about the elemental composition can then be overlaid on top of the magnified image of the sample using a process known as X-ray mapping. EDX can be used to identify and evaluate materials, including determining unknown elements, identifying contaminants, as well as for quality control screening and verification, and others (Abd Mutalib et al., 2017; Mishra et al., 2017).

EDX spectroscopy has been used in this study to detect and measure the CaP apatite formation on the surface of coaxial electrospun tubes upon immersion in SBF for 12 weeks. Bioactivity of control and HA-containing coaxial tubes were measured after 4, 8 and 12 weeks of immersion, using a Carl Zeiss Sigma variable pressure analytical SEM with Oxford microanalysis equipped with 80 mm silicon-drift detector for EDX. Three samples (n=3) of control and HA-containing tubes were measured at time point at an accelerating voltage of 20 kV. EDX analysis was performed at Imaging Spectroscopy and Analysis Centre (ISAAC) at the School of Geographical & Earth Sciences, University of Glasgow.

3.3.11 Measurement of BMP-2 release

The release of BMP-2 from the co-electrospun PCL-PLA/HA2 and PCL-PLA (control) scaffolds in vitro was quantified via enzyme-linked immunosorbent assay (ELISA) kit following the protocol provided by the manufacturer (R&D Systems, Inc., USA). First, the scaffolds were cut into 15mm diameter circles and placed in 24-well plates. BMP-2 was dissolved in PBS at concentration of 50ng/mL and then added on to the surface of the samples as a drop (250µl/sample). Samples were kept at room temperature and allowed to dry overnight. The next day, samples were placed in new wells and 1ml of phosphate buffered saline (PBS) was added to each membrane. At the desired time points (0.25, 1, 2, 4, 24, 48, 72 and 96 h), the

PBS was collected and stored at -20 °C until analysis, and the scaffold was re-incubated in 1 mL fresh PBS.

To prepare the 96-well plates for ELISA, the first step was to dilute the Capture Antibody (mouse anti-human BMP-2 capture antibody) which recognizes an epitope on human BMP-2 in PBS (1:120) and 100µl of the diluted solution was placed in each well of a 96 well plate. The plate was sealed and incubated overnight at room temperature. The next day, each well contents were aspirated and washed with Wash Buffer composing of PBS with 0.05% v/v Tween-20 (400 µl /well) for three times. After the last wash, the plate was inverted and blotted it against clean paper towels to remove any remaining. To block non-specific binding sites, 300 µl of Reagent Diluent were added to each well and incubated at room temperature for 1 hour. The plate were washed again with Wash Buffer after incubation and became ready to use. To measure BMP-2 release from samples, 100µl of standards, control and HA-containing samples were added to each well and covered with an adhesive strip followed by incubation for 2 hours at room temperature. After incubation, the plate was aspirated and washed with Wash Buffer three times. Then, 100 µl of the Detection Antibody (biotinylated mouse anti-human BMP-2 detection antibody) diluted in Reagent Diluent (1:60) were added to each well and then covered with a new adhesive strip and incubated for 2 hours at room temperature. After washing away any unbound substances, 100 µL of Streptavidin-HRP was added to each well and the plate was covered and wrapped in aluminum foil to avoid direct light and then incubated for 20 minutes at room temperature. Streptavidin-HRP is composed of Streptavidin (the biotin-binding protein) and the conjugated HRP which provides enzyme activity for detection. The plate were aspirated and washed again before adding 100 µL of Substrate Solution to each well. The plate was wrapped in foil again and incubated for another 20 minutes at room temperature. The final step included adding 50 µL of Stop Solution to each well followed by gentle tapping on the plate to ensure thorough mixing and then the optical density of each well was measured immediately using a microplate reader set to 450 nm with background checking at 570nm. Five samples (n=5) were used for each composition and each time point. The cumulative release ratio was calculated as the ratio of the cumulative mass of BMP-2 released at each time interval to its initial input amount in the scaffold, which was 12.5 ng mL^{-1}.

3.3.12 Cell culture

Electrospun scaffolds were sterilised by soaking in an 80 % ethanol (v/v) solution. Sterile scaffolds were washed several times in sterile PBS and finally soaked in Dulbecco's modified eagle medium (DMEM) supplemented with 10 % fetal bovine serum (FBS), 110 mg/L sodium pyruvate, 1000 mg L^{-1} glucose, 100 U ml^{-1} penicillin, 100 μg ml^{-1} streptomycin and 0.25 μg ml^{-1} amphotericin, 2 mM L-glutamine (hereafter referred to as expansion media). Prior to cell seeding, scaffolds were cut to fit into the wells of standard 24-well culture plates under sterile conditions.

Human mesenchymal stem cells (MSCs) (Promocell, UK) were expanded under standard culture conditions (5 % (v/v) CO_2 and 37 °C). To seed the scaffolds, cells were trypsinised, counted by haemocytometer and pipetted onto scaffolds at a density of 4000 cells/cm^2. Cells were cultured up to 21 days, with media changed every two days. Cells up to passage 3 were used for all experiments.

Cell-scaffold interactions were examined by scanning electron microscopy. At 1, 7, 14 and 21 days cell culture media was removed from cells in culture. Cells seeded scaffolds were washed in HEPES saline and fixed in 1.5% Glutaraldehyde/0.1M sodium cacodylate for 1 hour at 4 °C. Afterwards, the fixative solution was removed and scaffolds was submerged in 0.1M sodium cacodylate buffer rinse for 3 times (5 minutes each). Samples were post fixed in 1% osmium tetroxide buffer for 1 hour followed by three distilled water washes (10 minutes each) and then en bloc stained with 0.5% aqueous uranyl acetate (light sensitive stain) for 1 hour in dark area. For imaging, scaffolds were dehydrated through an ethanol gradient (30%, 50%, 70%, 90% and 100%) and then critically point dried using a Tousimis autosamdri-815 before mounted on SEM aluminium stubs and coated with gold-palladium as described in section 3.3.2. Cell culture and samples preparation for SEM was performed by Dr Tom Hodgkinson at the Centre for Cell Engineering and School of Chemistry, University of Glasgow respectively.

3.3.13 Statistical analysis

Results are expressed as mean ± standard deviation (SD) in all experiments. Statistical analysis was performed using a one- and two way analysis of variance

(ANOVA) with p-values less than 0.05 considered statistically significant, and Student's t-test method was conducted for pairwise comparisons.

Chapter 4- Optimisation of Ca/P content in PLA scaffolds

4.1 Introduction

The output of electrospinning can be controlled by a number of parameters, which have been classified into three groups: solution, process and ambient parameters as discussed in the literature review. Optimisation of these parameters is crucial to obtain continuous fibres with specific morphology and well-defined physical and mechanical properties. The effect of solution and process parameters on the morphology and mean diameter of electrospun fibres has been investigated for several polymers such as PLA, PCL and PHBV, but different results have been reported depending on the type of polymer and polymer-solvent system (Casasola et al., 2014; Katsogiannis et al., 2015; Sombatmankhong et al., 2006).

On the other hand, several research groups have studied the effect of incorporating nano-sized HA and TCP particles into electrospun polymeric scaffolds on their physical and biological properties, suggesting that their addition resulted in enhancement in thermal and mechanical properties as well as an increase of scaffold bioactivity (Rajzer et al., 2014; Sonseca et al., 2012; Sui et al., 2007; Zhang et al., 2015). However, the effect of incorporating different types and concentrations of micro-sized fillers into the scaffolds during electrospinning has been rarely reported.

This chapter focuses on optimising electrospinning parameters and CaP contents for PLA-chloroform solutions to produce scaffolds suitable for mechanical and degradation studies. This includes investigating the effect of applied voltage, polymer concentration, filler type and filler concentration on the morphology of electrospun fibres, mechanical properties and degradation/bioactivity behaviour of the scaffolds.

4.2 Materials and methods

PLA solutions filled with HA1, HA2 or TCP were prepared as described in section 3.2.1.1 and then electrospun on microscope slides (section 3.2.1.2). The applied voltage was varied from 0 to 19 kV to select the optimum electrospinning voltage. The morphological properties of the resultant PLA and PLA/filler scaffolds were observed using a Nomarski microscope as described section 3.3.1 and fibre diameter was measured using the resultant images and ImageJ software. Samples were immersed in either SBF (section 3.3.7.1) or distilled water in order to evaluate the bioactivity and degradation rate for up to 14 days. The degradation solutions were changed every 7 days and samples were extracted after 1, 3, 5, 7 and 14 days of immersion to measure their weight loss or gain (section 3.3.7.2). Mechanical properties were tested before and after 14 days degradation following the same procedure described in section 3.3.6. For each test, five samples ($n=5$) were tested for each PLA/filler composition and statistical analysis were performed as for section 3.3.13.

4.3 Results

4.3.1 Effect of solution concentration on electrospinning

All solutions containing 5% PLA had very low viscosity, hence, electrospinning using these solutions resulted into droplet formation (electrospraying) instead of fibres (Figure 4.1a), and using 10% PLA solutions resulted in electrospinning/electrospraying behaviour where a mixture of fibres, beads, and droplets were generated rather than smooth fibres. On the other hand, the viscosity of all solutions containing 25% PLA were too high to allow electrospinning. Electrospinning of 15%, and 20% PLA solutions produced smooth fibres with no beads detected. Considering the effect of fillers on solution viscosity, increasing the filler content to more than 20% led to highly viscous solutions which subsequently affected the electrospinning process, therefore, electrospinning were conducted with solutions containing only 10 and 20% filler content in 15% and 20% PLA solutions.

4.3.2 Effect of applied voltage on electrospinning

The applied voltage has a significant effect on the breakdown of the jet as it determines the strength of the electrical field experienced in the solution. At fixed flow rate of 1 ml/h, no fibres were produced at voltages less than 7 kV, while at voltages ranging between 7 kV and 10 kV, the solution jet produced a mix of fibres and dripping due to the elongation of Taylor cone at the tip of the needle. As the voltage was increased to between 11 kV and 14 kV, a continuous stable whipping jet were formed and electrospun mats produced. Finally, increasing the applied voltage above 14 kV produced discrete jets with an unstable Taylor cone which led to non-continuous formation of fibres. Therefore, the applied voltage was set at 13.7 kV throughout the rest of experiments.

4.3.3 Fibre characterisation

Electrospinning of 10% PLA solution with 0% filler led to large bead formation (Figure 4.1b), and by increasing the filler content in the solution, a mix of electrospinning and electrospraying were obtained as mentioned above. 15% and 20% PLA with no filler solutions were spun into randomly oriented, smooth fibres without beads (Figures 4.2a and b), however, introducing 10 and 20% of HA1 and HA2 into those solutions resulted in non-uniform fibres with rough surfaces and enlarged diameters (Figures 4.3 and 4.4). The incorporation of β-TCP into 15% and 20% PLA samples caused cluster formation along the fibres which increased in size with increasing TCP content (Figure 4.5). The average diameter of the electrospun fibres analysed using ImageJ are shown in Table 4.1.

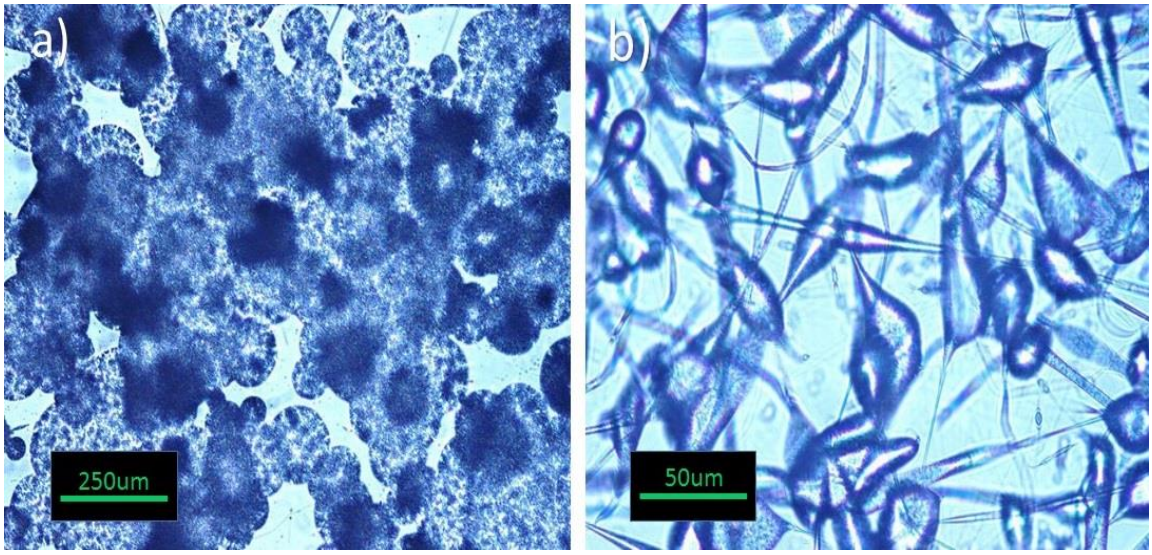

Figure 4.1 Electrospun fibres of non-filled PLA at 13.7kV and 1ml/h flow rate: a) 5% PLA (marker bar=250μm), b) 10% PLA (marker bar=50μm)

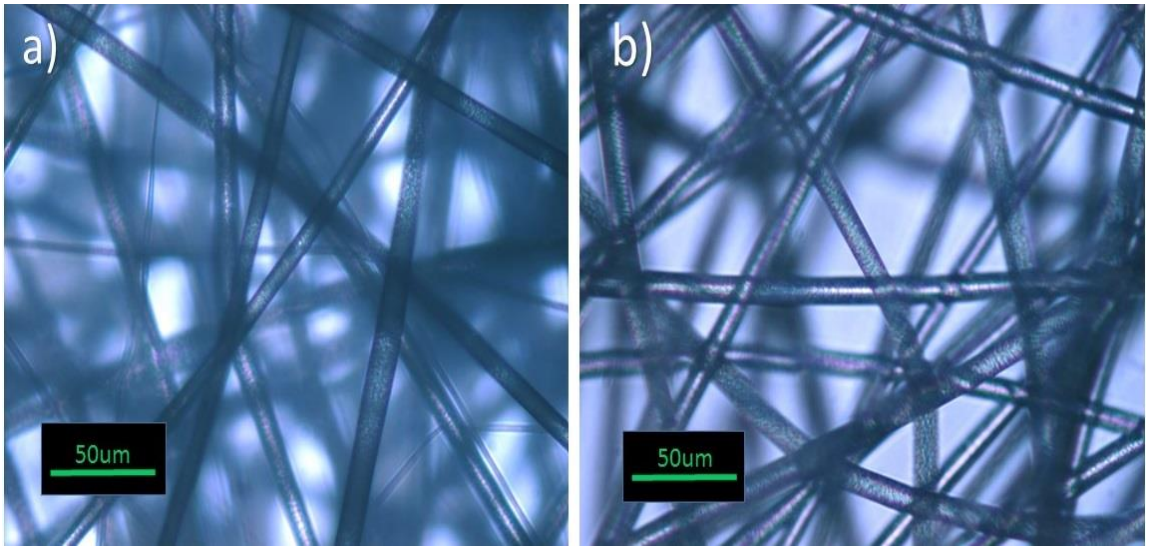

Figure 4.2 Electrospun fibres of non-filled PLA at 13.7kV and 1ml/h flow rate: a) 15% PLA, b) 20% PLA (all marker bars=50μm)

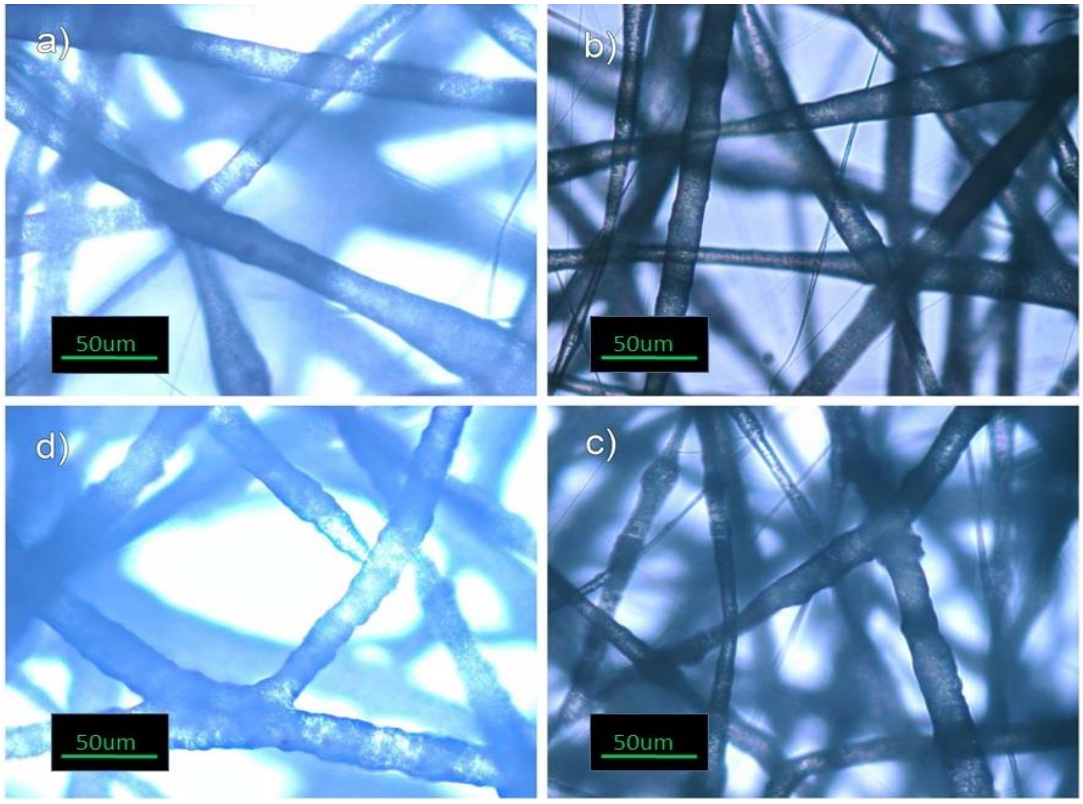

Figure 4.3 Electrospun fibres of 15% PLA at 13.7kV and 1ml/h flow rate with: a) 10% HA1, b) 20% HA1, c) 10% HA2, and d) 20% HA2 (all marker bars= 50μm)

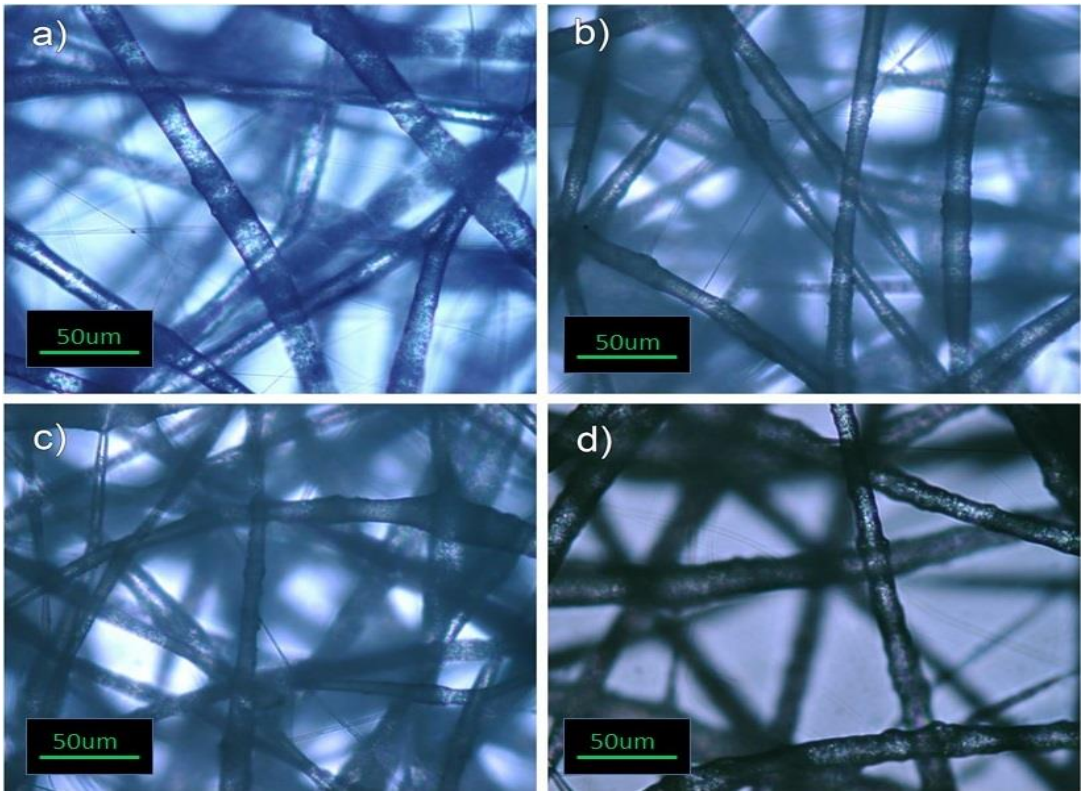

Figure 4.4 Electrospun fibres of 20% PLA at 13.7kV and 1ml/h flow rate with: a) 10% HA1, b) 20% HA1, c) 10% HA2, and d) 20% HA2 (all marker bars= 50μm)

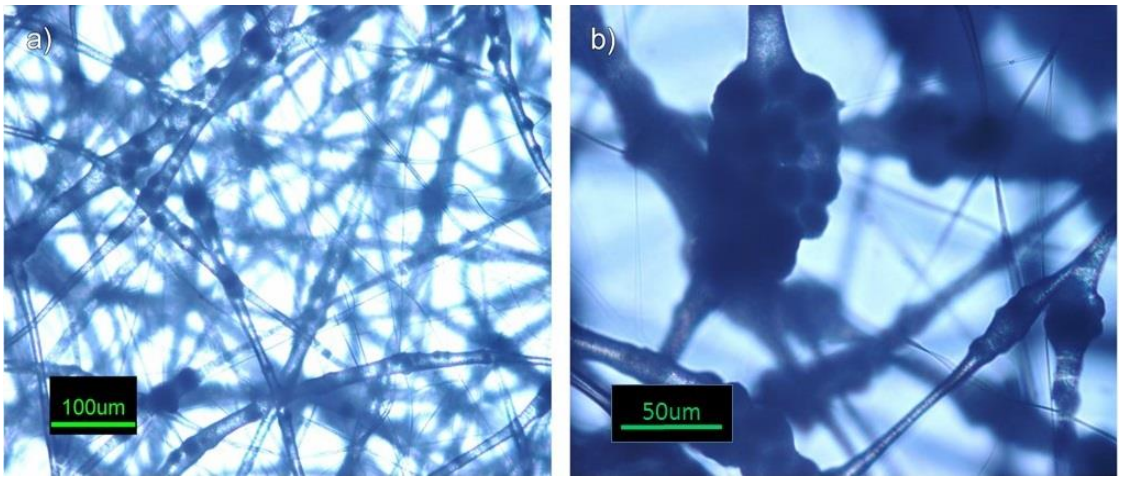

Figure 4.5 Microscope images of electrospun PLA at 13.7kV and 1ml/h flow rate with TCP at different magnifications a) scaffold at low magnification (marker bar=100μm), b) the shape of TCP clusters at higher magnification (marker bar=50μm)

Table 4.1 Fibre diameters of electrospun scaffolds for different PLA concentrations and calcium phosphate contents

Filler percentage	Fibre diameter (μm)	
	15% PLA	20% PLA
0 %	12.02 ± 0.64	13.60 ± 0.92
10% HA1	21.24 ± 4.32	21.00 ± 6.51
20% HA1	23.29 ± 6.23	20.01 ± 6.40
10% HA2	18.88 ± 6.72	18.72 ± 3.55
20% HA2	19.28 ± 4.24	17.24 ± 5.51
10% TCP	19.74 ± 1.97	18.83 ± 4.01
20% TCP	20.15 ± 8.40	19.26 ± 2.53

4.3.4 Bioactivity and degradation tests

Figures 4.6 and 4.7 represent the weight loss over 2 weeks in distilled water for 15% and 20% PLA samples, respectively, while Figures 4.8 and 4.9 shows the weight losses in SBF. Levels of significance for weight loss among samples with different filler content and at different time points are presented in Appendix A.1, Tables A.1 to A.7.

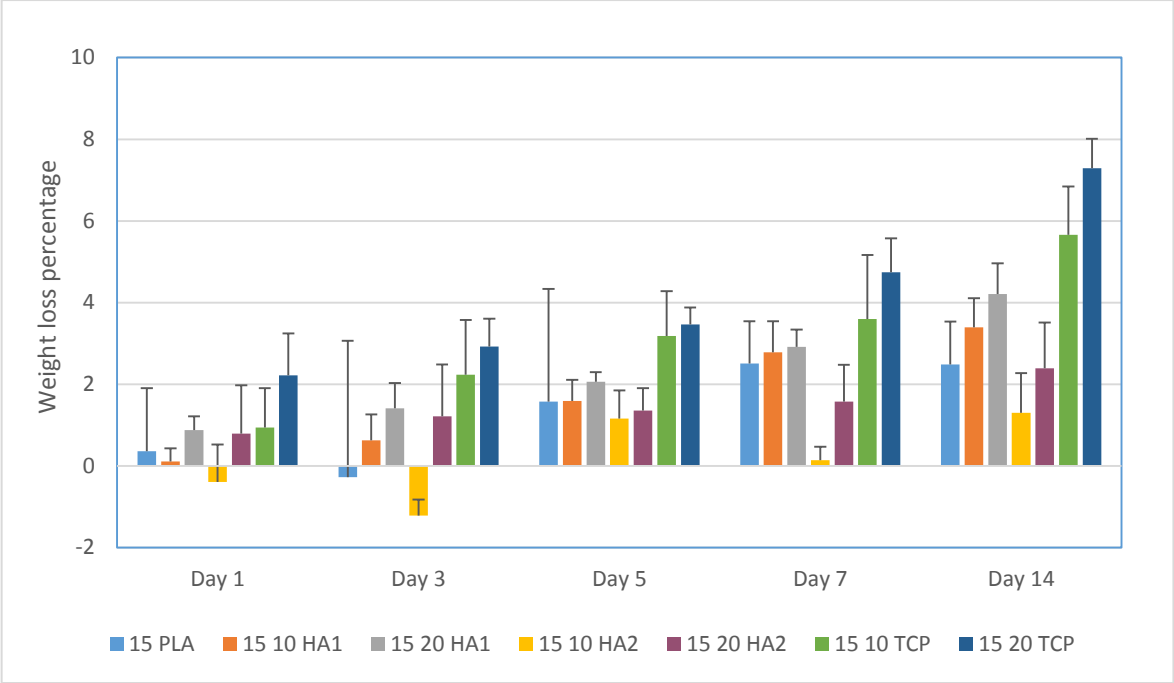

Figure 4.6 Weight loss for 15% PLA samples with no filler, 10 or 20% of HA1, HA2 or TCP in distilled water (n=5)

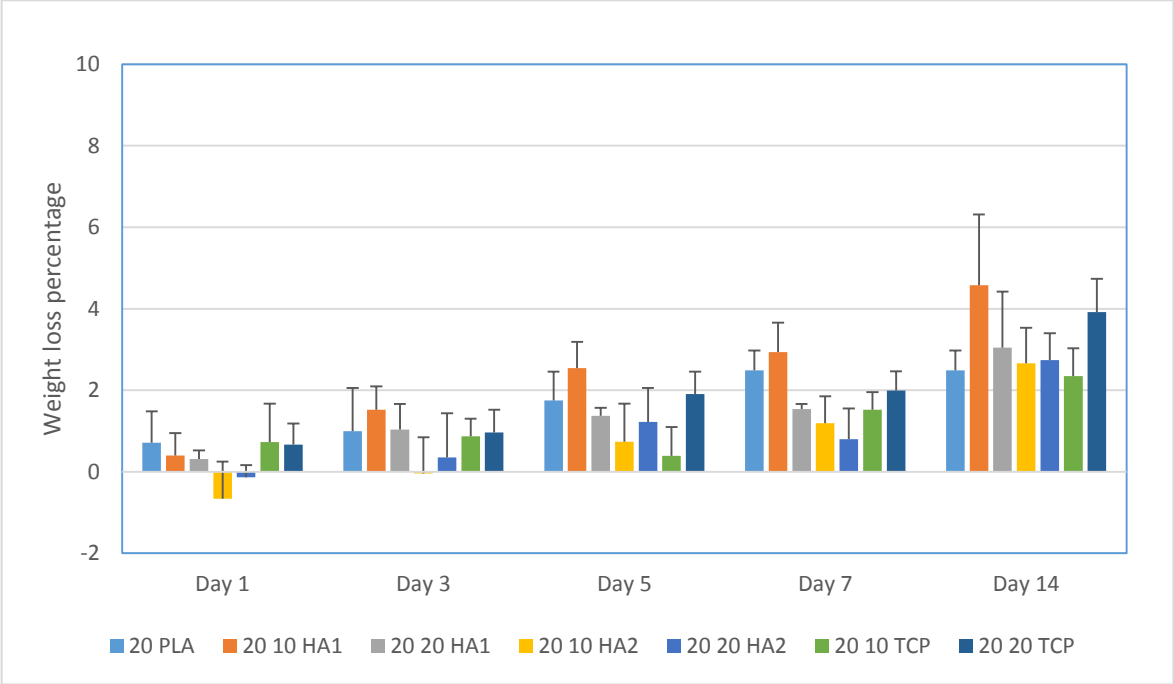

Figure 4.7 Weight loss for 20% PLA samples with no filler, 10 or 20% of HA1, HA2 or TCP in distilled water (n=5)

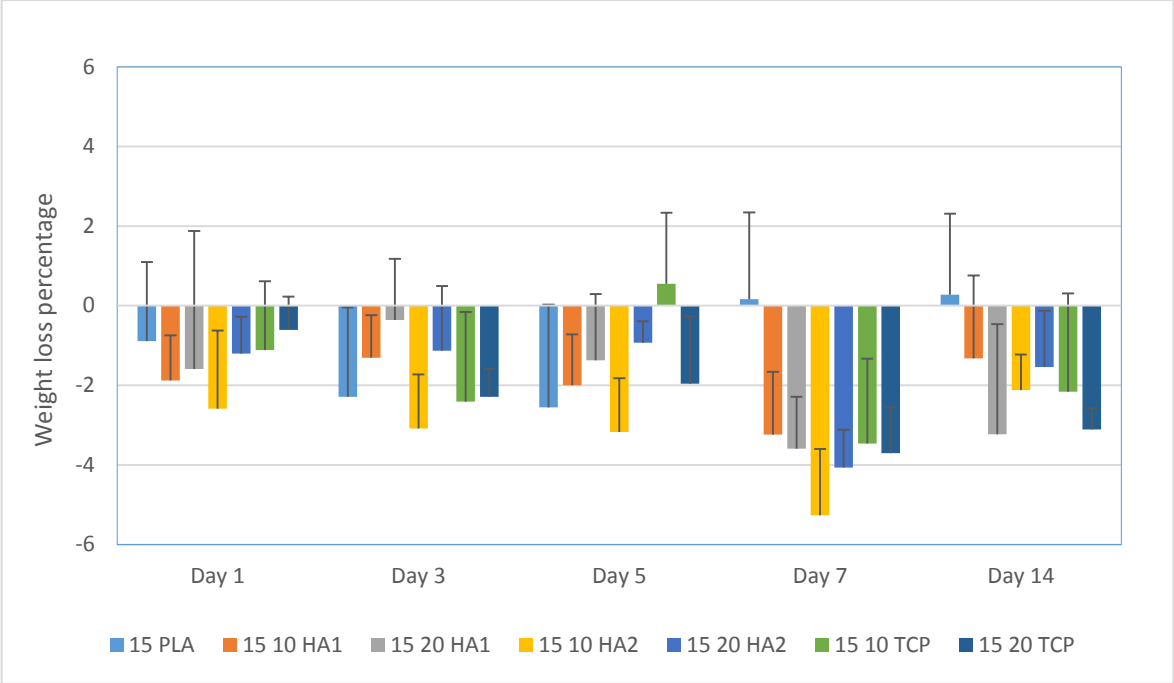

Figure 4.8 Weight loss 15% PLA samples with no filler, 10 or 20% of HA1, HA2 or TCP in SBF (n=5)

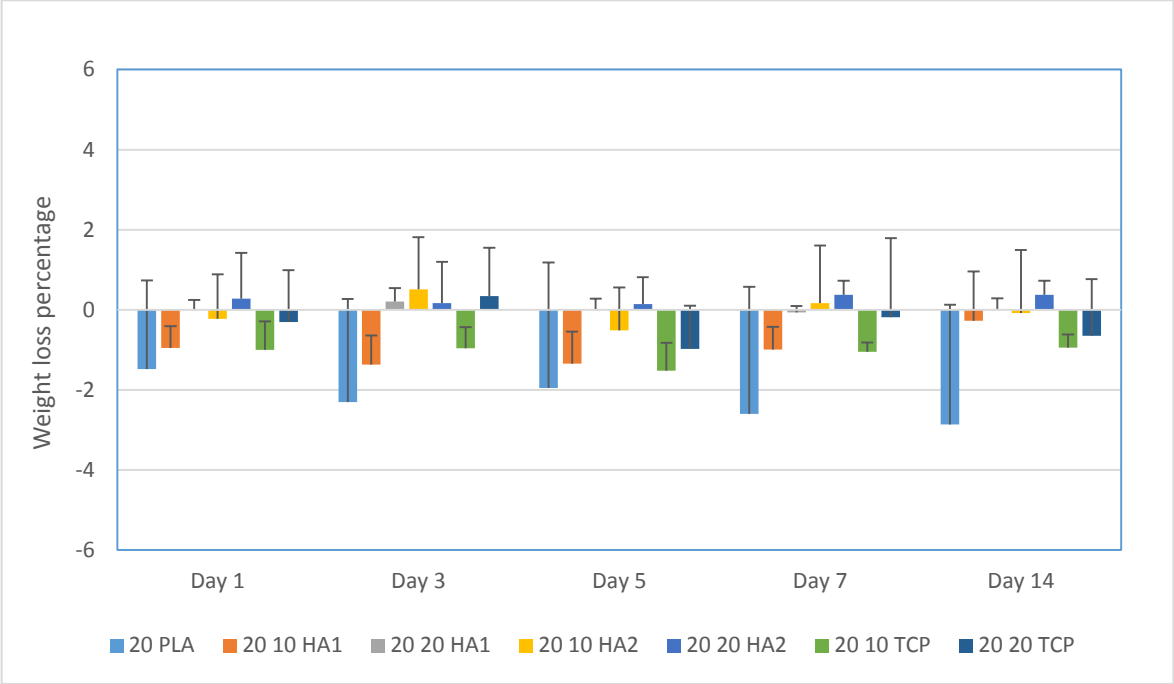

Figure 4.9 Weight loss for 20% PLA samples with no filler, 10 or 20% of HA1, HA2 or TCP in SBF (n=5)

4.3.5 Mechanical testing

The Young's moduli and ultimate tensile strength values for 15% and 20% PLA samples before degradation are shown in table 4.8. 15% PLA samples exhibited significant reduction in their strength and stiffness with increasing filler content, while for 20% PLA samples, increasing HA1 and HA2 did not affect significantly stiffness or strength. Generally, TCP samples were the weakest of all other samples. Statistical analysis for 15 and 20% PLA samples are presented in Appendix A.1, Tables A.8 and A.9 respectively.

Table 4.2 Young's moduli and ultimate tensile strength values for 15 and 20% PLA samples and different filler content before degradation

Filler percentage	**15% PLA**		**20% PLA**	
	Young's Modulus (Before degradation) /MPa	UTS (Before degradation) /MPa	Young's Modulus (Before degradation) /MPa	UTS (Before degradation) /MPa
0% filler	55.78 ± 15.02	1.300 ± 0.527	58.55 ± 11.15	1.428 ± 0.470
10% HA1	39.25 ± 9.47	0.735 ± 0.052	45.13 ± 2.56	1.137 ± 0.260
20% HA1	31.85 ± 3.26	0.460 ± 0.074	82.32 ± 16.56	1.041 ± 0.166
10% HA2	57.03 ± 7.00	1.059 ± 0.147	65.65 ± 12.61	1.394 ± 0.264
20%HA2	37.73 ± 6.81	0.546 ± 0.061	71.23 ± 5.57	1.165 ± 0.112
10% TCP	26.10 ± 15.08	0.465 ± 0.180	45.85 ± 7.51	0.890 ± 0.174
20% TCP	17.33 ± 4.86	0.361 ± 0.074	28.92 ± 3.41	0.552 ± 0.118

Figures 4.10 and 4.11 represent comparisons between Young's modulus values for 15 and 20% PLA samples with 10 or 20% HA1, HA2 or TCP in distilled water or SBF respectively before and after 2 weeks degradation.

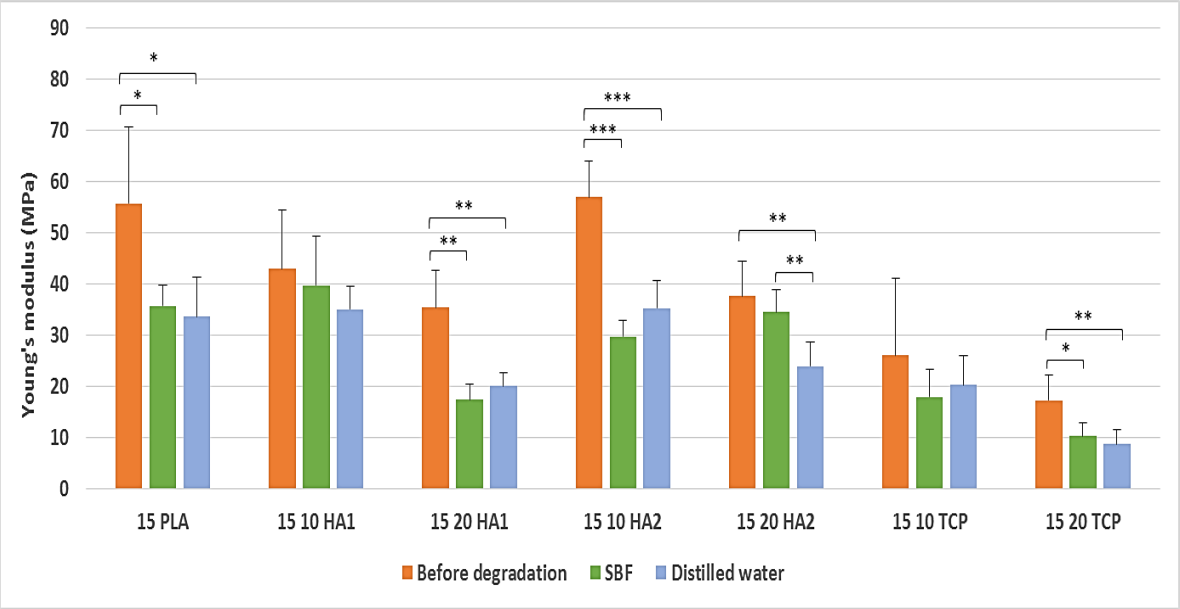

Figure 4.10 Young's moduli for 15% PLA samples with no filler, 10 or 20% of HA1, HA2 or TCP before and after degradation. * = $p < 0.05$, ** = $p < 0.01$, *** = $p < 0.001$

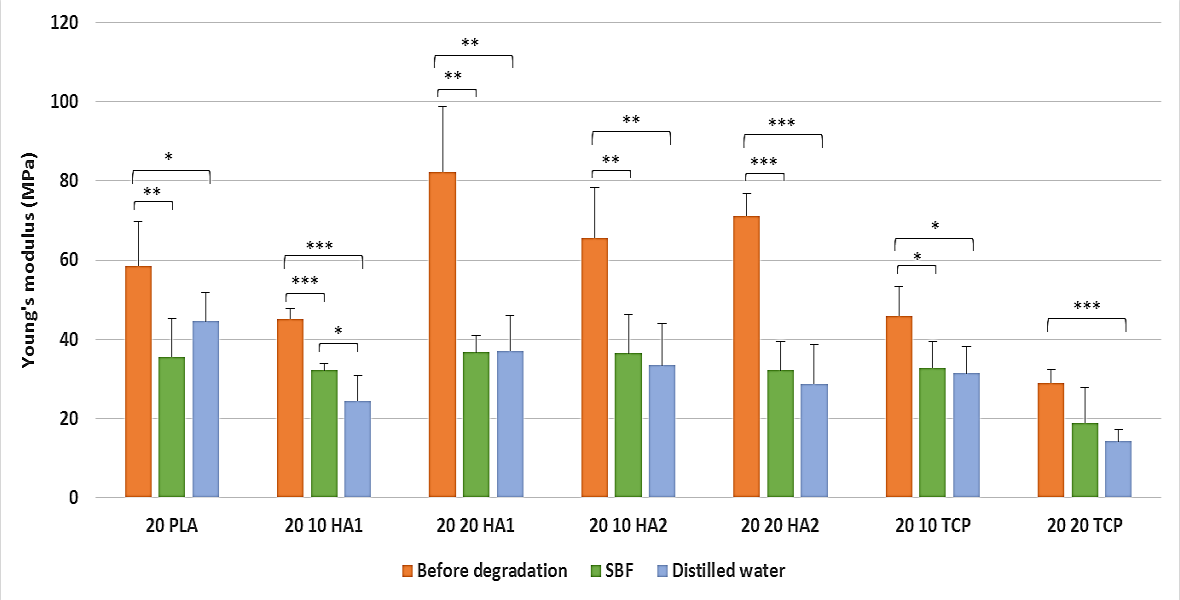

Figure 4.11 Young's moduli for 20% PLA samples with no filler, 10 or 20% of HA1, HA2 or TCP before and after degradation. * = $p < 0.05$, ** = $p < 0.01$, *** = $p < 0.001$

Figures 4.12 and 4.13 represent comparisons between tensile strength values for 15 and 20% PLA samples respectively before and after 2 weeks degradation.

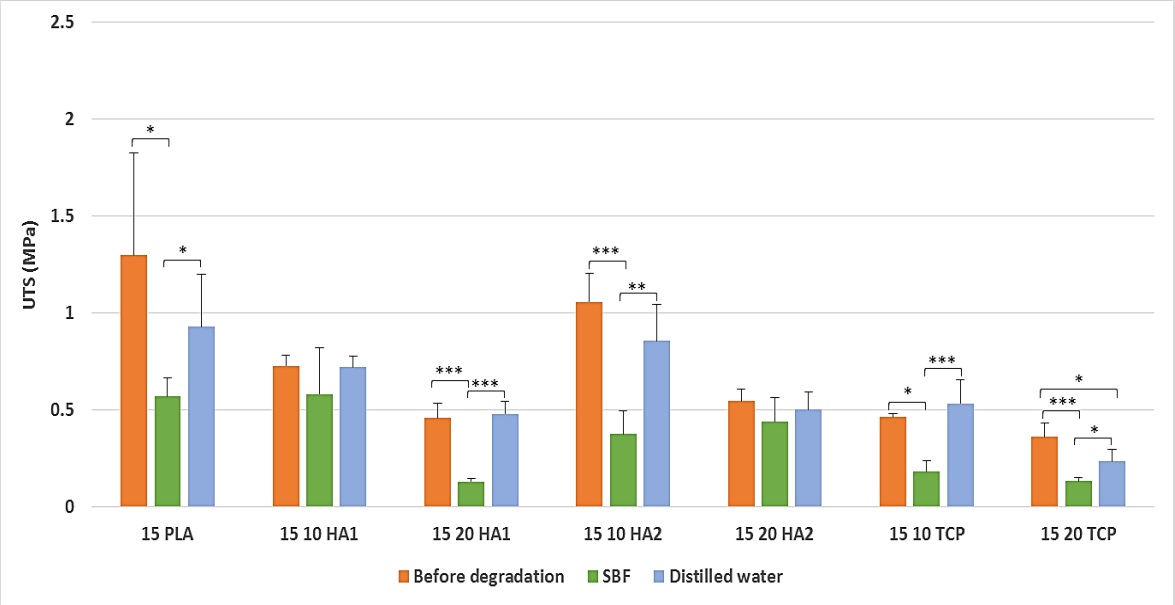

Figure 4.12 Tensile strength values for 15% PLA samples with no filler, 10 or 20% of HA1, HA2 or TCP before and after degradation. * = p < 0.05, ** = p < 0.01, *** = p< 0.001

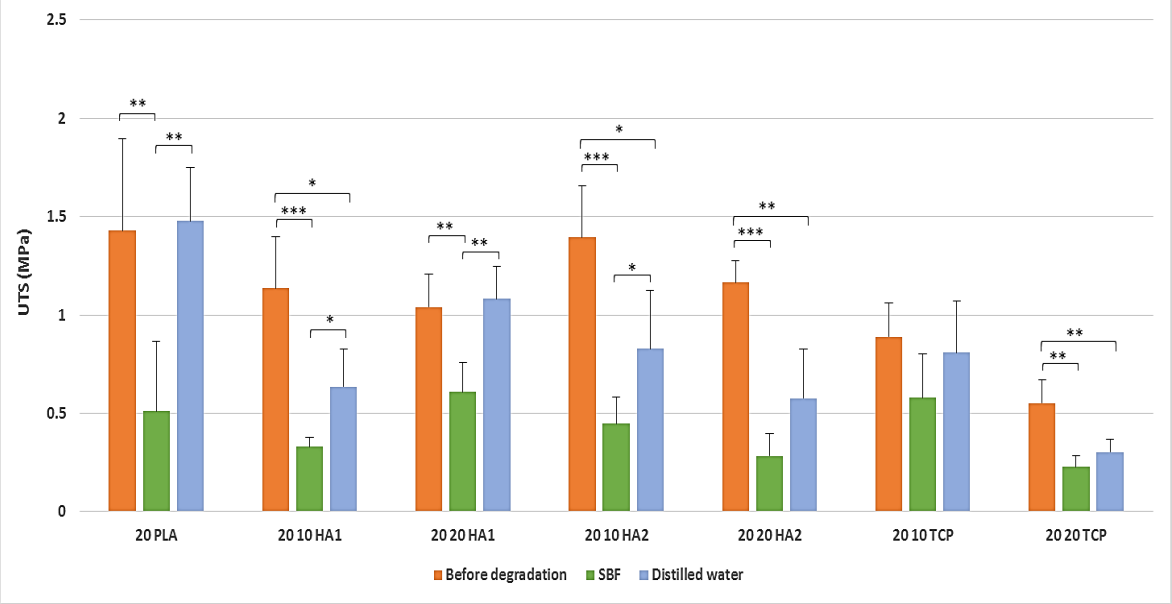

Figure 4.13 Tensile strength values for 20% PLA samples with no filler, 10 or 20% of HA1, HA2 or TCP before and after degradation. * = p < 0.05, ** = p < 0.01, *** = p< 0.001

4.4 Discussion

4.4.1 Effect of electrospinning parameters on fibres morphology

The electrospinning technique offers the advantage of producing scaffolds that mimic the architecture of the extracellular matrix of human tissues. Although electrospinning appears to be a technically simple and easy method to adapt, there are several processing parameters that need to be optimised in order to generate fibres instead of droplets or beaded morphologies. Optimisation of these variables to achieve desirable fibre morphology and properties represents the main challenge of the electrospinning process. The concentration of the polymeric solution is one of the most significant factors controlling fibre formation in electrospinning. It also has direct effect on the viscosity of solution and subsequently, the morphology of resultant fibres. Solutions of PLA concentration less than 15% failed to produce uniform fibres and exhibited a mixture of electrospray/electrospinning behaviour. McCullen et al. (2007) and Casasola et al. (2014) investigated the effect of PLA concentration on the morphology of electrospun fibres and they have found that PLA concentration below 12.5 % w/v leads to production of inconsistent fibres as well as beads formation, while PLA concentrations above 12.5 % w/v produce homogenous fibres with more chain entanglement and different fibre diameters.

By increasing the PLA concentration to 15 and 20%, electrospun scaffolds exhibited smoother fibres with high porosity (Figure 4.2). The average fibre diameters for 15% and 20% PLA solutions are 12.02 ±0.64 µm and 13.60 ±0.92 µm, respectively. However, solutions of 25% PLA concentration were too viscous and did not produce any fibres. According to Venugopal et al. (2005), Greiner and Wendorff (2007) and Sill and von Recum (2008), the concentration of polymeric solution influences both the viscosity and surface tension of the liquid which eventually decides the electrospinnability of the solution into nanofibres as well as the diameter size of the resulted fibres (increased fibre diameters as the polymer concentration increases). Thus, the charged jet of low concentration solutions fragments into discrete droplets before reaching the collector due to the effect of high surface tension, while at an increased polymeric concentration, chain entanglement between polymeric chains increases as the viscosity increases and fibres are ultimately formed. However, fibres cannot be created if the polymeric solution is too viscous due to too high polymer concentration, which slows and disrupts the flow of the polymer solution through the needle.

Zong et al. (2002) investigated the effects of solution properties and processing parameters on the structure and morphology of electrospun PDLLA membranes. A mixture of large bead defects and nanofibress were obtained on electrospinning PDLLA solutions of concentration less than 20% w/v in dimethyl formamide (DMF), while solutions with polymer concentration higher than 40% w/v were too viscous to allow electrospinning. Between these two extremes, the nanofibers produced became more uniform as the concentration, and hence viscosity, increased and the bead defects acquired larger diameters and became more spindle-shaped. They concluded that polymer concentration and salt addition have relatively larger effects on the fibre diameter than the other parameters.

Tan et al. (2005) obtained similar patterns when attempting to electrospin PLLA solutions of different concentrations and examining the effects on the resulting nanofibre morphology. Results showed that the diameter of the electrospun fibres dramatically decreased with decreasing polymer concentration from 4% to 1.25%, but the effect of surface tension became more dominant with decreased solution concentration/viscosity and beaded fibres were consequently produced.

The applied voltage is another the crucial factor within the electrospinning process. Charged jet ejection from Taylor Cone and fibre formation only occurs when the applied voltage is above the threshold voltage (Li and Wang, 2013). However, the influence of the applied voltages on the morphology and diameter of electrospun fibres is still controversial. Reneker and Chun (1996) have demonstrated that applied voltage does not have a significant impact on fibre diameter in the electrospinning of polyethylene oxide.

On the other hand, Zhang et al. (2005) studied the effect of voltage on fibre morphology and diameter distribution using poly(vinyl alcohol) (PVA)/water solutions. They showed that there is higher polymer ejection at higher voltages, facilitating the formation of larger fibre diameter. Lastly, Yördem et al. (2008) found that the applied voltage can influence fibre diameter, but the level of significances varies with polymer solution concentration and tip-to-collector distance.

The choice of solvent can also determine the structure of the resultant fibre as it affects the viscosity and conductivity of the solution. The use of chloroform as a solvent in electrospinning resulted in the production of fibres with bead-on-string morphology at low polymer concentrations while producing considerably large fibres diameter at higher concentrations (Gu et al., 2014; Katsogiannis et al.,

2015; Son et al., 2004), which could be attributed to the highly volatile nature of chloroform as well as its low dielectric constant.

Min et al. (2004) reported the effect of solvent dielectric constant on the fibre diameter of electrospun PLGA nanofibress. The average fibre diameter obtained using chloroform (dielectric constant= 4.81) was 760 nm, while PLGA dissolved in hexafluoroisopropanol (HFP) (dielectric constant= 16.7) yielded fibres with an average diameter of 310 nm. The morphologies of the fibres obtained with the two solvents were also very different. Similar observations were reported by You et al. (2005) while studying the influence of solvent polarity on PGA, PLA and PLGA. They demonstrated that PLA and PGA fibres electrospun using polar HFP resulted in fibres with average diameters of 310 nm and 290 nm, respectively, whereas electrospun PLGA fibres using the less polar chloroform as a solvent had an average fibre diameter of 760nm. Golecki et al. (2014), on the other hand, studied the effect of solvent evaporation on fibre morphology in rotary jet-spinning using chloroform and DMF as solvents with PLA. They suggested that using highly volatile solvents such as chloroform, leads to faster solvent evaporation, which increases polymer concentration and viscosity during drying, resulting in larger fibre diameters.

4.4.2 Effect of filler addition on fibre morphology

The incorporation of various types of fillers into electrospun polymers is one way to produce multifunctional composites which has been proved to be an effective way to improve the physical, biological and mechanical properties of the scaffolds. The type and particle size of the filler used with polymers in electrospinning has a strong impact on the fibre morphology and diameter. HA particles have been frequently applied alone or as a major component of bone repair biocomposite implants due to HA's non-toxicity, bioactivity and osteoconductivity, due to similarity of its chemical and crystalline structures to natural bone mineral (Murugan and Ramakrishna, 2005), whereas ß-TCP has been used as a bone repair bioceramic because of its high in vivo resorbability as well as its effect in promoting bone ingrowth and regeneration (Park et al., 2014). All the electrospun scaffolds containing HA1, HA2 and TCP showed nonwoven structures, with interconnected porous networks. Inclusion of HA1 and HA2 into PLA scaffolds led to significant changes on the surface morphology and diameter distributions (Figures 4.3 and 4.4). Both HAs were well dispersed into the fibres

and only few agglomerations were found on the surface. However, the surface became rougher with increased fibre diameter. Similar results were obtained by Novotna et al. (2014) who incorporated 5 and 15 wt% of nHA into electrospun PLA. They suggested that the roughness of the surface in PLA/HA fibres might be caused by the presence of nHA aggregates directly under or on the fibre surface. The tendency for the fibre diameter to increase with increasing HA content in electrospun PLGA scaffolds has also been reported by Lao et al. (2011).

Scaffolds with TCP also exhibited rough fibres surface but with higher agglomerations of TCP along the fibres as shown in Figure 4.5. Using higher TCP concentrations in the composite solution led to increased cluster size and number. These results are consistent with those of McCullen et al. (2009), Polini et al. (2011), Siqueira et al. (2015) and Masoudi Rad et al. (2017) who all reported increased surface roughness and TCP agglomerations with increasing TCP content in the scaffolds.

4.4.3 Bioactivity and degradation tests

Results of two weeks degradation test demonstrated that there were no statistically significant variations among non-filled 15 and 20% PLA samples immersed in either degradation solution over the period of two weeks, which indicates that increasing polymer concentration in electrospun scaffolds had no effect on degradation behaviour. Within the first week of immersion in SBF, the weight changes among 15 % PLA samples during the first 5 days of immersion were generally not significant, while at day 7 of immersion, samples containing all three types of fillers in different percentages showed a significant increase in their weights compared to non-filled 15% PLA samples ($p < 0.05$) and that could be attributed to apatite formation on the surface of fibres containing Ca/P fillers, while in second week of immersion, weight differences between filled and non-filled 15% PLA samples were generally reduced, which could be the result of increased degradation on the second week balancing mineral deposition. On the other hand, there were large variations in the weights of non-filled 15% PLA samples during degradation in distilled water, thus no significant variations were generally noticed between non-filled samples and samples containing HA1 and HA2 after two weeks immersion except for the samples containing 20% HA1 which showed significantly greater weight loss than non-filled samples on day 14 and 10% HA2 which showed significantly lower weight loss on day 7 of immersion. Samples

containing HA1 exhibited significantly higher weight loss compared to HA2 which could have resulted from poor interfacial adhesion between HA1 and the polymer matrix. However, the incorporation of TCP led to significant increases in degradation rate compared to non-filled samples and samples containing both types of HAs. Degradation rate increased with increasing TCP concentration. In general, the dissolution rates of calcium phosphates are inversely proportional to the Ca/P ratio, phase purity, crystalline size and surface area. ß-TCP with Ca/P= 1.5 is well known to have higher solubility than HA (Ca/P ratio=1.67) (LeGeros and LeGeros, 2013). Eggli et al. (1988) reported an in vivo study of a rabbit model in proximal tibial and distal femoral bone defect using 3 mm diameter ß-TCP and HA cylinders. Results revealed that up to 85 % of ß-TCP were resorbed after 6 months post-implantation whereas the volume reduction of the hydroxyapatite was only 5.4% after the same period.

According to Lam et al. (2008), the incorporation of the TCP particles into composites increases the rate of media diffusion, as the TCP dissolved or dislodged from the polymeric matrix and the numerous pits and caverns created would thus increase the surface area for media intrusion and attack throughout the more hydrophilic TCP network.

Masoudi Rad et al. (2017) studied the effect of using different ß-TCP concentrations (5, 10 and 15%) on two-layered bioactive membranes fabricated by electrospinning; one layer of their membranes was fabricated using poly glycerol sebacate (PGS)/polycaprolactone (PCL) and ß-TCP to provide guided bone regeneration (GBR) and other layer composed of PCL/PGS and chitosan to act as guided tissue regeneration (GTR). Degradation tests indicated that incorporation of TCP enhanced the hydrophilicity due to high surface energy of TCP nanoparticles which ultimately increased the biodegradation of the membranes, while bioactivity was found to increase with increasing ß-TCP content from 5 to 15%.

In another study, McCullen et al. (2009) fabricated electrospun composite scaffolds consisting of ß-TCP particles and PLA at varying loading levels of TCP (0, 5, 10, 20 wt %) and assessed the composite scaffolds' degradation, keeping the scaffolds under physiological conditions (37°C, 5% CO_2) in osteogenic cell culture medium, and measuring the endogenous calcium content on days 6, 12, 18. Results showed that electrospun scaffolds loaded with 10 and 20 wt% TCP demonstrated a large initial loss of calcium content from days 1 through 6 and continued to

release calcium from the scaffold for the duration of the experiment. They suggested the reason to be the formation of TCP agglomerates at high TCP concentrations which could account for the initial release of calcium from the scaffold loaded with 10 and 20 wt% TCP.

Weight changes in samples containing 20% PLA were less than 15% PLA samples and compared to non-filled 20% PLA samples, incorporation of filler did not affect degradation or bioactivity rate significantly. However, Table A.6 (Appendix A.1) indicates that the weight of all samples have reduced significantly in distilled water from day 1 of immersion to day 14, while weight changes for all samples among degradation days in SBF were minor.

Large weight variations were observed among most of 15 and 20% samples, which might resulted from drying the samples at room temperature after degradation, and since the sample weights are very small, the accuracy of results might be affected by the room temperate and humidity.

4.4.4 Mechanical testing

The mechanical properties of polymer based composites filled with inorganic particles depend on several parameters including: the type of filler used, the dispersion of the filler particles and the interaction at the polymer–filler interface (Patlolla et al., 2010). Table 4.2 indicates that the addition of increasing amounts of HA1 to 15% PLA samples resulted in significant reduction of stiffness and ultimate strength, however, adding 10% HA1 did not affect the properties significantly. On the other hand, incorporation of 10 and 20% HA2 into 15% PLA scaffolds led to lower reductions in the tensile properties than HA1 and the changes compared to non-filled scaffolds were not statistically significant. This reduction probably resulted from the agglomeration of HA particles within the scaffolds, creating weak links within PLA matrix and acting as stress concentrators, thus reducing the strength of the scaffolds (Rajzer, 2014), while the differences between HA1 and HA2 filled scaffolds could be due to improved distribution of HA2 within the polymer matrix compared to HA1. These results do not fully support the findings of the research published by Sui et al. (2007), where they found that addition of HA particles into PLLA solution led to significant increases in both values of Young's modulus and tensile strength, although the research did not report the amount of the HA added to PLLA solution and they

used nano HA instead of micro HA which can provide better HA dispersion. However, reductions in the tensile modulus and strength of electrospun scaffolds after adding of HA nano and micro particles were reported by Venugopal et al. (2008), Mi et al. (2014), Zhang et al. (2015) and Tanaka et al. (2016).

For samples made from 20% PLA concentration, the addition of either HA led to slightly higher Young's modulus, but did not affect the strength substantially. This is mainly because as the polymer concentration increases, the resultant scaffolds exhibited smoother fibres with improved diameter uniformity, and that will increase fibre cohesion points, thus, enhancing the tensile strength of the scaffold (Tarus et al., 2016). Incorporation of ß-TCP significantly decreased the mechanical properties of both 15% and 20% PLA samples which may result from cluster formation which caused breakage in the continuity of the resulted fibre chain and made the samples more fragile (Siqueira et al., 2015). These results are consistent with those of McCullen et al. (2009) and Masoudi Rad et al. (2017) who found that the deterioration in mechanical properties increased with increasing TCP content. After degradation in SBF, the UTS of all samples were significantly reduced to almost half of their before degradation values, while many samples have retained their tensile strengths or reduced slightly during distilled water degradation. On the other hand, Young's modulus values decreased at different rates after soaking in both media for all samples due to progressive weight loss during degradation. The differences in tensile strength values between distilled water and SBF samples result from SBF ions attack or due to samples swelling inside SBF which ultimately reduced their strength. These results agree with the findings of Johnson et al. (2009), which demonstrated that deionized water had the least effect on the tensile strength of electrospun PCL scaffolds over 28 days of immersion compared to other degradation medias such as plasma, saline, sodium bicarbonate, urine and milk.

It could also be seen that by increasing the filler percentage in the composite, the mechanical properties dropped faster during degradation. This is attributed to increased moisture absorption of PLA/filler scaffolds compared to neat PLA scaffolds, which occurs due to the weak interfacial adhesion between the filler particles and PLA. As the filler content increases, aggregations of filler particles within the scaffold increase and micro gaps are created at the PLA-filler interface. Water molecules could penetrate into these micro-voids or accumulate at the

filler-matrix interface, which results in a filler-matrix debonding, thus reducing the mechanical properties.

Besides the effect of degradation media and fillers, same samples were used for calculating weight loss during the whole immersion period, and during extraction from degradation solution and drying at each time point, mechanical loads were exerted on the samples, which could result in damage to the samples, thereby decreasing their mechanical strength.

4.5 Conclusions

Among various PLA solutions, only 15 and 20 wt% PLA solutions with either 0, 10 or 20 vol% of HA1, HA2 or TCP were able to produce uniform electrospun fibres. The introduction of CaP fillers into PLA solutions increased the fibre diameter while generally reducing the mechanical properties. Due to higher degradability of TCP compared to HA1 and HA2, as well as its low mechanical properties in vitro, no further experiments will be carry out using TCP ceramic.

Chapter 5- Effect of filler concentration and morphology

5.1 Introduction

Hydroxyapatite has been incorporated within a variety of polymeric matrices to improve polymer mineral bioactivity as well as enhance cell growth and response (Kouhi et al., 2015; Lao et al., 2011; Tyagi et al., 2009; Zhang et al., 2008). Most studies prefer to use nano-sized HA needles due to their high aspect ratio and uniform suspension as well as mimicking the natural bone structure. However, Peng et al. (2011) reported that needle-like micro-HA had better performance than nano-HA in PLLA-HA electrospun scaffolds in terms of cell proliferation and differentiation in aligned scaffolds at the early culture stages. In another study, Tetteh et al. (2014) electrospun nano and micro-size HA particles with polyether-urethane (PU) polymers (Z3A1 and Z9A1) and investigated the effect of particle size on fibre morphology, mechanical properties, biocompatibility, extracellular and calcified matrix production over a 28 day period. Their results revealed that inclusion of both sizes of HA particles in PU–HA solutions reinforced the scaffolds and increased the mechanical properties, although for Z9A1, both yield strength and Young's modulus of micro-HA containing scaffolds were significantly higher than those of nano-HA containing scaffolds. Hence, further study on the effects of micro-sized HA on scaffold properties is valuable.

This chapter examines the effect of increasing HA specific surface area and using high micro-sized HA content on the porosity, bioactivity, thermal stability and mechanical properties of the electrospun PLA composites.

5.2 Materials and methods

15 and 20% PLA scaffolds containing 10 or 20% (v/v) of HA1 or HA2 were produced as described sections 3.2.1.1 and 3.2.1.2. Samples were immersed in SBF for up to 28 days to evaluate their bioactivity and degradation rate, the solutions were changed every 7 days. The morphology of PLA and PLA/HA scaffolds before and after 28 days of immersion were observed using SEM as described in section 3.3.2. The apparent density and porosity of the electrospun scaffolds were calculated using a gravimetric method as described in section 3.3.5. Weight loss and water uptake were calculated at days 7, 14, 21 and 28 of immersion. The tensile properties of scaffolds were evaluated after 14 days of immersion as described in section 3.3.6. Due to the fragility of electrospun mats, mechanical testing samples were only extracted once after 14 days of immersion in order to reduce any handling effects on the samples. HA content in PLA scaffolds before immersion and the amount of apatite deposition on the scaffolds surfaces were measured by TGA as described in section 3.3.8. Finally, FTIR spectra were obtained for HA powder, electrospun PLA, PLA/HA scaffolds after 0, 14, and 28 days of SBF immersion using the method described in section 3.3.9.

5.3 Results

5.3.1 SEM and Porosity measurements

Figures 5.1 and 5.2 show the morphologies of electrospun 15 and 20% PLA fibres containing HA1 or HA2 before immersion in SBF. The total porosity and apparent density values of the scaffolds are listed in Table 5.1.

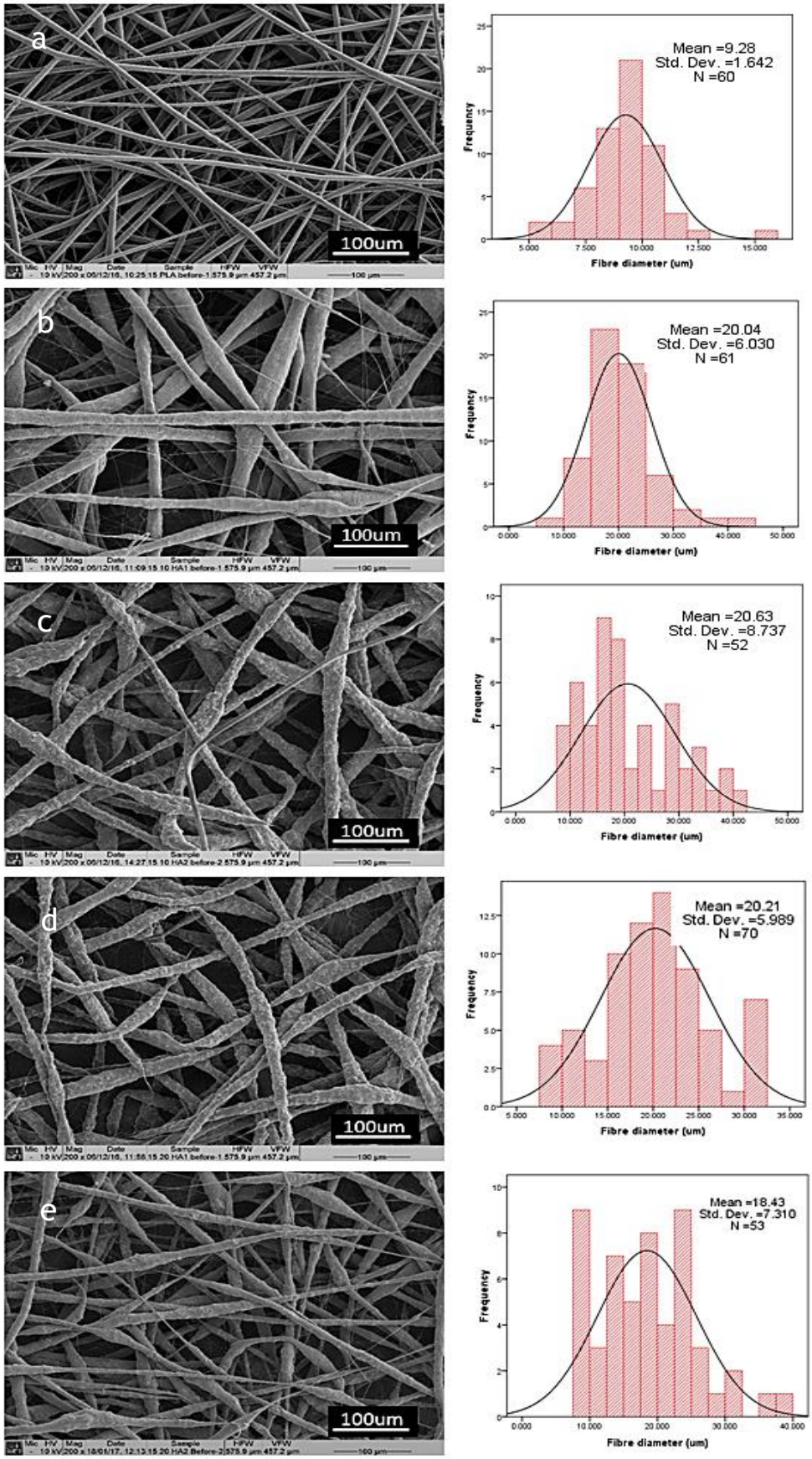

Figure 5.1 SEM images and fibre diameter distributions for electrospun 15% PLA with (a) no filler, (b) 10%HA1, (c) 10%HA2, (d) 20% HA1, and (e) 20% HA2 (marker bars= 100μm)

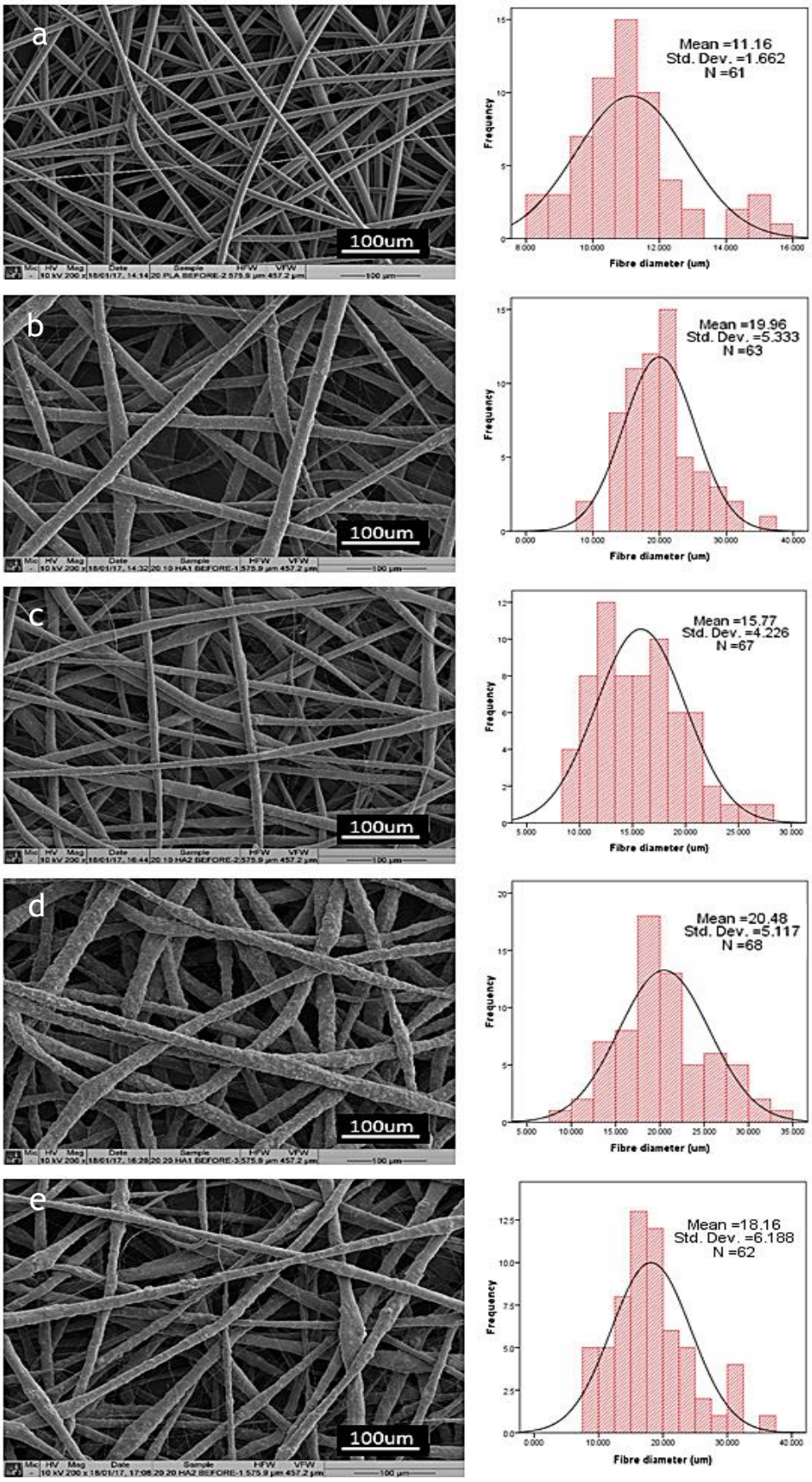

Figure 5.2 SEM images and fibre diameter distributions for electrospun 20% PLA with (a) no filler, (b) 10%HA1, (c) 10%HA2, (d) 20% HA1, and (e) 20% HA2 (marker bars= 100μm)

Table 5.1 Porosity and apparent density of PLA and PLA/HA composite scaffolds

Filler percentage	15% PLA		20% PLA	
	Porosity (%)	Density (g cm^{-3})	Porosity (%)	Density (g cm^{-3})
0 %	90.54 ± 1.22	0.124 ±0.015	91.41 ± 2.87	0.117 ±0.025
10% HA1	87.86 ± 2.93	0.174 ±0.042	89.40 ± 2.02	0.151 ±0.010
20% HA1	90.33 ± 1.74	0.157 ±0.019	88.34 ± 0.77	0.189 ±0.011
10% HA2	89.10 ± 0.92	0.156 ±0.013	87.86 ± 1.66	0.173 ±0.005
20% HA2	89.54 ± 2.68	0.170 ±0.047	88.23 ± 0.39	0.190 ±0.027

Figures 5.3 and 5.4 show the morphologies of electrospun scaffolds after 28 days of SBF immersion. For non-filled PLA scaffolds, the fibres maintained their shape and no swelling or ruptured fibres were noticed. Most of 20% PLA scaffolds filled with either HA1 or HA2 have also maintained their structure. However, at higher magnification, a number of ruptured or broken fibres were noticed in some 15% PLA samples and apatite precipitation was observed on the fibre surface of both HA1 and HA2 filled scaffolds after immersion (Figure 5.5).

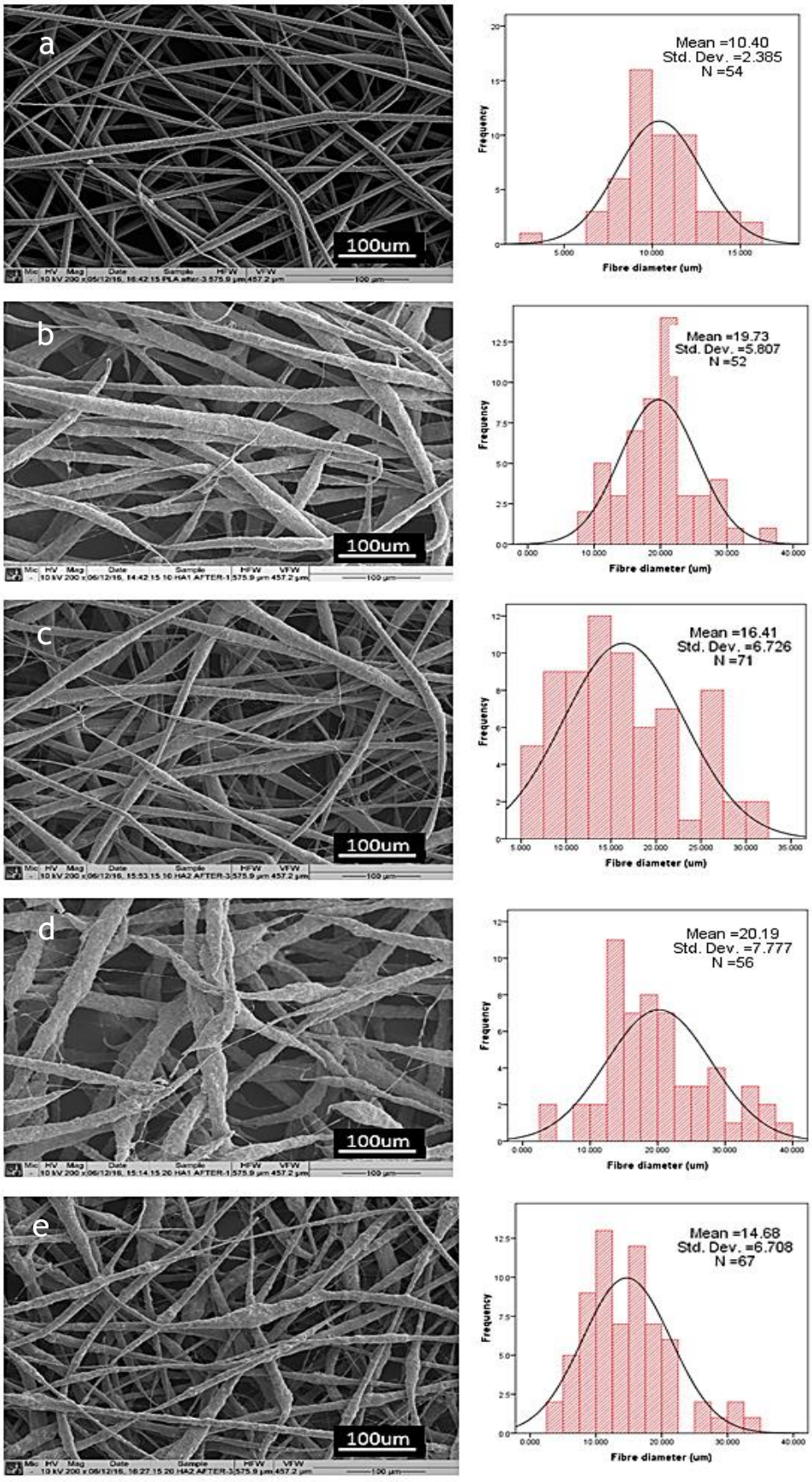

Figure 5.3 SEM images and fibre diameter distributions for electrospun 15% PLA with (a) no filler, (b) 10%HA1, (c) 10%HA2, (d) 20% HA1, and (e) 20% HA2 after immersion in SBF for 28 days (marker bars= 100μm)

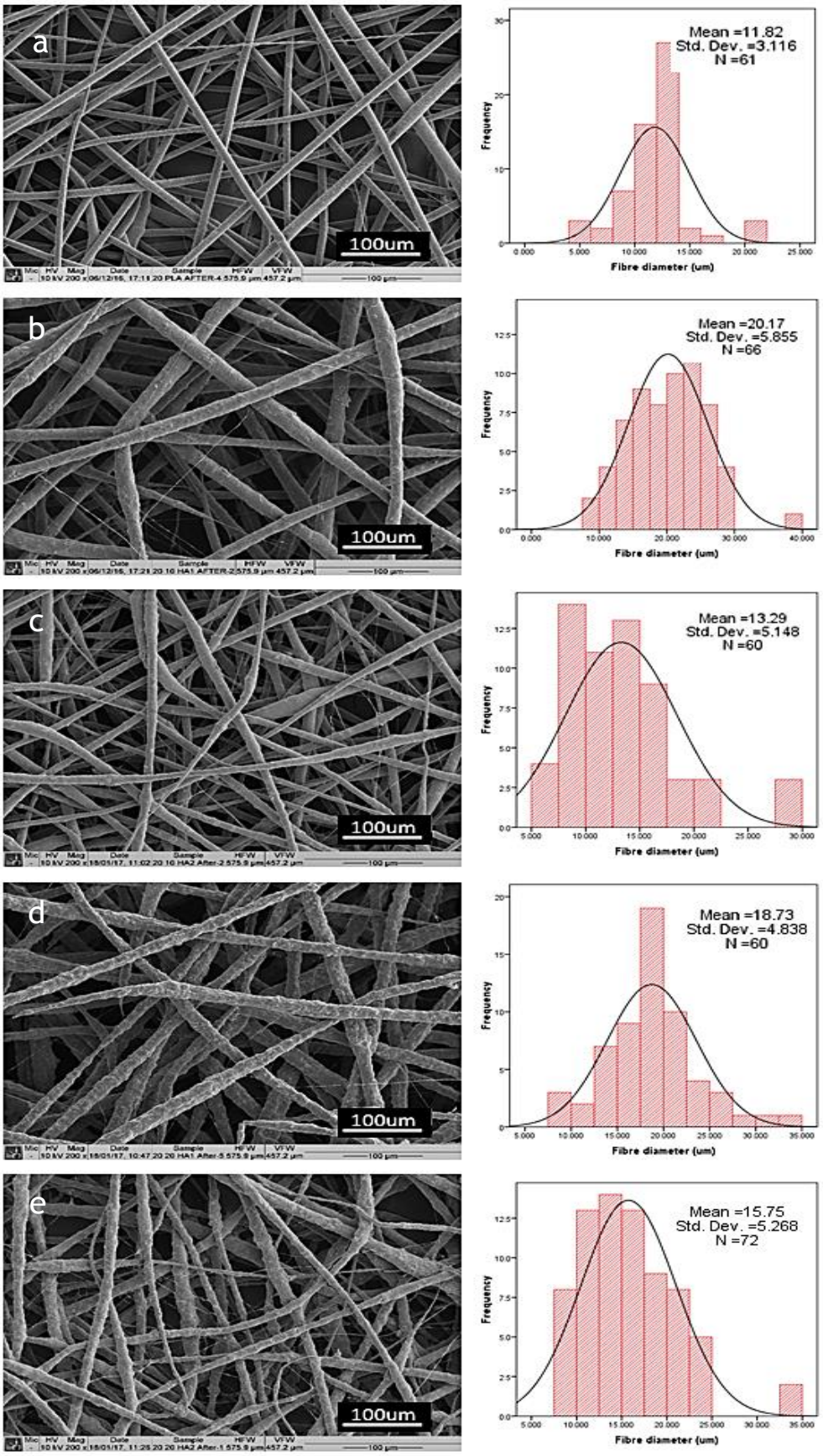

Figure 5.4 SEM images and fibre diameter distributions for electrospun 20% PLA with (a) no filler, (b) 10%HA1, (c) 10%HA2, (d) 20% HA1, and (e) 20% HA2 after immersion in SBF for 28 days (marker bars= 100μm)

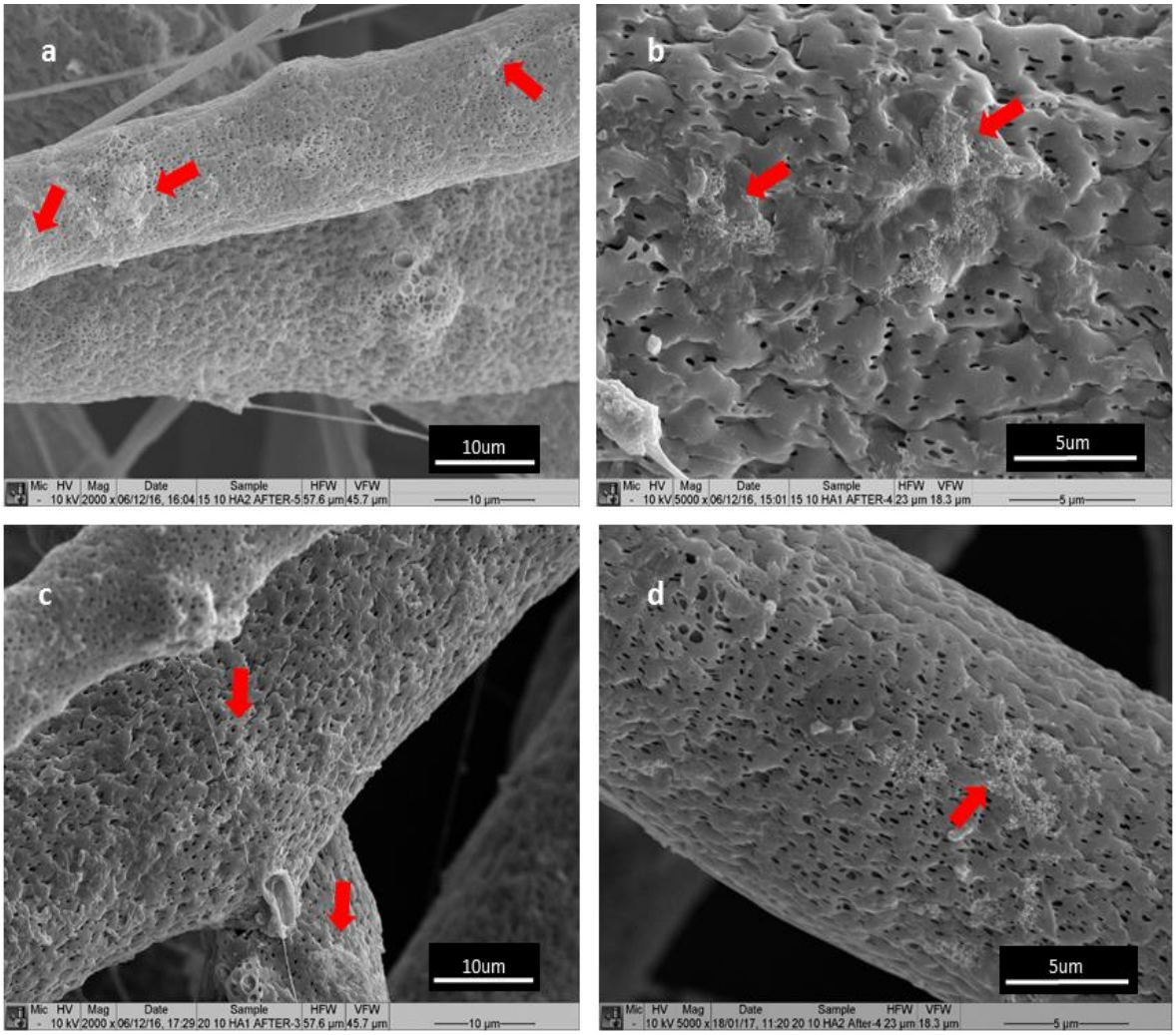

Figure 5.5 Higher magnification SEM images for electrospun (a) 15% PLA with 10% HA2, (b) 15% PLA with 10% HA1, (c) 20% PLA with 10% HA1, and (d) 20% PLA with 10% HA2 scaffolds after immersion in SBF for 28 days showing HCA formation on the surface of the fibres (marker bars for (a) and (c) =10μm, and for (b) and (d) =5μm)

5.3.2 Dissolution rate and water uptake

The water uptake and dry weight loss for non-filled and HA-filled PLA scaffolds over 1, 2, 4, 7, 14, 21, and 28 days of immersion in SBF are shown in Figures 5.6 and 5.7, respectively. Levels of significance for differences in weight loss and water uptake among samples with different filler content are presented in Tables A.10 to A.13, Appendix A.2.

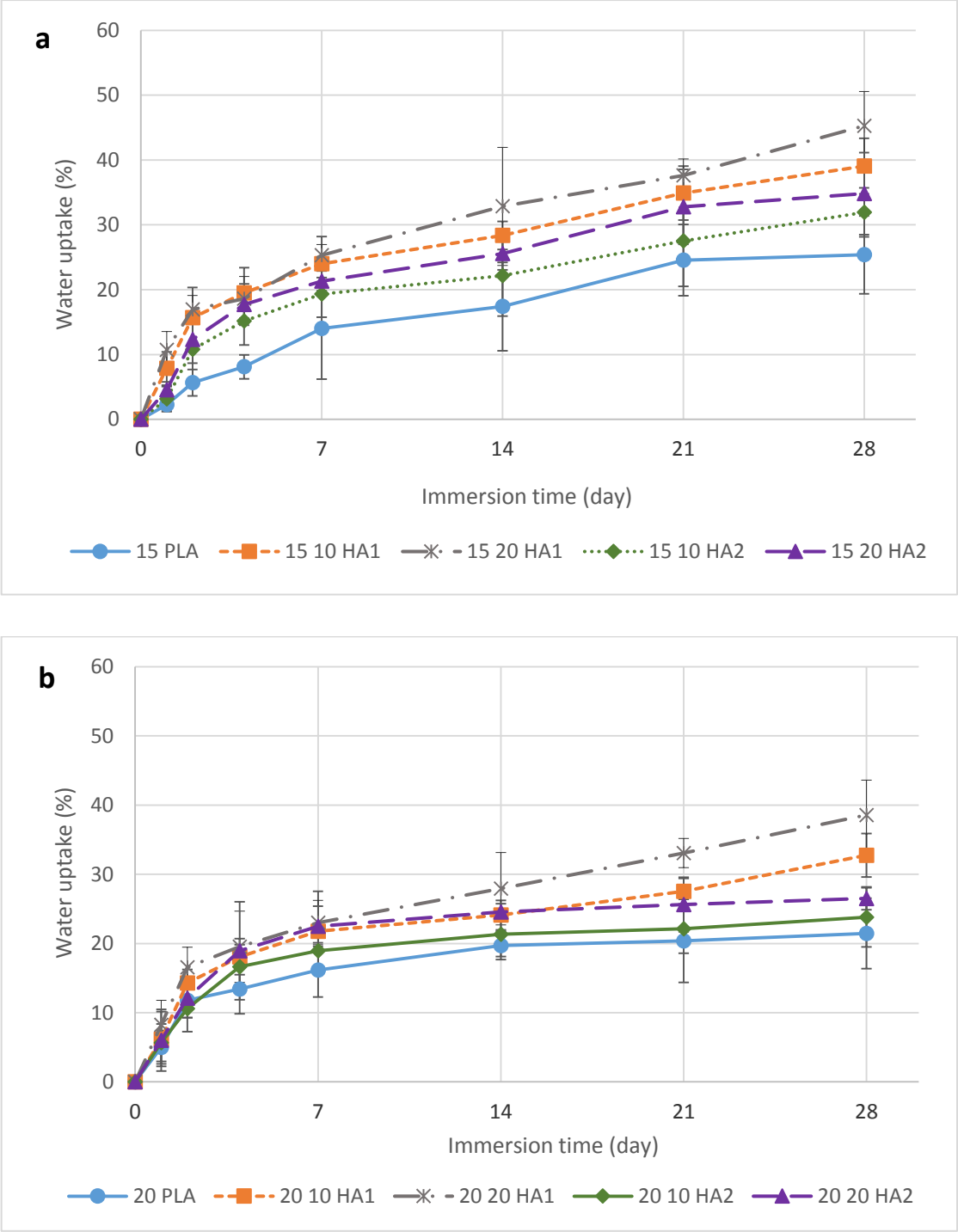

Figure 5.6 Water uptake of (a) 15% PLA samples and (b) 20% PLA samples with no filler or 10 or 20% of HA1 or HA2 during 28 days of immersion in SBF

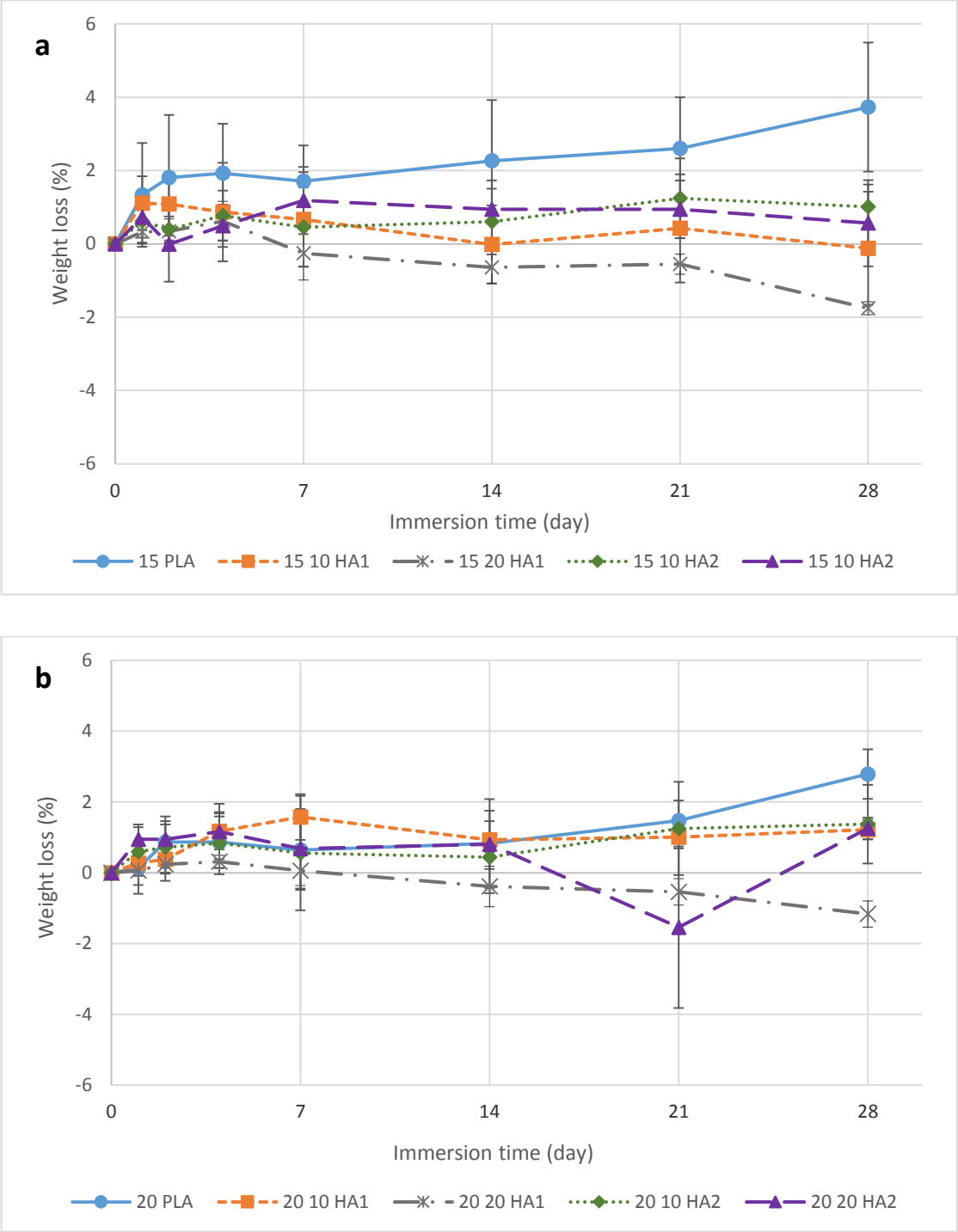

Figure 5.7 Weight loss of (a) 15% PLA samples and (b) 20% PLA samples with no filler or 10 or 20% of HA1 or HA2 during 28 days of immersion in SBF

5.3.3 Mechanical testing

The Young's moduli and ultimate tensile strength values for 15% and 20% PLA samples with 10 or 20% HA1 or HA2 after two weeks immersion in SBF are shown in Table 5.2. At day 28 of immersion, the samples were too fragile to test. These results are also presented graphically in Figures 5.8 and 5.9 along with Young's moduli and ultimate tensile strength values before immersion for comparison (the zero days data are taken from Table 4.2). Statistical analysis for tensile properties among samples with different filler content after SBF immersion are presented in Tables A.14 and A.16.

Table 5.2 Young's moduli and ultimate tensile strength (UTS) values for 15 and 20% PLA samples after 14 days of immersion in SBF

Filler percentage	**15% PLA**		**20% PLA**	
	Young's Modulus /MPa	UTS /MPa	Young's Modulus /MPa	UTS /MPa
0% filler	40.16 ± 3.05	0.861 ± 0.194	48.32 ± 5.17	1.062 ± 0.299
10% HA1	24.57 ± 2.54	0.319 ± 0.105	36.93 ± 4.27	0.625 ± 0.075
20% HA1	20.89 ± 1.60	0.245 ± 0.110	32.31 ± 1.85	0.530 ± 0.171
10% HA2	29.06 ± 1.52	0.611 ± 0.127	41.97 ± 3.39	0.872 ± 0.316
20%HA2	32.86 ± 4.90	0.488 ± 0.349	45.03 ± 5.51	0.710 ± 0.201

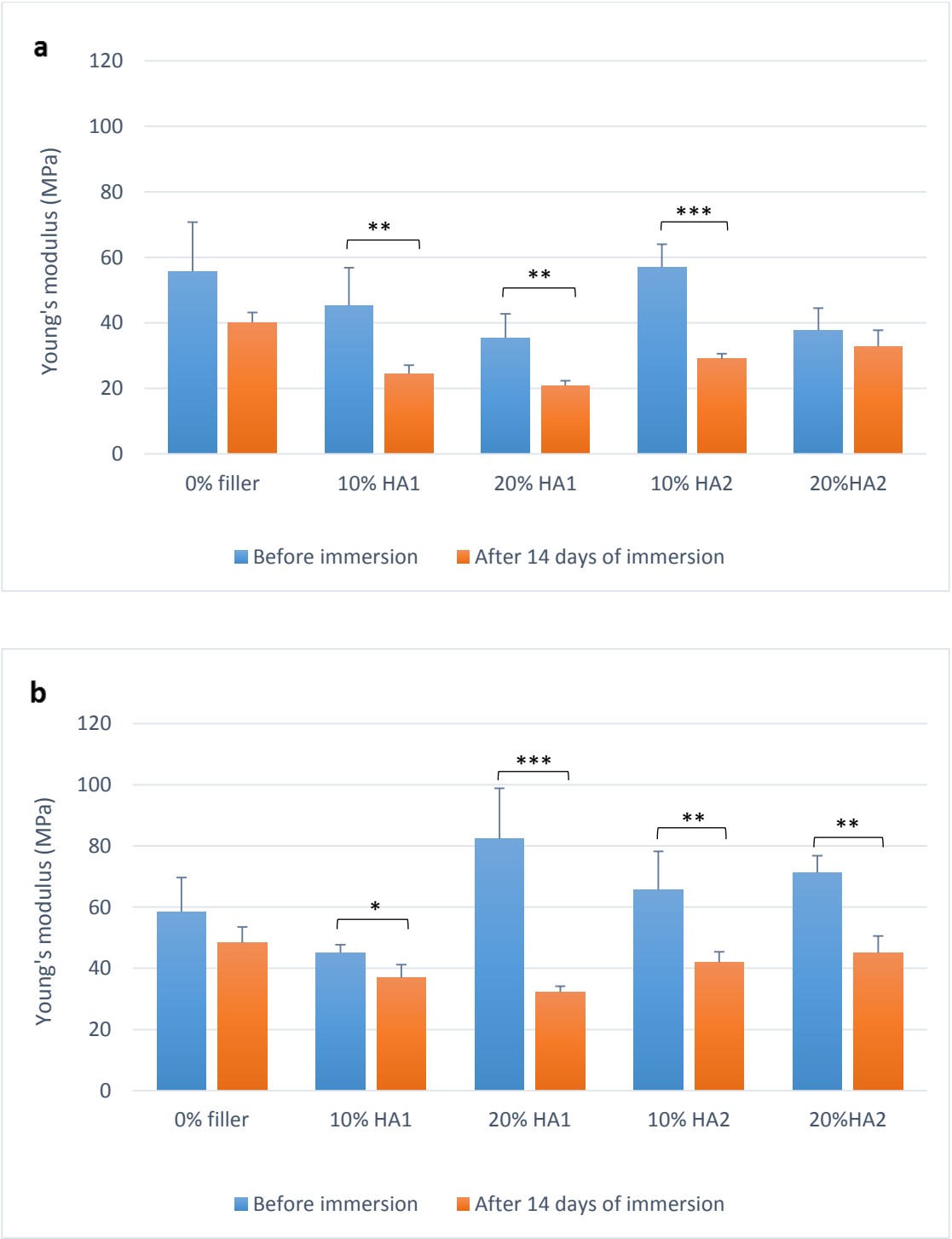

Figure 5.8 Young's moduli for (a) 15% PLA, and (b) 20% PLA samples with no filler or 10 or 20% of HA1 or HA2 before and after 14 days of immersion in SBF. * = $p < 0.05$, ** = $p < 0.01$, *** = $p < 0.001$

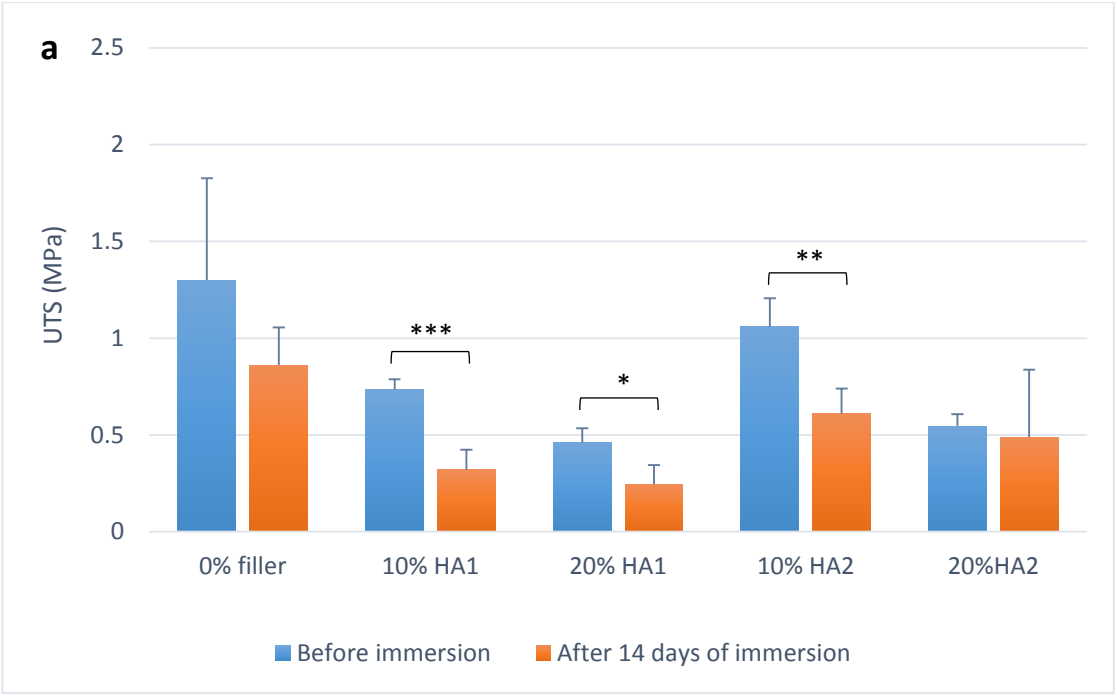

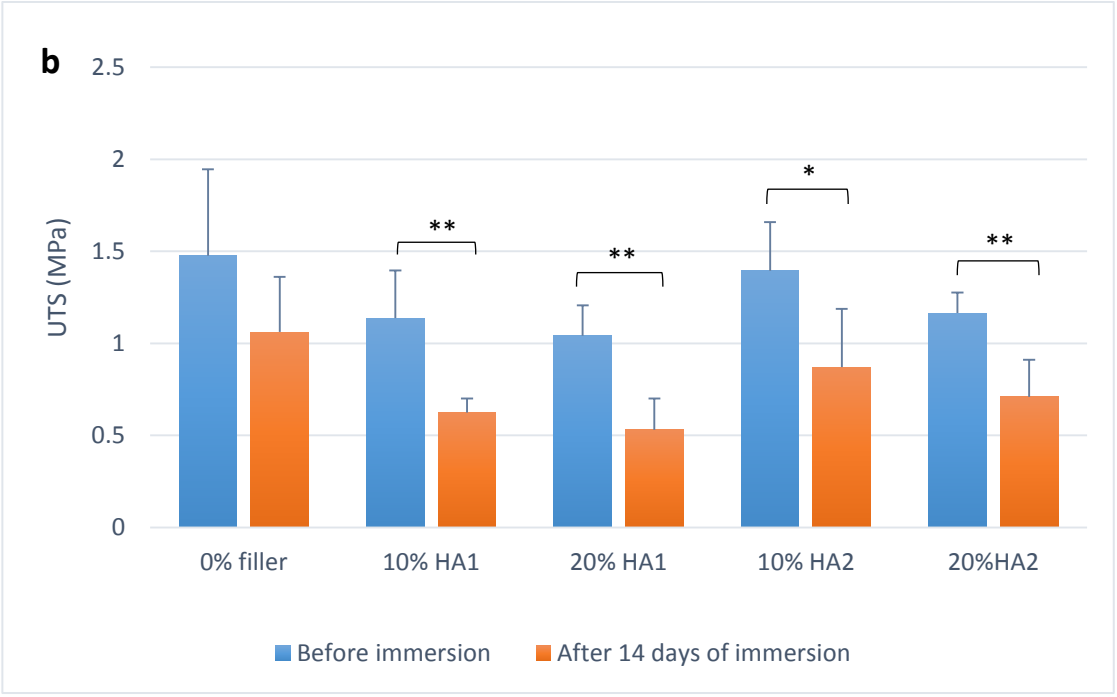

Figure 5.9 UTS values for (a) 15% PLA, and (b) 20% PLA samples with no filler or 10 or 20% of HA1 or HA2 before and after 14 days of immersion in SBF. * = $p < 0.05$, ** = $p < 0.01$, *** = $p < 0.001$

5.3.4 TGA

Figure 5.10 displays the thermogravimetric analysis of bulk PLA and electrospun non-filled PLA scaffold respectively, while Figures 5.11 to 5.14 show the thermogravimetric analysis of non-filled PLA and HA1 or HA2-filled scaffolds at various contents of the HA before and after 28 days of immersion in SBF. The onset and decomposition temperatures as well as the residue weight of all scaffolds and bulk PLA are listed in Table 5.3. It should be noted that the TGA graphs and the residue percentage are presented in weight%. Thus, 10 and 20 vol % of HA is equal to 22.08 and 38.93 wt %, respectively.

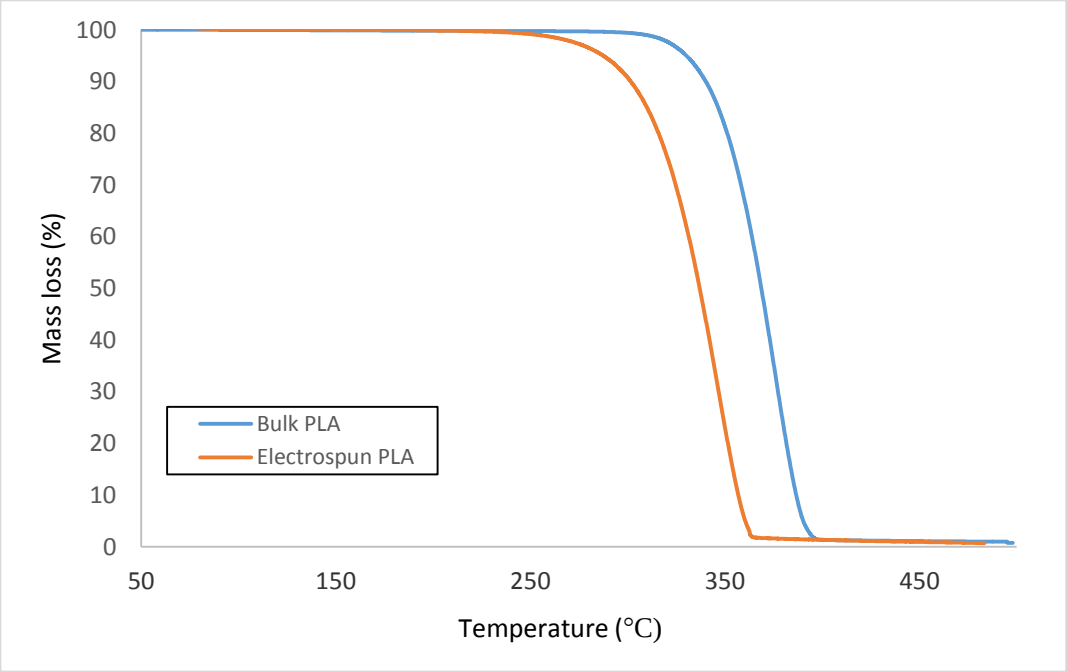

Figure 5.10 TGA curves of bulk and electrospun PLA

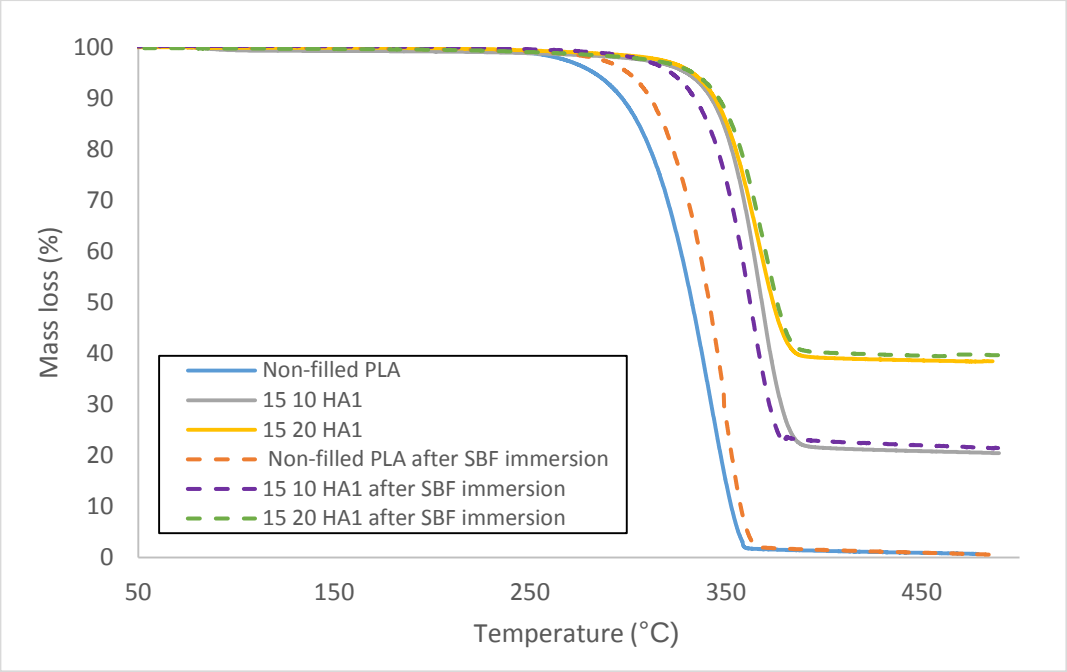

Figure 5.11 TGA curves of non-filled PLA scaffolds and HA1-filled scaffolds with 15% PLA concentration before and after SBF immersion for 28 days

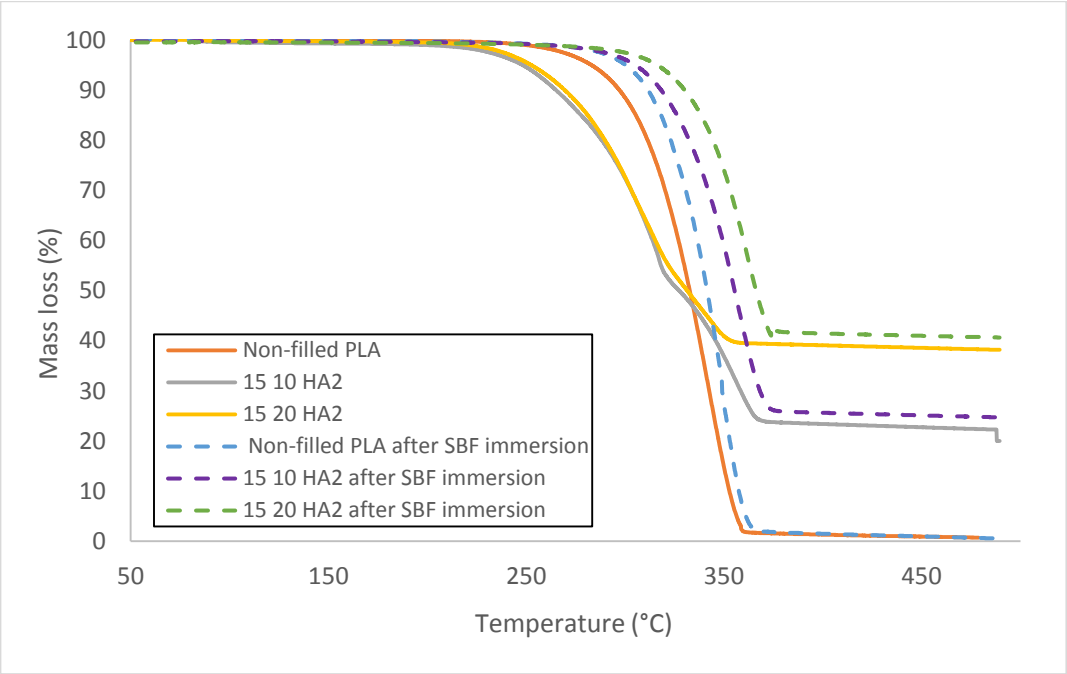

Figure 5.12 TGA curves of non-filled PLA scaffolds and HA2-filled scaffolds with 15% PLA concentration before and after SBF immersion for 28 days

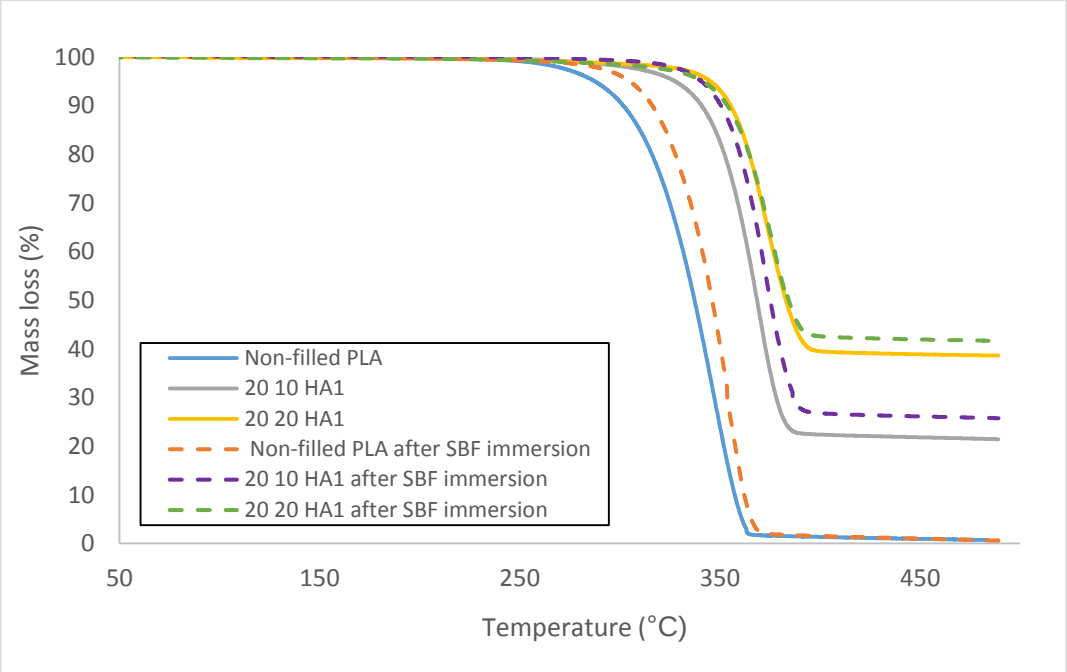

Figure 5.13 TGA curves of non-filled PLA scaffolds and HA1-filled scaffolds with 20% PLA concentration before and after SBF immersion for 28 days

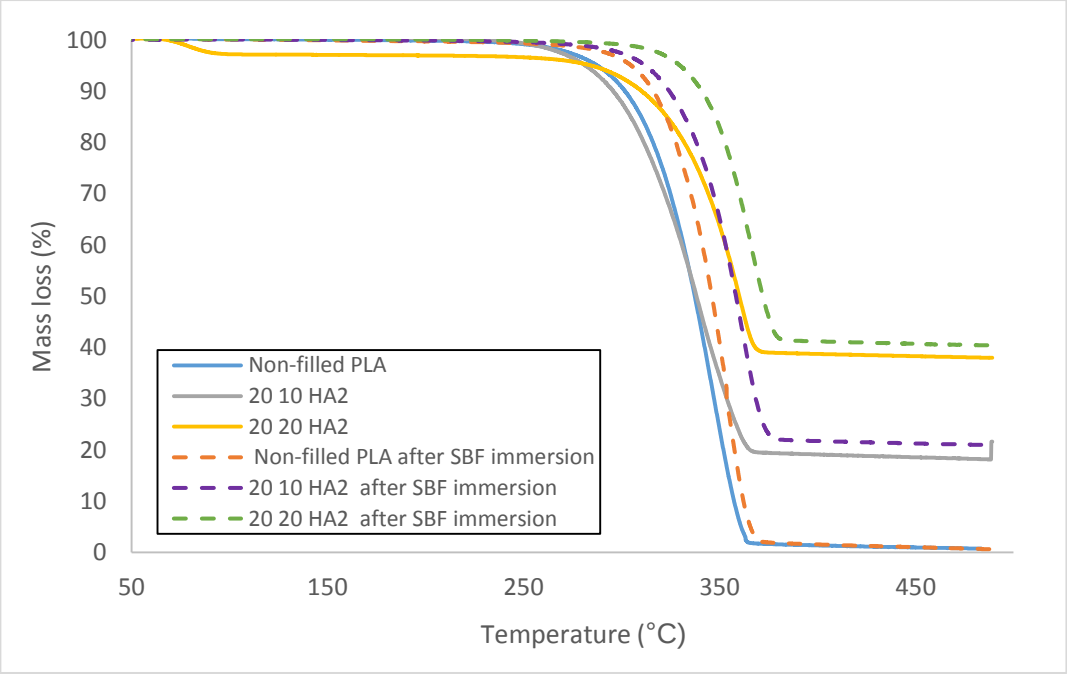

Figure 5.14 TGA curves of non-filled PLA scaffolds and HA2-filled scaffolds with 20% PLA concentration before and after SBF immersion for 28 days

Table 5.3 Thermal properties of PLA and PLA/HA composites before and after 28 days immersion in SBF

Sample	Before immersion			After SBF immersion		
	T_{onset} (°C)	T_d (°C)	Residue (%)	T_{onset} (°C)	T_d (°C)	Residue (%)
PLA particles	306.5	425.1	0.27	-	-	-
Electrospun PLA	236.0	400.6	0.73	245.2	407.5	0.25
15% PLA 10% HA1	291.1	417.4	20.33	285.8	421.3	21.34
15% PLA 20% HA1	297.7	427.2	38.49	288.2	422.6	39.40
15% PLA 10% HA2	227.6	388.6	19.98	258.3	410.1	23.92
15% PLA 20% HA2	230.4	379.9	37.48	267.9	415.7	39.12
20% PLA 10% HA1	280.6	409.1	21.30	293.7	423.6	25.56
20% PLA 20% HA1	295.4	425.6	40.05	283.4	429.9	41.59
20% PLA 10% HA2	245.4	400.3	20.84	263.5	410.0	22.61
20% PLA 20% HA2	247.1	405.8	37.86	269.8	418.5	40.26

5.3.5 FTIR

FTIR spectra of HA particles, non-filled 15 and 20% PLA, and 15 and 20% PLA filled scaffolds filled with either HA1 or HA2 at various content are shown in Figures 5.15 and 5.16, respectively. The spectral features identified from the FTIR spectra of HA1 and HA2-filled scaffolds were compared to literature and the assignments of the identified peaks are listed in Table 5.4.

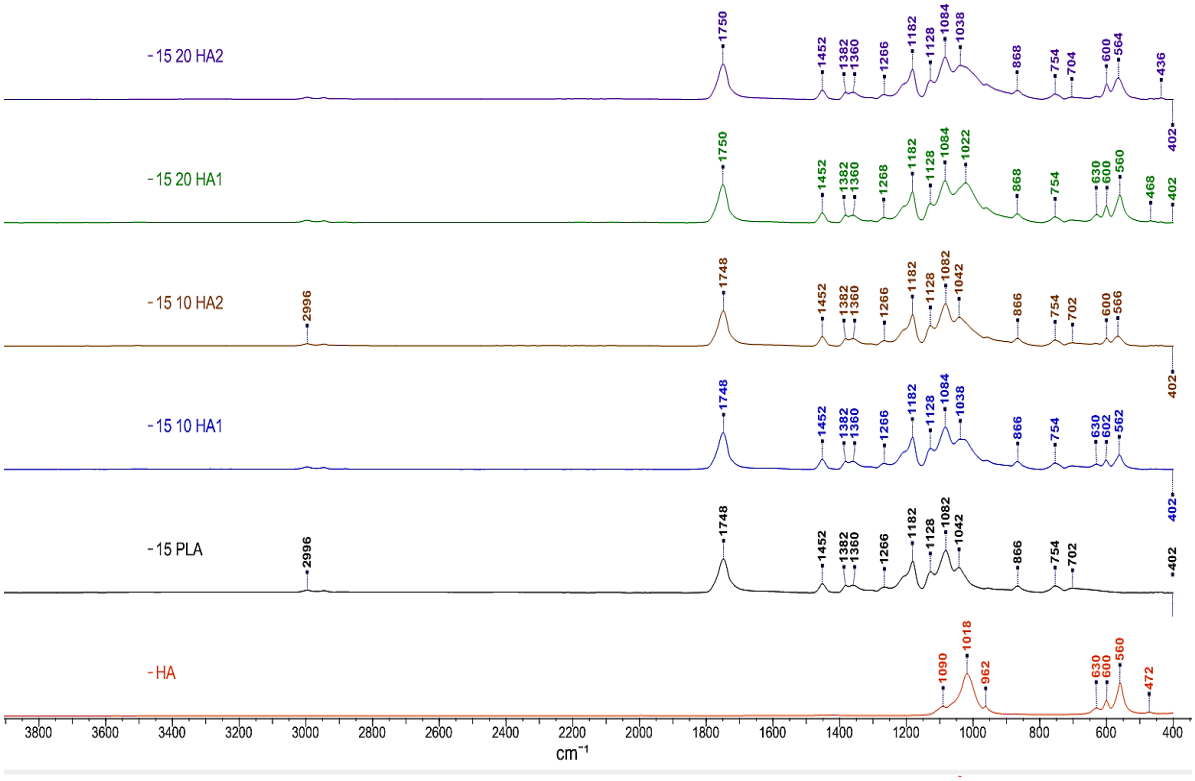

Figure 5.15 FTIR spectra of HA particles, non-filled 15% PLA, and 15% PLA with 10 or 20% HA1 or HA2

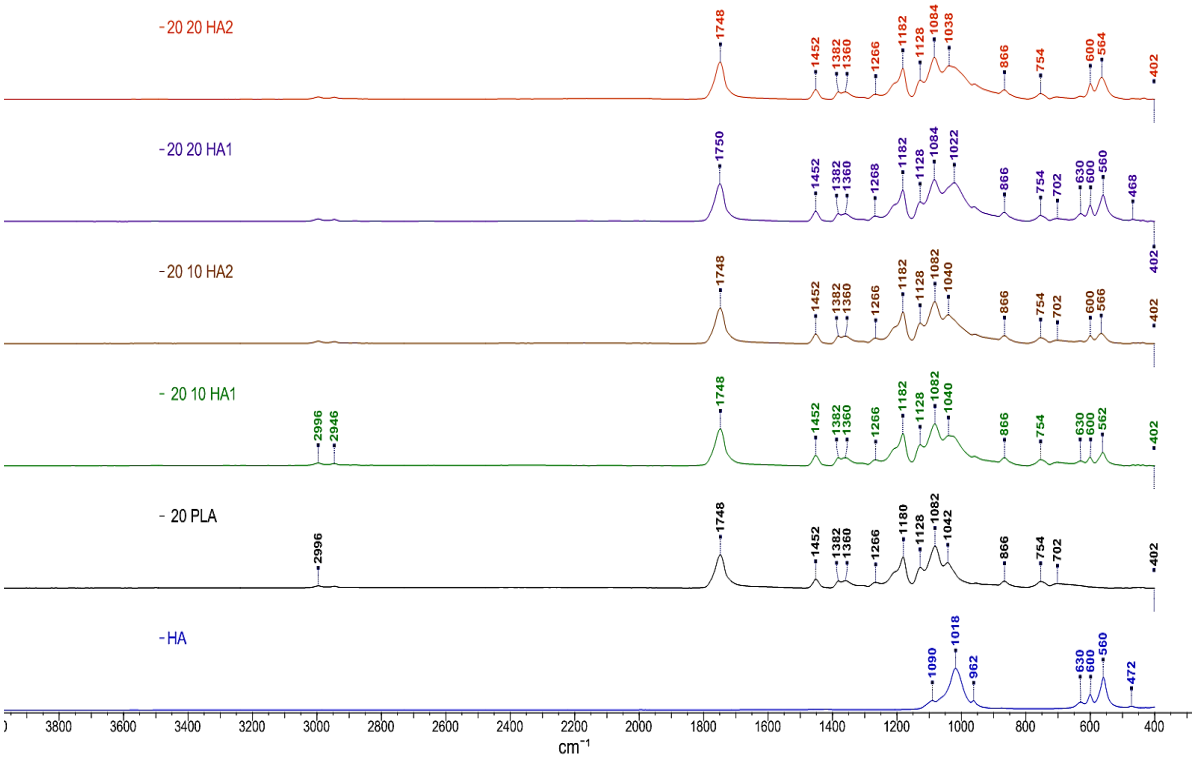

Figure 5.16 FTIR spectra of HA particles, non-filled 20% PLA, and 20% PLA with 10 or 20% HA1 or HA2

Table 5.4 Assignments of spectral features identified from the FTIR spectra of HA1 and HA2-filled scaffolds

Wavenumber (cm^{-1})	Assignment	References
866	Stretching of C–C bond (PLA)	(Kaynak and Kaygusuz, 2016)
1266, 1180, 1128, 1082, 1042	Stretching of C–O bond (PLA)	(Chieng et al., 2014; Kaynak and Kaygusuz, 2016)
1360, 1382, 1452	Deformation of C–H bond (PLA)	(Kaynak and Kaygusuz, 2016; Kemala et al., 2012; Zafar et al., 2016)
1748 or 1750	C=O of ester carbonyl groups (The main characteristic peak of PLA)	(Chieng et al., 2014; Kaynak and Kaygusuz, 2016; Kemala et al., 2012; Zafar et al., 2016)
2996, 2946	asymmetric and symmetric modes of stretching of C–H bonds respectively (PLA)	
630	OH- ions prove presence of HA	(Berzina-Cimdina and Borodajenko, 2012; Destainville et al., 2003; Rehman et al., 1995)
962	ν1 bending mode of PO_4^{3-} group	
472	ν2 bending mode of PO_4^{3-} group	
1018-1090	ν3 bending mode of PO_4^{3-} group	
560 - 600	ν4 bending mode of PO_4^{3-} group	

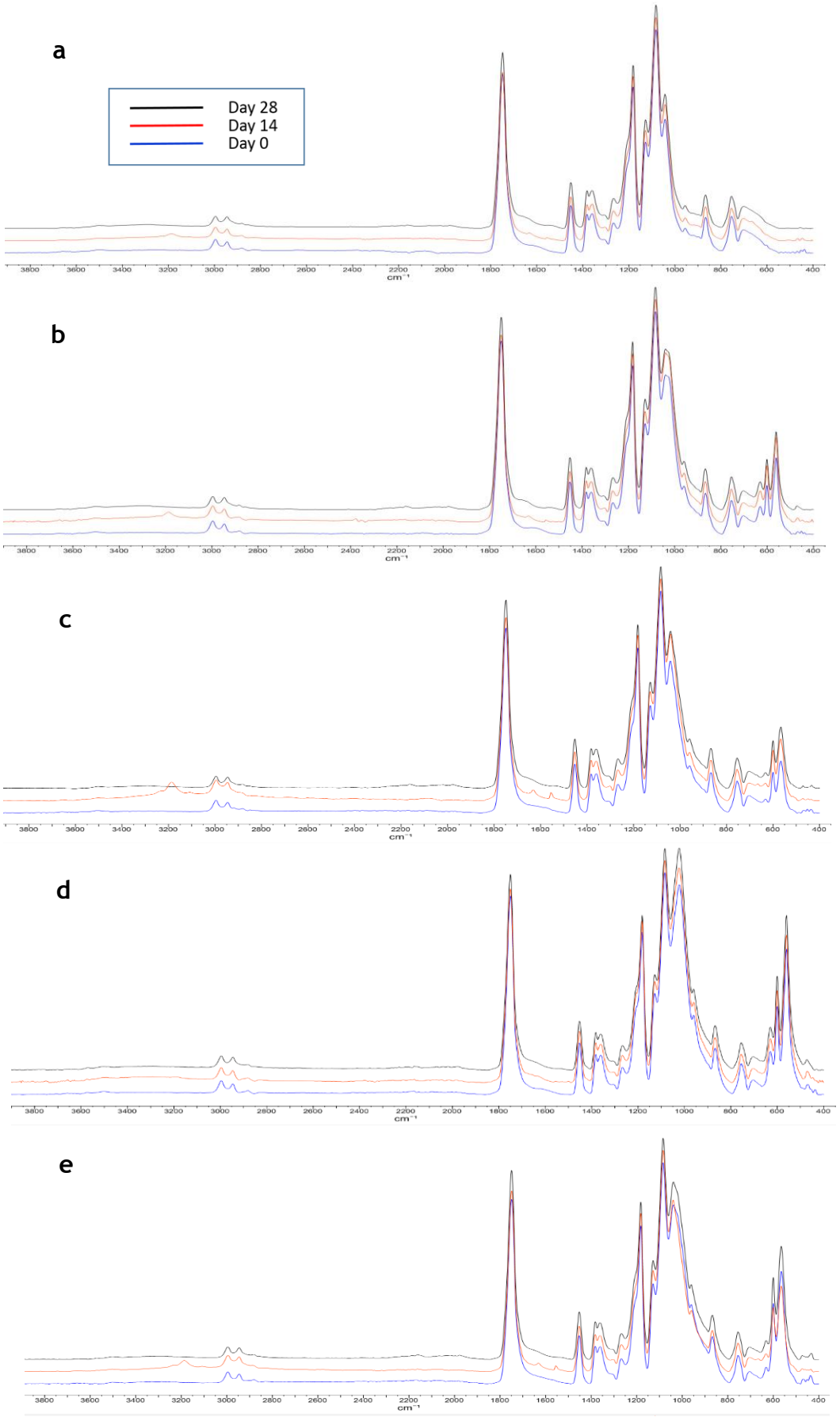

Figure 5.17 FTIR spectra of 15% PLA samples with (a) 0% HA, (b) 10% HA1, (c) 10% HA2, (d) 20% HA1, and (e) 20% HA2 at 0, 14, and 28 days of SBF immersion

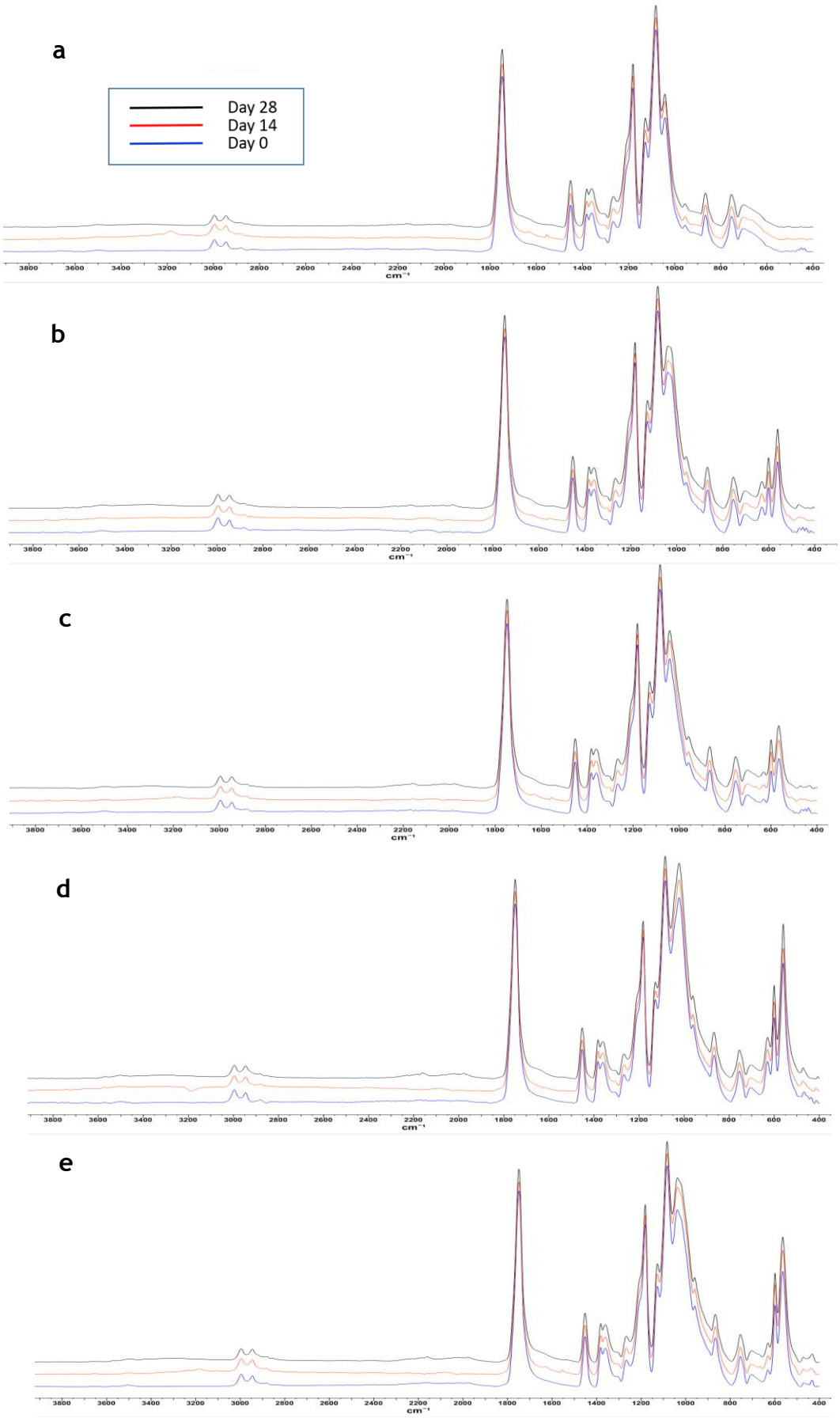

Figure 5.18 FTIR spectra of 20% PLA samples with (a) 0% HA, (b) 10% HA1, (c) 10% HA2, (d) 20% HA1, and (e) 20% HA2 at 0, 14, and 28 days of SBF immersion

5.4 Discussion

The porosity of biomaterial scaffolds play a significant role in bone formation in vitro and in vivo. Open porous surfaces and interconnected networks are crucial for tissue vascularization and cell proliferation, nutrition and migration to form new tissues. They also help to facilitate mechanical interlocking between the implant biomaterial and the surrounding natural bone, which helps increase the mechanical stability at this critical interface (Karageorgiou and Kaplan, 2005; Loh and Choong, 2013). The porosity of the non-filled PLA and PLA/HA scaffolds was determined (Table 5.1). All scaffolds exhibited satisfactorily high porosity even when the HA content was raised to 20% and no significant differences were observed between filled and non-filled scaffolds or between scaffolds containing HA1 and those containing HA2.

The surface properties of the implant, including the degree of surface roughness, chemistry, topography and energy/wettability influence the initial cellular response at the cell–material interface, ultimately affecting the neotissue formation (Agrawal and Ray, 2001; Feller et al., 2015). Figures 5.1 and 5.2 show SEM images for non-filled 15 and 20% PLA scaffolds before degradation. Both scaffolds exhibited uniform fibre diameter and relatively smooth surfaces with an average fibre diameters of 9.28±1.64 µm for 15% PLA scaffolds and 11.16±1.66 µm for scaffolds with 20% PLA concentration. The effect of solution concentration on fibre diameter has been previously discussed in section 4.4.1. Incorporation of either HA1 or HA2 increased the surface roughness of the composite fibres as well as increasing fibre diameter and irregularity. The roughness of the fibres was increased by increasing the filler content, while increased HA2 content increasing fibre diameter slightly, which might be due to agglomerate formation inside the fibres. However, no apparent change in fibres diameter was observed upon increasing HA1 content. Only few protuberances on the fibre surfaces were noticed upon including HA1 or HA2. Similar results of increased surface roughness upon incorporation of HA and graphene oxide nanoparticles was reported by Ma et al. (2012). Deng et al. (2007) also reported the roughness of the PLLA/HA hybrid scaffolds, although the average fibre diameter did not change significantly. In addition, it was also noticed that some fibres were discontinuous or ruptured which might be resulted from needle clogging due to HA incorporation that may have cause jet disruption during electrospinning.

High densities of nanopores were observed at the surface of both filled and non-filled electrospun PLA fibres. The pores were elliptical in shape and in the range of 200-350 nm in length for non-filled PLA scaffolds and from 250nm-1µm for PLA/HA scaffolds, with the longer dimension along with the fibre axis. Pores were larger where HA particles were closer to the surface of the fibres as shown in Figure 5.19.

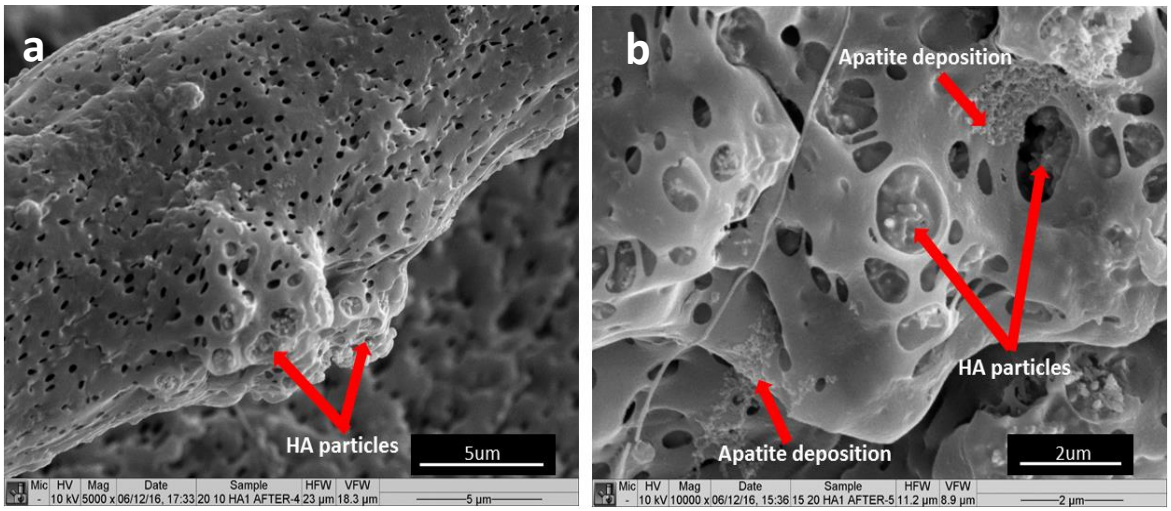

Figure 5.19 SEM images of (a) 20% PLA with 10% HA1 and (b) 15% PLA with 20% HA1 scaffolds showing the nanoporous structure of the fibre surface and HA particles inside the fibres (marker bar for (a)= 5µm and for (b)=2µm)

Pore formation occurs as a result of using highly volatile solvents such as chloroform or dichloromethane. According to Bognitzki et al. (2001), the fast evaporation of solvent give rise to local phase separation where two phases are formed in the polymeric solution: one that is solvent-rich and the other is solvent-poor. Ultimately, the solvent-rich regions are transformed into pores during the electrospinning process.

Srinivasarao et al. (2001), on the other hand, presented another mechanism for the formation of porous electrospun fibres which is called “breath figures”. Breath figures are imprints created as a result of the evaporative cooling during rapid evaporation of the solvent, therefore significantly cooling the surface of the electrospinning jet as it travels from the needle tip to the collector. As the jet surface cools, moisture in the air condenses and grows in the form of droplets that act as hard spheres due to convection currents on the surface of the jet. Finally, the water droplets evaporate as the jet dries on the collector, leaving imprints on

the surface of the electrospun fibres in the form of pores. Thus, the formation of breath figures requires the presence of a certain level of humidity in the atmosphere in addition to the use of volatile solvents. Unfortunately, the humidity in the laboratory was not measured but is assumed to be high.

Han et al. (2005) investigated pore formation on cellulose triacetate fibres using methylene chloride (MC) and a mixed solvent of MC/ethanol. Pores in the range of 200 to 500 nm were observed for the 90/10 solvent ratio of MC to ethanol. However, little or no pore formation was observed when the ethanol content was increased. In another study, Megelski et al. (2002) investigated the influence of polymer/solvent properties on the fibre surface morphology. They used a variety of solvents with different boiling points and vapour pressures to prepare polystyrene (PS) fibres including tetrahydrofuran (THF), carbon disulphide (CS_2), toluene, water and DMF. A very high density of pores were observed on PS fibres electrospun from THF, while the microtexture and nanopores disappeared when THF was replaced by DMF. Their results indicated that the volatility of the solvent significantly influenced the pore formation. Their study also investigated the effect of humidity and molecular weight on the surface morphology of PS fibres electrospun from PS/THF solution. They noted that increasing the humidity caused an increase in the number, diameter, shape and distribution of the pores along the PS fibres.

The presence of a porous structure at the fibre surface has several advantages such as: increasing the surface area and provide larger number of binding sites for drug loading which is a very useful property for tissue engineering applications. It might also be helpful for an increase in cell attachment and tissue compatibility. Finally, the porous structure can affect the roughness and wetting behaviour of the scaffolds, as well as specific adsorption processes (Kim et al., 2006; Zander, 2013).

Biomineralisation of biomaterials is one of the main properties governing their usefulness in bone regeneration (Lao et al., 2011). SEM images of non-filled 15 and 20% PLA scaffolds showed no significant morphological changes after 4 weeks of immersion in SBF. Fibres of both scaffolds maintained their shape and no significant swelling or reduction in fibre diameter were noted. In addition, no apatite formation was observed on the surface of the fibres, indicating poor mineralisation ability of the PLA fibres. This can be attributed to the fact that PLA

is hydrophobic and cannot provide enough active functional groups for the formation and growth of a mineralised HA layer. This finding is in agreement with Zhang et al. (2015) and Fu et al. (2016) who showed that the morphology of PLA fibres have no obvious change after soaking in SBF for 1,3, and 7 days, and the surfaces of PLA nanofibers were still smooth after incubation. However, Wang et al. (2017) reported increased surface roughness and the formation of plate-like structures and flaky features on the surface of electrospun PLA fibres after immersion in SBF for 7,14, and 21 days at 10°C, but these structures were not observed on the scaffolds investigated in this study.

Hydroxyapatite is a bioactive material that promotes the formation of new bone tissue by increasing osteoblast adhesion, osteointegration and deposition of calcium-containing minerals on its surface (Nejati et al., 2008). HA-mineralised electrospun scaffolds have been introduced as promising scaffolds for bone regeneration due to their ability to mimic both morphological features and chemical composition of natural bone ECM. Morphological analysis of PLA/HA1 and PLA/HA2 scaffolds indicate formation of an apatite layer on the surface of electrospun fibres after 28 days immersion in SBF as shown in Figure 5.5. In addition, an increased number of ruptured fibres were noticed after immersion in SBF since the thin regions along those fibres would represent weak points during hydrolysis. Ruptured or broken fibres were rarely observed in non-filled 15 or 20% PLA scaffolds before or after immersion in SBF. Increasing HA surface area or HA content in scaffolds did not show significant effects on the bioactivity of the fibres.

Although scaffolds containing HA1 or HA2 were more bioactive than non-filled scaffolds, the rate of apatite formation was generally lower than expected and the apatite layer did not cover the whole surface of fibres as reported previously (Hassan et al., 2014; Rajzer, 2014; Rajzer et al., 2014; Silva et al., 2014). There are three likely causes for the differences in apatite formation rate; the first cause might be related with the size of HA particles used in this study. The rate of calcium phosphate materials bioactivity is believed to be associated with the rate of material dissolution as well as the release of calcium and phosphate ions from the surface of the implant followed by the precipitation of a biological apatite layer (Porter et al., 2006). The previously mentioned studies incorporated nano-sized HA within their electrospun scaffolds instead of micro HA. Decreasing the

size of HA particle results in larger surface area exposed within the media which may have provide an increase in dissolution of Ca and P ions leading to greater apatite deposition and more protein adsorption, osteoblast adhesion and increased bone growth (Arsad et al., 2010; Coathup et al., 2013). Heo et al. (2009) fabricated nHA-PCL and mHA-PCL scaffolds with well interconnected macropores and total porosity of 73% using layer manufacturing process (LMP) and investigated the effects of particle size in vitro. Their results indicated that the calcium content and ALP activity of MSCs were significantly higher for the nHA-PCL scaffold than for the mHA-PCL scaffold after 14 days of culture, indicating that scaffold containing nano-sized HA particles had significantly higher bioactivity and better biocompatibility compared with the scaffold containing micro-sized HA.

In another study, Laranjeira et al. (2010) prepared two types of bioactive porous granules composed of nano or micro-HA agglomerates using a polyurethane sponge impregnation and burnout method. Granules of nanostructure-HA agglomerates exhibited higher surface area and porosity compared with micro-HA. In addition, a higher cell growth rate was achieved in nanostructure granules compared to micro-sized granules (76 and 40% increases, respectively), with the same gene expression of osteoblastic associated markers. Their findings indicated that porous granules of nano-HA agglomerates provided a more adequate environment for cell adhesion and migration, improving cell response.

Another possible reason for decreased deposition rate compared to the previous studies is the differences in fibre diameter of the obtained electrospun scaffolds. Increased fibre diameter may reduce the rate of mineralisation in SBF. He et al. (2014) compared an electrodeposition method and simulated body fluid (SBF) incubation method in terms of morphology, chemical composition, and deposition rate of calcium phosphate formed on electrospun scaffolds with fibre diameters ranging from 200 nm to about 1400 nm prepared using 6, 8, 10 and 12 wt% PLLA solutions. The rate of mineralisation varied with the fibre diameter but in opposite directions for the two mineralisation methods. Increasing fibre diameter led to faster mineralisation rate for the electrodeposition method, but slower mineralisation rate for the SBF incubation method. They attributed the differences in deposition rate to the different deposition mechanisms involved in the two methods. During electrodeposition, the deposition of calcium phosphate is aided by electrochemical reactions on the cathode surface that increase the local pH value and ultimately led to super-saturation of calcium phosphate at the

vicinity of the cathode. Electrospun PLLA fibres accumulated on the cathode served as an effective substrate for calcium phosphate deposition, which allowed positively-charged ions migrate towards the cathode due to the high porosity between the nanofibers. Rapid growth of apatite crystals on the fibre surface were achieved by retaining the supersaturation state through the applied electric field during electrodeposition process. Larger diameter fibres provided larger surface areas on individual fibres although a lower overall surface area to volume ratio, which allow the growth of larger and more stable mineral particles, resulting in an increased overall deposition rate during electrodeposition. However, in the case of SBF incubation, all fibres are basically exposed to the same non-accelerated deposition conditions (ionic strength, pH, etc.), and the nucleation sites compete equally for calcium and phosphate ions, which result in a slower overall deposition rate. In addition, smaller diameter fibres provide a larger total surface area than large diameter fibres, leading to faster mineral deposition in the SBF incubation process.

Lastly, it is also worth noting that while the complete encapsulation of HA particles within the fibre can enhance the mechanical stability of the resulting scaffold, the degree of bioactivity might be reduced due to the absence of bioactive particles on the fibres surface. The presence of HA particles on the surface may release more Ca and P ions to the SBF solution, thus inducing more bone-like mineral deposition on the fibre surface (Figure 5.19b). Jaiswal et al. (2013) compared the effects of HA addition, either incorporated within PCL–gelatin fibrous scaffold or induced on the surface by an alternate soaking method on the biological and mechanical performance of the scaffolds. Blending of HA particles with PCL–gelatin solution failed to show HA particles on the surface of the scaffold, while alternate soaking proved to be rapid and efficient for surface precipitation of HA over the scaffold. Their results indicated that the presence of hydroxyapatite on the surface of the scaffold enhanced ALP activity and promoted better cellular adhesion and proliferation as compared to the scaffold with blended HA. Soaked PCL-gelatin scaffolds had also exhibited higher Young's moduli and tensile strength as compared to blended PCL-gelatin-HA scaffolds.

Weight loss measurements showed that both non-filled and HA-filled scaffolds exhibited very slow degradation behaviour during 28 days of SBF incubation. The total weight loss for non-filled 15 and 20% PLA scaffolds were only 3.73% and 2.79%, respectively. These results were expected as PLA has a slow degradation

rate because of the hydrophobic methyl group in the backbone. Similar results were obtained by You et al. (2005), where they noticed no significant weight loss in electrospun PLA scaffolds after 45 days immersion in PBS at 37°C.

The degradation of PLA under aqueous conditions generally occurs in two stages: the first stage includes water diffusion into the amorphous regions of the polymer matrix, which are less organised allowing water to penetrate more easily. When most of the amorphous regions are degraded, the second stage of degradation starts as a hydrolytic attack proceeding from the edge toward the centre of the crystalline domains (Dong et al., 2009). Thus, the hydrolysis rate of PLA electrospun fibres is strongly influenced by the crystallinity, which depends on the composition of the polymer chains (the content of L and DL LA units), in addition to other factors such as the molecular weight and the morphological structure (You et al., 2005). The size of the resulted electrospun PLA fibres may also have a role in decreasing the degradation rate of the scaffolds. Cui et al. (2006) compared the in vitro degradation of 5% paracetamol-loaded electrospun PDLLA fibre with average diameters of 212 nm, 551 nm, and 1.31 μm with that of PDLLA cast film with a thickness of 100 μm. After incubation in the degradation medium, the fibre size of electrospun PDLLA increased and fibre space decreased. Electrospun mats with an average fibre diameter of 212nm lost 18% of their mass in 9 weeks, whereas casting film and a microfibrous electrospun mat with average fibre diameter of 1.31 μm lost only 8%.

The introduction of either HA1 or HA2 particles into the scaffolds decreased the mass loss rate significantly compared to neat PLA mats. This can be attributed to the dissolution of alkaline HA particles and the release of OH^- ions into the SBF which can neutralize the acidic degradable substances generated during the PLA degradation process. As a result, the autocatalytic degradation effect of acids on the polymeric material can be reduced, thus slowing down the degradation rate. HA incorporation thus can reduce or avoid the aseptic inflammation caused by the acidic substance, and it can improve the biocompatibility of the polymeric biomaterial. The effect of HA particles on slowing down the degradation rate of PLA scaffolds was also reported by Sui et al. (2007), Huang et al. (2013) and Huang et al. (2015).

With 15% PLA scaffolds, the variations between non-filled and HA1-filled scaffolds started to become significant from day 14 of immersion for both 10 and 20% HA1 scaffolds, while no significant differences were observed between non-filled and

HA2-filled scaffolds until day 21 of immersion. On the other hand, variations between non-filled and HA1, HA2-filled scaffolds were minor till day 28 of immersion. The rate of mass loss was significantly lower in 15% PLA scaffolds filled with HA1 scaffolds than in scaffolds filled with HA2. The reason for this difference is possibly due to the higher surface area of HA1 particles which can increase the ion release into the SBF due to the higher exposure to the medium compared to HA2 particles. However, the differences in mass loss between the two HAs scaffolds were reduced upon increasing the polymer concentration to 20%, which indicate that polymer concentration can have a strong impact on the mass loss rate for HA-filled scaffolds, possibly by enhancing the HA encapsulation within the scaffolds, thus reducing particles exposure to SBF. Increasing filler concentration from 10 to 20% led to further decreases in mass loss rate, but the effect was not significant, however, at 20% vol, it significantly increased the variations between the two HAs scaffolds.

Water uptake results, on the other hand, showed that HA-filled scaffolds had significantly higher water absorption rate than non-filled PLA scaffolds despite the reduced mass loss rate. The observed increase in water absorption among HA-filled scaffolds could be attributed to the presence of free and reactive hydroxyl groups on the HA particles which exhibit good affinity to water molecules (Tham et al., 2010). Besides, there are micro-voids in the interface between PLA and HA particles caused by the difference in the chemical nature of PLA and HA or due to non-uniform distribution of HA particles along the fibres. Thus, water molecules could penetrate into these micro-voids or accumulate at the PLA/HA interface, causing an increase in water absorption rate. These results are consistent with those of Rong et al. (2015) and Huang et al. (2015) who found that incorporation of HA particles into scaffolds resulted in increased water absorption while decreasing the mass loss rate. However, Sui et al. (2007) found that introduction of HA particles have decreased both mass loss and water uptake of PLA/HA scaffolds. They attributed the reduced water uptake to the dissolution of alkaline HA particles, which have blocked up the water uptake.

Scaffolds with HA1 exhibited higher water absorption rate than HA2-filled scaffolds. This is probably due to the higher surface area of HA1 particles which can increase water absorption by HA particles and penetration by increasing the cavities at the PLA/filler interface. To explain more, Figure 5.20 shows schematic HA1 and HA2 particles within the PLA matrix. The major difference between the

two HA grades is the surface areas, which are an order of magnitude different. Thus it may be assumed that the larger surface area needs more matrix to cover the particle surface completely (the shaded area) (Joseph et al., 2002), and consequently for the same amount of polymer matrix, larger voids can be created in PLA/HA1 interface compared PLA/HA2 as there is no external force added during the electrospinning to force the polymer matrix to fill the PLA/HA interface and cover the whole HA particles, which leads to increased water accumulation in HA1-filled scaffolds.

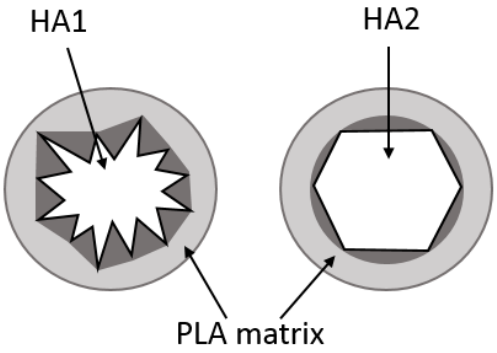

Figure 5.20 Representation of PLA matrix volume occupied by of HA1 and HA2 particles of equal particle diameter but with different surface areas (adapted from Joseph et al., 2002)

According to Suwanprateeb et al. (1997), the degree of water absorption depends on both filler content and the length of immersion. The higher the filler content, the more liquid which can diffuse into the composite due to the greater numbers of penetration sites. In this study, increasing HA1 or HA2 content from 10 to 20% vol resulted in slight increase in water absorption for both 15 and 20% PLA scaffolds, however, the differences between the two filler percentages were not significant. Water uptake rates were also slightly reduced by increasing PLA concentration to 20%. This possibly occurred because when the polymer concentration is increased, more polymer would cover the particles surfaces and the gaps existing between the HA particles and PLA matrix would be reduced, thus less water can accumulate in the scaffolds.

Biodegradation and tissue ingrowth are transient processes which have a major effect on the mechanical and structural properties of the implanted device over time. Therefore, in vitro evaluation of the mechanical properties of biomaterials composites is important since they are aimed for human implantation and should work at body temperature (Krynauw et al., 2011; Zhang and Tanner, 2003). Mechanical properties of non-filled PLA and PLA/HA scaffolds were evaluated after 14 days of soaking in SBF and compared to the composites mechanical properties before immersion as shown in Figures 5.8 and 5.9. All scaffolds exhibited reduction in their stiffness and strength values after immersion in SBF, however, the reduction in non-filled 15 and 20% PLA scaffolds were not significant for either UTS or Young's modulus. On the other hand, scaffolds containing both types of HAs showed faster reduction in tensile strength and modulus compared to neat PLA scaffolds which could be the result of the increased moisture absorption of HA-filled scaffolds. Increased water absorption and penetration via HA particles and micro-voids can reduce the interfacial adhesion between the filler and the matrix, and resulting in decreased tensile modulus and strength. A further decrease in mechanical properties of HA1 containing samples compared to HA2 samples, which could be due to the larger voids at PLA/HA1 interface and the higher moisture absorption of HA1 filled scaffolds which results in faster filler-matrix debonding, thereby reducing the mechanical stability. However, the differences between the two HAs samples became less significant when PLA concentration was increased to 20% as the differences in water absorption rates were also reduced. Furthermore, results have shown large variations in stiffness and strength values among 15 and 20% PLA scaffolds containing 10 and 20 vol% of HA1 or HA2 after immersion in SBF. It should be noted that in addition to the effect of filler content, other factors such as fibre dis-continuity, fusion and packing density, filler agglomeration within the fibres, formation of nano/micro cracks in the fibres during scaffolds processing can all affect the mechanical properties of the scaffolds and their influence may increase with filler incorporation. Thus giving an accurate reason for those variations in mechanical properties remains challenging without performing further analysis.

Thermogravimetric analysis has been extensively used to examine the thermal stability and decomposition of PLA and PLA based composites and to determine the amount of inorganic filler incorporated in the scaffolds (Liu et al., 2010, 2014). In this study, TGA was also used to measure the amount of apatite formed on the

fibre surfaces after immersion in SBF. Figures 5.11 to 5.14 showed that the mass percentages of HA particles incorporated in HA1 or HA2-filled scaffolds were in consistent with the actual amount of HA added into the polymer solutions before electrospinning. Since HA has a higher density than PLA (3.162 vs. 1.24 $g.cm^{-3}$), the precipitation of HA particles in PLA solutions can easily occur especially when high percentages of HA are used, which may reduce the total amount of HA within the electrospun fibres. TGA results indicated, however, that the solutions were electrospun with a minimal loss of HA. Scaffolds filled with both HAs showed an increase in the residue weight after immersion in SBF which confirms apatite formation on the surface of fibres. However, increasing the filler surface area or filler content in the scaffolds did not seem to have a significant impact on the amount of apatite formed after immersion. These observations are in agreement with SEM and weight loss results which indicated apatite formation on HA-filled scaffolds but slowly.

The thermal degradation of PLA occurs above 200°C and it depends on several factors such as time, temperature, filler incorporation and catalyst concentration (Garlotta, 2002). In addition, the processing method can also alter the thermal properties of the polymer. TGA results showed that electrospun PLA fibres have lower decomposition temperatures than bulk PLA which can be attributed to the increased surface area of electrospun fibres compared to bulk polymer, hence, the heat penetrated faster. This observation is in agreement with the studies of Nam et al. (2010), Fouad et al. (2013) and López de Dicastillo et al. (2017) who reported decreased thermal stability of electrosbun chitosan, PLGA and PV respectively compared to bulk polymers.

Scaffolds with HA1 showed an increase in the thermal stability compared to non-filled 15 and 20% PLA scaffolds. On the other hand, the thermal stability of HA2-filled scaffolds with 15% PLA concentration were surprisingly lower than both non-filled and HA1-filled scaffolds which could be due to higher exposure of OH groups on HA surface to the PLA matrix, leading to formation of some agglomerates within the fibres, thus reducing the thermal stability (Rakmae et al., 2010). However, for scaffolds with 20% PLA concentration, it gave higher onset temperatures than non-filled scaffolds which might be due to better dispersion of HA2 within the polymeric matrix, but was still lower than HA1-filled scaffolds. According to Ignjatovic et al. (2004) and Rakmae et al. (2010), there are two potential reasons for the enhanced thermal stability of polymer composites: either the well

dispersed filler provides good adhesion with the matrix and blocks polymer decomposition products or the filler particles act as a barrier preventing heat transfer. Thus, it seems logical that HA1 can provide higher thermal stability than HA2 due to its higher surface area which can provide better insulation to PLA against thermal degradation. Thomas et al. (2011) investigated the effect of filler geometry and surface chemistry on the degree of reinforcement and thermal stability of nitrile rubber nanocomposites. They used fillers such as layered silicate, calcium phosphate and titanium dioxide which have different particle size and chemistry. Their results revealed that nanocomposites filled with layered silicate exhibited higher thermal stability compared to the other fillers. They attributed this to the layered structure of the silicate which effectively intercalates with the matrix due to the availability of more surface area per unit volume producing considerable increase in the thermal stability compared to the other fillers with more spherical particles.

FTIR results of scaffolds containing both types of HAs (Figures 5.15 and 5.16) showed additional peaks at 468, 560, 602, 630, and 1022 cm^{-1} compared to neat PLA scaffolds, which belong to the OH^{-1} and $PO4^{-3}$ bands of HA. Sui et al. (2007) reported development of a new peak assigned to COO^{-} at 1600 cm^{-1} as well as formation of a weak OH peak around 3500 cm^{-1} in the FTIR spectra of electrospun PLLA/HA scaffolds as a result of the interaction between COOH in PLLA and Ca^{2+} in HA. However, no additional HA peaks were present in the PLA/HA spectra obtained in this study, confirming the mechanical incorporation of HA in the polymer phase without chemical bonding. The intensities of HA-specific bands in the composite spectrum are in agreement with the quantity of HA incorporated in the scaffolds.

Previous studies reported a significant increase of HA-specific bands intensities due to apatite formation on the fibre surface after few days of SBF immersion in addition to the higher intensity and lower width at half maximum of the C=O band at 1759 cm^{-1} due to polymer degradation (Chlopek et al., 2009; Rajzer et al., 2014; Sooksaen et al., 2015). Interestingly, no significant changes appeared on either non-filled and HA-filled scaffolds spectra after 28 days of SBF immersion except for very small increase in the intensity of 560 and 630 cm^{-1} peaks in HA-filled samples assigned for the phosphate group of hydroxyapatite which suggest the formation of apatite layer on the surface of the samples. However, by comparing these results to SEM, weight loss, and TGA results, a significant variation in FTIR

results before and after immersion would not be expected due to low degradation and bioactivity rate of samples. Additionally, detection of the precipitated apatite peaks would be challenging due to the high penetration depth of FTIR energy into the samples (0.5-5μm) compared to the thickness of apatite layer formed on the scaffolds surfaces.

5.5 Conclusions

Introducing either of the HAs into electrospun PLA scaffolds led to slower degradation and higher in vitro bioactivity compared to neat PLA scaffolds. HA2 showed higher mechanical stability over 14 days of SBF immersion compared to HA1, while differences in the degradation and apatite formation rates from using the two different types of HAs were generally minor. On the other hand, scaffolds containing HA1 exhibited enhanced thermal stability over HA2-filled scaffolds due to higher surface area of HA1 particles.

Due to slow degradation and apatite formation of the scaffolds, degradation and bioactivity tests should be carried out over longer period of time, and since HA1-filled scaffolds showed faster reductions in mechanical properties in vitro compared to HA2-filled scaffolds, coaxial electrospinning experiments will be carry out using HA2 filler.

Chapter 6- Coaxial electrospinning of core-shell PCL-PLA/HA scaffolds

6.1 Introduction

Coaxial electrospinning has gained increasing popularity in biomedical applications ranging from tissue regeneration to wound healing and drug delivery. The production of uniform fibre morphology and well-defined core and shell structure is crucial for controlled delivery of bioactive molecules for these applications (Li et al., 2014). Various previous studies have focused on the production and optimisation of coaxial electrospun scaffolds with HA incorporated in the central core of the fibres to increase the stiffness and strength of the fibres (Shao et al., 2016; Tang et al., 2016; Zhou et al., 2018). However, HA can enhance specific biological activities such as cell adhesion, proliferation, differentiation and, when osteoblasts or stem cells are involved, in mineralisation. In addition, HA is considered to be a promising biomaterials for adsorbing proteins and then releasing them (Talal et al., 2009). Thus incorporating HA in the outer layer of coaxial electrospinning seems more relevant. However, in coaxial electrospinning the diameter of the inner core is generally larger than the thickness of the outer layer, so obtaining an even distribution of the HA in the shell or outer layer is generally more difficult.

This chapter is focused on optimising coaxial electrospinning parameters to produce core and shell biodegradable scaffolds with PCL as the core material and PLA/HA2 mixture as the shell material. This includes optimising the core solution using different solvent systems and polymer concentrations, studying the effect of solvent system on the morphology and mechanical properties of electrospun PLA/HA2 fibres (shell layer), and examining the influence of flow rate ratio between the core and shell solutions on the coaxial fibre uniformity. The effect of HA incorporation on the morphology, mechanical properties and protein absorption of coaxial scaffolds were also investigated.

6.2 Materials and methods

The first part of coaxial fibrous scaffolds production included optimisation of the core solution (PCL) through dissolving PCL granules in chloroform, acetone, and chloroform/acetone mixture as described in section 3.2.2.1. As for the shell solution, 15 and 20% w/v PLA with 20% v/v HA2 solution were first prepared using chloroform as the solvent as in section 3.2.1.1. However, these solutions were too viscous for coaxial electrospinning as they are pumped to the coaxial needle through 1mm diameter PTFE tubes which slowed the solution motion and produced unstable electrospinning. Thus, 15% w/v PLA solution with 20% v/v HA2 were prepared using 2:1 mixture of chloroform and acetone as in section 3.2.2.1. Samples were electrospun following the method described in section 3.2.2.2. Core and shell PCL-PLA were also electrospun following the same method and were used as control samples. The morphology of the resulted scaffolds were characterised using either Normaski microscope or SEM, while the total porosity and pore diameter were evaluated using the gravimetric method, mercury porosimetry, and DiameterJ analysis as described in sections 3.3.5.

Four different methods were employed to identify the core and shell structure within the fibres: firstly, samples were placed into liquid nitrogen and manually broken prior to sputter coating in order to observe the cross sections of the fibres in SEM. In the second method, small square pieces were cut from the fibrous scaffolds and embedded in Epon resin before slicing them into thin (~70nm thick) sections using an ultramicrotome. The thin sections were then collected on aluminium stubs, sputter coated and viewed using either SEM or TEM as described in sections 3.3.2 and 3.3.3. Lastly, rhodamine B and FITC dyes were added to the core and shell solutions respectively following the methods described in section 3.3.4 and the resulted scaffolds were then observed using laser scanning confocal microscopy (Zeiss LSM 880).

The tensile mechanical properties were evaluated for PCL, PLA/HA, core and shell PCL-PLA, and core and shell PCL-PLA/HA scaffolds. The cumulative release of BMP-2 from the co-electrospun PCL-PLA and PCL-PLA/HA2 scaffolds at 0.25, 1, 2, 4, 24, 48, 72 and 96 hr was determined using an ELISA kit following the procedure described in section 3.3.11. Finally, the interaction between the MSCs and coaxial scaffolds with and without HA was observed at days 1, 7, 14, and 21 of culture using SEM as described in section 3.3.12.

6.3 Results

6.3.1 Normaski microscope and SEM

Electrospinning of PCL solutions dissolved in chloroform at 15 and 20% w/v concentrations led to droplet formation (electrospraying) instead of fibre formation (electrospinning) as shown in Figure 6.1a, while 25% PCL solution was barely electrospun due to the high viscosity of the solution but resulted in uniform fibre formation with fibre diameter of 10.67± 1.28μm (Figure 6.1b).

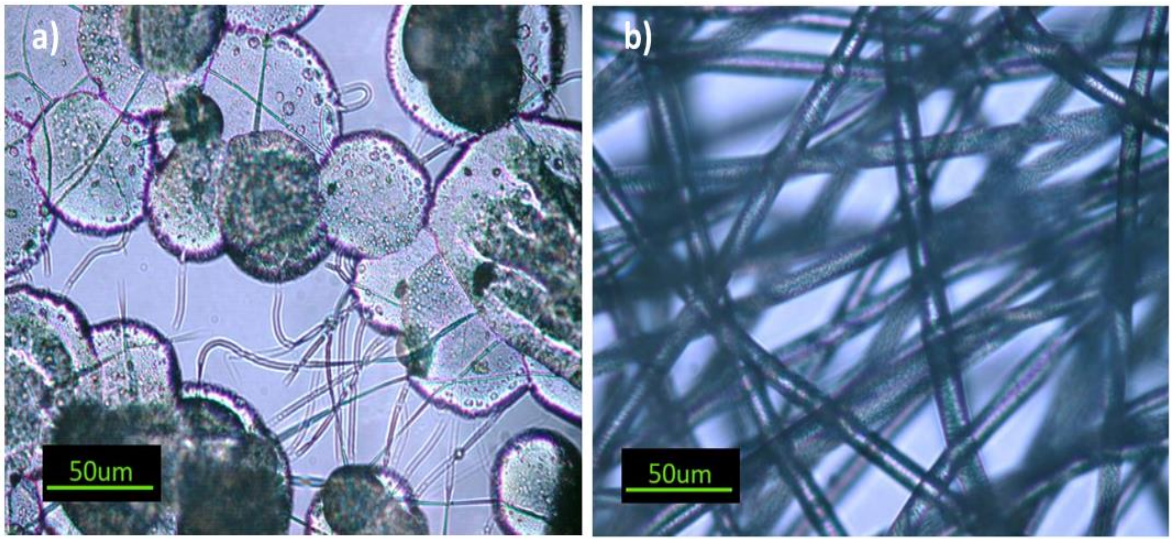

Figure 6.1 Electrospraying or electrospinning of PCL solutions dissolved in chloroform: a) 20% PCL leading to electrospraying, b) 25% PCL leading to electrospinning (marker bars=50μm)

In contrast, PCL solutions dissolved in acetone at 15 and 20% w/v concentrations were both electrospinnible and produced non-beaded fibres with a wide range of diameters as shown in Figure 6.2a. However, the Taylor cone was not stable, thus it split into multiple jets soon after electrospinning started as shown in Figure 6.2b.

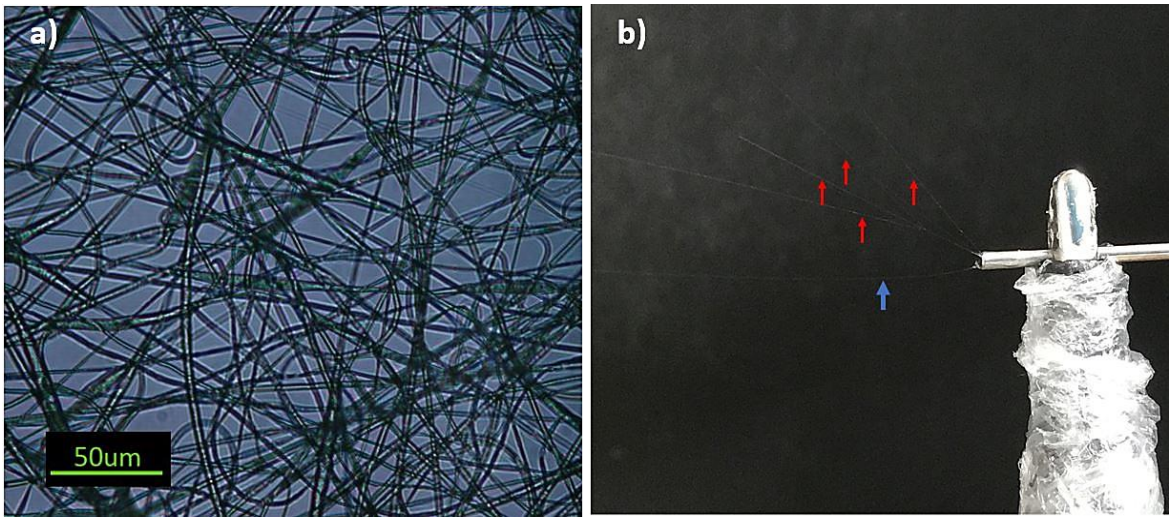

Figure 6.2 Electrospinning of PCL solutions dissolved in acetone: a) 20% PCL (marker bar=50μm), b) multiple Taylor cones formed at the needle tip (the blue arrow indicate the primary jet and the red arrows indicate the secondary jets)

Dissolving the PCL in a binary solvent system composed of chloroform and acetone (2:1 ratio) at 15 and 20% w/v concentration resulted in more uniform fibre production (Figure 6.3) and the multi-jet phenomena was eliminated. Scaffolds of 20% PCL solution concentration had higher fibre uniformity than 15% PCL solution. Thus, 20% PCL solution was chosen for the core phase of coaxial electrospinning.

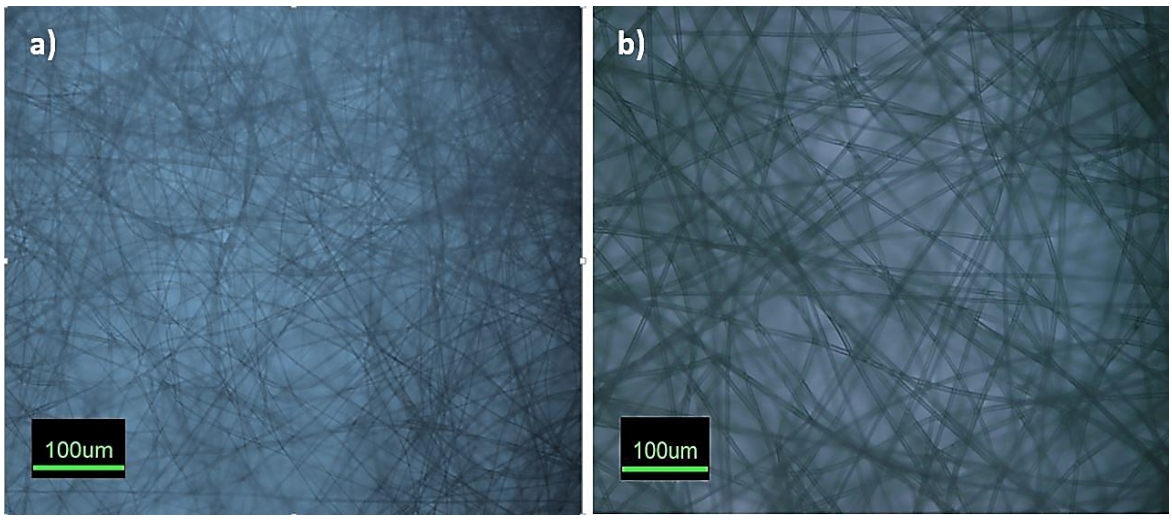

Figure 6.3 Electrospinning of PCL solutions dissolved in chloroform: acetone solvent system: a) 15% PCL, b) 20% PCL (marker bars=100μm)

The same binary solvent system was also used to prepare the shell solution which is composed of 15% w/v PLA with 20% v/v HA2. Figure 6.4 shows the morphology and fibre distribution curve of electrospun 15% PLA with 20% HA2 prepared with chloroform/acetone solvent system. A range of fibres widths can be seen, including some very fine fibrils. However in the thicker fibres the presence of the HA particles on the fibre surfaces is obvious

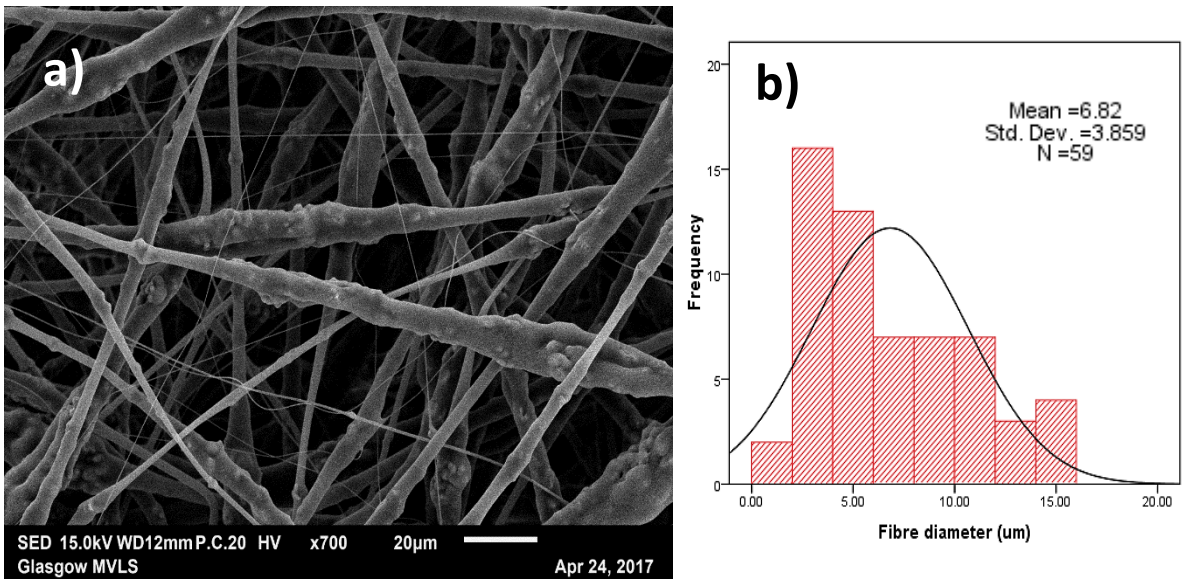

Figure 6.4 a) SEM of electrospun 15% PLA with 20% HA2 using (2:1) chloroform: acetone solvent system (marker bar=20µm) and b) histogram of the fibre diameters obtained using ImageJ

To optimise the coaxial electrospinning, coaxial PCL-PLA/HA2 scaffolds were electrospun at three core:shell flow rate ratios: 1:3, 2:3 and 3:3. Figure 6.5 shows the morphology of the resultant scaffolds under Normaski microscope.

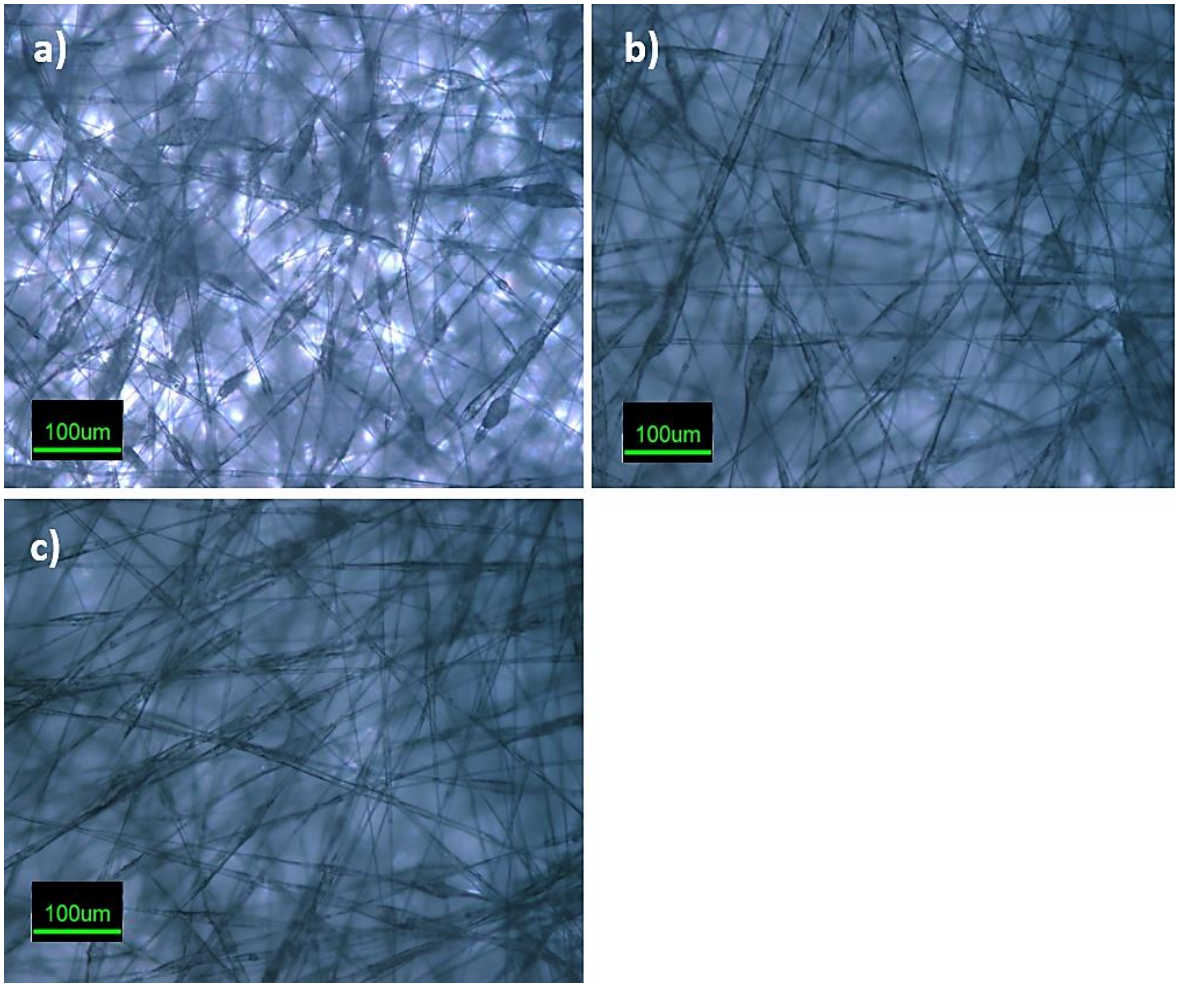

Figure 6.5 Morphology of core-shell PCL-PLA/HA2 fibres using (a) 1:3, (b) 2:3, and (c) 3:3 core:shell flow rate ratio (marker bars=100μm)

Electrospinning at 1:3 flow rate ratio produced beaded fibres, while electrospinning at 2:3 and 3:3 flow rate ratios yielded more uniform, non-beaded fibres. Scaffolds produced at 2:3 and 3:3 flow rate ratios were further examined with SEM to examine the surface morphology as shown in Figure 6.6. Fibre diameters were measured using ImageJ and were 5.91± 3.47μm and 6.06± 2.89μm for 2:3 and 3:3 flow rates respectively.

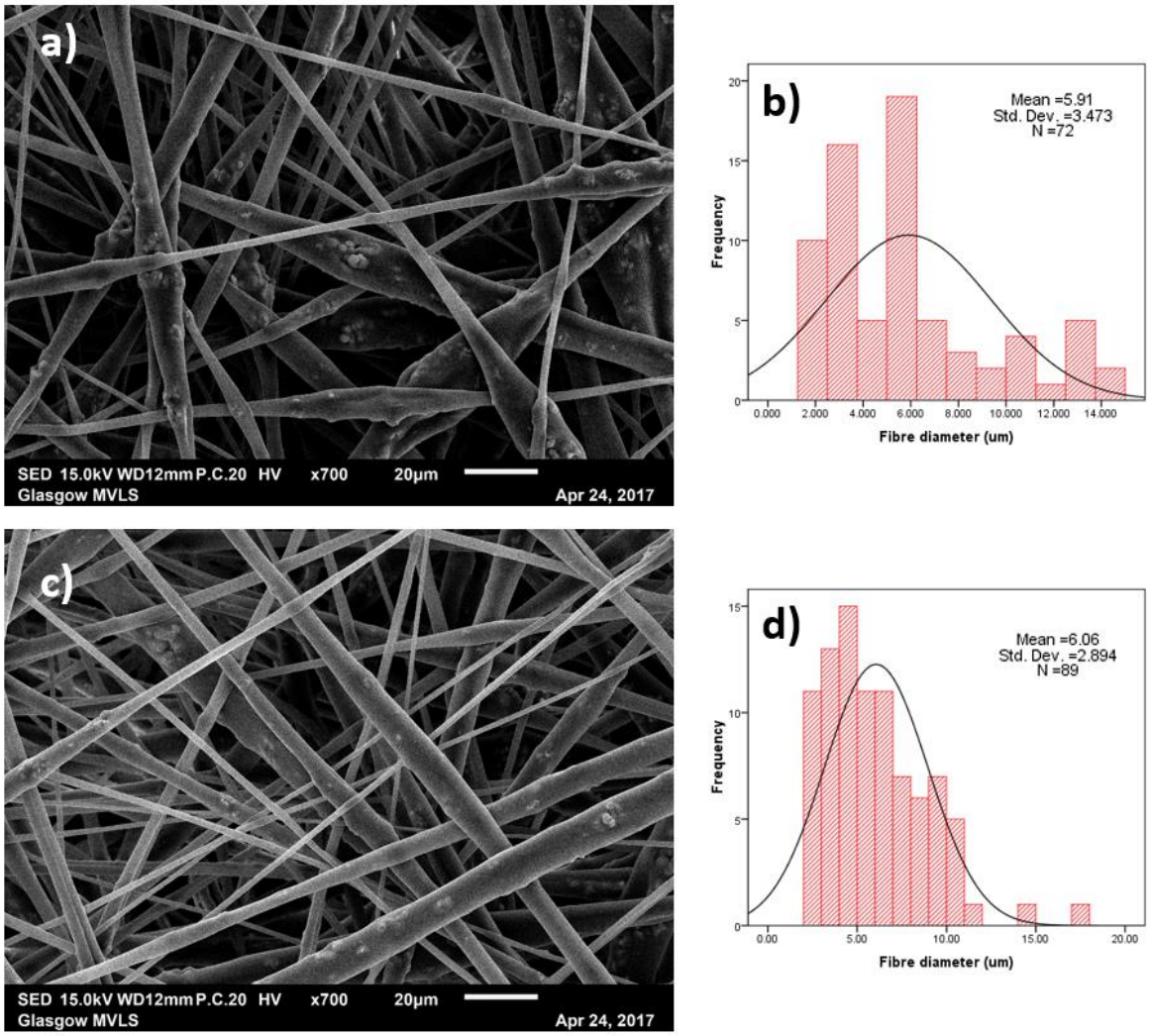

Figure 6.6 SEM images of core-shell PCL-PLA/HA2 fibres electrospun at (a) 2:3 and (c) 3:3 core:shell flow rate ratio (marker bars=20µm) with (b) and (d) showing the histograms of the fibre diameters for 2:3 and 3:3

Core and shell PCL-PLA (control samples) were electrospun at a flow rate ratio of 3:3 for comparison. Figure 6.7 shows the morphology of the resultant fibres. Scaffolds also had some twin or grooved fibres as indicated by the arrows. The resulted scaffolds had smooth and uniform fibres with nanoporous surface and an average diameter of 4.42 ±1.14µm.

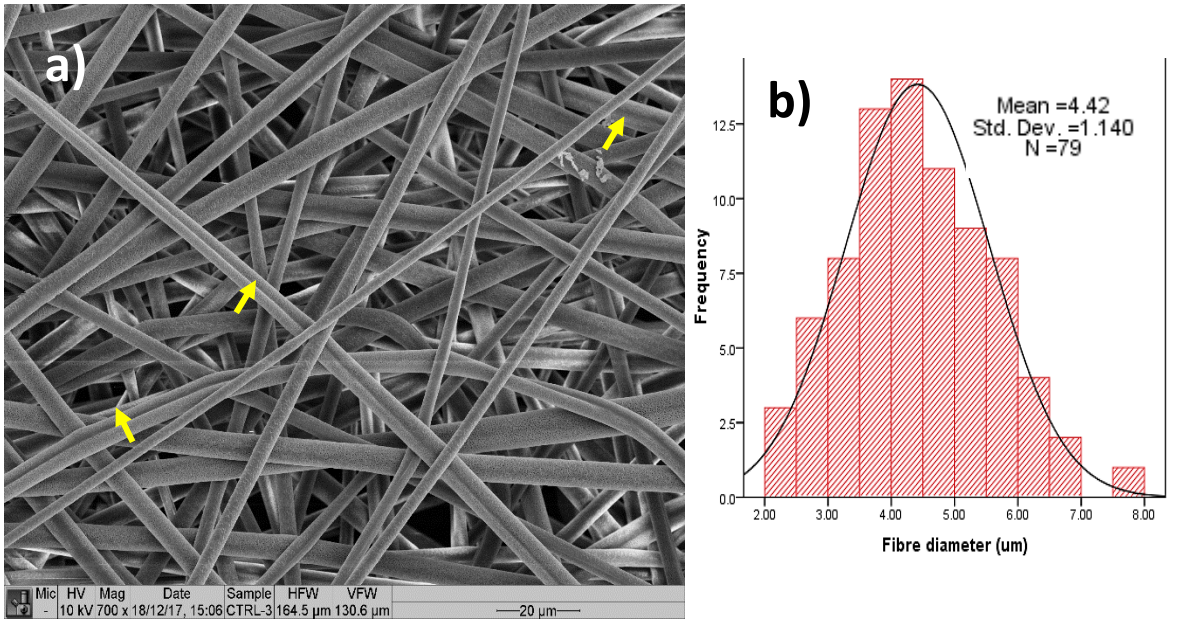

Figure 6.7 a) SEM image of core-shell PCL-PLA fibres electrospun at 3:3 core:shell flow rate ratio. Arrows indicate twin or grooved fibres within the scaffold (marker bar=20µm), b) histogram of the fibre diameters obtained using ImageJ

To verify the core and shell structure within the fibres, control and HA-containing scaffolds electrospun at 3:3 flow rate ratio were immersed in liquid nitrogen and then manually fractured to examine the fibre ends. However, only HA-containing samples were valid for testing in this method. Control samples were hard to fracture due to the high ductility of the scaffolds. Therefore, the fibres were cut with sharp razor blade after immersing in liquid nitrogen for few minutes. However, the fibres ends were still damaged and could not be imaged clearly. Figure 6.8 shows individual fibre morphology of coaxial HA-containing scaffolds.

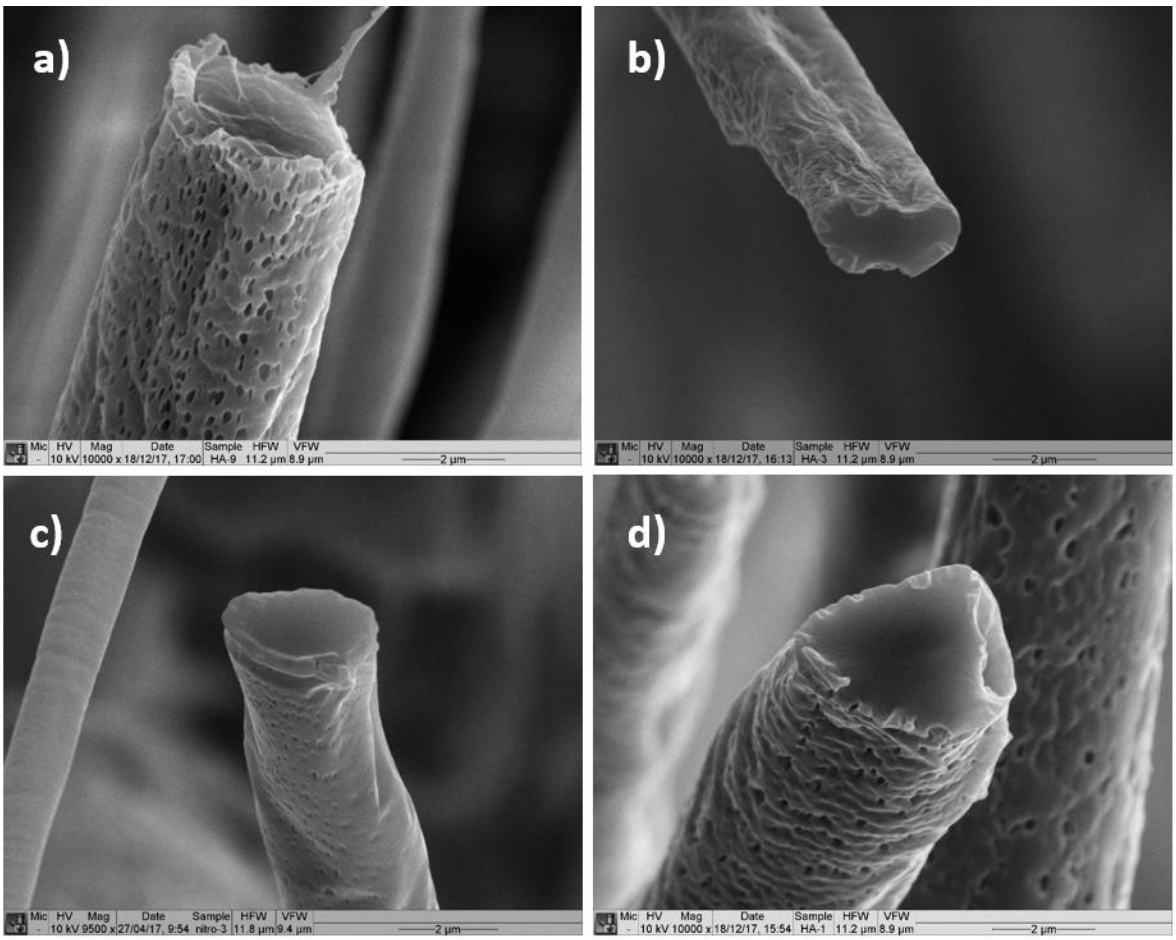

Figure 6.8 SEM images of fractured PCL-PLA/HA2 coaxial fibres electrospun at 3:3 core:shell flow rate ratio: (a) hollow fibre, (b) twin or grooved fibre, (c) and (d) core and shell fibres (marker bars=2μm)

SEM images of resin embedded HA-containing coaxial scaffolds electrospun at flow rate ratio of 3:3 (Figures 6.9 and 6.10) show that the fibres have core and shell structure with shell thickness of 0.72±0.22μm. Thus, the ratio of core diameter to overall fibre diameter is about 0.88:1 giving an area ratio of 0.77:1. Images have also shown the micro HA particles positioned in the outer layer of the fibres.

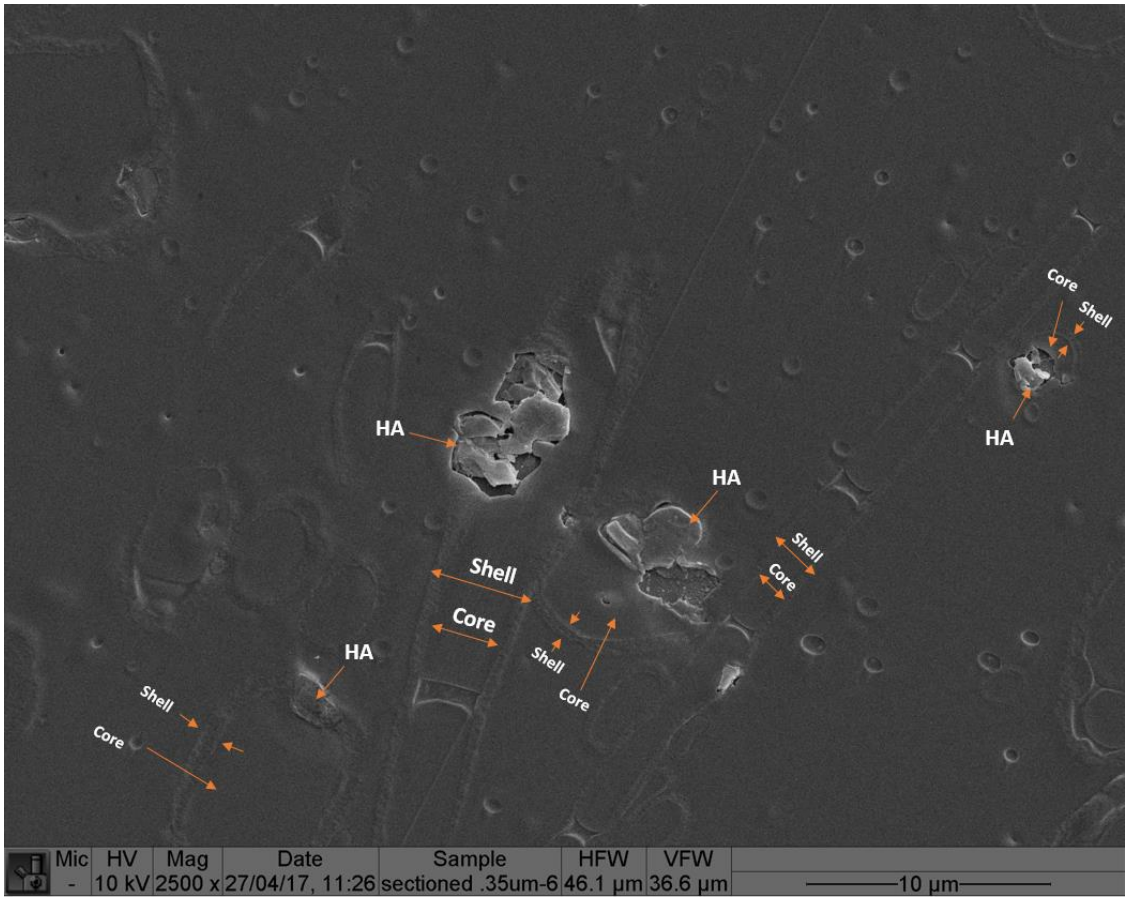

Figure 6.9 SEM image of resin embedded PCL-PLA/HA2 fibres coaxial electrospun at 3:3 core:shell flow rate ratio showing both longitudinal and transverse sections of the fibres (marker bar=10µm)

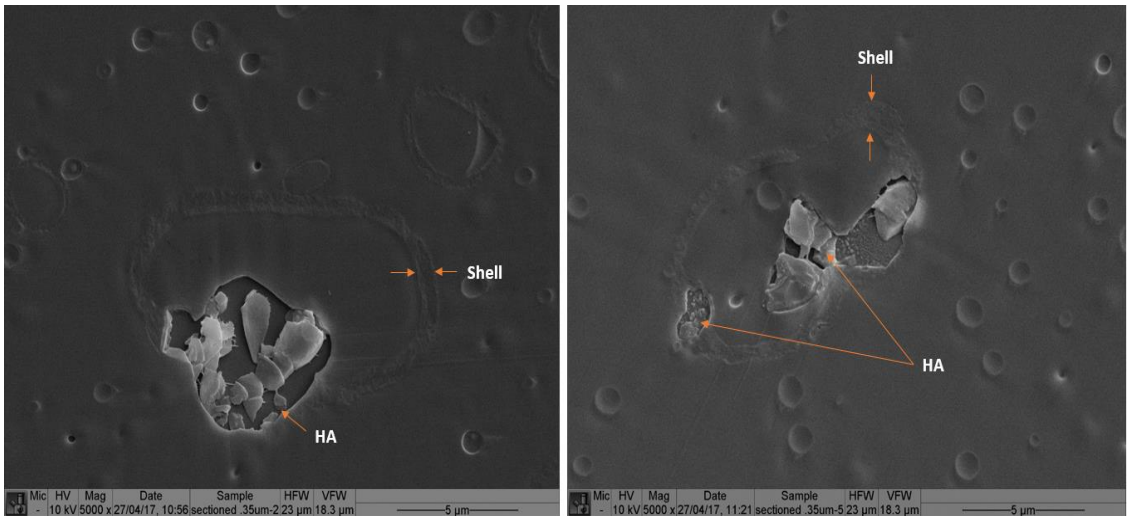

Figure 6.10 SEM images of resin embedded PCL-PLA/HA2 coaxial fibres electrospun at 3:3 core:shell flow rate ratio showing transverse sections of the fibres (marker bars=5µm)

6.3.2 TEM

Figures 6.11 and 6.12 shows TEM images of resin embedded control coaxial fibres electrospun at 2:3 and 3:3 core:shell flow rate ratio respectively. It should be noted that the TEM density of the PCL core material and the embedding Epon resin are similar and lower the PLA. Fibres of both scaffolds exhibited core and shell structure with only few single component fibres. The thickness of the shell layer was largely variable among fibres and in some cases, it was discontinuous as indicated by the red arrow in Figure 6.11b.

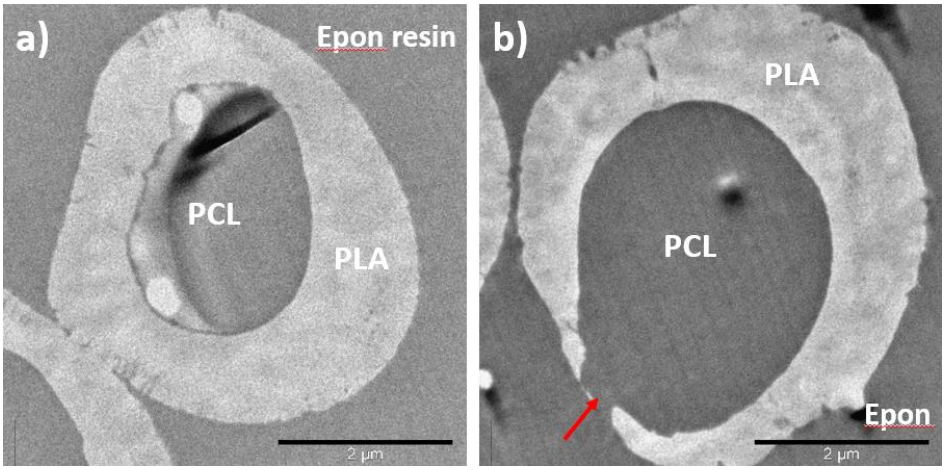

Figure 6.11 TEM images of resin embedded PCL-PLA fibres coaxial electrospun at 2:3 core:shell flow rate ratio showing (a) fibre with thick shell layer covering the core completely and (b) fibre with discontinuous shell layer (red arrow) (marker bars=2µm)

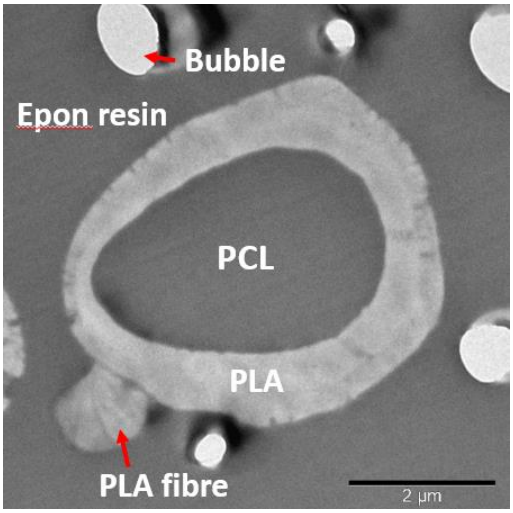

Figure 6.12 TEM image of resin embedded PCL-PLA coaxial fibres electrospun at 3:3 core:shell flow rate ratio showing core and shell fibre configuration in addition to a PLA fibre with no core component (red arrow) (marker bar=2µm)

Figures 6.13 and 6.14 shows TEM images of resin embedded control coaxial fibres electrospun at 2:3 and 3:3 core:shell flow rate ratio respectively. Fibres of both scaffolds also show core and shell structure with HA particles protruding either to the surface of the fibres (blue arrows in Figure 6.14) or to the inside core layer. The HA particles are brittle and have fractured during the sectioning process explaining the fragments of HA surrounded by gaps seen on the TEM sections of the composite fibres.

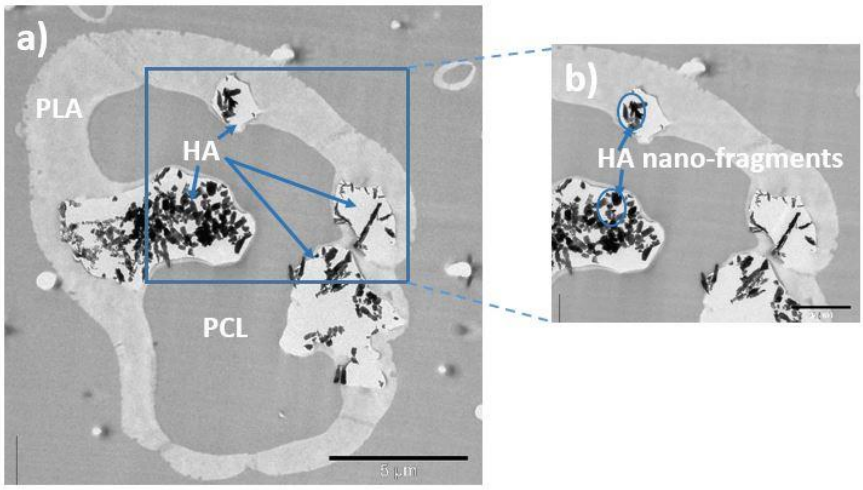

Figure 6.13 TEM images of resin embedded PCL-PLA/HA2 coaxial fibres electrospun at 2:3 core:shell flow rate ratio showing (a) core and shell fibre configuration and (b) higher magnification image of the fibre showing HA nano-fragments (marker bars=5µm for (a) and 2µm for (b))

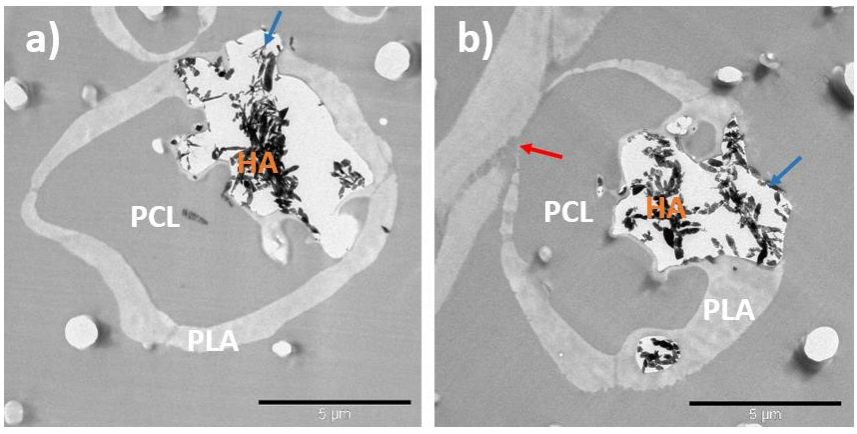

Figure 6.14 TEM images of resin embedded PCL-PLA/HA2 coaxial fibres electrospun at 3:3 core:shell flow rate ratio showing (a) core and shell fibre with shell layer covering the fibre completely and (b) fibre with discontinuous shell layer (red arrow). The blue arrows indicate the partial encapsulation of HA particles (marker bars=5µm)

6.3.3 Laser scanning confocal microscopy

Figures 6.15 to 6.18 shows the confocal microscopy images for the control and HA-containing coaxial scaffolds electrospun at 2:3 and 3:3 core:shell flow rate ratios, respectively. The red channel in Figures below shows the PCL core layer labelled with rhodamine B while the green channel shows the PLA/HA2 shell layer labelled FTIC. The yellow channel shows the combined red and green channels (i.e. the core and shell layers of the fibre).

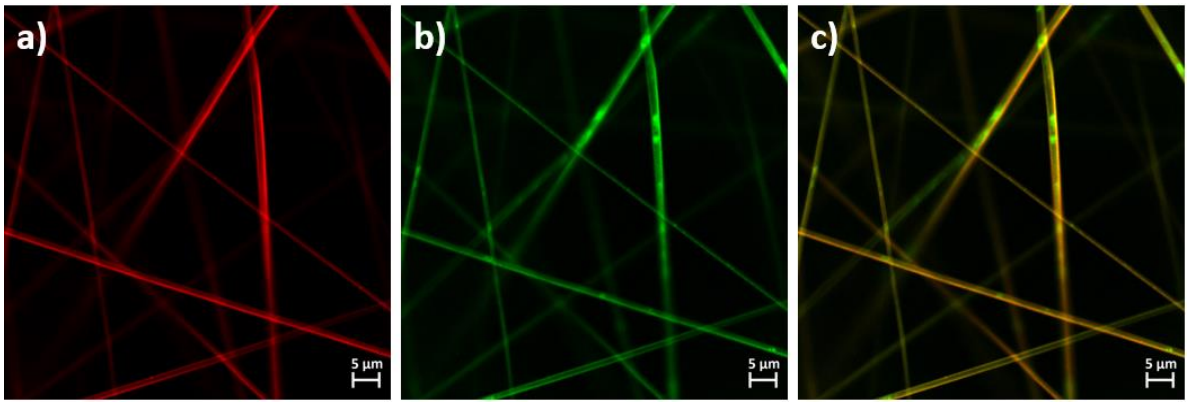

Figure 6.15 Confocal microscope images of core and shell PCL-PLA fibres electrospun at 2:3 core:shell flow rate ratio showing (a) the core component (PCL) labelled with rhodamine B, (b) the shell component (PLA) labelled with FITC and (c) the combined core and shell channels (marker bars=5µm)

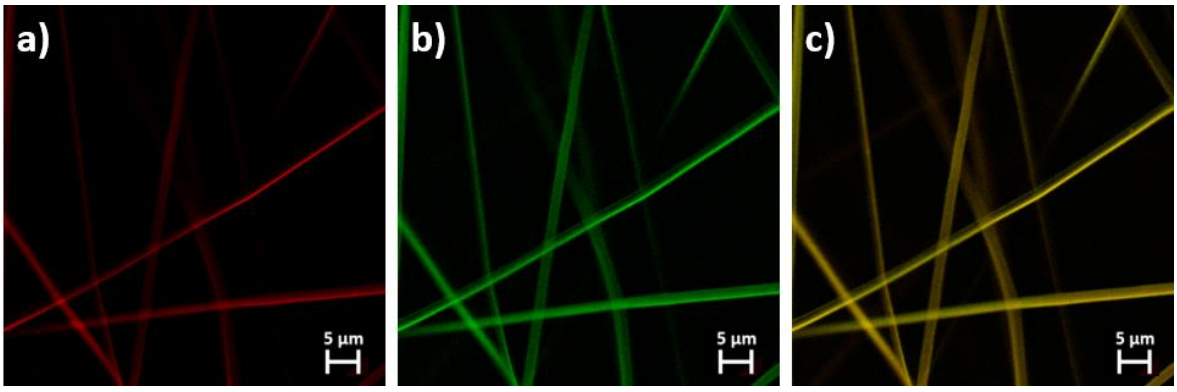

Figure 6.16 Confocal microscope images of core and shell PCL-PLA fibres electrospun at 3:3 core:shell flow rate ratio showing (a) the core component (PCL) labelled with rhodamine B, (b) the shell component (PLA) labelled with FITC and (c) the combined core and shell channels (marker bars=5µm)

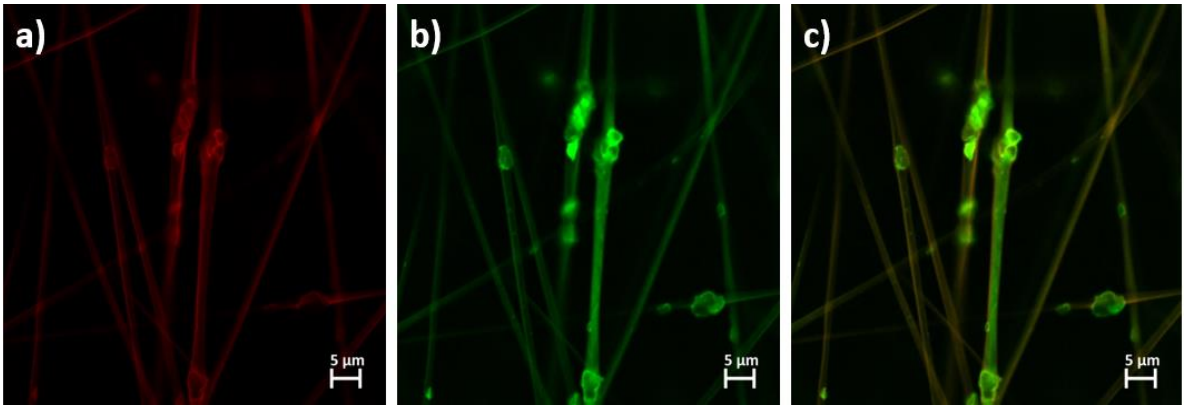

Figure 6.17 Confocal microscope images of core and shell PCL-PLA/HA2 fibres electrospun at 2:3 core:shell flow rate ratio showing (a) the core component (PCL) labelled with rhodamine B, (b) the shell component (PLA/HA2) labelled with FITC and (c) the combined core and shell channels (marker bars=5µm)

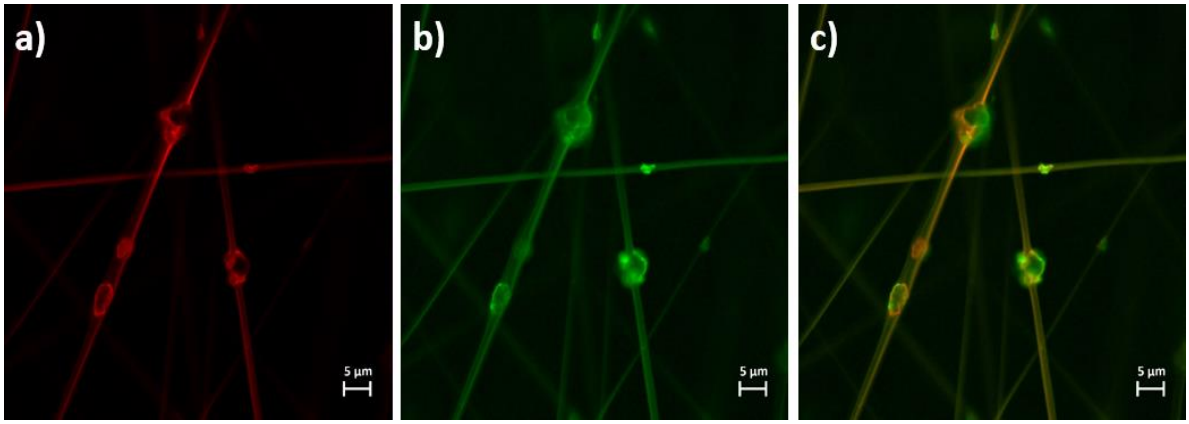

Figure 6.18 Confocal microscope images of core and shell PCL-PLA/HA2 fibres electrospun at 3:3 core:shell flow rate ratio showing (a) the core component (PCL) labelled with rhodamine B, (b) the shell component (PLA/HA2) labelled with FITC and (c) the combined core and shell channels (marker bars=5µm)

6.3.4 Porosity

Table 6.19 lists the porosities and pore diameter range of coaxial PCL-PLA/HA2 scaffolds (3:3 flow rate ratio) measured by gravimetric, mercury porosimetry, and DiameterJ plugin techniques. The pore size distribution over the differential volume obtained from mercury porosimetry is shown in Figure 6.19 with the major peak centred at 18µm. The values given by the three techniques are very different and the reasons for this will be considered in detail in the Discussion.

Table 6.1 Total porosity and pore diameter range for coaxial PCL-PLA/HA2 scaffolds electrospun at 3:3 core:shell flow ratio

Technique	Number of samples	Total porosity (%)	Pore diameter range (µm)
Gravimetric	5	88.25 ± 3.41	N/A
Mercury porosimetry	1	7.19	Intrusion: 267.21 to 0.0054 Extrusion: 0.0054 to 9.125616
DiameterJ	5	38.32 ± 7.81	0.25 to 27.03

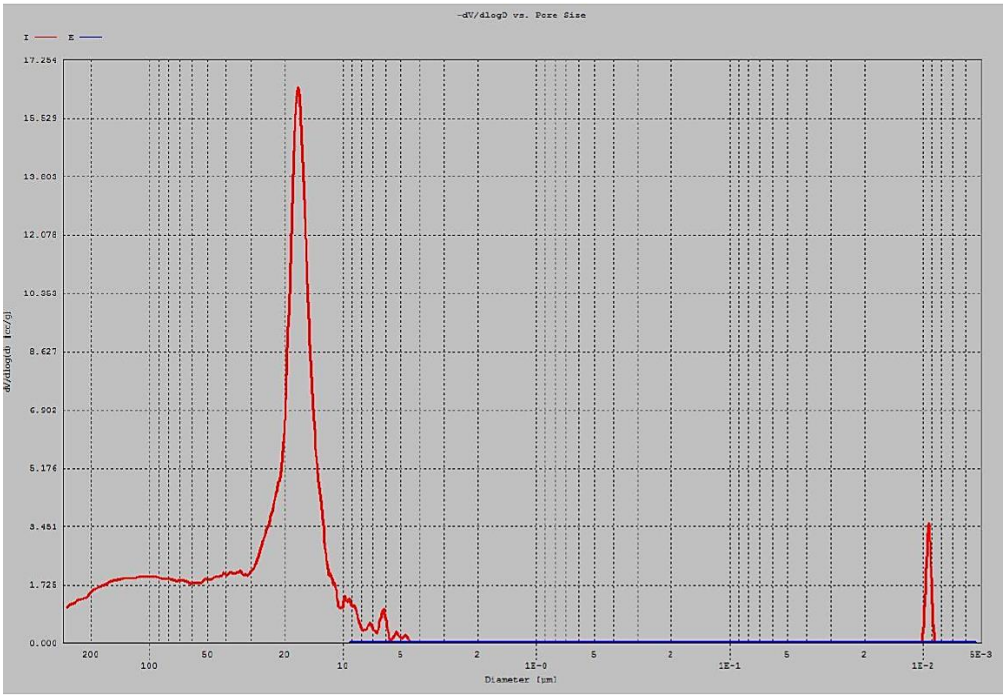

Figure 6.19 Pore size distribution of coaxial PCL-PLA/HA sample electrospun at 3:3 core:shell flow rate ratio obtained from mercury porosimetry technique showing the differential volume (Y-axis) versus pore diameter (in µm)

6.3.5 FTIR

FTIR spectra of electrospun 20% PCL, 15% PLA with 20% HA2, and coaxial PCL-PLA/HA2 at 2:3 and 3:3 flow rate ratios are shown in Figure 6.20. The spectral features identified from the FTIR spectra of PCL scaffolds were compared to literature and the assignments of the identified peaks are listed in Table 6.2, while the spectral features of PLA/HA2 scaffolds are listed in Table 5.10. Coaxial scaffolds electrospun at 2:3 and 3:3 flow rate ratios have shown combined features of both core and shell components which indicate the incorporation of both phases within the fibres. However, no additional peaks are seen indicating that no chemical bonding has occurred between either of the polymers and the HA particles.

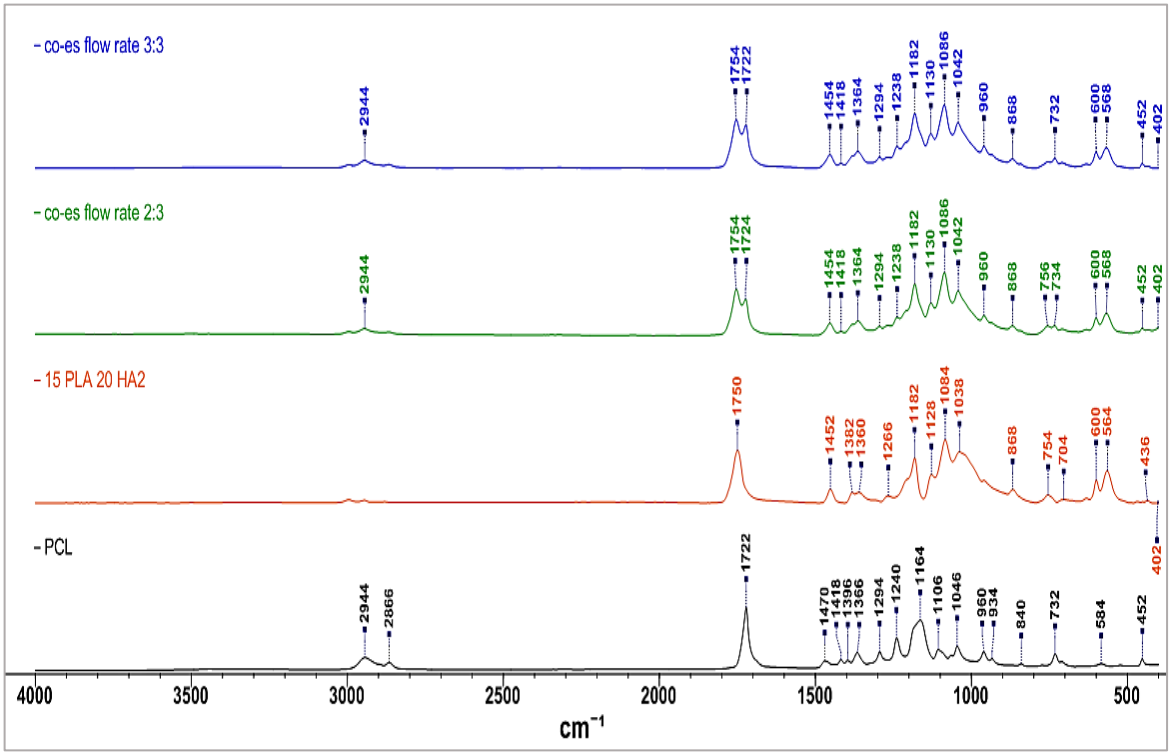

Figure 6.20 FTIR spectra of electrospun 20% PCL, 15% PLA with 20% HA2, and core and shell PCL-PLA/HA2 at 2:3 and 3:3 core:shell flow rate ratio

Table 6.2 Assignments of spectral features identified from the FTIR spectra of PCL scaffolds

Wavenumber (cm^{-1})	Assignment	References
1722	C=O stretching (The main characteristic peak of PCL)	(Chen et al., 2010; Elzein et al., 2004; Khatri et al., 2013; Kim and Kim, 2014; Uma Maheshwari et al., 2014)
2944, 2866	asymmetric and symmetric modes of stretching of C–H bonds respectively	
1294	C–O and C–C stretching in the crystalline phase	
1418, 1366	C–H bending	
1240,1164	asymmetric and symmetric modes of COC stretching respectively	

6.3.6 Mechanical testing

The tensile properties for electrospun 15% PLA, 20%PCL, 15%PLA with 20%HA2 scaffolds in addition to co-electrospun PCL-PLA and PCL-PLA/HA2 scaffolds at core:shell flow rate ratios of 2:3 and 3:3 are shown in Table 6.3. The results are also presented graphically in Figure 6.21.

Table 6.3 Mechanical properties of electrospun core and shell PCL-PLA and PCL-PLA/HA2 at 2:3 and 3:3 core:shell flow rate ratio along with those of their individual components

Scaffold	Solvent	Young's modulus (MPa)	UTS (MPa)	Elongation at break (%)
20% PCL	Chloroform/acetone	4.92 ± 0.77	0.837 ± 0.200	323.17± 119.09
15%PLA 20% HA2	Chloroform	37.73 ± 6.81	0.546 ± 0.061	16.13 ± 4.91
15%PLA 20% HA2	Chloroform/acetone	59.54 ± 9.66	0.263 ± 0.055	13.09 ± 2.90
Core-shell PCL-PLA (2:3)	Chloroform/acetone	25.52 ± 7.52	0.708 ± .0261	89.02 ± 11.63
Core-shell PCL-PLA (3:3)	Chloroform/acetone	41.23 ± 8.59	1.259 ± 0.396	102.61 ± 17.44
Core-shell PCL-PLA/HA2 (2:3)	Chloroform/acetone	15.20 ± 1.80	0.398 ± 0.066	23.32 ± 9.58
Core-shell PCL-PLA/HA2 (3:3)	Chloroform/acetone	31.33 ± 5.04	0.680± 0.101	30.53 ± 4.36

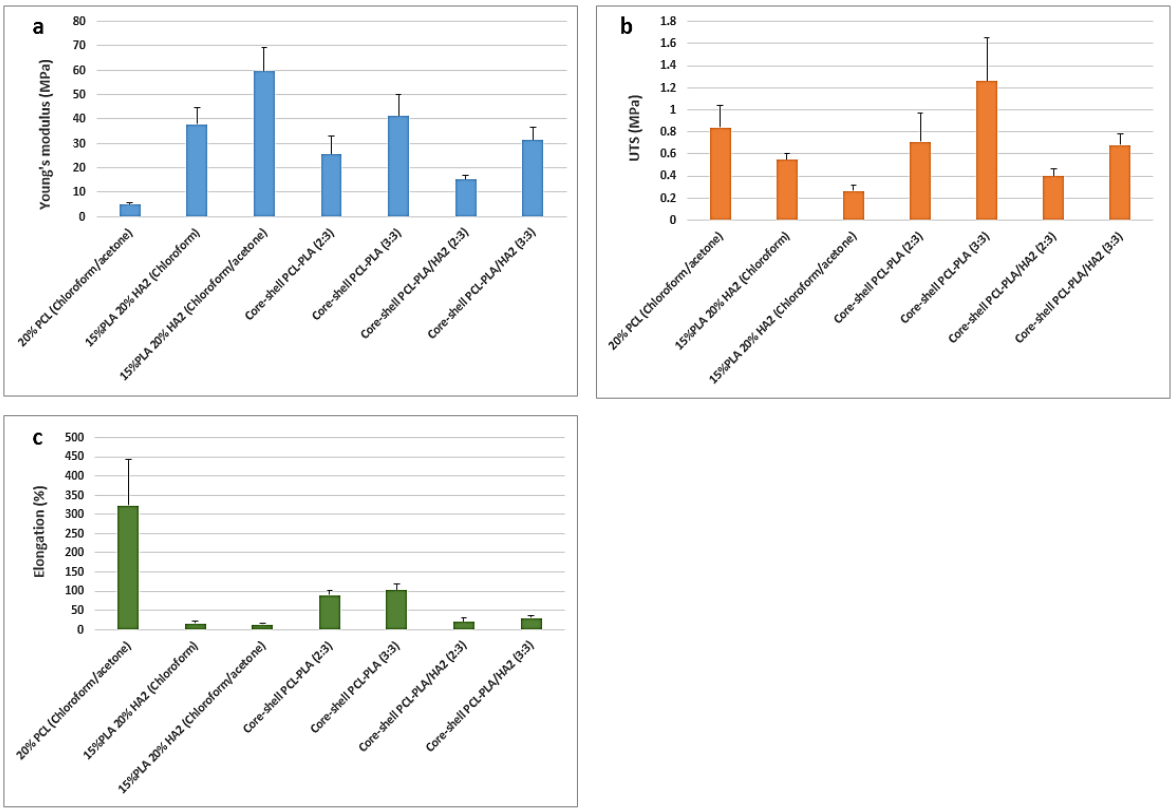

Figure 6.21 Mechanical properties of electrospun 20% PCL, 15% PLA with 20% HA2, and core and shell PCL-PLA and PCL-PLA/HA2 at core:shell flow rate ratio. (a) Young's modulus, (b) UTS and (c) elongation at failure

Representative stress-strain curves of the coaxial control and HA-containing scaffolds electrospun at 2:3 and 3:3 flow rate ratio in addition to their monolithic fibres are shown in Figure 6.22.

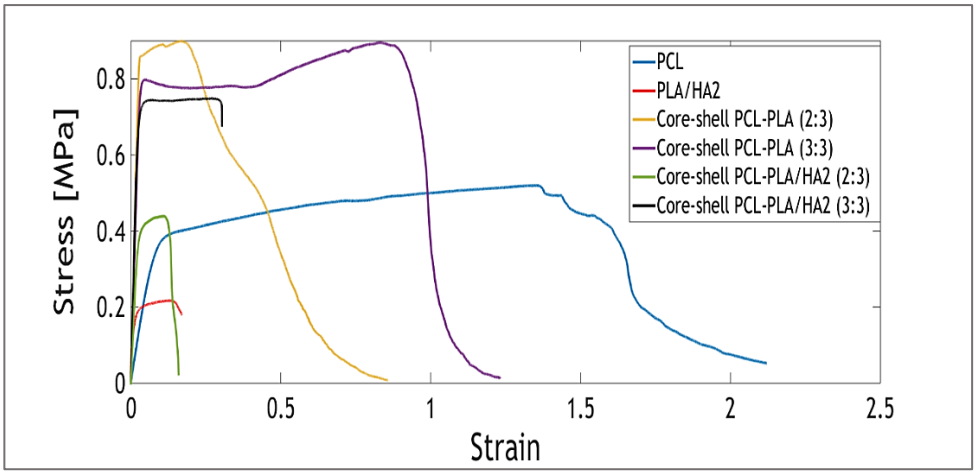

Figure 6.22 Representative stress–strain curves of electrospun PCL, PLA/HA2, coaxial control and HA-containing scaffolds at 2:3 and 3:3 core:shell flow rate ratio

6.3.7 BMP-2 release

The cumulative release of BMP-2 over 96 hours for coaxial PCL-PLA (control) and PCL-PLA/HA2 scaffolds is shown in Figure 6.23. Two regions are observed, the first 4 hours showed high release rate and then a second linear phase of 0.05% per hour and 0.0666% per hour for the control and HA-containing scaffolds respectively. Thus, BMP-2 release behaviour showed minimal difference between the control and HA-containing samples over 96 hours.

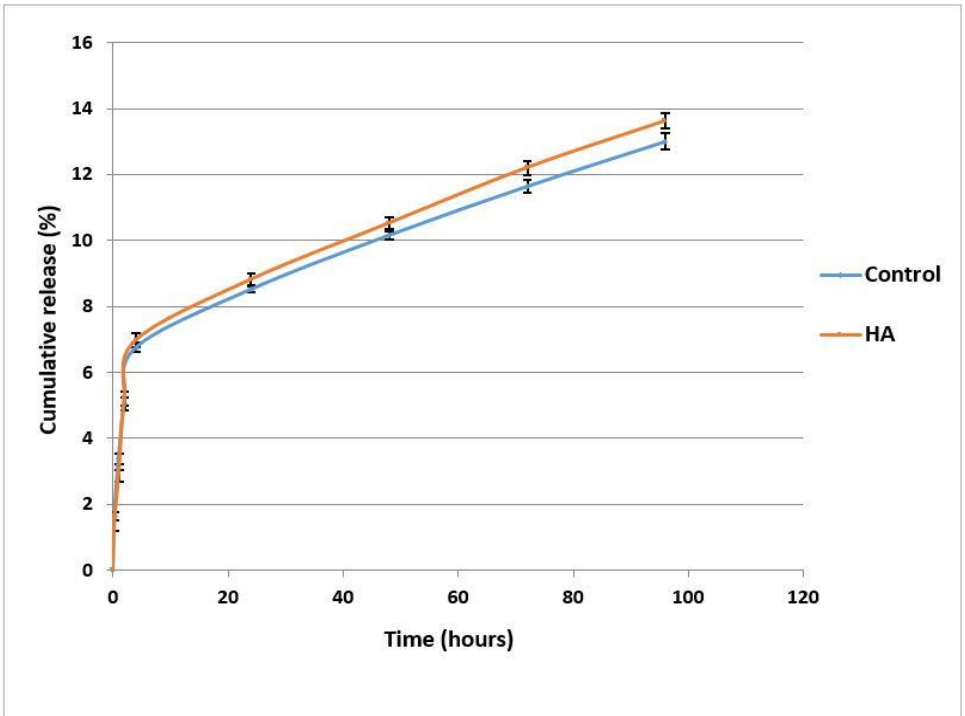

Figure 6.23 Cumulative release of BMP-2 from coaxial control and HA-containing scaffolds

6.3.8 Cell Culture

Figures 6.24 and 6.25 shows SEM images of MSC adhesion and interaction with control and HA-containing coaxial scaffolds respectively at day 1, 7, 14, and 21 of culture. On both scaffolds the cells have grown well and attached on to the surface of the fibres. At days 1 to 14 there appear to be more cells on the HA containing samples than on the controls. However at day 21 there appear to be more cells on the control surfaces, including (Figure 6.23n) deep within the scaffold.

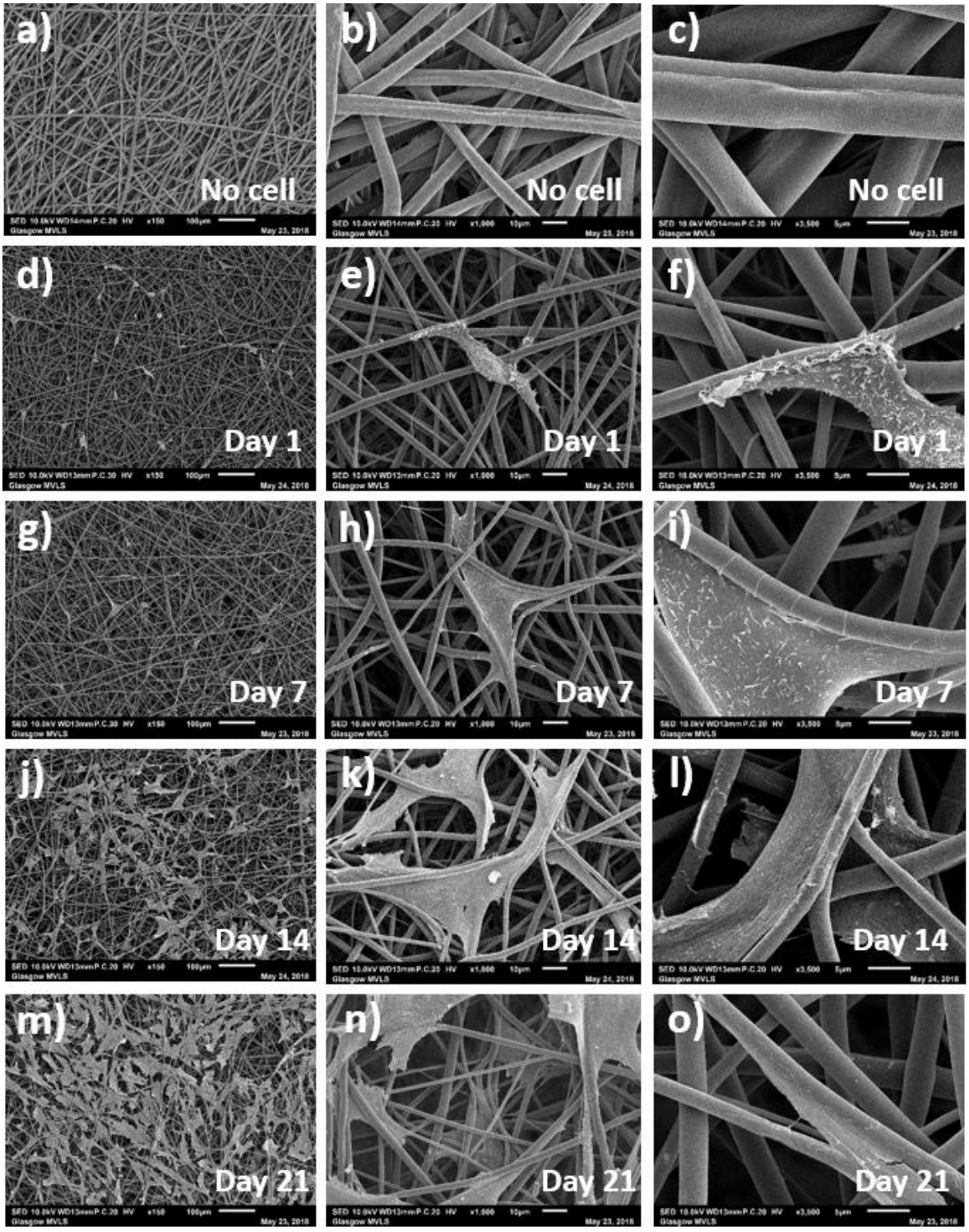

Figure 6.24 SEM images of coaxial control scaffolds at different magnifications showing (a-c) fibres before cell culture and after (d-f) 1 day, (g-i) 7 days, (j-l) 14 days and (m-o) 21 days of MSCs culture (marker bars for (a), (d), (g), (j) and (m)=100 μm, for (b), (e), (h), (k) and (n)= 10μm and for (c), (f), (i), (l) and (o)= 5μm)

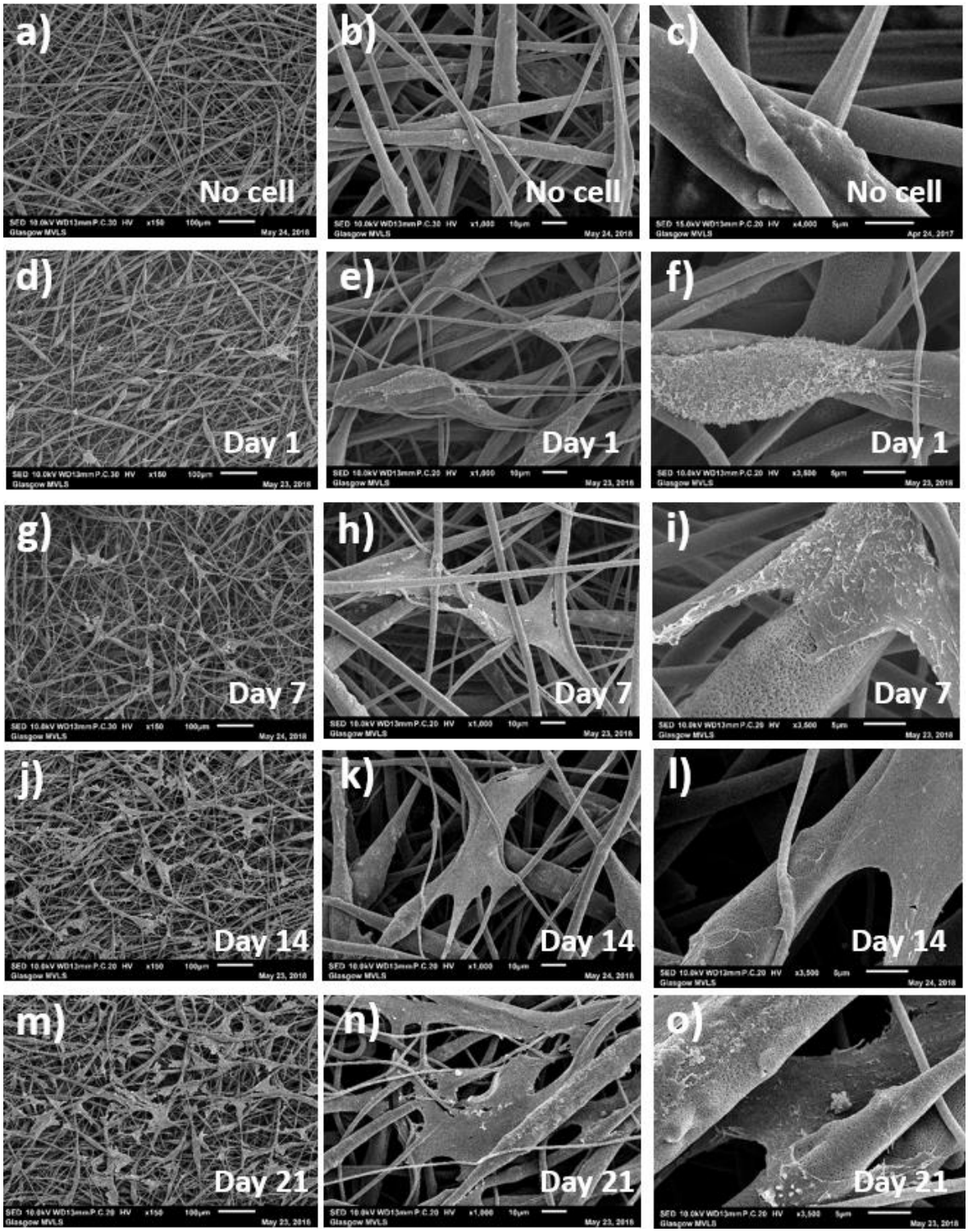

Figure 6.25 SEM images of coaxial HA-containing scaffolds at different magnifications showing (a-c) fibres before cell culture and after (d-f) 1 day, (g-i) 7 days, (j-l) 14 days and (m-o) 21 days of MSCs culture (marker bars for (a), (d), (g), (j) and (m)=100 μm, for (b), (e), (h), (k) and (n)= 10μm and for (c), (f), (i), (l) and (o)= 5μm)

6.4 Discussion

15 and 20% PCL solutions made with chloroform alone failed to produce fibres during electrospinning. Uniform fibres were only produced when the PCL concentration was increased to 25%. However, increasing the concentration to 25% led to increased needle clogging which in turn caused disturbance of electrospinning due to the high viscosity of the PCL solution. These results were unexpected since electrospinning of PCL dissolved in chloroform at different concentrations starting from 5% w/v have been previously reported by several studies (Ferreira et al., 2014; Hsu and Shivkumar, 2004b; Vaz et al., 2005; Yoshimoto et al., 2003). However, this study used different electrospinning parameters than previously reported such as flow rate, applied voltage, tip to collector distance and probably most importantly needle size which might effected the electrospinnibility of PCL. On the other hand, electrospinning of 15 and 20% PCL solutions made with acetone solvent caused formation of multiple Taylor cones or what it is known as "multi-jet single needle electrospinning" (Figure 6.2b), where the jet splits into a multitude of jets almost at the tip of the needle, or the jet can undergo significant elongational flow before it starts to splitting (or splaying) into smaller jets. In this study, the jet was splitting at the tip of the needle into one major jet with two to five secondary jets. According to Hohman et al. (2001) and Yarin et al. (2001), the evolution of jet instabilities which can cause jet branching or jet breakdown into multiple jets is a complex phenomenon that is governed by several factors such as solution rheology, surface tension and the rate of solvent evaporation. Eda et al. (2007), on the other hand, found that a cloud of jets could be produced using solvents with a high dielectric constant, while Vaseashta (2007) produced 2–3 jets using a relatively high voltage power supply (about 30kV) and a collector with significant curvature. In this study, however, it is believed that the high dielectric constant of acetone compared to chloroform (20.7 vs 4.81) is the reason for multi-jet formation since the voltage was the same for both experiments (13.7kV) and the ground collector used to collect the electrospun fibres was flat. Koombhongse et al. (2001) have shown that the characteristics of the fibres in obtained during electrospinning may depend on the extent of jet bending instability, splitting and branching. This effect could be seen in Figure 6.2a where the resultant fibres were non-uniform and the scaffolds had wide fibre diameter distribution which might be caused by jet splitting during electrospinning. Although multi-jet electrospinning has been

demonstrated to be an optimal approach for enhancing the production rate of electrospinning and many techniques were employed to control the formation of stable multi-jets during electrospinning process (Liu et al., 2015; Vaseashta, 2007; Zhou et al., 2009), jet splitting from core solution during coaxial electrospinning would not be useful as some of the resultant fibres would not have core and shell morphology and would consist of core only.

By dissolving 15 and 20% w/v PCL in a binary solvent system of chloroform and acetone in 2:1 v/v ratio, uniform fibres were produced (Figure 6.3), the multi-jet phenomena disappeared, however, electrospinning of 20% PCL solution produced more uniform scaffolds than 15% PCL solution, with an average fibre diameter of 3.05±1.73 μm and 5.10±0.66 μm for 15 and 20% PCL scaffolds respectively. These findings are consistent with those of Gu and Ren (2005) who used the same binary solvent system with the same v/v ratio to electrospin amorphous PLA (PDLA) at solution concentrations of 3, 5 and 7% w/v. Their results showed that polymer concentration plays a significant role in determining the fibre diameter. Fibres with more uniform diameter and lower variations in diameter were obtained when higher concentrations and higher applied voltage were used. Therefore, 20% PCL solution was chosen for the core part of coaxial electrospinning.

As for the shell solution, the same binary solvent system was used for several reasons including reduced viscosity compared to chloroform alone as well as enhanced conductivity and dielectric constant due to the presence of acetone which consequently enhanced the electrospinning process. Furthermore, using the same solvent system for the core and shell solutions will help reduce the interfacial tension between the two solutions as mentioned in the literature, which should favour producing uniform core-shell fibres (Malherbe et al., 2010; Sun et al., 2003; Yu et al., 2004). SEM results showed that the PLA/HA2 scaffolds produced with chloroform/acetone solvent system (Figure 6.4) had significantly smaller fibre diameter compared to the scaffolds produced from dissolving PLA/HA2 in chloroform alone (6.82±3.86 μm vs. 18.43±7.31μm respectively). According to Hsu and Shivkumar (2004), the bending instability of electrospinning jet increases with higher dielectric constant, which leads to reduced fibre diameter due to increased jet path in addition to increased deposition area of the fibres. It was also noticed that due to the reduction in fibre diameter, HA

agglomerations were increased along the fibre and HA particles were shown to be closer to the fibre surface which increased the surface roughness compared to the larger fibres produced with chloroform alone (Figure 5.1e), where the polymer had higher coverage to HA particles and the fibre surfaces were smoother. Increased HA protuberances might be useful for increasing the bioactivity rate as well as enhancing the cell attachments.

The flow rate ratio of core and shell solutions affects the uniformity and stability of the core jet flow (Khajavi and Abbasipour, 2012). Several studies have found that the core and shell layer dimensions can be tailored by keeping one flow rate constant while changing the other one (Huang et al., 2015; Nguyen et al., 2011; Zhang et al., 2006). In order to optimise fibre morphology in this study, core and shell solutions were fed at 1:3, 2:3 and 3:3 flow rate ratios. At flow rate ratio of 1:3, scaffolds exhibited beads on a string morphology as shown in Figure 6.5a, while coaxial electrospinning at flow rates ratios of 2:3 and 3:3 yielded non-woven bead-free fibres with average fibre diameter of 5.91± 3.47μm and 6.06±2.89μm, respectively (Figure 6.5b and c). The fibres surface of both coaxial scaffolds also exhibited nanoporous structure which resulted from solvents volatility as discussed in Chapter 5. Co-electrospun fibres at 3:3 flow rate ratio, however, exhibited more homogenous size distribution compared to fibre of 2:3 flow rate ratio as shown in Figure 6.6. Wang et al. (2012) examined electrospun core and shell polyacrylonitrile (PAN) - poly[bis(*p*-methylphenoxy)]phosphazene (PMPPh) fibre morphology at different core:shell flow rate ratios including 3:1, 2:1, 1:1, 1:2, and 1:3 and found that core:shell flow rate ratio of 1:1 produced more uniform morphology with decreased fibre size compared to the other ratios. Gonçalves et al. (2015), on the other hand, co-electrospun poly(vinyl alcohol) (PVA)-PLA fibres at core:shell flow rate ratios of 1:1, 1:2 and 1:4 and found that core and shell fibres obtained with the same flow rate for both solutions were not smooth with heterogeneous size distribution, while electrospinning at flow rate ratio of 1:4 produced larger fibre diameters, but with more homogeneous distribution. It should be noted that the viscosities of core and shell solutions play a decisive role in controlling fibre diameter as well as the core and shell thickness in coaxial electrospinning process (Kaerkitcha et al., 2017). Thus, polymer concentration, filler type and filler concentration are all important factors that

can significantly alter fibre uniformity and control layers dimensions besides the flow rate ratio between the core and shell solutions.

Control samples had reduced fibre diameter and smoother surface compared to HA-containing scaffolds (4.42 ±1.14μm) which is expected due to the particle size of HA as discussed in Chapter 4.

Formation of twin (or grooved) fibres were noticed in both control and HA containing samples. These grooved fibres are characterised with a flat, dumbbell shape cross section instead of the regular circular cross section of electrospun fibres (Figure 6.8b). Different mechanisms were proposed to explain the formation of double fibres. According to Koombhongse et al. (2001), the atmospheric pressure tends to collapse the thin glassy skin initially formed on the liquid jet during solvent evaporation, giving a flat, ribbon like structure. In other words, solvent vaporization lead to the rapid formation of a thin, elastic glassy shell. When solvent evaporation from the core proceeds, the core contracts and pulls radially inward on the shell, resulting in a compressive hoop stress in the shell. On the other hand, Huang et al. (2012) produced grooved fibres using 10% polystyrene in 2:1 v/v acetone: DMF mixture. They attributed the formation of the grooves to the rapid evaporation of acetone leading to void formation in the acetone rich areas at the initial spinning surface which elongates as the jet stretches thereby forming the grooves (Figure 6.26). While voids on electrospun fibres might possibly play a part in the formation of the grooves, it seems unlikely, however, that the voids stretching can results in groove formation along the entire length of the fibres.

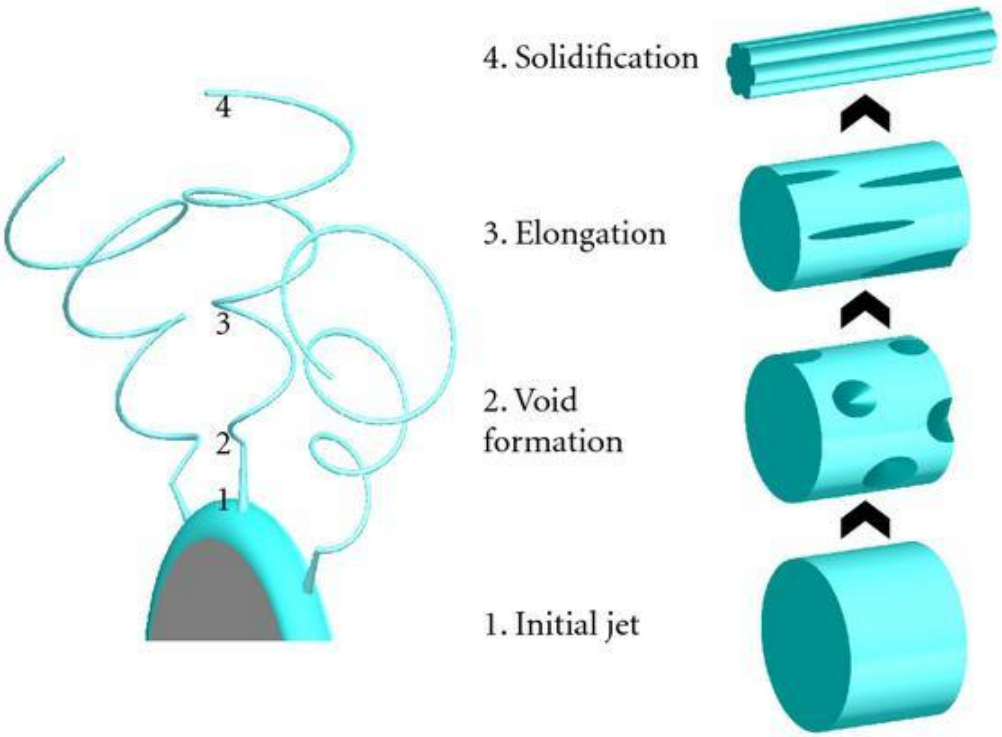

Figure 6.26 Schematic illustration of groove formation mechanism (from Huang et al., 2012)

Liu et al. (2015) studied the effect of solvent system on the structure of electrospun polystyrene fibres. Using a single solvent, fibres with surface structure such as wrinkled beads, smooth fibres and porous fibres were obtained. However, single groove and multiple grooves on the fibres surface were only obtained when binary solvent systems were used. Their results indicated that there must be sufficient differences in the evaporation rate between the two solvents to initiate groove formation. Finally, another possible reason for double fibres formation beside the solvent effect is the high flow rate of core solution which results in decreasing the thickness of the shell layer. As the core flow rate increases, the inability of the shell thin wall to support the increasing fibre diameter eventually causes it to collapse and form flat and grooved fibres.

Theoretically, three different types of fibres can be possibly produced when using coaxial electrospinning: well-defined core and shell fibres which would be the ideal result; solid fibres that is made by either the core or shell solution; or compound fibres resulting from mixture of the core-shell solutions (Li et al.,

2014). The flow rate of the core and shell solutions directly controls the diameter and structure of the core-shell fibres, especially the thickness of the two layers (Elahi et al., 2013). Scaffolds were freeze-fractured (using liquid nitrogen) to determine if the fibres exhibited coaxial geometry. This method has been reported in several studies, where they used it to examine the cross sectional area of the coaxial fibres and determine the geometry of the constituent layers, thus providing a supporting evidence to presence of core and shell structure besides TEM and other imaging techniques. SEM images of fractured (3:3) coaxial fibres with HA in the outer layer (Figure 6.8) did not show any exposed core layer or distinct borders separating between the core and shell layers as some studies suggest (Horner et al., 2016; Wang et al., 2015; Xu et al., 2013). However, it did show very few hollow fibres as shown in Figure 6.8a. Li et al. (2014) attributed the projection of the core from the shell to the increase of drug content within the core or sheath layers which makes the nanofibers brittle and easier to fracture, and thus the core projects a little from the shell after breaking. In this study, the core was composed of PCL without any drug content and despite the high HA content in the shell layer, the scaffolds remained hard to break and no projection of PCL (core layer) were noticed in the broken fibres. However, the present findings seem to be consistent with Yu et al. (2011) research findings which showed no significant variation between the core and shell layers under field emission SEM (FESEM) even though TEM results have clearly demonstrated that the fibres have coaxial geometry (Figure 6.27).

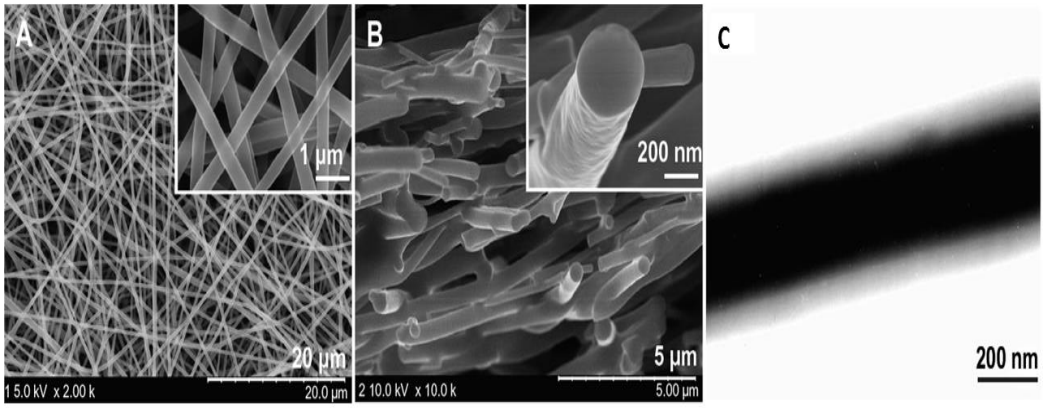

Figure 6.27 Characterisation of the electrospun PVP/acyclovir-PVP/sucralose/ sodium dodecyl sulfate (SDS) core-shell nanofibers with: (A) FESEM images of nanofibre surfaces, (B) FESEM images of fibres cross-sections, and (C) TEM image of the fibre showing the core and shell structure (From Yu et al., 2011)

SEM images of the fractured fibres in the current study, however, demonstrated distinctively different textures between the thin outer layer of the fibres, showing nanoporous, non-homogenous rough surface which might be considered as the shell layer, and the thick inner layer of the fibres which was smooth and solid and constitutes around 90% of the whole fibre diameter.

Cross-sectional specimens of the HA-containing coaxial fibres (3:3) produced using an ultramicrotome confirmed the above observations where they showed core and shell structured fibres with thin shell layer ranging from 300 to 830nm in thickness. Micro-HA particles were embedded in the shell layer of the coaxial fibres. However, due to the large size of the HA particle (d_{50}= 3.59µm) compared to the shell thickness, the embedded particles were either protruding from the surface of the fibres, or into the core layer causing non-uniformity in the coaxial structure of the fibres. Because the fibres were randomly oriented, both longitudinal and transverse sections of the coaxial fibres were visible in the SEM images as shown in Figure 6.9. Interestingly, the longitudinal fibres have shown small gaps in the core layer which usually occurs when using either very low core:shell flow rate ratio or low polymer concentration (in the core), leading to insufficient inner polymer mass to form a continuous core (Qu et al., 2013; Tong et al., 2012). However, in this study, 20% w/v PCL concentration solution was used (relatively high) and 3:3 core:shell ratio were used, so neither conditions was not applied.

Despite using the same solvent system for both solutions, it could be possible that PCL solution had higher conductivity compared to PLA/HA2 solution, which causes the electric field produced during coaxial electrospinning to pull the core faster than is supplied by the syringe pump. This causes a discontinuous flow of the core solution which leads to a core-shell structure that has missing core polymer at certain points (Yu et al., 2004).

Cross-sections of control and HA-containing coaxial fibres (2:3 and 3:3 core:shell flow rate ratios) embedded in Epon resin were also examined with TEM. Fibres of all scaffolds have clearly shown the core (dark area) and shell (light area) configuration with no mixing between the layers. Fibres of both control and HA-containing scaffolds had non-uniform shell thickness or non-concentric core and shell structure which can be attributed to the whipping motion of the fibres during electrospinning in addition to the effect of gravitational force on the compound Taylor cone stability which also determines the resultant fibre quality. Some fibres also had discontinuous shell layers which might have resulted from needle blockage during electrospinning. However, control fibres electrospun at 2:3 core:shell had relatively thicker shell than 3:3 scaffolds (~600nm-1.5μm vs ~400nm-1μm). Few single component (PLA) fibres were also observed in both control and HA-containing HA-scaffolds. Most of the previous studies have only focused on the core-shell portion of the fibres (Doan et al., 2016; Horner et al., 2016; Huang et al., 2015; Wang et al., 2012; Zhang et al., 2004) while, as mentioned earlier, fibres made by either the core or shell solution are also commonly produced during coaxial electrospinning. Reznik et al. (2006) recognised the fact that core-shell droplet at the tip of the needle does not necessarily result in core solution entrainment and not all fibres possess core-shell structure with coaxial electrospinning process. Therefore, they proposed to use a protruded inner needle to facilitate core solution entrainment, though no experimental work was done to support this idea. In HA-containing scaffolds, HA appeared in TEM as white gaps of the same size and shape as HA particles (Figure 3.1b) filled with black fragments. It seems likely that sample cutting with the ultramicrotome has broken up the HA to its original nano particles. The non-uniformity of shell layer had increased in HA-containing fibres due to HA protuberances and the thickness was ranged from ~700 nm to 2.3μm for fibres with 2:3 flow rate ratio vs ~200 to 1.8μm for fibres 3:3 flow rate ratio. As a result,

HA-containing fibres electrospun at 2:3 core:shell flow rate ratio had higher encapsulation of HA particles compared to fibres with 3:3 flow rate ratio which showed increased HA protuberances on the surface of the fibres.

Finally, control and HA-containing coaxial fibres with FTIC labelled PLA/HA2 shell phase and rhodamine B labelled PCL core phase were used to visualise the incorporation of the core and shell phases in individual fibres (Figures 6.15 to 6.18). The green fluorescence from FITC and red fluorescence from rhodamine B suggested that the core and shell phases co-existed in the co-electrospun fibres and the core phase was continuous within the fibres. However, the boundaries between the two layers were hard to distinguish for both 2:3 and 3:3 flow rate scaffolds and no differences were noticed in the scaffolds with increased the core flow rate. Similar results were obtained by Ji et al. (2010) and Vysloužilová et al. (2017) as their confocal microscopy images showed the core and shell phases, but without distinct boundaries between the layers. However, Blackstone et al. (2014) obtained confocal microscopy images for their core and shell PCL-gelatin scaffolds with clear boundaries between the layers at different core:shell flow rate ratios, but they did not report the fluorescence labelling method or the test specifications. For the HA-containing scaffolds, the HA particles on the shell layer were surprisingly observed on the red channel which is specified for the core phase. By comparing these findings with the resin embedded samples (Figures 6.9 and 6.10), HA particles were protruding into the core layer despite being attached to the shell due to their large particle size. Thus, it could be possible that they appeared on the red channel along with core component due to those internal protuberances which caused them mixed with the rhodamine B tagged PCL, while HA parts that are protruding outside the fibres appeared more intensely in the green channel.

3D images of the control and HA-containing coaxial scaffolds were constructed using Imaris software and z-stacks images from the confocal microscope. Although this method is helpful to show specific features of the scaffolds such as fibre fusion or cell distribution and nuclei (in cultured electrospun scaffolds), it was not an accurate method to determine the structure of the coaxial fibres and whether the shell is completely covering the core or not as it depends on the reconstruction parameters, such as the threshold of the green (FITC) and red (rhodamine B)

channels. Thus, the results can be very subjective depending on the operator and the sample tested. Figure 6.28 shows 3D images of the control and HA-containing scaffolds reconstructed by Imaris software using two different threshold points for the red and green channels.

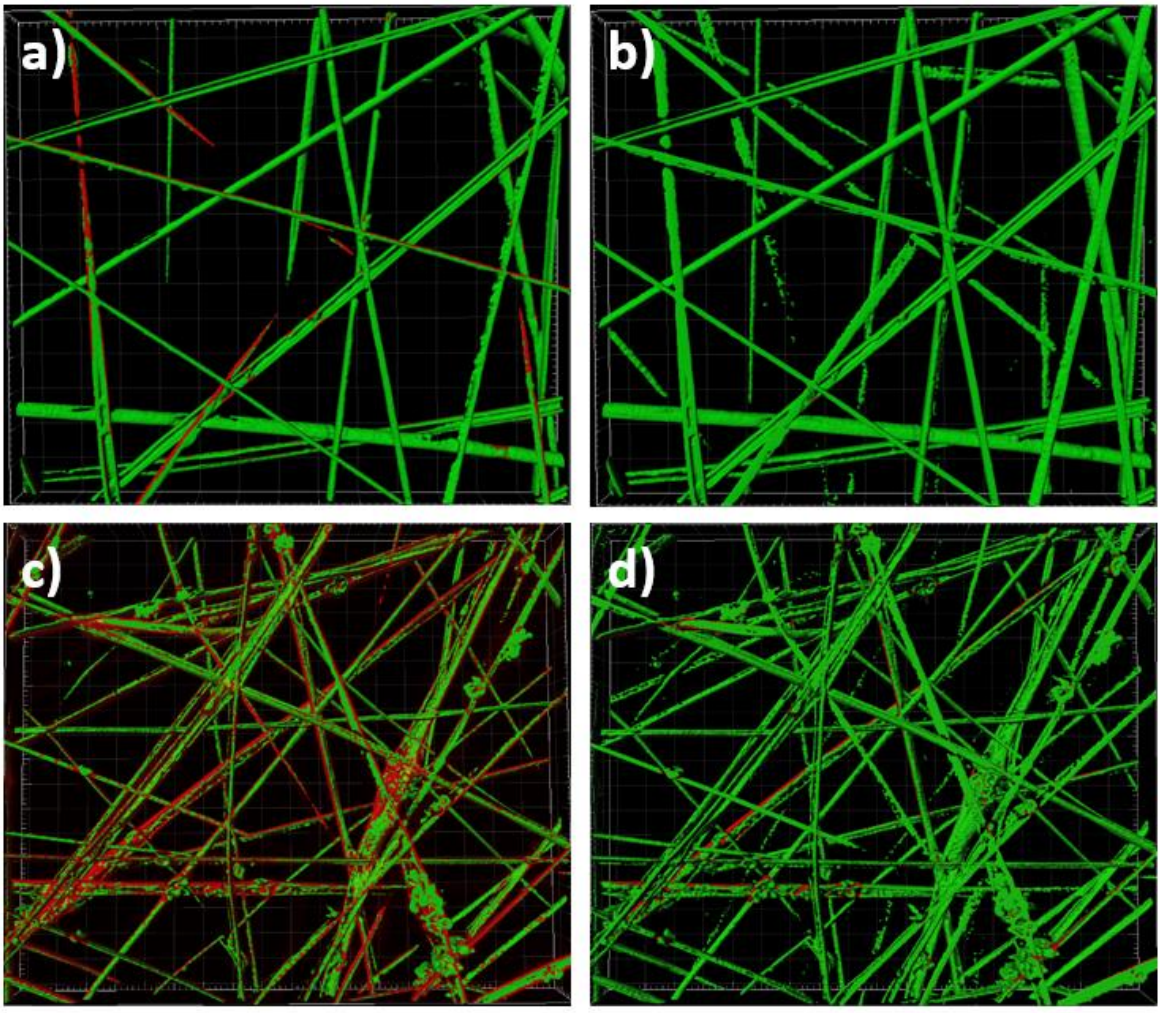

Figure 6.28 3D images of (a) control and (c) HA-containing coaxial scaffolds reconstructed with Imaris software and z-stacks from confocal microscopy. (b) and (d) are the same images as (a) and (b) but with different threshold points for the red and green channels

Natural bone has a 3D architecture with multi-scale porosity ranging from nanoscale to submicro and microscale, which provides a microenvironment for cell and tissue growth. This multi-scale structure not only provides a large number of binding sites for cell membrane receptors, but also determines and maintains cell functionality. Thus, an ideal bone scaffold should match the internal structure of

natural bone in addition to the external shape and composition (Gao et al., 2017). The necessity for porous structures in bone regeneration has been demonstrated by Kuboki et al. (1998) using a rat ectopic model and solid and porous particles of hydroxyapatite for BMP-2 delivery. No new bone was formed on the solid particles, while in the porous scaffolds direct osteogenesis occurred. In this study, the porosity of core and shell PCL-PLA/HA2 were evaluated using three common methods for porosity measurements: gravimetric method, mercury porosimetry, and image analysis using DiameterJ (ImageJ plugin). However, there was a significant variation between the results for the three methods used. Those variations are believed to have resulted from the way each method analyses the porosity of the samples and the appropriateness of those methods for electrospun scaffolds in specific. The gravimetric method is a simple technique that depends on the bulk and apparent density of the sample to calculate the total porosity. For coaxial electrospun scaffolds, however, the bulk density cannot be accurately calculated because the fibres are in core and shell form and the exact percentage of each layer in the whole scaffold is unknown. Thus, bulk density was roughly estimated to 1.30 g cm^{-3}. Another issue related with using the gravimetric method is measuring the thickness of the electrospun scaffolds. The high porosity and fragility of electrospun scaffolds made them compressible when they experience a load. Thus, the micrometer screw gauge may lead to a systematic error in the readings due to sample compression. Affandi et al. (2010) compared the difference between the thickness measured using a white light profilometer and that obtained using a micrometer for electrospun Polyacrylonitrile and Nylon scaffolds. Their results showed that the thickness measured using the white light profilometer was significantly larger than that measured from the micrometer. Thickness measurements made by the micrometer was less than half that obtained from the profilometer in some cases with a difference of more than 10 μm.

Mercury porosimetry, on the other hand, is a well-known technique that is often used to study the porosity and pore size of porous structures and relies mainly on the pressure applied to force the mercury to penetrate into the pores areas of the samples. Thus, a relationship can be found between the applied pressure and the size of the pores. Although mercury porosimetry has been has been largely used for the characterisation of nanofibres up to now (Hekmati et al., 2014; Keun Kwon et al., 2005; Kim et al., 2003), the applicability of this technique to electrospun

scaffolds is still questionable due to two limiting factors which can largely affect the accuracy of the obtained results: first, the Washburn equation (Eq. 3.4) assumes that all pores are cylindrical in shape, which is not the case in electrospun scaffolds. SEM images have clearly showed that the geometry of electrospun scaffolds pores are not cylindrical, but rather polygonal and highly interconnected. Therefore, the values calculated by the conversion of pressure to pore diameter in the Washburn equation cannot be considered as exact pore diameters (Lowery et al., 2010). Additionally, mercury porosimetry cannot measure the porosity of closed pores as mercury does not intrude into them. de With and Glass (1997) have mentioned that high accuracy of mercury porosimetry can only be reached if (nearly) spherical pores are present. The second limiting factor is related to the high applied pressure on the mercury to intrude into the scaffold pores. Electrospun scaffolds can deformed easily, even under low pressure of mercury because they are soft materials. Thus, the shapes, locations, sizes and volume of the pores within the fibres might change too, leading to erroneous conclusions regarding pores size and volume as well as the total porosity percentage. In this study, the mercury porosimetry analysis were done according to University of Strathclyde instrument's protocol and the pressure was applied in two stages: the low pressure intrusion stage, typically at 1-50 psi (6.9-344.7 kPa), where the mercury fills the large vacancies and any gap within the material folds/layers (voids in the mm range). At the high pressure stage, up to 40,000 psi (275.8 MPa), the mercury will intrude the real porosity (in the range of micro- to nano-size) and this is when measurements are taken. Thus, it is highly possible that pores were deformed or damaged during testing, and that produced low porosity percentage. Pham et al. (2006) reported no significant differences between the results of gravimetric and mercury porosimetry methods when they measured the porosity of electrospun PCL microfibers (4-10μm diameter) using a maximum of 50 psi (344.7 kPa) pressure on the scaffolds. On the other hand, Keun Kwon et al. (2005) obtained lower porosity results from mercury porosimetry (56–63%) compared to gravimetric method (69–76%) when they applied 14.5 to 30,000 psi (96.5 kPa-20.6 MPa) pressure. It should also be noted that the pores of electrospun scaffolds are not solid as those of hydrogels or ceramics, so they might expand due to fibre flexibility during mercury intrusion (Rnjak-Kovacina and Weiss, 2011; Rutledge et al., 2009; Semnani, 2017; Širc et al., 2012).

Finally, image analysis techniques have also been used to measure pore characteristics due to their convenience to detect individual pores of nonwoven fibres. DiameterJ is an ImageJ plugin that was developed to calculate the average fibre diameter as well as porosity and pore size of porous scaffolds by using images of the scaffold as input. This tool, just like any other image analysis technique, is based on image processing, but it is more rapid, flexible and an easy-to-use method compared to other techniques. To analyse an image, DiameterJ uses two-step process: SEM images are first segmented into a binary images using sixteen default segmentation algorithms available in ImageJ/Fiji. Then, the segmented images are analysed using the following algorithms: super pixel diameter approach which gives a single fibre diameter for each image without providing a histogram, or fibre diameter histogram algorithm which determines the fibre diameter at every pixel along the fibre lengths to produce a histogram of fibre diameters. Despite the simplicity and the speed of DiameterJ (an image can be analysed within 60 seconds), it has several major drawbacks that are generally common with other image analysis techniques. Firstly, the initial segmentation of the image is a critical step which can affects the results dramatically. The global thresholding scheme uses a single constant threshold to segment the image. Thus, it is very sensitive to any inhomogeneity in the grey level distribution of objects and background pixels and can lead to high noise level. This is particularly true in the scaffold SEMs as the lower fibres appear darker than the surface fibres. Pre-processing of SEM images might therefore be necessary to reduce or remove the noise and restore a suitable image before segmentation (Semnani, 2017). Figure 6.29 shows SEM image of coaxial PCL-PLA/HA2 with its segmentation results from DiameterJ, while Figure 6.30 shows the differences in DiameterJ porosity calculations for different segmentations of the same SEM image.

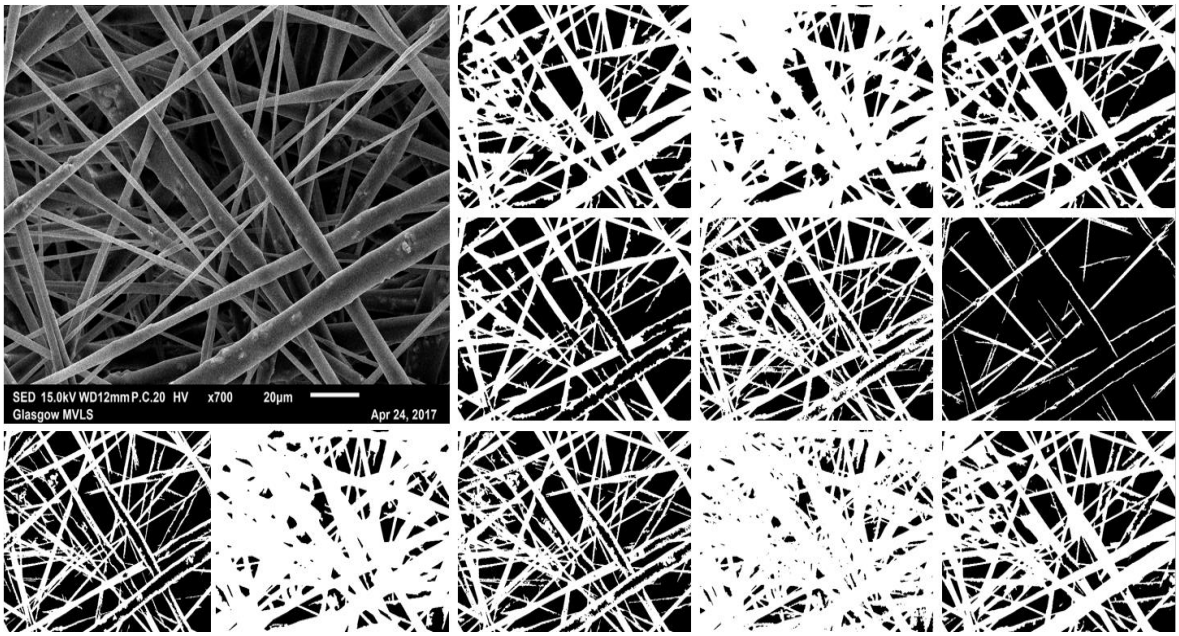

Figure 6.29 SEM image of core-shell PCL-PLA/HA2 fibres along with segmentation results obtained from DiameterJ

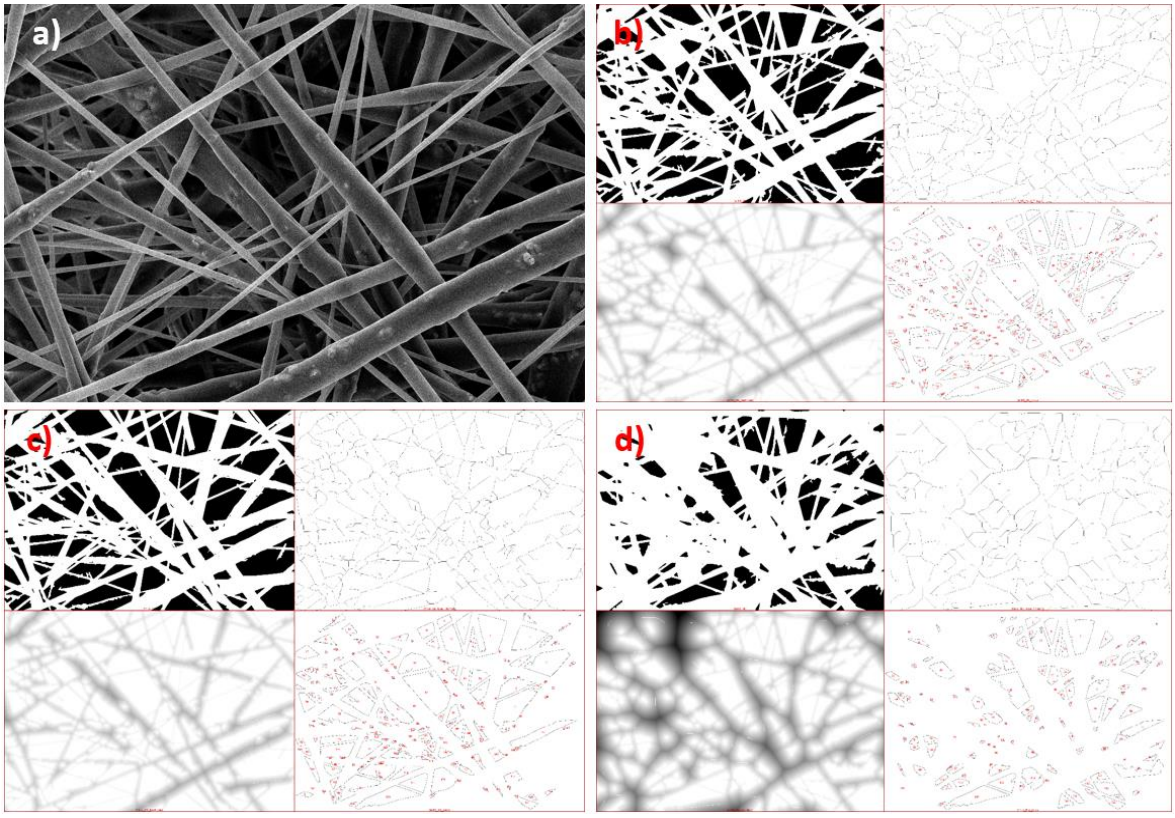

Figure 6.30 Comparison of porosity calculations for different segmentations using DiameterJ (a) original SEM image (b), (c), and (d) montage results of DiameterJ for three different segmentations showing mesh holes measurements

On the other hand, image analysis methods, in general, can only analyse the upper layers of electrospun fibres, and this analysis cannot give the global information of whole scaffolds pore size as it ignores the deeper layers and consider them as a background (Hekmati et al., 2014). Ghasemi-Mobarakeh et al. (2007) suggested using different thresholds on the same image in order to analyse various surface layers of nanofibres mat. Also, to obtain higher accuracy with DiameterJ, fibres should not be smaller than 10 pixels or greater than 10% of the smallest dimension of the image because that can produce errors above 10% (Hotaling et al., 2015).

Given the above discussion, the gravimetric method seems to be the most reliable method compared to mercury porosimetry and DiameterJ for measuring the total porosity of electrospun scaffolds, while pore size can be estimated by measuring individual pores from SEM images.

FTIR spectra of coaxial scaffolds of both 2:3 and 3:3 flow rate ratios showed both characteristics peaks of electrospun PCL and PLA-HA2 fibres which confirm the presence of the core and shell components in the scaffolds. Neither coaxial scaffold spectra showed any new peaks which would demonstrate chemical reactions occurring between the layers of the scaffold. These results agree with the findings of Qian et al. (2014), Huang et al. (2015), Wei et al. (2016), and Li et al. (2017), in which they showed that FTIR spectra of coaxial scaffolds contained mixed peaks of both core and shell layers. However, the findings of Park (2010) and Gonçalves et al. (2015) showed that FTIR spectra of coaxial scaffolds were similar to the spectra of pure shell layer with no additional peaks from the core layer. As mentioned in the Discussion of Chapter 5, the penetration depth of the attenuated total reflection FTIR (ATR FTIR) used in this study typically ranges between 0.5 and 5 μm. Therefore, a combination of core and shell peaks is expected since the penetration depth is high compared to the fibre diameter (~6 μm). The intensity of PCL peaks at 1722,1418,and 1294 cm^{-1} were lower in both coaxial scaffolds compared to pure PCL scaffolds, while the peaks at 1470 and 1164 cm^{-1} disappeared in the coaxial scaffolds which could be because the PCL is enveloped by the PLA-HA2 layer (Li et al., 2017). However, the intensity of PCL peaks were higher in the scaffolds with flow rate ratio of 3:3 compared to 2:3 scaffolds, which could be due to the increased core flow rate in the scaffolds with the higher core:shell flow ratio.

The mechanical properties of core and shell fibres are important for their successful applications in tissue engineering. The tensile properties of the core and shell components in addition to the coaxial scaffolds are shown in Table 6.3. The electrospun PCL scaffolds gave a characteristic response for elastomeric materials, with a low Young's modulus of 4.92±0.77 MPa and high elongation at break of over 300%. Similar mechanical behaviour of electrospun PCL scaffolds were reported by Croisier et al. (2012) and Qian et al. (2014).

Since changing the solvent system for PLA/HA2 scaffolds had a significant effect in reducing the fibre diameter, the mechanical properties of PLA/HA2 scaffolds made with chloroform/acetone solvent system were evaluated and compared to those made using chloroform alone. Scaffolds made with chloroform/acetone exhibited higher tensile modulus (59.54±9.66 MPa) compared to scaffolds made with chloroform alone (37.73±6.81 MPa), while the ultimate tensile strength was significantly reduced (0.263±0.055 MPa vs 0.546±0.061 MPa). There has been considerable debate in the literature about the correlation between fibre diameter and the mechanical properties of the electrospun scaffolds. Huang et al. (2004), Wong et al. (2008), Linh et al. (2010), and Doustgani (2016) reported that scaffolds with lower fibre diameter gave higher stiffness and tensile strength but lower ductility, due to higher crystallinity and orientation. In contrast, McManus et al. (2006) showed that the values of tensile modulus and strength were increasing as fibre diameter increased. Lastly, Butcher et al. (2017) suggested that there are other aspects of the electrospun scaffold morphology that have greater significance to the mechanical properties than fibre diameter, such as pore size and the interaction between fibres. So far, however, there has been little discussion about the impact of reducing fibre diameter on electrospun composites with high content of micro fillers. In this study, reducing the fibre diameter of 15% PLA scaffolds with 20% micro-HA increased the Young's modulus and reduced the tensile strength. It seems possible that the reduction in tensile strength is due to the increased number of HA protuberances on the surface of the fibres when the fibre diameter was reduced which might be due to the large particle size of HA used (d_{50}= 3.59μm) or due to the formation of HA aggregates along the fibres. Thus, the lack of adequate polymer matrix to immobilize the HA particles within the fibres and the heterogeneous dispersion of filler along the fibres decreases the interfacial bonding between the polymer and filler in addition to increasing

the stress concentration points within the scaffold which ultimately reduced the tensile strength.

For coaxial electrospun scaffolds, tensile testing showed that the mechanical properties of the core and shell structured mats were located intermediate between the features of the core and shell monolithic fibres. Coaxial PCL-PLA/HA2 scaffolds electrospun at both 2:3 and 3:3 core:shell flow rate ratios had increased tensile strength and elongation compared with PLA/HA2 alone, while the stiffness of the coaxial scaffolds has decreased significantly. The reduction in Young's modulus for coaxial scaffolds could have resulted from the non-uniform distribution of core solution along the fibres due to the HA particles and the presence of small voids in the core as shown in Figure 6.9. Additionally, increasing the core flow rate further increased the mechanical properties which might be attributed to the enhanced fibre diameter homogeneity in the scaffolds electrospun at 3:3 core:shell flow rate ratio compared to scaffolds of 2:3 flow rate ratio. On the other hand, control coaxial scaffolds without HA exhibited significantly higher ductility, strength and stiffness than HA containing scaffolds which was expected due to the brittle nature of HA. However, the ductility of control scaffolds was significantly increased compared to 15% PLA scaffolds made with chloroform alone as a solvent while stiffness and strength values were slightly reduced. The results of both control and HA containing coaxial samples suggest that the mechanical properties of the coaxial scaffolds was largely influenced by the mechanical properties of the core layer, owing to the fact that it constitutes the largest part of the fibre, as shown in SEM and TEM results. In fact, Nguyen et al. (2011), Huang et al. (2015) and Horner et al. (2016) obtained different mechanical properties from their coaxial electrospun scaffolds by changing the flow rate ratio between the core and shell which consequently changed the dimensions of the two layers, while Chen et al. (2010) demonstrated that the mechanical properties of their core and shell thermoplastic polyurethane (TPU)-collagen can be modulated by changing the TPU (core) concentration in the coaxial system. Thus, tailored mechanical properties can be obtained by controlling the thickness and structure of the core and shell layers of the fibres.

Numerous in vitro and in vivo studies have demonstrated that bone morphogenetic protein-2 (BMP-2) can induce osteogenic differentiation of mesenchymal stem

cells (MSCs) (de Guzman et al., 2013; Krishnan et al., 2017). However, there are a number of factors that influence the osteoinductivity of BMPs in general including: BMP concentration, the properties of the carrier, and the effect of local and systemic growth factors and hormones (Groeneveld and Burger, 2000). Even though BMPs can induce bone formation when added as a solution without being bounded to a carrier (Wozney et al., 1990), the dose required for inducing endochondral bone formation can be dramatically reduced if BMP is combined with an appropriate carrier (Groeneveld and Burger, 2000; Urist et al., 1984). An ideal carrier should prevent the degradation of BMPs while preserving their bioactivity and promote a sustained release in a controlled manner to promote new bone formation at the defect site (Sheikh et al., 2015). Thus, electrospun scaffolds have been used as BMP carriers due to their high surface area which allows higher protein absorption and encapsulation efficiency, their ability to modulate release and their ease of operation (Agarwal et al., 2008; Tao et al., 2017).

In this study, the release profile of BMP-2 from the PCL-PLA (control) and PCL-PLA/HA2 scaffold in vitro was determined using ELISA (Figure 6.23). A burst release of about 8.8% of the BMP-2 was observed in both scaffolds during the first 24 hours. The release rate was subsequently decreased to become more uniform with about 1.2-1.6% released every 24 hours, and approximately 12.8% and 13.6% of the total BMP-2 was released from the control and HA-containing scaffolds respectively after 4 days. Talal et al. (2009) measured the absorption and release of fetal calf serum and bovine serum albumin proteins from trilayer PLA and HA-PLA composite membranes reinforced with PLA fibres for the same time point used in this study using a BioRad assay. Their membranes were moulded using a hand lay-up procedure. Their results revealed that HA-containing composites exhibited significant increase in the total protein absorption compared to those without HA. HA-containing composites also allowed a more gradual and sustained release of protein for periods of up to 96h, suggesting that the incorporation of HA into these membranes was the key factor for improved protein kinetics and membrane permeability. However, in this study, no significant difference were noticed in the protein release behaviour between control scaffolds and HA-controlling scaffolds. In fact, both types of scaffolds had the same release kinetics and retained more than 85% of BMP-2 after 96 hours, while in Talal et al. (2009), HA and non-HA membranes released more than 90% of the protein after 96h. This indicates that

for the tested time points, the manufacturing technique of protein carrier had a greater effect on the protein release behaviour than HA incorporation. While these findings suggest that the produced coaxial scaffolds can be used as an efficient carrier for the sustained release of BMP-2, which can ultimately effect osteogenic differentiation and bone regeneration, the release behaviour should be measured over longer time periods in order to define the exact release mechanism and determine the influence of HA incorporation in the shell layer.

The interaction between cells and their environment plays a crucial role in determining cell function. The major advantage of electrospun fibres is that they favour cell attachment due to their higher surface area which help absorb proteins and promoting binding sites (Zafar et al., 2016). Cell adhesion is a dynamic process that results from specific interactions between cell surface molecules and their appropriate ligands. Adhesion occurs between adjacent cells (cell-cell adhesion) and between cells and the extracellular matrix (ECM) or substrate (cell-matrix adhesion or cell-substrate adhesion) (Lotfi et al., 2013). Cell adhesion on control and HA-containing coaxial scaffolds and the morphology of the adhered cells were observed using SEM (Figures 6.24 and 6.25). MSCs adhered on the surfaces of both scaffolds, and as the culture time was increased, the number of cells increased and their morphology were changed from round or spindle-shaped to well-spread with filopodia and lamellipodia-like extensions. Cells were able to adhere and spread on multiple fibres and at different depths from the surface, but mostly extending along a preferred fibre axis (Figure 6.24 e, l and o). At day 14, the cells and fibres started to form an interconnected network. The presence of nanopores on the surface of fibres facilitated cell adhesion, as shown in Figure 6.25f and i where cell filopodia were seen to be in direct contact with the surface nanopores. Incorporation of HA did not affect cell attachment and spreading significantly. However, cell spreading was slightly lower in HA-containing scaffolds at day 21 of culture which might either be attributed to the increased fibre diameter and non-uniformity compared to control scaffolds (Chen et al., 2007; Kurokawa et al., 2017) or due to osteogenic differentiation of MSCs on HA-containing scaffolds.

6.5 Conclusions

Changing the solvent system of the electrospinning solutions while keeping the polymer/ polymer-filler concentration constant affected the stability of the Taylor cone during electrospinning and led to alteration in the scaffolds morphology and mechanical properties.

Core and shell PCL-PLA/HA2 scaffolds were successfully produced using coaxial electrospinning. The uniformity of the produced fibres were depended on the flow rate ratio between the core and shell solutions, with the highest fibre uniformity achieved at a flow rate ratio of 3:3. However, coaxial electrospinning at both 2:3 and 3:3 core:shell flow rates have produced fibres with core and shell configuration with few fibres containing only PLA without the core. TEM of HA-containing scaffolds showed that increasing the core flow rate had also forced HA particles to protrude on to the surface of the fibres which could enhance the bioactivity of the scaffolds. Incorporation of HA within the shell of coaxial fibres had increased fibre and shell thickness and non-uniformity.

Electrospinning of core and shell PCL-PLA/HA2 fibres has significantly enhanced the tensile strength and elongation at break compared to PLA/HA2 fibres produced by single electrospinning, while the toughness of the scaffolds was significantly reduced. The mechanical properties were largely affected by the core size within the fibres.

Control and HA-containing coaxial fibres electrospun at 3:3 core:shell flow rate exhibited slow and sustained release of BMP-2 over 96 hours with only small variations between the two scaffold types, and supported cell adhesion and spreading over 21 days of culture.

Chapter 7- 3D Coaxial Electrospun Scaffolds

7.1 Introduction

Modification of an electrospinning collector is a common method to produce 3D electrospun scaffolds for tissue engineering applications. Recently, tubular electrospun scaffolds have found increasing use in vascular and neural tissue engineering as well as growth factor delivery due to their uniform thickness and mechanical strength (Brown et al., 2012; Naito et al., 2011). For example, Thomas et al. (2009) produced a trilayer tubular electrospun scaffold of 20 cm length and 4 mm inner diameter which mimics the complex matrix structure of native arteries using sequential electrospinning of blends of polydioxanone (PDO) and proteins onto a 4 mm diameter rod. On the other hand, Subramanian et al. (2011) fabricated uniaxially aligned tubular PLGA scaffolds for neural tissue engineering using a grounded rotating mandrel (3 mm in diameter) with small insulating gaps which behaved as an auxillary electrode to allow the deposition of longitudinally oriented fibres onto the insulating portion of the rod.

In this chapter, electrospun tubular coaxial scaffolds have been produced for bone tissue applications using a rotating needle collector. The effect of the collector on fibre diameter, alignment and mechanical properties have been evaluated, and the impact of HA incorporation on bioactivity, degradation profile, and mechanical properties was also tested over 12 weeks.

7.2 Materials and methods

To produce the tubular scaffolds, core and shell solutions (20% PCL and 15%PLA with 20% HA2 respectively) were dissolved in 2:1 mixture of chloroform and acetone following the procedure described in section 3.2.2.1. Solutions were then loaded separately into 5 mL plastic syringes and co-electrospun into the rotating needle collector as described in section 3.2.3 with PCL as the core and PLA with or without HA as the outer shell. Control (with no HA) and HA-containing scaffolds were co-electrospun on G16 and G21 stainless steel needles for 8-10 minutes and then left to dry for 10-15 minutes before extraction from the collector. The morphology of the electrospun tubes were observed using SEM and fibre orientation was measured using the SEM images and MATLAB software, while the total porosity of the scaffolds was calculated using the gravimetric method. In order to evaluate and compare the dissolution rate and bioactivity among the control and HA-containing scaffolds, samples were immersed in 85 mL of either Phosphate Buffered Saline (PBS) or SBF at 37°C for 12 weeks. PBS solution of pH 7.4 was prepared by dissolving PBS tablets (Gibco™) in distilled water (1 tablet per 500mL). The solutions were changed every 7 days. Six samples of each scaffold type (n=6) were extracted after 4, 8 and 12 weeks to measure their water uptake and weight loss following the method described in section 3.3.7.2. Apatite formation on the surface of fibres after each time point were detected using EDX while the mechanical properties were evaluated using tensile testing as described in section 3.3.6. Tensile properties were tested in the axial direction only due to the small diameters of the scaffolds.

7.3 Results

7.3.1 SEM and structures of the scaffolds

Tubular PCL-PLA and PCL-PLA/HA2 co-electrospun scaffolds were fabricated using rotating needle collector with two needle size: G16 and G21 giving surface speeds of 31.09 and 15.43 mm s^{-1}, respectively. Scaffold dimensions (length, outer and inner diameter) are listed in Table 7.1. Morphology of the tubular scaffolds are shown in Figure 7.1, indicating the macroscopic structures (Figure 7.1 a, b) and microscopic cross sections (Figure 7.1 c, d) of the scaffolds.

Table 7.1 Tubular coaxial scaffolds dimensions

Needle collector gauge size	Control		HA-containing		Length (mm)
	OD (mm)	ID (mm)	OD (mm)	ID (mm)	
G16 (OD=1.35mm) Speed= 15.54 mm s^{-1}	2.83± 0.40	1.19± 0.18	2.92± 0.56	1.21± 0.08	~52
G21 (OD=0.67mm) Speed= 7.71 mm s^{-1}	1.89± 0.11	0.57± 0.05	1.99± 0.07	0.61± 0.03	~37

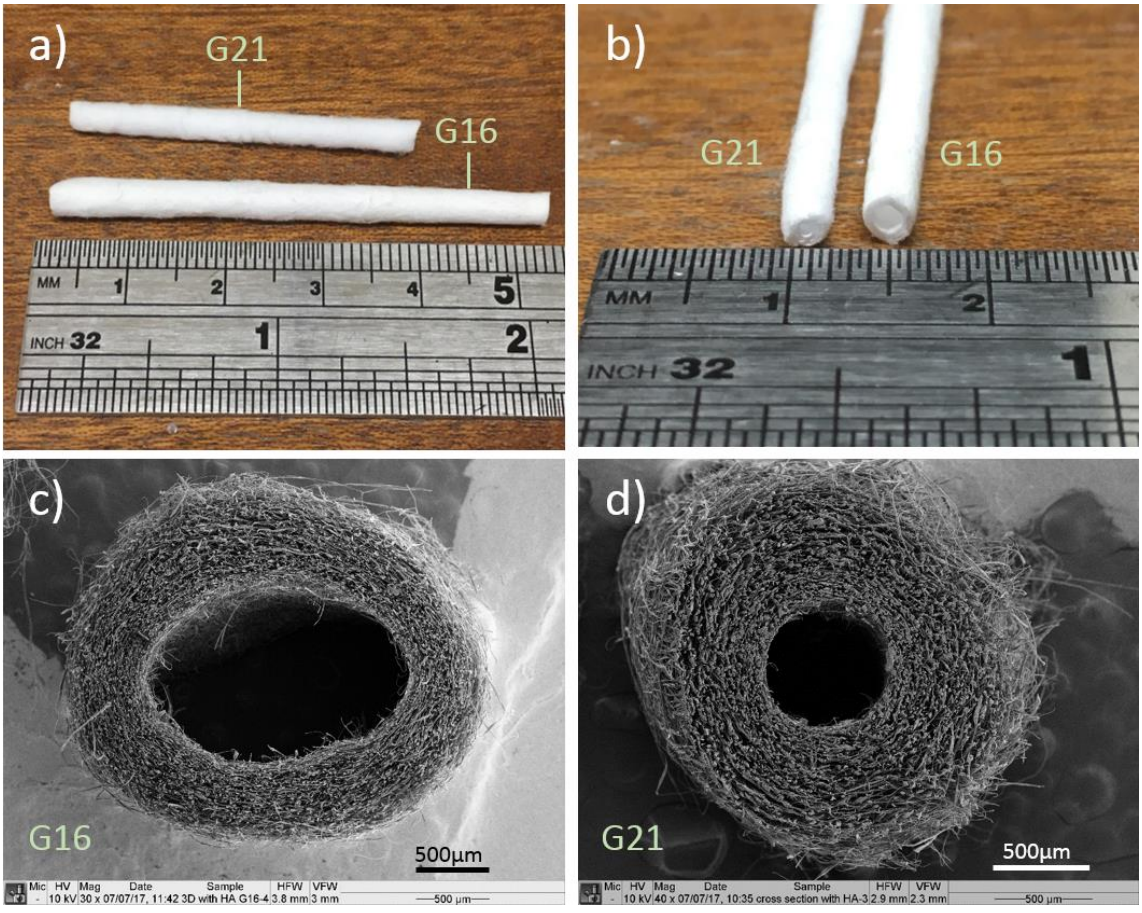

Figure 7.1 Macroscopic and microscopic structures of the PCL-PLA/HA2 tubular scaffold. a) and b) show the dimensions of the tubes while c) and d) show SEM images of G16 and G21 tube cross sections, respectively (marker bars=500 µm)

PCL-PLA (control) coaxial tubular scaffolds had uniform fibres with higher alignment compared to the 2D coaxial sheets. The average fibre diameters for G16 and G21 tubular scaffolds were 5.78±1.52μm and 5.84±0.91μm, while the calculated porosities were 85.6±3.4% and 91.3±3.5%, respectively compared to 4.42 ±1.14μm and 90.34 ±2.91% for the 2D sheets. Figure 7.2 shows the morphologies of electrospun control scaffolds along with their fibre alignment patterns and fibre diameter distribution curves. Images and analysis of 2D coaxial sheets are included for comparison.

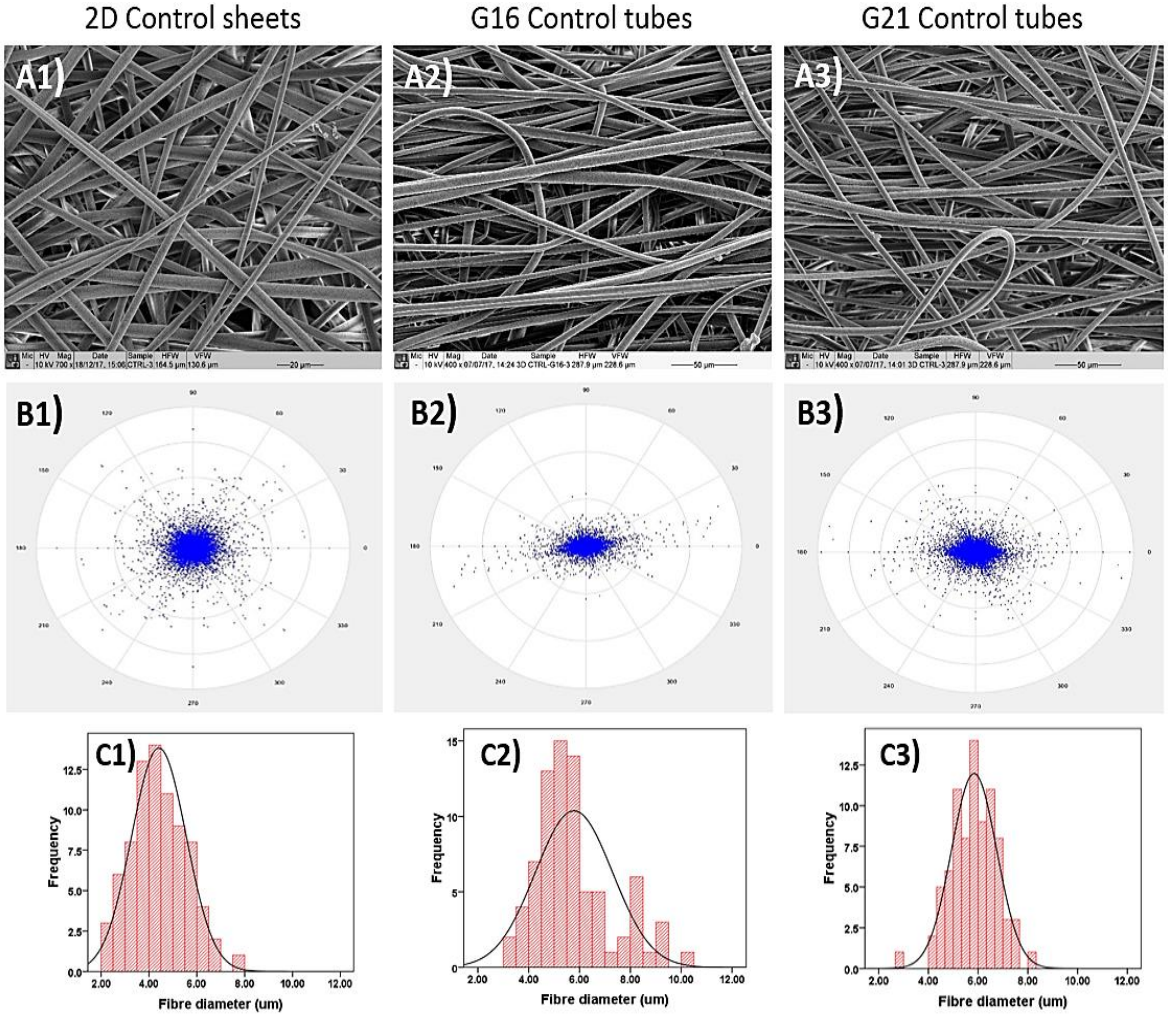

Figure 7.2 A: SEM micrographs of (A1) 2D control sheets, (A2) G16 tubular control scaffolds, and (A3) G21 tubular control scaffolds (marker bars= 20μm for A1, and 50μm for A2 and A3). B: the calculated fibre alignment pattern for (B1) 2D sheets, (B2) G16 tubular grafts, and (B3) G21 tubular grafts. The lower panel (C1-C3) shows the fibre diameter distribution of the 2D mats, G16, and G21 tubular scaffolds, respectively

HA-containing tubes also show increased fibre alignment, however, the fibres were more stretched compared to the control fibres and the 2D sheets had an increased non-uniformity. The average fibre diameters for G16 and G21 tubular scaffolds were 9.65± 5.01µm and 9.08± 4.51µm and the calculated porosities were 88.2±4.0% and 90.4±2.4%, respectively compared to 6.06± 2.89µm and 88.25 ± 3.41% for the 2D sheets. Figure 7.3 shows the morphologies of 2D and tubular electrospun HA-containing scaffolds along with their fibre alignment pattern and fibre diameter distribution curves.

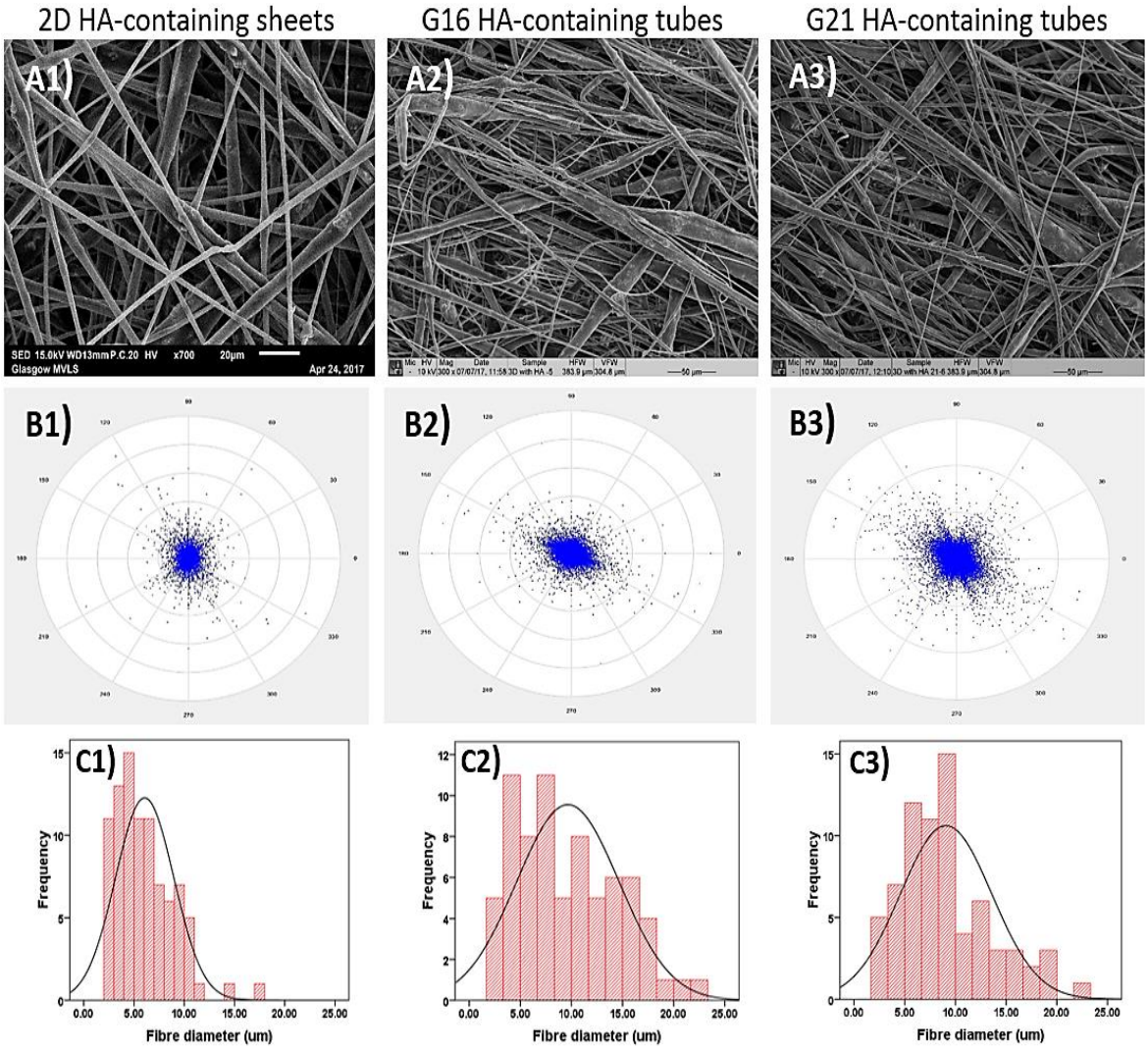

Figure 7.3 A: SEM micrographs of (A1) 2D HA-containing sheets, (A2) G16 tubular HA-containing scaffolds, and (A3) G21 tubular HA-containing scaffolds (marker bars= 20µm for A1, and 50µm for A2 and A3). B: the calculated fibre alignment pattern for (B1) 2D sheets, (B2) G16 tubular grafts, and (B3) G21 tubular grafts. The lower panel (C1-C3) shows the fibre diameter distribution of the 2D mats, G16, and G21 tubular scaffolds, respectively

During SEM imaging of tubular control scaffolds, a few broken fibres were found. The broken fibres exhibited clear core and shell configuration as shown in Figure 7.4. However, no broken fibres were detected during SEM imaging of the HA-containing tubes. Again, nanopores were seen on the fibre surfaces.

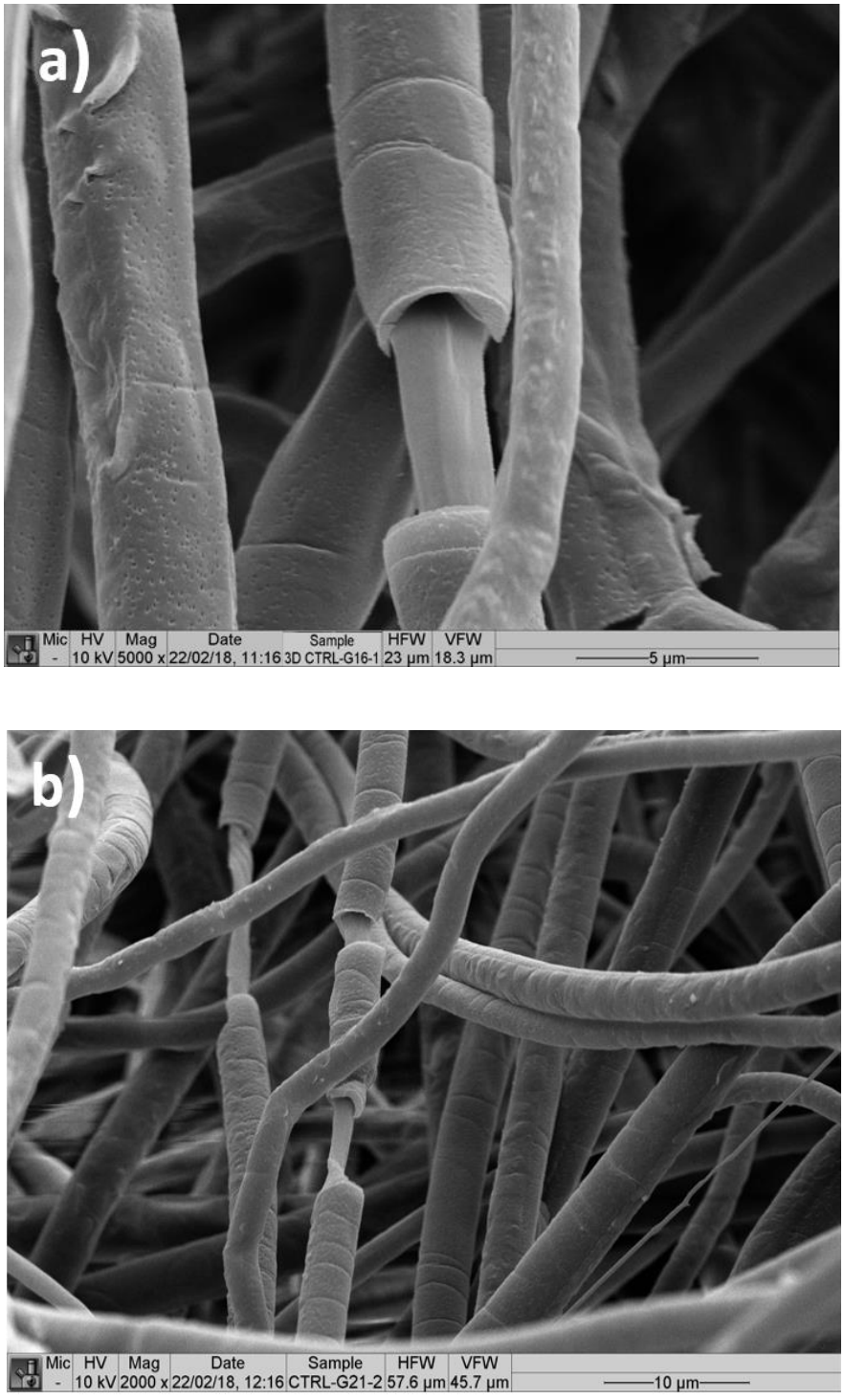

Figure 7.4 SEM micrographs of (a) G16, and (b) G21 control tubular scaffolds showing broken fibres with core and shell configuration (marker bars= 5µm and 10µm for a and b, respectively)

Figure 7.5 shows the morphologies of control scaffolds after 4, 8, and 12 weeks of immersion in either PBS or SBF. In both solutions, the fibres maintained their shape and no fibre swelling was noticed after immersion although all samples were dried for SEM. In addition, no apatite formation were observed on the fibres surface upon immersion in SBF even after 12 weeks.

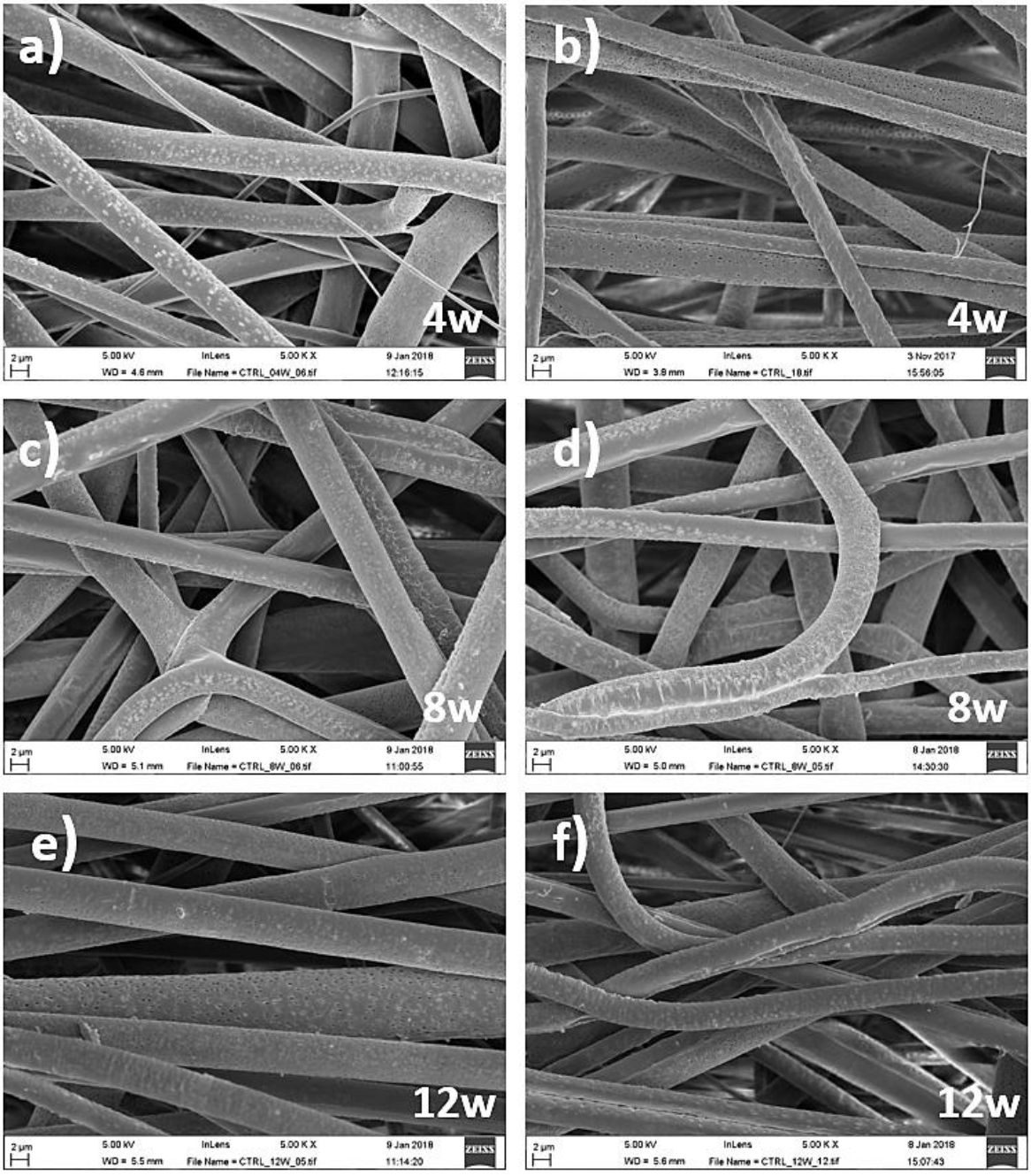

Figure 7.5 SEM images of control coaxial tubular scaffolds after immersion in PBS (a, c, and e) or SBF (b, d, and f) for 4, 8, and 12 weeks, respectively (all marker bars= 2μm)

Most of HA-containing fibres have also preserved their structure during immersion in PBS (Figure 7.6). However, few broken fibres were observed at week 12 of immersion (indicated by the blue arrows in Figure 7.6e). The breakage of the fibres occurred at the narrow regions of the fibres.

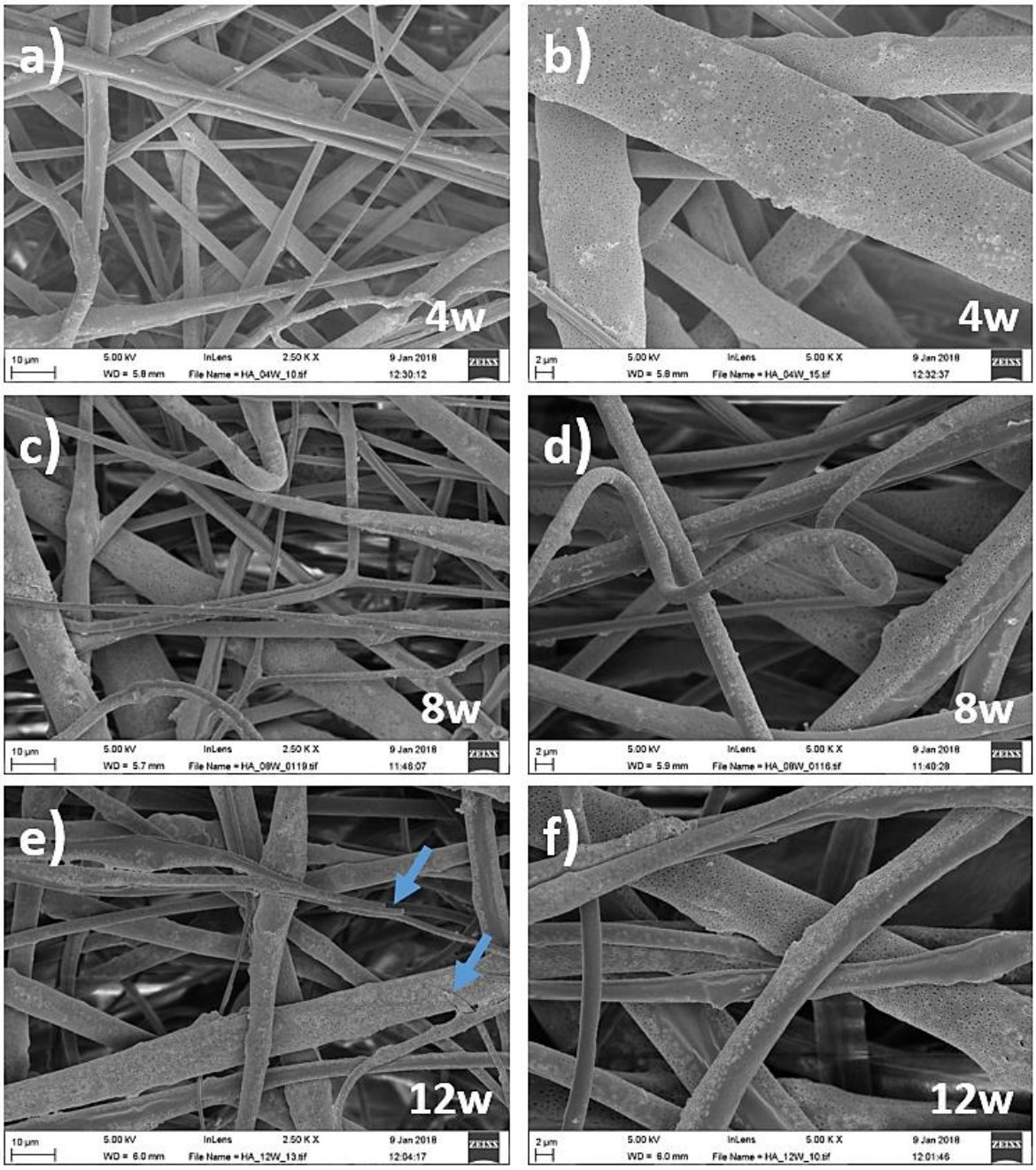

Figure 7.6 SEM images of HA-containing tubular scaffolds at two magnifications after immersion in PBS for 4, 8, and 12 weeks, respectively. Blue arrows indicate broken fibres (marker bars for a, c, and e = 10μm, and for b, d, and f= 2μm)

In SBF, the tubular scaffolds containing HA particles showed high levels of bioactivity where white layers of apatite were formed on the surface of the fibres first seen at week 4 of immersion. The extent and thickness of the apatite layer grew with increasing immersion time. Figure 7.7 shows the SEM images of HA-containing fibres at week 4, 8, and 12 of SBF immersion with apatite layer on the surface of the fibres.

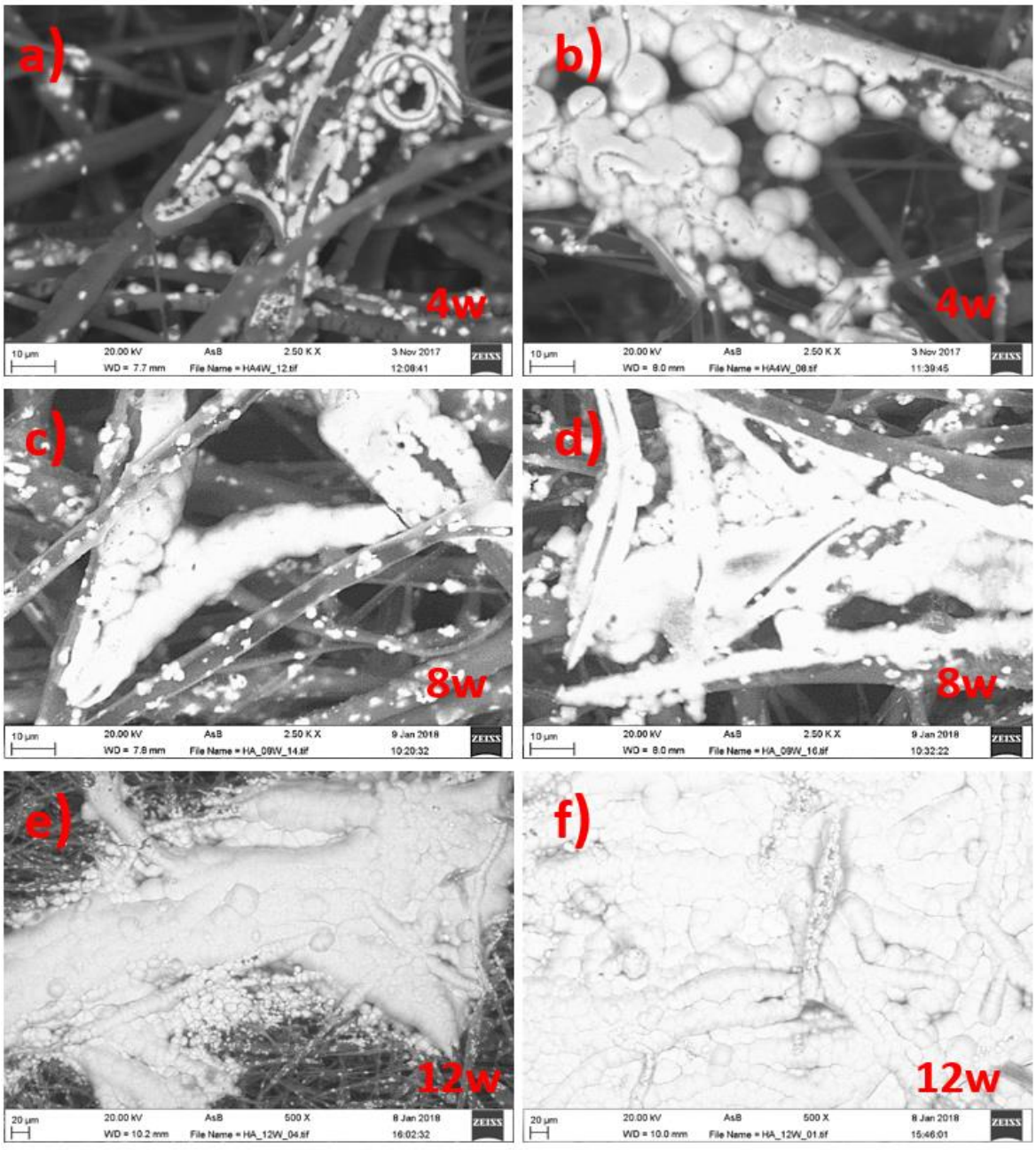

Figure 7.7 SEM images for HA-containing coaxial scaffolds after immersion in SBF for 4 weeks (a, b), 8 weeks (c, d), and 12 weeks (e, and f) showing HCA formation on the surface of the fibres (marker bars for (a-d) =10μm, and for (e) and (f) =20μm)

7.3.2 Water uptake and dissolution rate

The water uptake and dry weight loss percentages for control and HA-containing coaxial scaffolds over 4, 8, and 12 weeks of immersion in PBS and SBF are shown in Figures 7.8 and 7.9, respectively. Minimal differences were seen in water uptake and weight loss percentages between the control and HA-containing scaffolds in PBS, but in SBF the standard deviations were substantially larger. The control scaffolds showed continuous weight loss during 12 weeks of SBF immersion while for HA-containing scaffolds, the weight loss percentage have noticeably decreased at week 12 of immersion. Statistical analysis of samples weight loss and water uptake during PBS or SBF immersion are presented in appendix A.4.

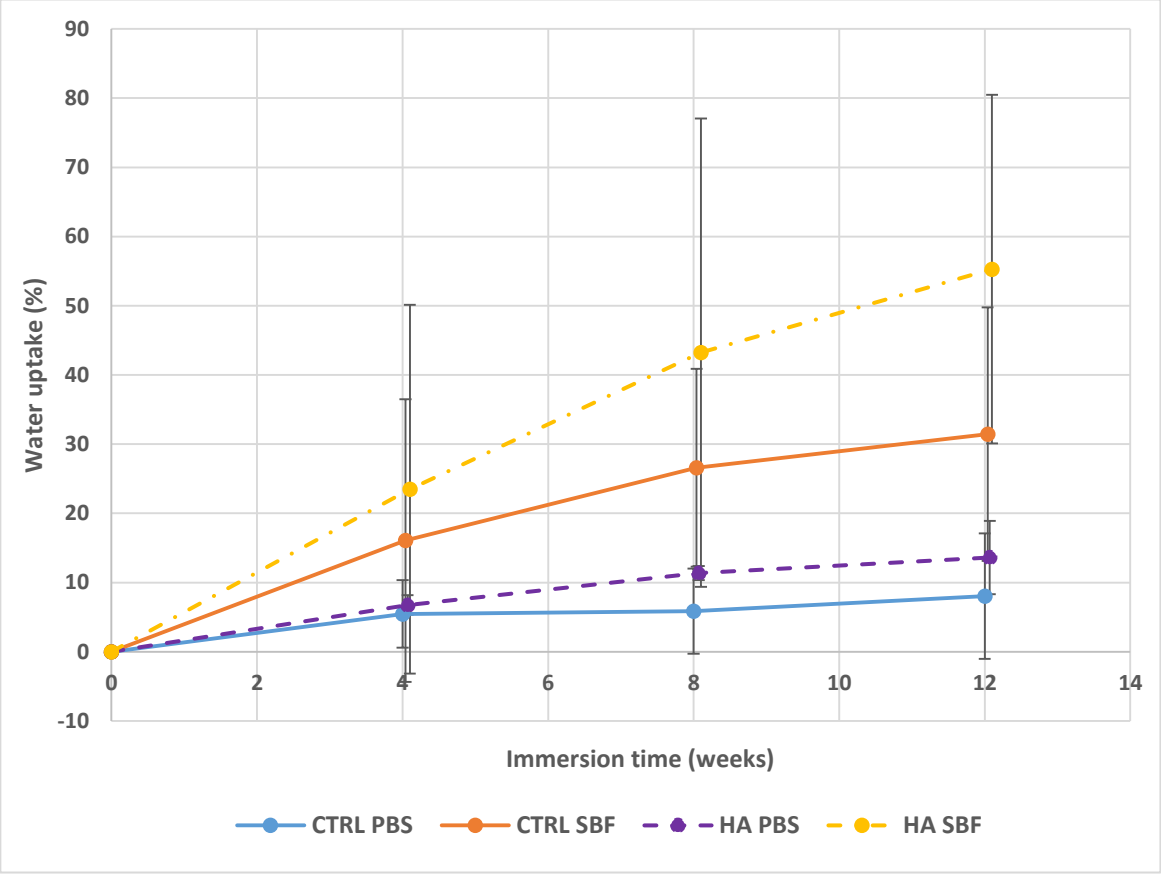

Figure 7.8 Water uptake percentage of control and HA-containing samples during 12 weeks of immersion in PBS and SBF

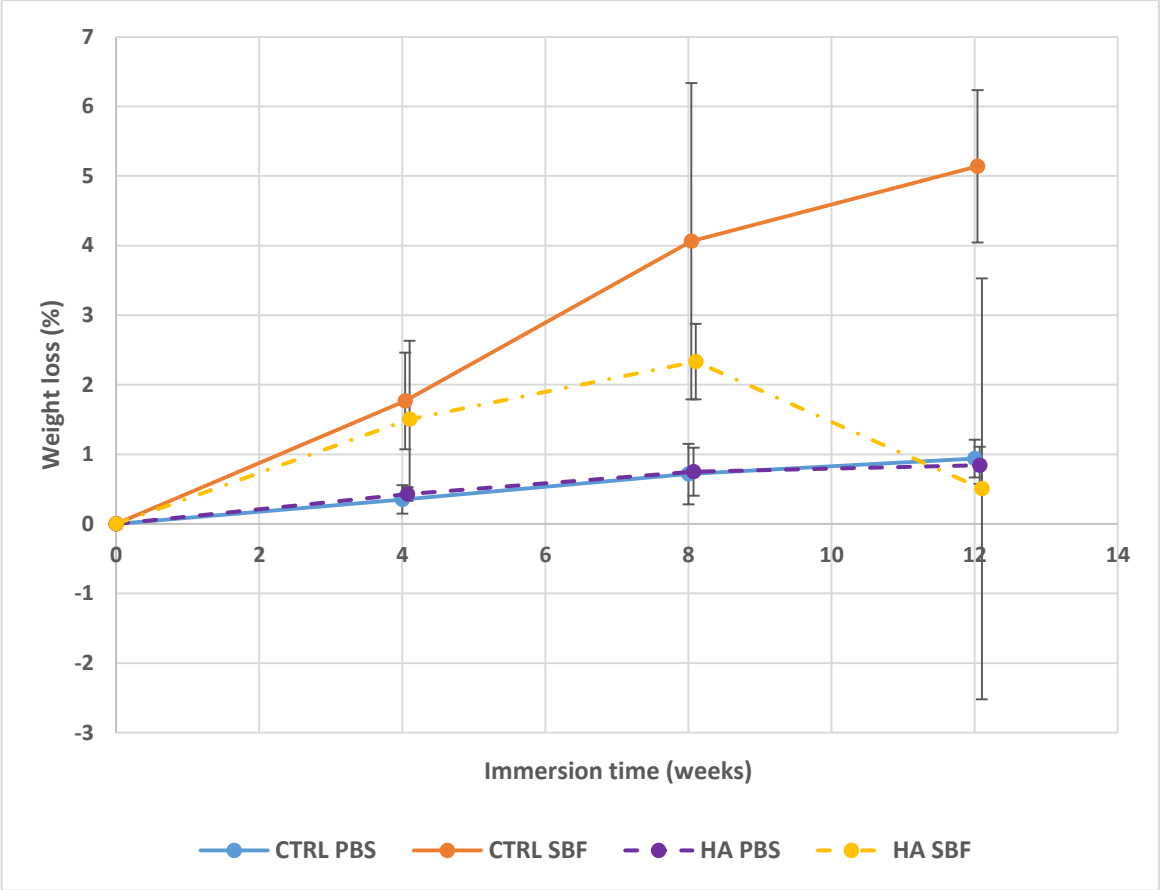

Figure 7.9 Weight loss percentage of control and HA-containing samples during 12 weeks of immersion in PBS and SBF

7.3.3 EDX

Figures 7.10 to 7.13 show the EDX spectra of control scaffolds along with their element mapping after 0, 4, 8 and 12 weeks of immersion in SBF, while Figures 7.14 to 7.17 show the EDX spectra and elemental mapping of HA-containing scaffolds after the same times of immersion in SBF.

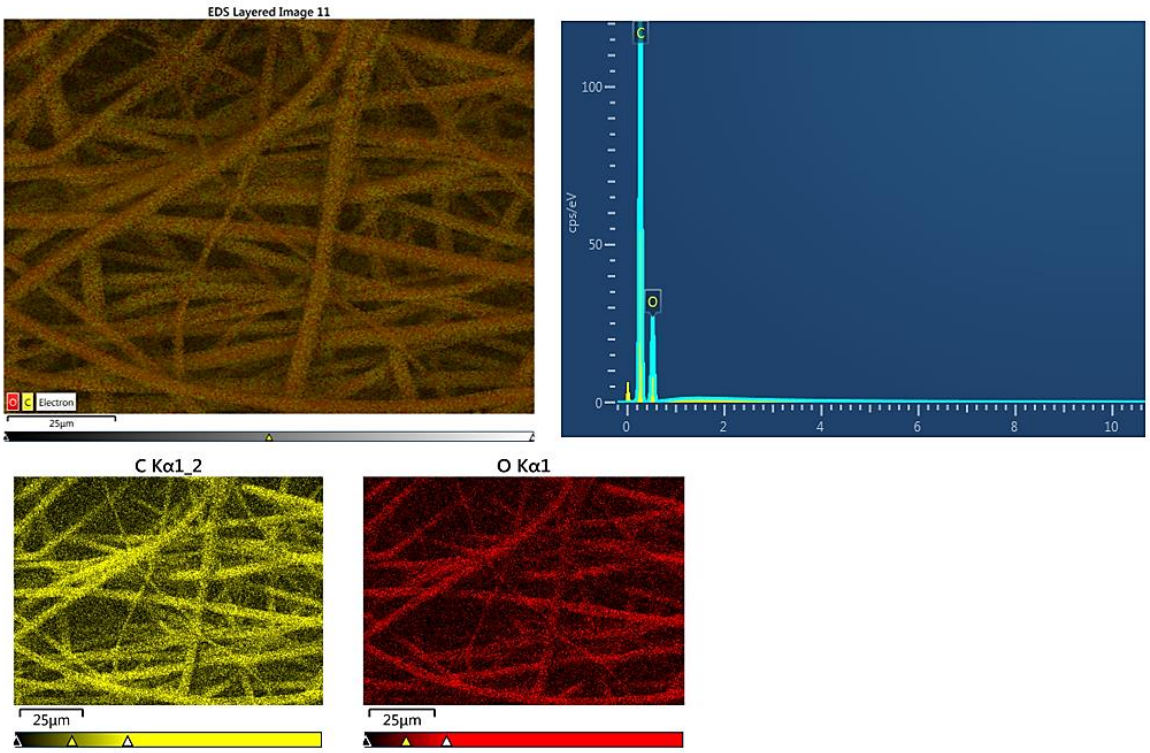

Figure 7.10 EDX spectrum and mapping of control fibres before immersion in SBF showing carbon (C) and oxygen (O) only

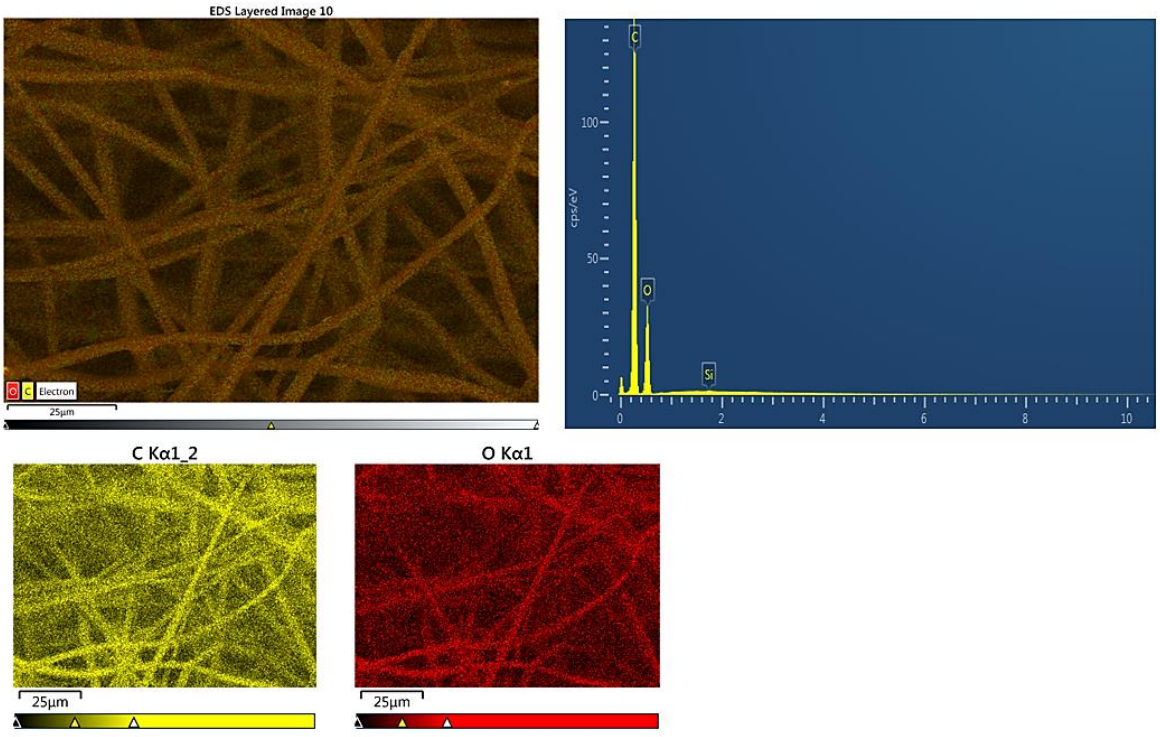

Figure 7.11 EDX spectrum and mapping of control fibres after 4 weeks immersion in SBF showing carbon (C) and oxygen (O) only

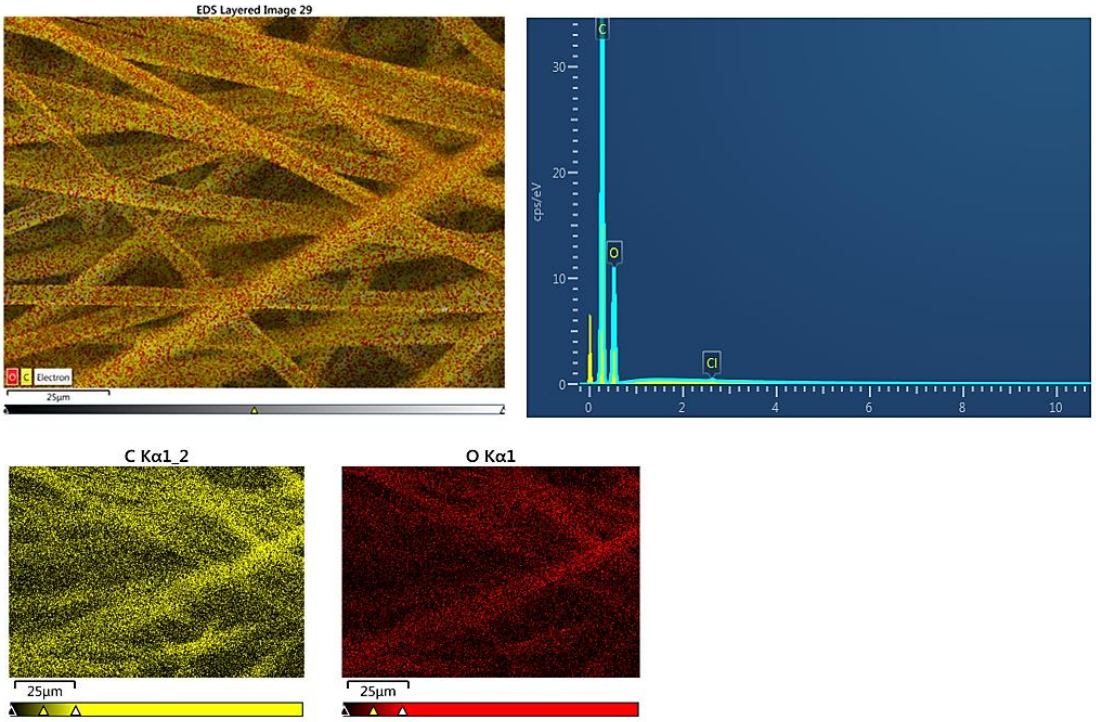

Figure 7.12 EDX spectrum and mapping of control fibres after 8 weeks immersion in SBF showing carbon (C) and oxygen (O) only

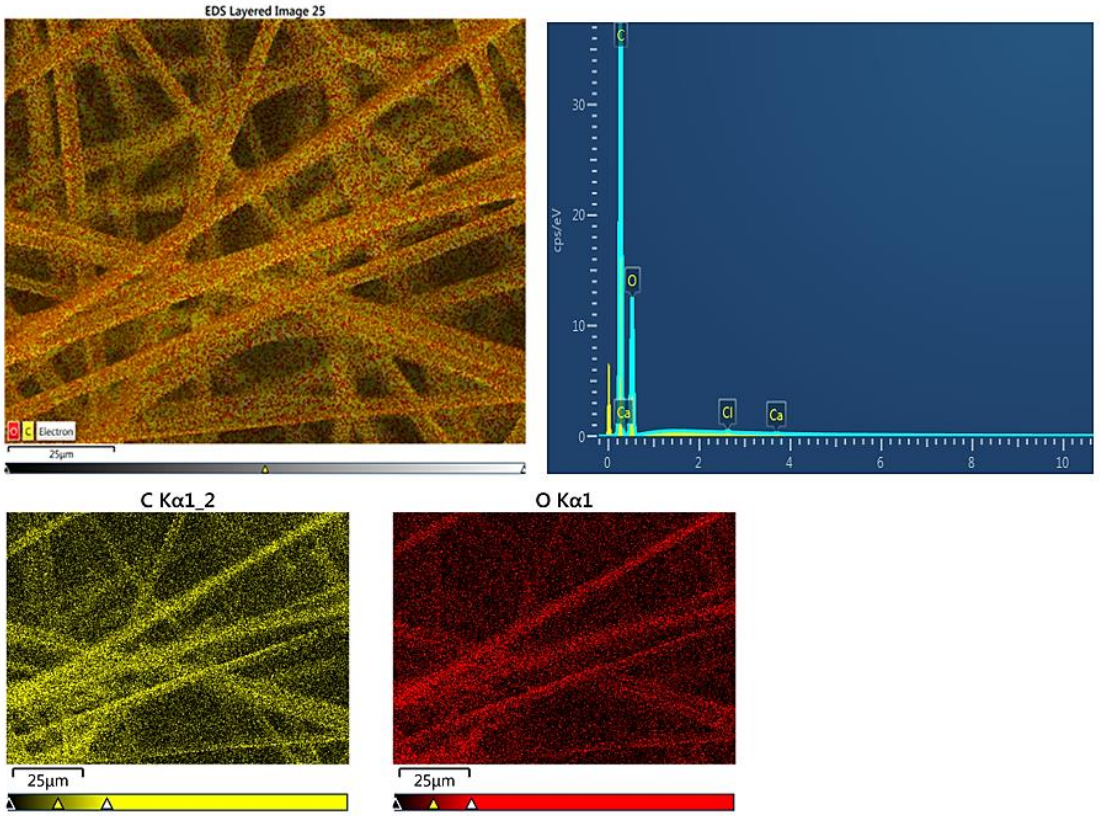

Figure 7.13 EDX spectrum and mapping of control fibres after 12 weeks immersion in SBF showing carbon (C) and oxygen (O) only

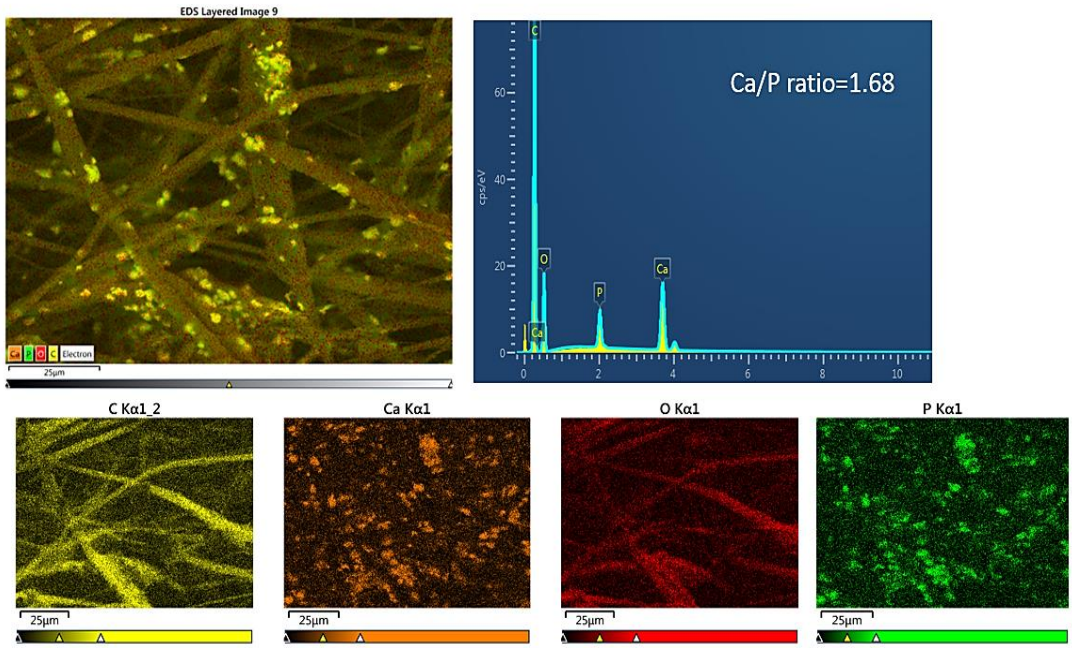

Figure 7.14 EDX spectrum and mapping of HA-containing fibres before immersion in SBF showing carbon (C), calcium (Ca), oxygen (O) and phosphorus (P)

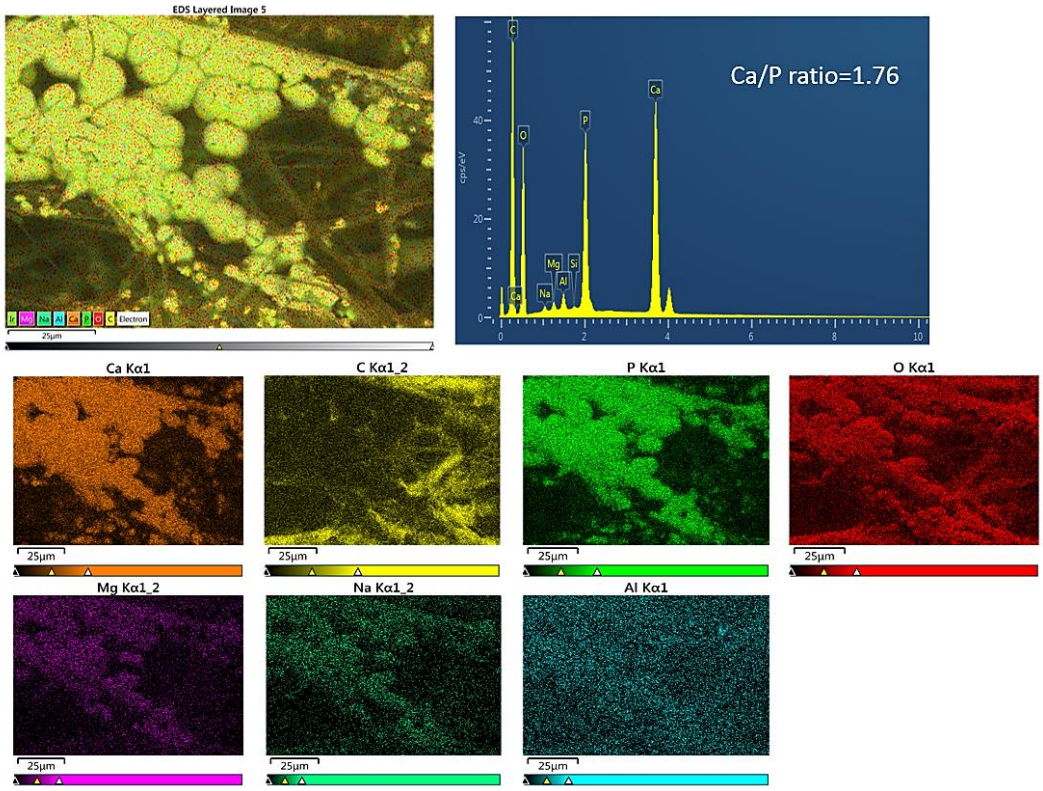

Figure 7.15 EDX spectrum and mapping of HA-containing fibres after 4 weeks immersion in SBF showing calcium (Ca), carbon (C), phosphorus (P), oxygen (O), magnesium (Mg), sodium (Na) and aluminium (Al)

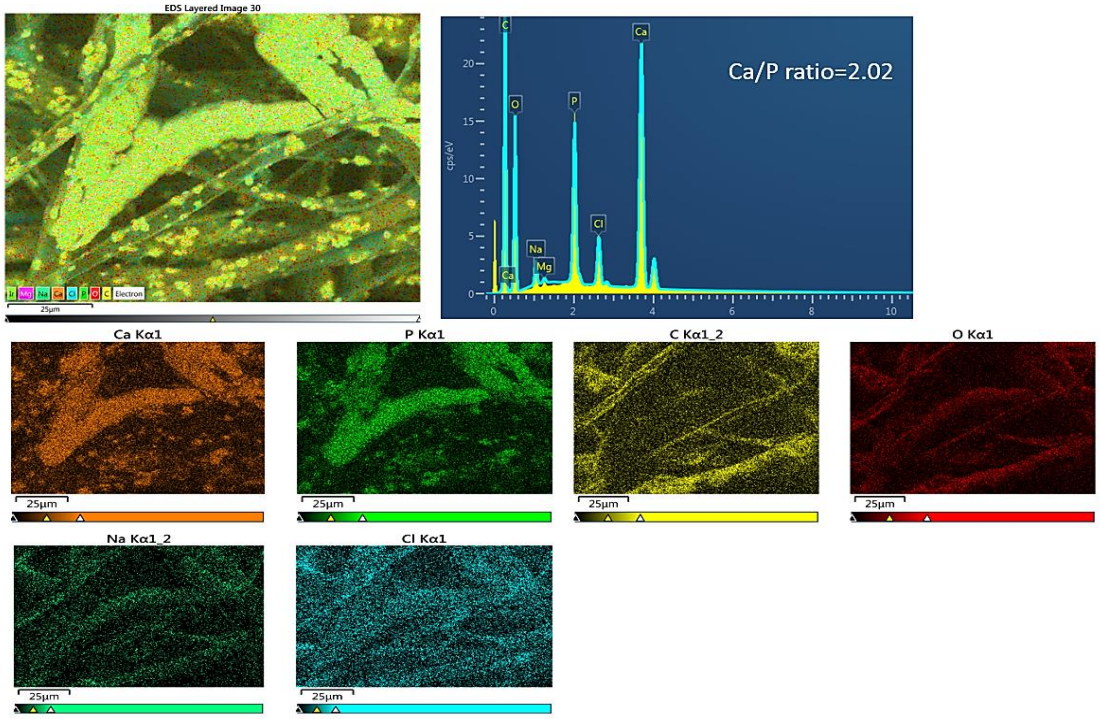

Figure 7.16 EDX spectrum and mapping of HA-containing fibres after 8 weeks immersion in SBF showing calcium (Ca), phosphorus (P), carbon (C), oxygen (O), sodium (Na) and chloride (Cl)

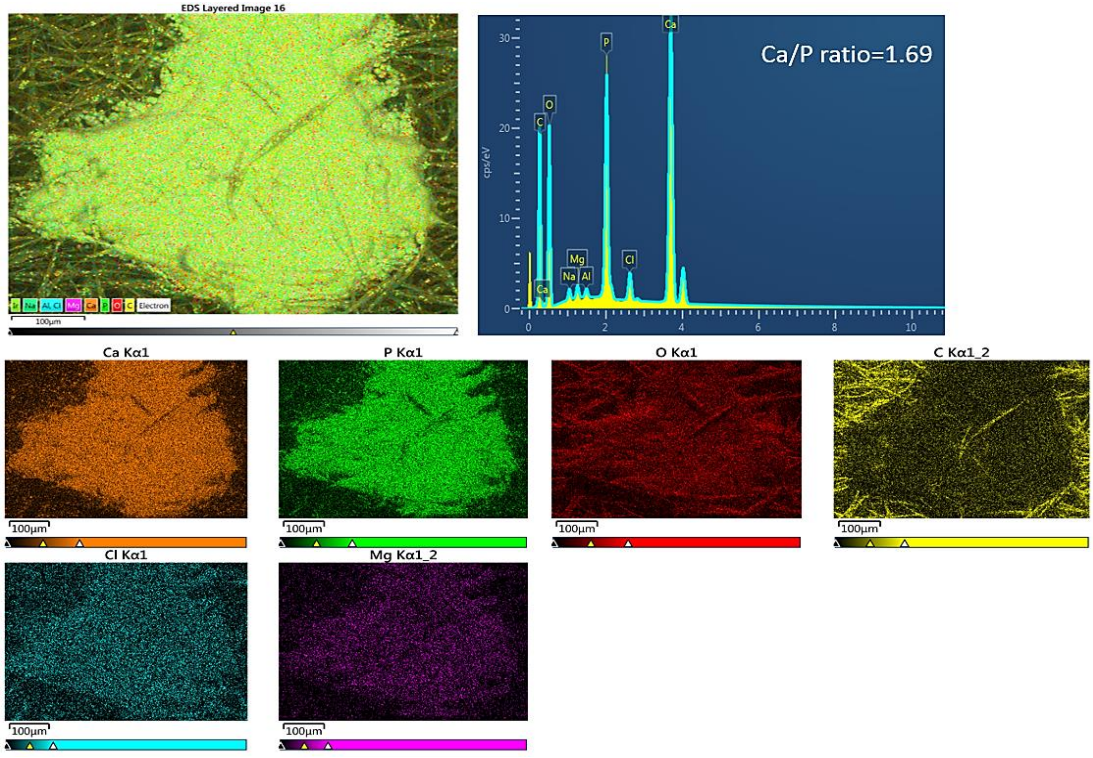

Figure 7.17 EDX spectrum and mapping of HA-containing fibres after 12 weeks immersion in SBF calcium (Ca), phosphorus (P), oxygen (O), carbon (C), chloride (Cl) and magnesium (Mg)

7.3.4 Mechanical testing

Coaxial tubular scaffolds (3D) with and without HA exhibited reduced mechanical properties compared to the coaxial 2D sheets. Figure 7.18 shows representative stress-strain curve of the electrsoun tubular scaffolds with and without HA.

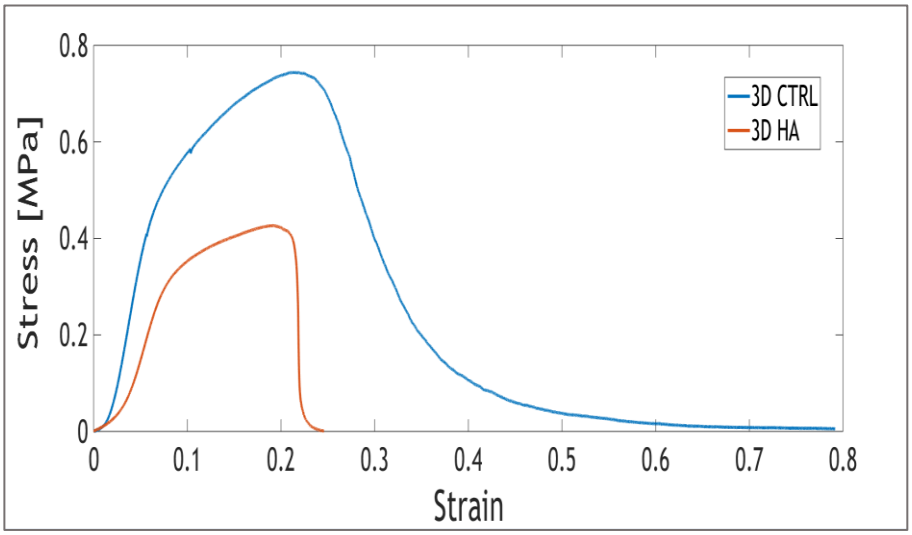

Figure 7.18 Representative stress-strain curves of the tubular control and HA-containing scaffolds

The Young's moduli, ultimate tensile strength, elongation percentage for control and HA-containing tubular scaffolds before and after 12 weeks immersion in PBS or SBF are shown in Figure 7.19. Statistical analysis of the tensile properties are presented in appendix A.4.

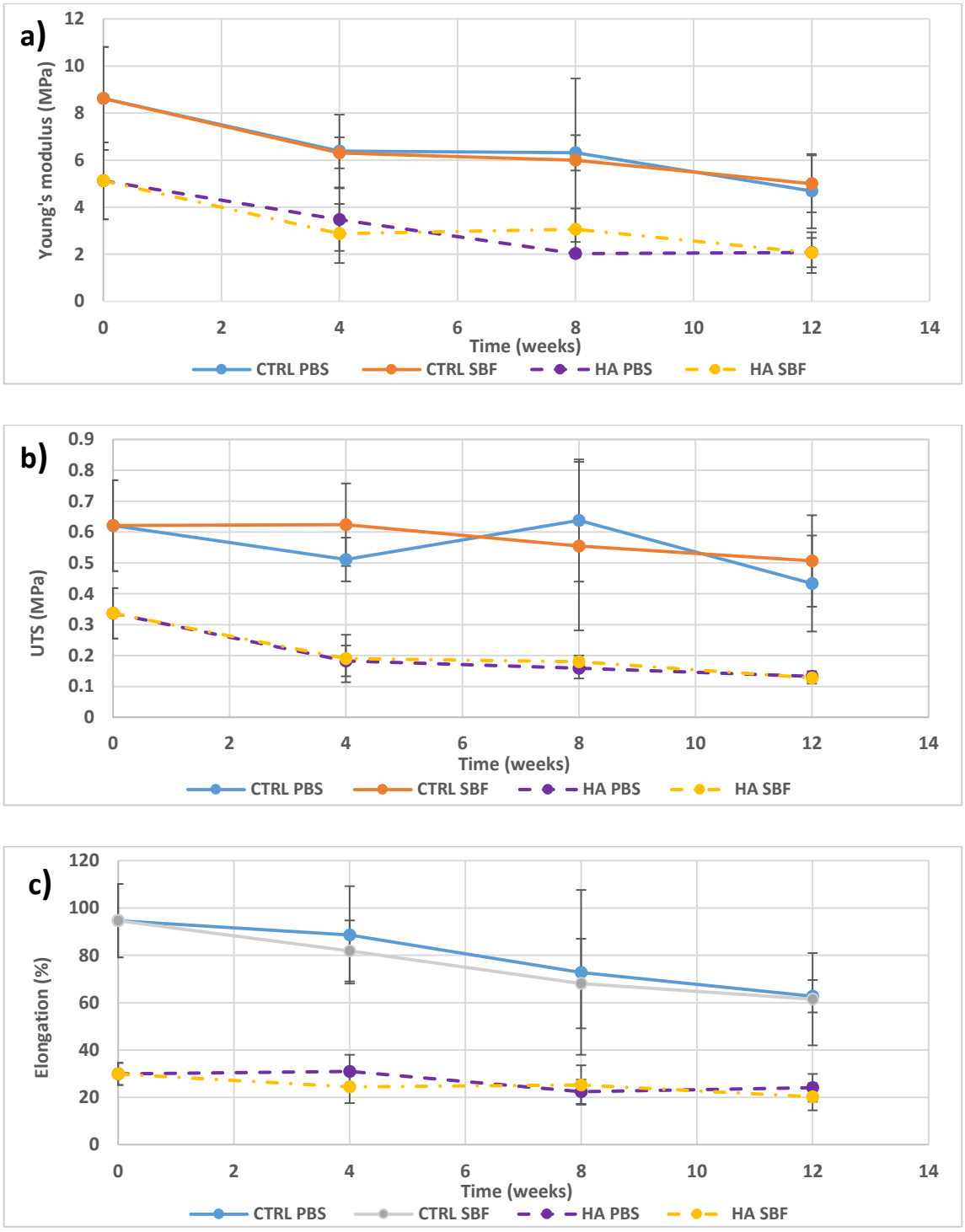

Figure 7.19 Tensile properties of coaxial control and HA-containing tubular scaffolds before and after 12 weeks immersion in PBS or SBF. (a) Young's moduli, (b) UTS and (c) elongation to failure

7.4 Discussion

Several approaches have been employed to manufacture tubular structures for tissue engineering purposes including: extrusion, moulding, dip coating, bioprinting and electrospinning. For many tissue engineers, tubular scaffolds are fundamental as they imitate various anatomical structures in the body such as urethra, blood vessels, larynx and intestines. They are also employed in clinical applications such as nerve guides and bone defects (Jungst et al., 2015). In this study, core and shell tubular scaffolds were produced by coaxial electrospinning and using a rotating needle collector. Coaxial electrospinning were carried out for 10 minutes for each sample. The resultant electrospun tubes on a G16 needle (Figure 7.1c) had an external diameter of around 2.86 mm and wall thickness of around 1.65 mm, while the external diameter and wall thickness of tubular scaffolds with the G21 needle collector were ~1.95 and 1.35 mm respectively (Figure 7.1d) with no significant differences between control and HA-containing scaffolds. The thickness of tubes was easily tuned by varying the duration of electrospinning. As for the fibre morphology, SEM images of control scaffolds (Figure 7.2A2 and A3) showed uniform, bead-free fibres with average diameters of 5.78±1.52 and 5.84±0.911 μm for G16 and G21 needle collectors, respectively which is slightly higher than the fibre diameter in the 2D control sheets electrospun onto microscope slides (4.42±1.14 μm). Jungst et al. (2015) examined the effect of collector diameter and rotational speed on the diameter of electrospun PCL fibres using 1, 3, and 4.76 mm rotating cylindrical collectors rotating at five different speeds to give surface velocities of 62.8, 125.7, 251.3, 377, and 628.3 mm min^{-1}. They found that varying the diameter and tangential speed of the collector did not affect the fibre diameter significantly.

Nguyen and Anderson (2015) also investigated the impact of increasing mandrel rotational speed on the size and orientation of electrospun Poly(D, L-lactic-co-glycolic) acid 85:15 fibres. Their results showed that increasing the mandrel speed from 14000 rpm to 37000 rpm did not exhibit any pronounced impact of the average size of fibres. However, it decreased the standard deviation of fibre angular deviation from 39° to 17°.

On the other hand, Alfaro De Prá et al. (2017) found that using a drum collector with 2000 rpm rotational speed decreased the PCL fibre diameter significantly from 1142 ± 391 nm to 663 ± 334 nm compared to using a stationary collector.

They attributed the reduction in diameter to the stretching force caused by high rotation during fibre deposition on the collector.

While using the rotating collector did not affect fibre diameter, some electrospun tubes exhibited an increased circumferential alignment of the fibres compared to the 2D fibrous sheets electrospun on the stationary collector (Figure 7.2B1-B3), while other tubes maintained the random orientation of their fibres. Besides the expansion of electrospinning from 2D dimensional to 3D constructs, a rotating drum has been used for fabrication of fibrous scaffolds with a well-controlled structure. However, to produce highly aligned fibres by this method, it is necessary for the collector surface speed to match or exceed the rate at which fibre is produced (typically up to thousands of rpm); otherwise, randomly oriented or buckled fibres will be collected. On the other hand, fibre breakage may occur if the rotating speed of the collector is too high (Huang et al., 2003; Kiselev and Rosell-Llompart, 2012). Another limitation associated with achieving highly oriented fibres using a rotating collector is that the collected aligned fibres can only reach a thickness of a few fibre layers as increasing the thickness causes disoriented fibres formation because of residual charge accumulation on the deposited fibres, which interferes with the alignment of incoming fibres (Shang et al., 2010; Teo and Ramakrishna, 2006).

According to Shang et al. (2010), alignment of electrospun fibres can influence cell orientation. Their results showed that periodontal ligament cells (PDL) extended and aligned to a spindle-like shape on their aligned PLGA scaffolds, while cells on randomly oriented scaffolds had a polygonal shape stretching across multiple fibres. The aligned fibres have also promoted directed cell movement while the random oriented fibres hampered the migrational behaviour of the cells. Similar cellular behaviour was also reported by Hwang et al. (2009) using mouse fibroblast L929 cells and aligned PLGA microfibres.

As for HA-containing coaxial tubes, the outer diameter and wall thickness of G16 and G21 HA tubes did not vary significantly from the control scaffolds (Table 7.1), and electrospinning on rotating needles has also improved fibre alignment compared to 2D sheets (Figure 7.3). However, unlike the control scaffolds, electrospinning on rotating needles caused fibre stretching during electrospinning, and that in turn led to increased fibre non-uniformity due to increased HA agglomerations within the fibres, in addition to HA protuberances on the fibre

surfaces as a result of the large particle size. Because of these agglomerations, scaffolds from both G16 and G21 needles had large fibre diameter distributions from about 2μm to over 22μm with average diameters of 9.65± 5.01 and 9.08± 4.51 μm for G16 and G21 needle collectors, respectively.

Unlike the 2D coaxial sheets where it was rare to find broken fibres showed clear core and shell configurations for either control and HA-containing scaffolds, broken fibres were observed during SEM imaging of the control tubes which clearly showed the core and shell configuration within the fibres (Figure 7.4). The breakage of the fibres might occurred due to the exerted force on the fibres during tubes extraction from the needle collector which also caused some stretch marks on the fibres surface in addition to fibres breakage. However, no broken fibres were found with HA-containing tubes.

Although the fibres were densely packed around the needle collector during electrospinning, the porosity of the coaxial tubes, calculated by gravimetric method, did not vary significantly from 2D sheets and ranged from 85 to 91% for both G16 and G21 needle collectors with no significant difference between control and HA-containing tubes. These results confirm that including HA within the fibres does not affect scaffold porosity despite increasing the fibre diameter. Also, the porosity results showed no significant variation between G16 and G21 tubes. However, more needle sizes need to be tested to characterise in depth the effect of collector size on the total porosity of the electrospun tubes.

Biodegradability is a critical feature in tissue engineering scaffolds and drug delivery carriers as fibre degradation is essential to promote the ingrowth of new tissue, while the degradation rates should be matched with the rate of neo-tissue formation in order to provide a smooth load transition from the scaffold to the tissue. In addition, the release rate and effective lifetime of drug delivery devices can be regulated through the degradation of fibrous mats (He et al., 2012). On the other hand, Kokubo (1991) proposed that the fundamental requirement for an artificial material to bond to living bone is the formation of bonelike apatite on its surface when implanted in the living body, and that this in vivo apatite formation can be reproduced by soaking the material in SBF (Heydary et al., 2015; Kokubo and Takadama, 2006). Therefore, control and HA-containing coaxial tubes

were soaked in PBS or SBF for 4, 8, and 12 weeks at 37°C, pH = 7.4 to analyse their biological and biodegradation response.

Both control and HA-containing samples immersed in PBS exhibited very slow degradation (Figure 7.9) with a weight loss rate of 0.3-0.4% every 4 weeks and a total weight loss of 0.94± 0.27% and 0.84± 0.26% for control and HA-containing samples respectively after 12 weeks incubation. These results are expected since PCL and PLA are known to have very slow degradation rates even in their nanofibrous form, while the inclusion of HA particles has also shown to decrease the degradation rate of the scaffolds as discussed earlier (section 5.4). On the other hand, control samples immersed in SBF have shown a significant increase in the weight loss rate compared to PBS, although the weight loss remained generally low during the 12 weeks of immersion with a total weight loss of 5.14± 1.09%. The difference in sample degradation rates between PBS and SBF could result from the different composition of the two solutions with SBF containing higher ion concentrations than PBS (Table 3.3). As for the HA-containing samples, during the first 4 weeks of immersion, the samples exhibited similar degradation behaviour as the control samples, with no noticeable difference in their degradation rates. However, after week 4, the weight loss rate started to decrease substantially, but not significantly different, compared to control samples (2.33±0.54% vs 4.06± 2.26% for HA and control samples, respectively). By week 12 of SBF immersion, the samples exhibited significant reduction in weight loss rate, compared to control samples, with a total weight loss of 0.50±3.02%. Since the presence of HA did not affect the hydrolysis rate in PBS significantly during the whole period of immersion, the reduction in weight loss rate can thus be attributed to apatite formation on the fibre surfaces.

Control and HA samples immersed in SBF also exhibited a significant increase in water uptake after week 4 of immersion compared to PBS samples (Figure 7.8) which could be resulted from the higher dissolution rate in SBF compared to PBS. In both solutions, HA samples had higher water uptake than control samples due to the higher affinity of HA particles for water molecules and the presence of nano/micropores at the PLA/HA interface. However, the differences were not statically significant due to the high standard deviations.

SEM was used to observe the morphological changes in the PBS and SBF incubated samples at week 4, 8, and 12 of incubation. No noticeable changes were noticed in the control fibres after immersion in either solutions over 12 weeks (Figure 7.5). These results were expected since control scaffolds showed less than 10% dissolution rate in both degradation solutions. In addition, no apatite-like materials were precipitated on the surface of the SBF immersed fibres at any time of incubation which confirms that PCL-PLA coaxial fibres have no ability to induce bone-like mineral growth due to their hydrophobic nature and lack of sufficient functional groups. HA-containing fibres incubated in PBS have also preserved their microstructure during the immersion period with no apatite formed on the fibre surfaces and only few broken fibres were found at week 12 of immersion (Figure 7.6). However, for HA-containing samples immersed in SBF, apatite nucleation from the exposed HA particles on the fibres surface was observed after week 4 of immersion and cauliflower-like apatites were formed on the fibrous composites (Figure 7.7). In addition, some fibres cracked opened with HA particles exposured along the fibres which were also noticed after immersion (Figure 7.20). The exposition of HA particles to the SBF solution offered favourable areas for apatite nucleation. Thus, apatite precipitation was higher on or near the cracked open fibres.

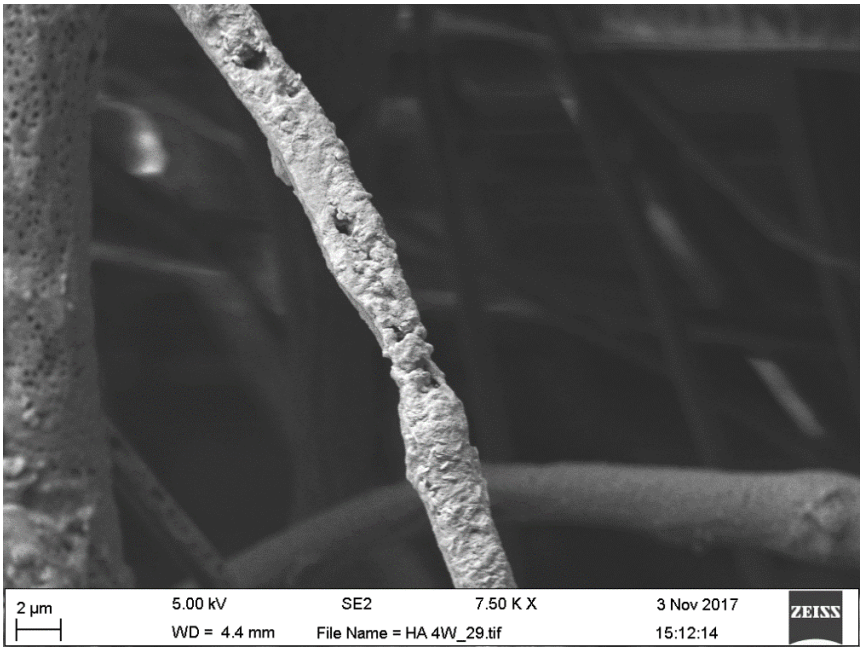

Figure 7.20 SEM image of HA-containing sample after 4 weeks immersion in SBF showing a cracked open fibre with exposed HA-particles and apatite precipitation along the fibre (marker bars= 2µm)

According to Kim et al. (2004), HA particles experience three characteristic surface structural changes after immersion in SBF in the process of apatite formation on their surface. The first surface structural change includes the formation of a Ca-rich amorphous calcium phosphate (ACP) layer on HA surface as a result of the interaction of the negatively charged HA surface (due to the existence of hydroxyl and phosphate groups) with the calcium ions in the SBF. The second surface structural change includes the formation of Ca-poor ACP on the HA as a consequence of the interaction between the positively charged Ca-rich ACP layer with the negative phosphate ion in the SBF. In the last surface change, the Ca-poor ACP on the HA surface starts to crystallise into apatite with bone mineral-like composition and structure. Figure 7.21 summarises schematically the mechanism of bone-like apatite formation on HA surfaces in SBF.

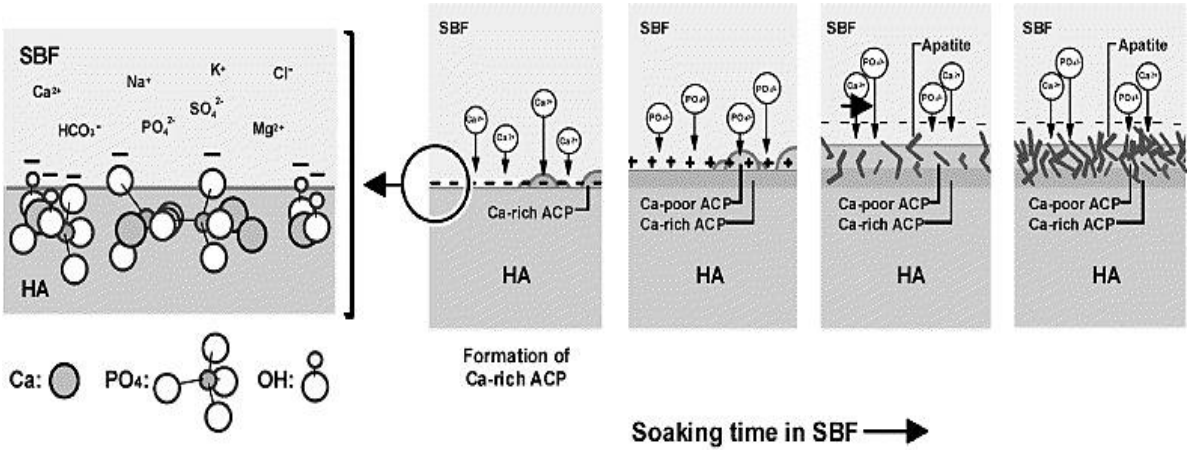

Figure 7.21 Schematic presentation of the origin of negative charge on the HA surface and the process of bone-like apatite formation in SBF as suggested by Kim et al. (2004)

In this study, the thickness and area of the apatite layer formed on the coaxial HA-containing fibres was shown to increase with increasing soaking time as a result of incorporating the calcium and phosphate ions in the SBF (Kim et al., 2004, 2005), and after soaking for 12 weeks in SBF, large areas of the scaffolds were covered by a thick white layer of bone-like apatite (Figure 7.7 e and f).

Moreover, elemental analysis of both control and HA scaffolds before and after SBF incubation was carried out using EDX to determine their chemical composition and to characterise the deposition observed by SEM on composite fibres after SBF

immersion. EDX spectra of control samples showed two main peaks of carbon and oxygen which are attributed to both PLA and PCL. However, there were no peaks for calcium or phosphate belonging to the bone-like apatite after any time point of SBF immersion which confirms SEM and weight loss results that control scaffolds were not bioactive even after 12 weeks of SBF immersion.

On the other hand, EDX spectra of HA-containing samples before immersion confirmed the presence of HA within the fibres due to the presence of calcium and phosphorus peaks in the sample spectra. After immersion in SBF, EDX mapping of elements composition over the white precipitated layer showed that it was mainly composed of calcium and phosphorus atoms related to HA formation. The intensity of peaks for those atoms as well as their atomic percentage were increased with increasing soaking time. The Ca/P ratio was calculated using the EDX data from different samples and sites and the resulted ratio values of Ca/P were ranged between 1.69 and 2.02 which is higher than the stoichiometric value for hydroxyapatite (1.67), indicating the formation of carbonated HA of B-type HCA with carbonate ions CO_3^{-2} substituting for phosphate ions PO_4^{-3} (Castro et al., 2012; Dziadek et al., 2017). A previous in vitro study has demonstrated that the osteoblast cells adhesion was increased significantly on calcium phosphates with higher Ca/P ratios (up to 2.5) (Ergun et al., 2008).

Tensile testing results of control and HA-containing tubular scaffolds (Figure 7.18) have shown a significant reduction in their tensile strength and stiffness compared to the 2D coaxial sheets (Table 6.3) while the elongation to failure was not affected significantly. Since tubular scaffolds fibres exhibited more aligned arrangement compared to the 2D sheets, the difference in tensile properties could possibly have resulted from the higher surface resistance offered by the entwined fibres in the random 2D scaffolds (Subramanian et al., 2011). In addition, the orientation of the aligned electrospun fibres directly influences the mechanical strength of the scaffolds. Randomly distributed fibres give rise to isotropic mechanical properties while aligned fibres produce anisotropic mechanical properties with the highest strength of the scaffold obtained in the direction of the fibre alignment. In this study, the tubular scaffolds were tested in the axial direction while the fibres were aligned circumferentially, thus lower mechanical properties were produced compared to the 2D sheets. Prabhakaran et al. (2013)

evaluated the tensile properties of their circumferentially aligned PHBV/collagen scaffolds in both axial and circumferential directions and found that the aligned nanofibers exhibited anisotropic behaviour, whereas the tensile strength and Young's modulus in the circumferential direction was significantly higher compared to the values obtained along the axial direction.

Ranjbar-Mohammadi et al. (2016) fabricated circumferentially aligned fibrous scaffolds of poly(L-lactic acid) and gum tragacanth, a plant produced polysaccharide, (PLLA/GT) in various ratios (100:0, 75:25, and 50:50) by electrospinning for peripheral nerve regeneration and compared their mechanical properties in both directions (longitudinal and circumferential) to the mechanical properties of randomly oriented scaffolds of the same PLLA/GT ratios. The tensile strength and Young's modulus of aligned fibres along the axial direction were lower than that in the circumferential direction, while the tensile strength and stiffness in circumferential direction were significantly higher compared to the similar formulation in random nanofibers, suggesting that aligned fibres were more suitable for the regeneration of stronger and stiffer tissues such as nerves.

The tensile properties of tubular control and HA-containing scaffolds were also evaluated after 4, 8 and 12 weeks of immersion in SBF and PBS. In general, all samples have maintained most of their structural integrity in both media even after 12 weeks of incubation. Control samples have shown a gradual reduction in their tensile properties over the incubation period, however, they generally preserved their tensile strength and stiffness over the 12 weeks of incubation in both solutions, while the flexibility started to reduce significantly in SBF at week 8 of incubation as a result of progressive fibre degradation. On the contrary, HA-containing samples have maintained their ductility with only minor reductions in both solutions while their strength and stiffness were reduced significantly during immersion in both PBS and SBF. As with control samples, the reduction in tensile strength and modulus was also gradual during the incubation period. This reduction can be attributed to the increased water absorption in the polymer-filler interface which leads to filler de-bonding and ultimately reduces the scaffold strength. In addition, the presence of cracked open fibres within the scaffolds during immersion would also reduce their strength and stiffness as the fibres will lose their structure in addition to some of their HA content (particles with weak

polymer bonding). However, the ductility was mainly preserved due to the core component (PCL) which gave mechanical stability to the tubes as it is known for its slow degradation. Finally, no statistically significant differences were found between the mechanical properties of scaffolds immersed in PBS and those immersed in SBF for both control and HA-containing samples as scaffolds immersed in both solutions exhibited similar mechanical behaviour.

7.5 Conclusions

Electrospinning on rotating needle collector did not affect fibre diameter for both control and HA samples. However, it improved the fibre alignment around the collector and increased fibre non-uniformity in HA-containing tubes.

Tubular scaffolds with and without HA have shown slow degradation profiles in PBS and SBF due to the hydrophobic nature of the scaffolds components. However, HA-containing tubes have exhibited high level of bioactivity in SBF by forming thick layers of B-type carbonated apatite precipitation on the fibres surface while no apatite was formed on control fibres over the 12 weeks of SBF immersion.

By increasing fibre alignment, scaffolds showed anisotropic mechanical behaviour with reduced mechanical properties when tested against to fibre orientation. Lastly, both tubular scaffolds have shown gradual reduction in their tensile properties after 12 weeks of immersion in PBS or SBF. The reduction in tensile strength and stiffness were more significant in HA-containing scaffolds compared to control scaffolds. However, the two types of scaffolds have preserved most of their ductility during immersion in degradation solutions.

Chapter 8- General Discussion

Coaxial electrospinning is a modified electrospinning technique where a blunt-tip coaxial needle is used to extrude core and shell solutions without mixing during electrospinning, thus producing fibres with a core and shell structure (Moghe and Gupta, 2008; Sun et al., 2003). Many authors have investigated core and shell scaffolds placing the active elements, including calcium phosphates, in the core layer (Aragon et al., 2017; Doan et al., 2016; Shao et al., 2016; Zhou et al., 2017). However, the surface response to a biomaterial controls the subsequent behaviour, thus in this study the bioactive CaPs were optimised in the shell layer. Scaffolds were also developed to include the highest content of CaPs filler possible while preserving the structural and mechanical integrity of the electrospun fibres. The rationale for high CaP content is that the bioactivity of composites is increased with increasing CaP content (Ma and Tang, 2014; Yu et al., 2005; Zhang et al., 2009)

In order to produce coaxial scaffolds, in either 2D sheets or 3D tubes, three main elements had to be optimised: the shell component, the core component and electrospinning process parameters. Optimisation of these elements together in one step would be challenging since the interaction between them is complex, with variation of one element often altering another. In addition, each element has several controlling factors. Therefore, each element was optimised separately and then the coaxial electrospinning was carried out to produce 2D sheets and tubular scaffolds with core and shell structured fibres.

To select the appropriate PLA/filler composition to be used as the shell layer in coaxial electrospinning, PLA scaffolds of different PLA concentrations filled with either HA1, HA2, or TCP were produced through single-needle electrospinning. Increasing polymer and filler concentrations have largely affected spinning continuity and the resultant fibre morphologies due to their effect on the viscosity of the solutions. PLA dissolved in chloroform with a concentration below 15% produced fibres with “beads-on-string” morphology while PLA solution with concentration higher than 20% failed to produce any fibres. The addition of fillers up to 20% vol. produced scaffolds with enlarged fibre diameter compared to non-filled PLA scaffolds. However, HA1 and HA2 dispersed more evenly within the fibres compared to TCP, which tends to agglomerate into clusters that increased in number and size with increasing TCP content (Figure 4.5). This led to the

formation of non-uniform fibres compared to non-filled and HA-filled PLA scaffolds. Agglomerations of TCP within the fibres can be formed due to the inherent van der Waals interactions between individual TCP particles (McCullen et al., 2009). Varying the applied voltage, on the other hand, affected the spinning continuity, but did not have a significant effect on the fibre morphology, therefore it was kept at 13.7kV.

Mechanical testing results (Table 4.2) showed that incorporation of all three types of fillers generally reduced the tensile strength and stiffness of the PLA scaffolds, indicating an ineffective load-transfer between the polymer matrix and the filler that prevented the reinforcement process occurring (Bianco et al., 2011). The mechanical behaviour of electrospun scaffold was affected by a number of interconnected factors including: fibre uniformity, filler type, filler concentration and polymer concentration. Lin et al. (2017) have also attributed the decreased mechanical properties to the lack of chemical bonding between the polymer and the filler particles as the filler is only embedded in the polymer matrix (mechanical bonding). Thus, it is difficult for the filler particles to play an effective role in enhancing the mechanical strength of scaffolds. However, TCP-filled scaffolds had lower tensile properties compared to HA1 and HA2-filled scaffolds resulting from fibre non-uniformity and cluster formation along the fibres. Additionally, TCP-filled PLA scaffolds exhibited a higher degradation rate than non-filled and HA-filled scaffolds due to the higher solubility of TCP particles (Gao et al., 2017). Based on these results, electrospun TCP-filled scaffolds were considered inappropriate for long term tissue engineering applications.

Dissolution rate of HA1 and HA2-filled scaffolds over 28 days in SBF were lower than non-filled PLA scaffolds, due to neutralization of acidic end groups created by PLA degradation, thus reducing the amount of autocatalysis occurred (Huang et al., 2015).

Scaffolds filled with either HA1 or HA2 have shown higher bioactivity than non-filled PLA scaffolds by forming apatite precipitations on the fibre surfaces. However, the levels of bioactivity were lower than expected with only small thin patches of HCA layer formed on the fibres surface after 28 days of immersion in SBF (Figure 5.5). The decreased bioactivity level on the fibre surface was produced by the higher fibre diameter and thus encapsulation of the filler particles (Sadat-Shojai et al., 2016). Apatite formation on HA-containing scaffolds was also

confirmed by TGA analysis which showed an increase in weight after immersion in SBF. However, FTIR did not show any significant variations in scaffolds peaks after SBF immersion due to the high penetration depth of the ATR-FTIR used compared to the thickness of the apatite layer formed on the fibres surface.

Mechanical properties of non-filled and HA-filled scaffolds have shown a significant reduction after 14 days of immersion in SBF, while they were too fragile to test at day 28 of immersion. HA1-filled scaffolds exhibited faster decline in their tensile strength than HA2-filled scaffolds due to the larger specific surface area of the HA1 which permits increased water penetration through the cavities created at PLA/HA interface.

In addition to the effect of polymer and filler concentrations, fibre uniformity and diameter was also shown to be affected by the type of solvent used to prepare the electrospinning solutions. The average fibre diameter of electrospun PLA/HA2 was reduced from 18.43± 7.31μm to 6.82± 3.86 μm by changing the solvent system from chloroform to chloroform and acetone (2:1 ratio) while keeping the PLA and HA concentrations constant. However, reducing the fibre diameter led to increased HA agglomerations along the fibre due to the large particle size of the HA (d50= 3.59μm).

To optimise the core solution, PCL was dissolved using three solvent systems: chloroform, acetone, and 2:1 chloroform:acetone mixture. Electrospinning of PCL solution dissolved in the chloroform:acetone binary solvent system produced more homogeneous fibres compared to the other solvent systems, thus it was selected as the core solution.

SEM imaging of core and shell PCL-PLA/HA2 fibres with core:shell flow rate ratio of 3:3 showed uniform fibres with some HA protuberance on the surface of fibres in addition to an increased homogeneity in the fibre size distribution compared to fibres with 2:3 core:shell flow rate ratio.

The flow rate ratio between the core and shell solutions in coaxial electrospinning controlled coaxial fibre uniformity in addition to the layers dimensions. This in turn had a strong impact on the mechanical properties of the coaxial scaffolds which showed improved stiffness and strength values with increasing the core size within the fibres. The mechanical properties of coaxial PCL-PLA/HA2 fibres have

also shown higher tensile strength and ductility compared to single PLA/HA2 fibres.

Four different techniques, which were previously reported in literature, were employed in order to investigate the core and shell structure of the electrospun fibres produced with coaxial electrospinning including manual fibre fracture after immersing the scaffolds in liquid nitrogen, confocal microscopy with two different fluorescent dyes for the core and shell solutions, and embedding the fibres in resin and then slice them with ultramicrotome to image the cross sections with either SEM or TEM (Blackstone et al., 2014; Horner et al., 2016; Kalra et al., 2009; Peng et al., 2012). Among these techniques, examining the fibres cross sections with SEM or TEM have gave the most useful information about fibre structure, layers thickness, and HA embedding within the fibre. TEM and SEM images of coaxial fibres cross sections confirmed the presence of core and shell structure within control and HA-containing fibres at both 2:3 and 3:3 core:shell flow rate ratio. HA particles embedded in the shell layer were protruding either into the core layer or out of the surface of the fibres due to the large particle size.

Coaxial electrospinning using a rotating needle collector produced tubular scaffolds with increased circumferential fibre alignment compared to the 2D sheets obtained using a stationary collector. Fibre non-uniformity in HA-containing scaffolds increased due to the fibre stretching which occurred during electrospinning.

Tensile testing of tubular scaffolds exhibited anisotropic mechanical behaviour and showed decreased mechanical properties of both control and HA-containing scaffolds compared to the 2D sheets. Tubular scaffolds have also shown gradual reduction in their mechanical properties during 12 weeks of immersion in either PBS or SBF (Figure 7.8).

Immersion of coaxial HA-containing tubes in SBF for 28 days induced apatite precipitation on the fibre surface at significantly higher rates compared to PLA/HA1 and PLA/HA2 scaffolds produced with conventional electrospinning. The thickness and extent of the apatite layer was increased with increasing the immersion time. At week 12, large areas of HA-containing tubes were covered with thick layers of B-type carbonated apatite, while no apatite crystals were noticed on the surface of coaxial control samples due to the lack of active sites for apatite nucleation.

The obtained results thus have highlighted two important differences between single fibre obtained by the conventional single-needle electrospinning and core and shell structured fibre obtained by coaxial electrospinning in terms of fibre configuration which, in turn, had a strong impact on the bioactivity level and mechanical properties of the scaffolds before and after immersion in degradation solutions.

According to Tong et al. (2010), incorporation of filler particles into the electrospun fibres depends on the relative size of the fibres. If the diameter of the fibre is significantly larger than that of the filler particles, the particles can be totally encapsulated within the fibre, which can enhance the mechanical strength of the fibre, but reduce its bioactivity. However, if the diameters of both fibre and filler particles are similar, filler particles tend to encapsulate partially within the fibre which is beneficial for the bioactivity of the fibre, but not for its mechanical properties. In this study, Electrospun PLA/HA scaffolds made using single-needle electrospinning and chloroform alone as the solvent had enlarged fibre diameter and HA particles were almost fully encapsulated within the fibre (Figure 8.1A), which in turn reduced the bioactivity level of the scaffolds compared to the previously reported literature on HA-containing electrospun scaffolds (Hassan et al., 2014; Rajzer, 2014; Rajzer et al., 2014; Silva et al., 2014).

On the other hand, reducing fibre diameter by changing the solvent system into chloroform:acetone to increase the partial encapsulation of HA particles and enhance the bioactivity of the scaffold have also increased HA agglomerations within the fibres (Figure 8.1B). Aggregated HA particles act as stress concentrators and severely deteriorates the mechanical properties (Atif and Inam, 2016), thus the mechanical strength was reduced significantly (Table 6.3).

With core and shell PCL-PLA/HA fibre (Figure 8.1C), the large HA particles were embedded in shell layer of the fibre, which is significantly thinner than HA particle size, especially with 3:3 core-to-shell flow rate ratio. This forced HA particles to protrude out of the fibre surface as shown in TEM results (section 6.3.2), which led to significant increase in the rate of apatite precipitation on the coaxial fibre during SBF immersion due to increased direct HA contact with SBF which provided more nucleation sites on fibre surface. On the other hand, the mechanical strength of the fibres was less affected by the reduced fibre diameter or the partial encapsulation of HA due to the presence of the thick PCL core layer. These results

are consistent with those of Horner et al. (2016), who demonstrated that the mechanical properties of coaxial electrospun fibres can be regulated by controlling the composition and the dimension of the core layer, regardless of the shell chemistry. The presence of the core layer has also helped preserve the mechanical integrity of the coaxial scaffolds after immersion in degradation solutions compared to single fibre PLA/HA2 scaffolds as PCL has very slow degradation, thus the coaxial scaffolds were less affected by the increased water penetration.

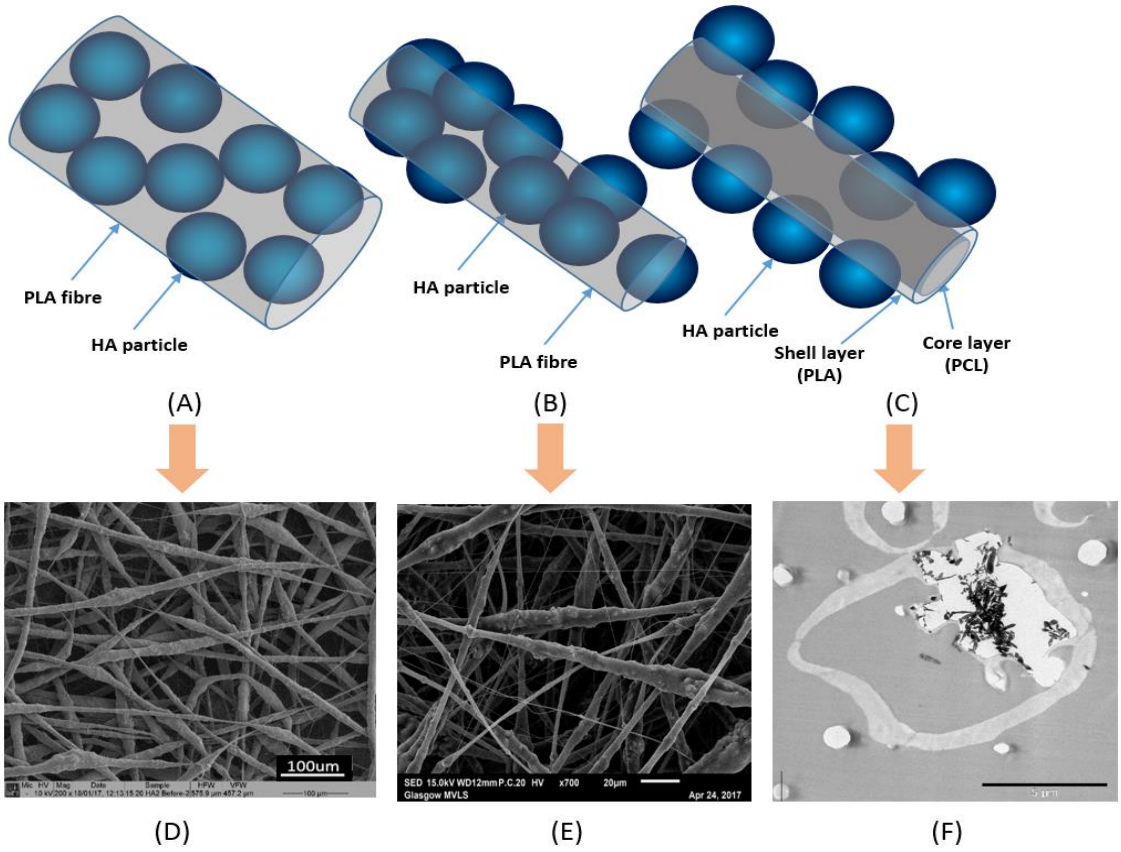

Figure 8.1 Schematic diagrams and micrographs showing HA microparticles incorporation in electrospun fibres (A) total encapsulation of HA particles within electrospun PLA/HA2 fibres obtained using chloroform as a solvent, (B) partial encapsulation of HA particles within electrospun PLA/HA2 fibres obtained using (2:1) chloroform: acetone solvent system, (C) partial encapsulation of HA particles within electrospun core and shell PCL-PLA/HA2 fibres, (D) Figure 5.1e showing SEM image of electrospun 15% PLA with 20% HA2 using chloroform alone, (E) Figure 6.4 showing SEM image of electrospun 15% PLA with 20% HA2 using (2:1) chloroform: acetone solvent system, and (F) Figure 6.14a showing TEM image of core and shell PCL-PLA/HA2 fibre with core: shell flow rate ratio of 3:3 (marker bars=100μm for D, 20μm for E, and 5μm for F)

The results in this research have also emphasised the role of fibre orientation, which was altered by changing the collector type from stationary to rotating collector, on the mechanical properties of the scaffolds. Although using a rotating needle collector did not yield a completely oriented fibre due to the low rotational speed of the collector used, the enhanced circumferential alignment of the tubular scaffolds fibre compared to the 2D sheets have significantly affected the mechanical behaviour of the scaffolds. The tubular scaffolds, which were tested perpendicular to the main fibre orientation, have shown reduced stiffness and strength compared to the randomly oriented 2D sheet despite having the same fibre composition. This is because the direction of the applied load during the tensile testing of aligned fibre scaffolds governs their mechanical behaviour (Kumar and Vasita, 2017; Nerurkar et al., 2007). In addition, Wei et al. (2009) have suggested that the increase in fibres fusion in the randomly oriented scaffolds would increase their strength compared to the aligned fibres with less fibres fusion. Thus, the mechanical properties of electrospun scaffolds is also dependent on the degree of fusion among the fibres. The increased fibre non-uniformity and HA protuberances for HA-containing fibres resulted from using a slowly rotating needle collector might also contributed to the increased bioactivity level of the tubes during SBF immersion.

Chapter 9- Conclusions and Future Work

9.1 Conclusions

From the results presented in this thesis the following conclusions can be drawn:

1. Electrospinnibility of polymeric solution and the morphology of the resultant fibres depend largely on the viscosity of the solution, which in turn is effected by the type of polymer used, solvent system, polymer concentration and filler concentration.

2. PLA dissolved in chloroform at concentrations between 15 and 20 wt% produced uniform non-woven electrospun fibres, while solutions with PLA concentration less than 15 wt% or higher than 20 wt% were not spinnible due to too high or too low viscosity.

3. HA1 and HA2 particles was found to be well dispersed in electrospun 15 and 20 wt% PLA fibres up to the addition of 20 vol% (~40 wt%), however increasing the HA content beyond 20 vol% disrupted electrospinning process due to the high viscosity of the PLA/HA solution.

4. Electrospinning of PLA solutions with either 10 or 20 vol% TCP produced scaffolds with TCP agglomeration along the fibres.

5. The tensile properties of electrospun PLA scaffolds were significantly decreased with increasing filler content. Electrospun PLA scaffolds with TCP showed further decrease in their stiffness and tensile strength values compared to PLA scaffolds filled with HA1 or HA2.

6. PLA composites filled with TCP had faster degradation rate than non-filled and HA-filled PLA scaffolds due to the high solubility of TCP. On the other hand, introducing HA1 or HA2 into PLA scaffolds led to slower degradation and higher in vitro bioactivity compared to non-reinforced PLA scaffolds.

7. Electrospinning with highly volatile solvents such as chloroform leads to nanopores formation along the fibres.

8. Increasing filler content or filler surface area did not affect the porosity of electrospun PLA fibres.

9. Electrospun PLA fibres showed decreased thermal stability compared to bulk PLA due to the higher surface area of the electrospun fibres.

10. Increasing filler surface area leads to enhanced thermal stability as it provides better insulation against thermal degradation of the polymer.

11. The bioactivity level of HA1 and HA2-filled scaffolds was not significantly affected by HA surface area. However, it was affected by the fibre diameter and the presence of HA particles on the surface of the fibres.

12. Mechanical stability of HA2-filled scaffolds in vitro over 14 days was higher than HA1-filled scaffolds due to enhanced dispersion of HA2 within PLA matrix and reduced cavities in PLA/HA2 interface.

13. Fibre uniformity and the dimension of core and shell layers in coaxial electrospinning depend on the flow rate ratio between the core and shell solutions. Coaxial electrospun scaffolds with 3:3 core:shell flow rate ratio had more even fibre diameter distribution and larger core size compare to scaffolds with 1:3 and 2:3 core:shell flow rate ratio.

14. Inclusion of PCL as core component significantly increased the tensile strength and ductility of HA-containing scaffolds.

15. The mechanical properties of coaxial scaffolds can be tailored by modulating the thickness and structure of the core and shell layers of the fibres.

16. Coaxial scaffolds with and without HA incorporation exhibited gradual and sustained BMP-2 release with only 3.2-3.4% of the protein released over the first 96h.

17. Electrospinning with a rotating needle collector improves fibre alignment compared to a stationary collector while increasing HA-containing fibre non-uniformity. However, it does not affect fibre diameter significantly.

18. Coaxial PCL-PLA/HA2 fibres exhibited significantly higher bioactivity compared to PLA/HA scaffolds due to higher exposure of HA particles on the fibre surface. Apatite formation increased with increasing SBF immersion time.

19. Coaxial tubular scaffolds with and without HA incorporation showed gradual loss in their mechanical properties over 12 weeks of immersion on PBS or SBF while preserving their structural integrity. Thus, they exhibited significantly higher mechanical stability in vitro compared to non-filled and HA-filled PLA scaffolds which lost their structural integrity after 28 days of immersion in SBF.

9.2 Future work

1. While the produced coaxial scaffolds in this study had high bioactivity level and good mechanical stability in vitro, the mechanical properties are still not high enough for load bearing applications, thus consideration must be given to combine coaxial electrospinning with other scaffolds manufacturing techniques to enhance the mechanical properties. For example, combining coaxial PCL-PLA/HA2 scaffolds with self-reinforced PLA-PLA-TCP composites manufactured using pre-pregging process (Bleach, 2001; Mustafa, 2012), where the self-reinforced composites can form the core of the combined scaffold to provide the mechanical strength while the coaxial PCL-PLA/HA2 electrospun fibres form the outer layer to provide good bioactivity and cell attachment.
2. Measuring BMP-2 release from the coaxial scaffolds with and without HA incorporation over 28 days to determine the release mechanism of the scaffolds and examine the effect of HA incorporation on protein release over long period.
3. Further cell culture work should be carried out on the coaxial scaffolds to fully assess the in vitro biological response.
4. Optimise the core component of coaxial scaffolds using different polymers, copolymers, or polymer blends to improve the mechanical strength of the scaffolds.

5. The effect of collector size and speed on coaxial fibre morphology and orientation needs to be investigated.
6. Examine the mechanical behaviour of tubular coaxial scaffolds at different load directions, thus quantifying the anisotropy.
7. The effect of using nano-sized HA particles instead of micro-sized HA on the mechanical properties and bioactivity of coaxial scaffolds needs to investigated.

References

Abd Mutalib, M., Rahman, M.A., Othman, M.H.D., Ismail, A.F., Jaafar, J., 2017. Scanning Electron Microscopy (SEM) and Energy-Dispersive X-Ray (EDX) sectroscopy. In: Hilal, N., Ismail, A., Matsuura, T., Oatley-Radcliffe, D. (Eds.), Membrane Characterization. Elsevier B.V., pp. 161–179.

Affandi, N.D.N., Truong, Y.B., Kyratzis, I.L., Padhye, R., Arnold, L., 2010. A non-destructive method for thickness measurement of thin electrospun membranes using white light profilometry. J. Mater. Sci. 45, 1411–1418.

Agarwal, S., Wendorff, J.H., Greiner, A., 2008. Use of electrospinning technique for biomedical applications. Polymer. 49, 5603–5621.

Agrawal, C.M., Ray, R.B., 2001. Biodegradable polymeric scaffolds for musculoskeletal tissue engineering. J. Biomed. Mater. Res. 55, 141–150.

Akbarzadeh, R., Yousefi, A.M., 2014. Effects of processing parameters in thermally induced phase separation technique on porous architecture of scaffolds for bone tissue engineering. J. Biomed. Mater. Res. - Part B Appl. Biomater. 102, 1304–1315.

Akter, F., Ibanez, J., 2016. Bone and Cartilage Tissue Engineering. In: Akter, F. (Ed.), Tissue Engineering Made Easy. Elsevier Inc., pp. 77–97.

Alfaro De Prá, M.A., Ribeiro-do-Valle, R.M., Maraschin, M., Veleirinho, B., 2017. Effect of collector design on the morphological properties of polycaprolactone electrospun fibers. Mater. Lett. 193, 154–157.

Allen, M.R., Burr, D.B., 2013. Bone Modeling and Remodeling. In: Burr, D.B., Allen, M.R. (Eds.), Basic and Applied Bone Biology. Elsevier Inc., pp. 75–90.

Amini, A.R., Laurencin, C.T., Nukavarapu, S.P., 2012. Bone tissue engineering: recent advances and challenges. Crit. Rev. Biomed. Eng. 40, 363–408.

Andrady, A.L., 2007. Factors affecting nanofiber quality. In: Andrady, A.L. (Ed.), Science and Technology of Polymer Nanofibers. John Wiley & Sons, Inc, pp. 81–110.

Aragon, J., Navascues, N., Mendoza, G., Irusta, S., 2017. Laser-treated electrospun fibers loaded with nano-hydroxyapatite for bone tissue engineering. Int. J. Pharm. 525, 112–122.

Arsad, M.S.M., Lee, P.M., Hung, L.K., 2010. Morphology and particle size analysis of hydroxyapatite micro- and nano-particles. In: CSSR 2010 - 2010 International Conference on Science and Social Research. pp. 1030–1034.

Ascenzi, A., Bonucci, E., 1967. The Tensile Properties of Single Osteons. Anat. Rec. 158, 375–386.

Ascenzi, A., Bonucci, E., 1968. The compressive properties of single osteons. Anat. Rec. 161, 377–391.

Atif, R., Inam, F., 2016. Reasons and remedies for the agglomeration of multilayered graphene and carbon nanotubes in polymers. Beilstein J. Nanotechnol. 7, 1174–1196.

Augustine, R., Thomas, S., Kalarikkal, N., 2014. In Vitro Degradation of

Electrospun Polycaprolactone Membranes in Simulated Body Fluid 211–220.

Azevedo, H., Reis, R., 2004. Understanding the enzymatic degradation of biodegradable polymers and strategies to control their degradation rate. In: Reis, R.L., Román, J.S. (Eds.), Biodegradable Systems in Tissue Engineering and Regenerative Medicine. CRC Press LLC, pp. 177–202.

Azimi, B., Nourpanah, P., Rabiee, M., Arbab, S., 2014. Poly (ε-caprolactone) fiber: An overview. J. Eng. Fiber. Fabr. 9, 74–90.

Bambole, V., Yakhmi, J.V., 2016. Tissue engineering: Use of electrospinning technique for recreating physiological functions. In: Grumezescu, A. (Ed.), Nanobiomaterials in Soft Tissue Engineering: Applications of Nanobiomaterials. Elsevier Inc., pp. 387–455.

Bartold, P.M., Xiao, Y., Lyngstaadas, S.P., Paine L., M.L., Snead, M.L., 2006. Principles and applications of cell delivery systems for periodontal regeneration. Periodontology 41, 123–135.

Belinha, J., 2014. Bone Tissue. In: Belinha, J. (Ed.), Meshless Methods in Biomechanics: Bone Tissue Remodelling Analysis. Springer, pp. 221–249.

Bellido, T., Plotkin, L.I., Bruzzaniti, A., 2013. Bone Cells. In: Burr, D.B., Allen, M.R. (Eds.), Basic and Applied Bone Biology. Elsevier Inc., pp. 27–45.

Berzina-Cimdina, L., Borodajenko, N., 2012. Research of Calcium Phosphates Using Fourier Transform Infrared Spectroscopy. In: Theophanides Theophile (Ed.), Infrared Spectroscopy – Materials Science, Engineering and Technology. InTech, pp. 123–148.

Best, S.M., Porter, A.E., Thian, E.S., Huang, J., 2008. Bioceramics: Past, present and for the future. J. Eur. Ceram. Soc. 28, 1319–1327.

Bhardwaj, N., Kundu, S.C., 2010. Electrospinning: A fascinating fiber fabrication technique. Biotechnol. Adv. 28, 325–347.

Bianco, A., Bozzo, B.M., Del Gaudio, C., Cacciotti, I., Armentano, I., Dottori, M., D'Angelo, F., Martino, S., Orlacchio, A., Kenny, J.M., 2011. Poly (L-lactic acid)/calcium-deficient nanohydroxyapatite electrospun mats for bone marrow stem cell cultures. J. Bioact. Compat. Polym. 26, 225–241.

Blackstone, B.N., Drexler, J.W., Powell, H.M., 2014. Tunable engineered skin mechanics via coaxial electrospun fiber core diameter. Tissue Eng. Part A 20, 2746–55.

Bleach, N.C., 2001. Optimisation of degradable bioactive polymer composites. Queen Mary, University of London.

Bognitzki, M., Czado, W., Frese, T., Schaper, A., Hellwig, M., Steinhart, M., Greiner, A., Wendorff, J.H., 2001. Nanostructured Fibers via Electrospinning. Adv. Mater. 13, 70–72.

Bonucci, E., 2000. Basic Composition and Structure of Bone. In: Yuehuei H., A., Draughn, R.A. (Eds.), Mechanical Testing of Bone and the Bone-Implant Interface. CRC Press, pp. 3–17.

Bose, S., Roy, M., Bandyopadhyay, A., 2012. Recent advances in bone tissue engineering scaffolds. Trends Biotechnol. 30, 546–554.

Bosworth, L.A., Alam, N., Wong, J.K., Downes, S., 2013. Investigation of 2D and 3D electrospun scaffolds intended for tendon repair. J. Mater. Sci. Mater. Med. 24, 1605–1614.

British Standards Institution, 1999. Textiles — Tensile properties of fabrics. Part 1: Determination of maximum force and elongation at maximum force using the strip method. BS ISO 13934-1.

Brown, T.D., Slotosch, A., Thibaudeau, L., Taubenberger, A., Loessner, D., Vaquette, C., Dalton, P.D., Hutmacher, D.W., 2012. Design and fabrication of tubular scaffolds via direct writing in a melt electrospinning mode. Biointerphases 7, 1–16.

Brunski, J.B., 2013. Metals: Basic principles. In: Ratner, B.D., Allan S. Hoffman, Schoen, F.J., Lemons, J.E. (Eds.), Biomaterials Science: An Introduction to Materials in Medicine (Third Edition). Elsevier, pp. 111–119.

Budyanto, L., Goh, Y.Q., Ooi, C.P., 2009. Fabrication of porous poly(L-lactide) (PLLA) scaffolds for tissue engineering using liquid-liquid phase separation and freeze extraction. J. Mater. Sci. Mater. Med. 20, 105–111.

Burr, D.B., Akkus, O., 2013. Bone Morphology and Organization. In: Burr, D.B., Allen, M.R. (Eds.), Basic and Applied Bone Biology. Elsevier Inc., pp. 3–25.

Butcher, A.L., Koh, C.T., Oyen, M.L., 2017. Systematic mechanical evaluation of electrospun gelatin meshes. J. Mech. Behav. Biomed. Mater. 69, 412–419.

Cai, S., Xu, H., Jiang, Q., Yang, Y., 2013. Novel 3D electrospun scaffolds with fibers oriented randomly and evenly in three dimensions to closely mimic the unique architectures of extracellular matrices in soft tissues: Fabrication and mechanism study. Langmuir 29, 2311–2318.

Cameron, R.E., Kamvari-Moghaddam, A., 2012. Synthetic bioresorbable polymers. In: Jenkins, M., Stamboulis, A. (Eds.), Durability and Reliability of Medical Polymers. Woodhead Publishing Limited, pp. 96–118.

Canillas, M., Pena, P., De Aza, A.H., Rodríguez, M.A., 2017. Calcium phosphates for biomedical applications. Bol. la Soc. Esp. Ceram. y Vidr. 56, 91–112.

Caplan, A., 1991. Mesenchymal stem cells. J. Orthop. Res. 9, 641–50.

Cardon, L.K., Ragaert, K.J., Koster, R.P., 2010. Design and fabrication of biocomposites. In: Ambrosio, L. (Ed.), Biomedical Composites. CRC Press, pp. 25–43.

Carrodeguas, R.G., De Aza, S., 2011. α-Tricalcium phosphate: Synthesis, properties and biomedical applications. Acta Biomater. 7, 3536–3546.

Casasola, R., Thomas, N.L., Trybala, A., Georgiadou, S., 2014. Electrospun poly lactic acid (PLA) fibres: Effect of different solvent systems on fibre morphology and diameter. Polymer. 55, 4728–4737.

Castro-Aguirre, E., Iñiguez-Franco, F., Samsudin, H., Fang, X., Auras, R., 2016. Poly(lactic acid)—Mass production, processing, industrial applications, and end of life. Adv. Drug Deliv. Rev. 107, 333–366.

Castro, F., Ferreira, A., Rocha, F., Vicente, A., António Teixeira, J., 2012. Characterization of intermediate stages in the precipitation of hydroxyapatite at 37°C. Chem. Eng. Sci. 77, 150–156.

Causa, F., Netti, P.A., Ambrosio, L., Ciapetti, G., Baldini, N., Pagani, S., Martini, D., Giunti, A., 2006. Poly-ε-caprolactone/hydroxyapatite composites for bone regeneration: In vitro characterization and human osteoblast response. J. Biomed. Mater. Res. - Part A 76, 151–162.

Chakaravarthi, S.S., Robinson, D.H., 2009. Biodegradation and autocatalysis of polylactides. In: Wuisman, P.I.J.., Smit, T.H. (Eds.), Degradable Polymers for Skeletal Implants. Nova Science Publishers, pp. 167–180.

Chan, K.H.K., Kotaki, M., 2009. Fabrication and morphology control of poly(methyl methacrylate) hollow structures via coaxial electrospinning. J. Appl. Polym. Sci. 111, 408–416.

Chandra, R., Rustgi, R., 1998. Biodegradable polymers. Prog. Polym. Sci. 23, 1273–1335.

Chen, G.-M., Zou, T.-M., Chen, L., Huang, Y.-P., 2010. Crystallization properties of polycaprolactone induced by different hydroxyapatite nano-particles. Asian J. Chem. 22, 5902–5912.

Chen, H., Peng, Y., Wu, S., Tan, L.P., 2016. Electrospun 3D fibrous scaffolds for chronic wound repair. Materials. 9, 1–12.

Chen, J.H., Liu, C., You, L., Simmons, C.A., 2010. Boning up on Wolff's Law: Mechanical regulation of the cells that make and maintain bone. J. Biomech. 43, 108–118.

Chen, M., Patra, P.K., Warner, S.B., Bhowmick, S., 2007. Role of fiber diameter in adhesion and proliferation of NIH 3T3 fibroblast on electrospun polycaprolactone scaffolds. Tissue Eng. 13, 579–587.

Chen, R., Huang, C., Ke, Q., He, C., Wang, H., Mo, X., 2010. Preparation and characterization of coaxial electrospun thermoplastic polyurethane/collagen compound nanofibers for tissue engineering applications. Colloids Surfaces B Biointerfaces 79, 315–325.

Chen, Z., Song, Y., Zhang, J., Liu, W., Cui, J., Li, H., Chen, F., 2017. Laminated electrospun nHA/PHB-composite scaffolds mimicking bone extracellular matrix for bone tissue engineering. Mater. Sci. Eng. C 72, 341–351.

Chieng, B.W., Ibrahim, N.A., Yunus, W.M.Z.W., Hussein, M.Z., 2014. Poly(lactic acid)/poly(ethylene glycol) polymer nanocomposites: Effects of graphene nanoplatelets. Polymers. 6, 93–104.

Chlopek, J., Morawska-Chochol, A., Paluszkiewicz, C., Jaworska, J., Kasperczyk, J., Dobrzyński, P., 2009. FTIR and NMR study of poly(lactide-co-glycolide) and hydroxyapatite implant degradation under in vivo conditions. Polym. Degrad. Stab. 94, 1479–1485.

Choi, E.J., Son, B., Hwang, T.S., Hwang, E.H., 2011. Increase of degradation and water uptake rate using electrospun star-shaped poly(d,l-lactide) nanofiber. J. Ind. Eng. Chem. 17, 691–695.

Claxton, N.S., Fellers, T.J., Davidson, M.W., 2006. Laser scanning confocal microscopy. Encycl. Med. Devices Instrum. 1979, 1–37.

Coathup, M.J., Cai, Q., Campion, C., Buckland, T., Blunn, G.W., 2013. The effect of particle size on the osteointegration of injectable silicate-substituted

calcium phosphate bone substitute materials. J. Biomed. Mater. Res. - Part B Appl. Biomater. 101 B, 902–910.

Coles, S.R., Wooldridge, A., 2015. Optimising solutions for electrospinning. In: Mitchell, G.R. (Ed.), Electrospinning: Principles, Practice and Possibilities. The Royal Society of Chemistry, pp. 57–70.

Colnot, C., 2011. Cell sources for bone tissue engineering: Insights from basic science. Tissue Eng. Part B Rev. 17, 449–457.

Cooley, J.F., 1902. Apparatus for electrically dispersing fluids. 692631.

Cools, P., Ghobeira, R., Van Vrekhem, S., De Geyterand, N., Morent, R., 2016. Non-thermal plasma technology for the improvement of scaffolds for tissue engineering and regenerative medicine - A review. In: Mieno, T. (Ed.), Plasma Science and Technology - Progress in Physical States and Chemical Reactions. InTech, pp. 173–211.

Croisier, F., Duwez, A.S., Jérôme, C., Léonard, A.F., Van Der Werf, K.O., Dijkstra, P.J., Bennink, M.L., 2012. Mechanical testing of electrospun PCL fibers. Acta Biomater. 8, 218–224.

Cui, W., Li, X., Zhu, X., Yu, G., Zhou, S., Weng, J., 2006. Investigation of drug release and matrix degradation of electrospun poly(DL-lactide) fibers with paracetanol inoculation. Biomacromolecules 7, 1623–1629.

Currey, J.D., 2002. The structure of bone tissue. In: Bones: Structure and Mechanics. Princeton University Press, pp. 3–27.

Davis, F.J., Mohan, S.D., Ibraheem, M.A., 2015. Introduction. In: Mitchell, G.R. (Ed.), Electrospinning: Principles, Practice and Possibilities. The Royal Society of Chemistry, pp. 1–21.

Davis, R., Mauer, L., 2010. Fourier transform infrared (FT-IR) spectroscopy: a rapid tool for detection and analysis of foodborne pathogenic bacteria. In: Mendez-Vilas, A. (Ed.), Current Research, Technology and Education Topics in Applied Microbiology and Microbial Biotechnology. Formatex Research Center, pp. 1582–1594.

de Guzman, R.C., Saul, J.M., Ellenburg, M.D., Merrill, M.R., Coan, H.B., Smith, T.L., Van Dyke, M.E., 2013. Bone regeneration with BMP-2 delivered from keratose scaffolds. Biomaterials 34, 1644–1656.

de With, G., Glass, H.J., 1997. Reliability and reproducibility of mercury intrusion porosimetry. J. Eur. Ceram. Soc. 17, 753–757.

Deitzel, J.., Kleinmeyer, J., Harris, D., Beck Tan, N.C., 2001. The effect of processing variables on the morphology of electrospun nanofibers and textiles. Polymer. 42, 261–272.

Deng, M., Kumbar, S.G., Nair, L.S., Weikel, A.L., Allcock, H.R., Laurencin, C.T., 2011. Biomimetic structures: Biological implications of dipeptide-substituted polyphosphazene-polyester blend nanofiber matrices for load-bearing bone regeneration. Adv. Funct. Mater. 21, 2641–2651.

Deng, X.-L., Sui, G., Zhao, M.-L., Chen, G.-Q., Yang, X.-P., 2007. Poly(L-lactic acid)/hydroxyapatite hybrid nanofibrous scaffolds prepared by electrospinning. J. Biomater. Sci. Polym. Ed. 18, 117–130.

Destainville, A., Champion, E., Bernache-Assollante, D., 2003. Synthesis, characterization and thermal behaviour of apatite tricalcium phosphate. Mater. Chem. Phys. 240–242, 489–492.

Díaz, J.E., Barrero, A., Márquez, M., Loscertales, I.G., 2006. Controlled encapsulation of hydrophobic liquids in hydrophilic polymer nanofibers by co-electrospinning. Adv. Funct. Mater. 16, 2110–2116.

Doan, T.Q., Leslie, L.S., Kim, S.Y., Bhargava, R., White, S.R., Sottos, N.R., 2016. Characterization of core-shell microstructure and self-healing performance of electrospun fiber coatings. Polymer. 107, 263–272.

Dong, Y., Liao, S., Ngiam, M., Chan, C.K., Ramakrishna, S., 2009. Degradation Behaviors of Electrospun Resorbable Polyester Nanofibers. Tissue Eng. Part B Rev. 15, 333–351.

Dorozhkin, S. V., 2009a. Calcium orthophosphates in nature, biology and medicine. Materials. 2, 399–498.

Dorozhkin, S. V., 2009b. Calcium orthophosphate-based biocomposites and hybrid biomaterials. J. Mater. Sci. 44, 2343–2387.

Dorozhkin, S. V., 2013. Calcium orthophosphate-based bioceramics. Materials. 6, 3840–3942.

Dorozhkin, S. V., 2016. Biological properties and in vivo behavior. In: Calcium Orthophosphate-Based Bioceramics and Biocomposites. Wiley-VCH, pp. 205–226.

Dorozhkin, S. V, Epple, M., 2002. Biological and medical significance of calcilum phosphates. Angew. Chemie Int. Ed. 41, 3130–3146.

Doshi, J., Reneker, D.H., 1995. Electrospinning process and applications of electrospun fibers. J. Electrostat. 35, 151–160.

Doustgani, A., 2016. The effect of electrospun poly (lactic acid) and nanohydroxyapatite nanofibers' diameter on proliferation and differentiation of mesenchymal stem cells. Nanomedicine J. 3, 217–222.

Downes, R.N., Vardy, S., Tanner, K.E., Bonfield, W., 1991. Hydroxyapatite-polyethylene composite in ophthalmic surgery. In: Bonfield, W., Hastings, G.W., Tanner, K.E. (Eds.), Bioceramics: Proceedings of the 4th International Symposium on Ceramics in Medicine. Butterworth-Heinnemann Ltd, pp. 239–246.

Du, L., Xu, H., Zhang, Y., Zou, F., 2016. Electrospinning of polycaprolatone nanofibers with DMF additive: The effect of solution proprieties on jet perturbation and fiber morphologies. Fibers Polym. 17, 751–759.

Duan, N., Geng, X., Ye, L., Zhang, A., Feng, Z., Guo, L., Gu, Y., 2016. A vascular tissue engineering scaffold with core–shell structured nano-fibers formed by coaxial electrospinning and its biocompatibility evaluation. Biomed. Mater. 11, 035007.

Dunne, M., Corrigan, O.I., Ramtoola, Z., 2000. Influence of particle size and dissolution conditions on the degradation properties of polylactide-co-glycolide particles. Biomaterials 21, 1659–1668.

Dziadek, M., Zagrajczuk, B., Menaszek, E., Dziadek, K., Cholewa-Kowalska, K.,

2017. Poly(ε-caprolactone)-based membranes with tunable physicochemical, bioactive and osteoinductive properties. J. Mater. Sci. 52, 12960–12980.

Eda, G., Liu, J., Shivkumar, S., 2007. Solvent effects on jet evolution during electrospinning of semi-dilute polystyrene solutions. Eur. Polym. J. 43, 1154–1167.

Eda, G., Shivkumar, S., 2007. Bead-to-fiber transition in electrospun polystyrene. J. Appl. Polym. Sci. 106, 475–487.

Eggli, P.S., Muller, W., Schenk, R.K., 1988. Porous hydroxyapatite and tricalcium phosphate cylinders with two different pore size ranges implanted in the cancellous bone of rabbits. A comparative histomorphometric and histologic study of bony ingrowth and implant substitution. Clin. Orthop. Relat. Res. 232, 127–138.

Elahi, F., Lu, W., Guoping, G., Khan, F., 2013. Core-shell Fibers for Biomedical Applications - A Review. Bioeng. Biomed. Sci. J. 3, 1–14.

Eliaz, N., Metoki, N., 2017. Calcium phosphate bioceramics: A review of their history, structure, properties, coating technologies and biomedical applications. Materials. 10.

Elzein, T., Nasser-Eddine, M., Delaite, C., Bistac, S., Dumas, P., 2004. FTIR study of polycaprolactone chain organization at interfaces. J. Colloid Interface Sci. 273, 381–387.

Ergun, C., Liu, H., Webster, T.J., Olcay, E., Yilmaz, Ş., Sahin, F.C., 2008. Increased osteoblast adhesion on nanoparticulate calcium phosphates with higher Ca/P ratios. J. Biomed. Mater. Res. - Part A 85, 236–241.

Eriksen, E.F., 2010. Cellular mechanisms of bone remodeling. Rev. Endocr. Metab. Disord. 11, 219–227.

Essien, E.R., Adams, L.A., Igbari, F.O., 2016. Mechanical properties and in vitro physico-chemical reactivity of gel-derived SiO2 -Na2O-CaO-P2O5 glass from sand. J. Chinese Chem. Soc. 63, 618–626.

Fathi, M., Yacoubi, A. El, Massit, A., Chafik, B., Idrissi, E., 2015. Wet chemical method for preparing high purity α and β -tricalcium phosphate crystalline powders. Int. J. Sci. Eng. Res. 6, 139–143.

Feller, L., Jadwat, Y., Khammissa, R.A.G., Meyerov, R., Schechter, I., Lemmer, J., 2015. Cellular responses evoked by different surface characteristics of intraosseous titanium implants. Biomed Res. Int. 2015, 1–8.

Ferreira, J.L., Gomes, S., Henriques, C., Borges, J.P., Silva, J.C., 2014. Electrospinning polycaprolactone dissolved in glacial acetic acid: Fiber production, nonwoven characterization, and in vitro evaluation. J. Appl. Polym. Sci. 131, 37–39.

Fihri, A., Len, C., Varma, R.S., Solhy, A., 2017. Hydroxyapatite: A review of syntheses, structure and applications in heterogeneous catalysis. Coord. Chem. Rev. 347, 48–76.

Fouad, H., Elsarnagawy, T., Almajhdi, F.N., Khalil, K.A., 2013. Preparation and in vitro thermo-mechanical characterization of electrospun PLGA nanofibers for soft and hard tissue replacement. Int. J. Electrochem. Sci. 8, 2293–2304.

Frasnelli, M., Sglavo, V.M., 2016. Effect of Mg2+doping on beta-alpha phase transition in tricalcium phosphate (TCP) bioceramics. Acta Biomater. 33, 283–289.

Fratzl, P., Weinkamer, R., 2007. Nature's hierarchical materials. Prog. Mater. Sci. 52, 1263–1334.

Fu, Q.-W., Zi, Y.-P., Xu, W., Zhou, R., Cai, Z.-Y., Zheng, W.-J., Chen, F., Qian, Q.-R., 2016. Electrospinning of calcium phosphate-poly(D,L-lactic acid) nanofibers for sustained release of water-soluble drug and fast mineralization. Int. J. Nanomedicine 11, 5087–5097.

Gahhos, F., Ariyan, S., 1984. Facial fractures: Hippocratic management. Head Neck Surg. 6, 1007–1013.

Gajjar, C.R., King, M.W., 2014. Resorbable Fiber-Forming Polymers for Biotextile Applications. In: Resorbable Fiber-Forming Polymers for Biotextile Applications. Springer International Publishing, pp. 7–10.

Ganz, J., 2015. Hippocrates, Celsus and Galen: Head Injury, the Brain, and the Bone. Hist. Med. 2, 78–88.

Gao, C., Peng, S., Feng, P., Shuai, C., 2017. Bone biomaterials and interactions with stem cells. Bone Res. 5, 17059.

Garg, T., Singh, O., Arora, S., Murthy, R.S.., 2012. Scaffold: A Novel Carrier for Cell and Drug Delivery. Crit. Rev. Ther. Drug Carr. Syst. 29, 1–63.

Garlotta, D., 2002. A Literature Review of Poly (Lactic Acid). J. Polym. Environ. 9, 63–84.

Gentleman, E., Ball, M.D., Stevens, M.M., 2009. Biomaterials. In: Medical Sciences. Encyclopedia of Life Support Systems (EOLSS), pp. 43–86.

Ghanbarzadeh, B., Almasi, H., 2013. Biodegradable polymers. In: Chamy, R. (Ed.), Biodegradation Life of Science. InTech, pp. 141–185.

Ghasemi-Mobarakeh, L., Semnani, D., Morshed, M., 2007. A novel method for porosity measurement of various surface layers of nanofibers mat using image analysis for tissue engineering applications. J. Appl. Polym. Sci. 106, 2536–2542.

Ghosh, R., Sarkar, R., 2016. Synthesis and characterization of sintered beta-tricalcium phosphate: A comparative study on the effect of preparation route. Mater. Sci. Eng. C 67, 345–352.

Ghosh, S.K., Nandi, S.K., Kundu, B., Datta, S., De Dipak, K., Roy, S.K., Basu, D., 2008. In vivo response of porous hydroxyapatite and β-tricalcium phosphate prepared by aqueous solution combustion method and comparison with bioglass scaffolds. J. Biomed. Mater. Res. - Part B Appl. Biomater. 86, 217–227.

Giraud-Guille, M.M., 1988. Twisted plywood architecture of collagen fibrils in human compact bone osteons. Calcif. Tissue Int. 42, 167–180.

Giunchedi, P., Conti, B., Scalia, S., Conte, U., 1998. In vitro degradation study of polyester microspheres by a new HPLC method for monomer release determination. J. Control. Release 56, 53–62.

Golecki, H.M., Yuan, H., Glavin, C., Potter, B., Badrossamay, M.R., Goss, J.A., Phillips, M.D., Parker, K.K., 2014. Effect of solvent evaporation on fiber morphology in rotary jet-spinning. Langmuir 30, 13369–13374.

Gombotz, W.R., Petite, D.K., 1995. Biodegradable Polymers for Protein and Peptide Drug Delivery. Bioconjug. Chem. 6, 332–351.

Gonçalves, R.P., da Silva, F.F.F., Picciani, P.H.S., Dias, M.L., 2015. Morphology and Thermal Properties of Core-Shell PVA/PLA Ultrafine Fibers Produced by Coaxial Electrospinning. Mater. Sci. Appl. 06, 189–199.

Göpferich, A., 1996. Mechanisms of polymer degradation and erosion. Biomaterials 17, 103–114.

Göpferich, A., Tessmar, J., 2002. Polyanhydride degradation and erosion. Adv. Drug Deliv. Rev. 54, 911–931.

Greiner, A., Wendorff, J.H., 2007. Electrospinning: A fascinating method for the preparation of ultrathin fibers. Angew. Chemie - Int. Ed. 46, 5670–5703.

Groeneveld, E.H., Burger, E.H., 2000. Bone morphogenetic proteins in human bone regeneration. Eur. J. Endocrinol. 142, 9–21.

Grøndahl, L., Jack, K.S., 2010. Composite materials for bone repair. In: L. Ambrosio (Ed.), Biomedical Composites. CRC Press, pp. 101–126.

Gu, S.-Y., Ren, J., 2005. Process optimization and empirical modeling for electrospun poly(D,L-lactide) fibers using response surface methodology. Macromol. Mater. Eng. 290, 1097–1105.

Gu, X., Song, X., Shao, C., Zeng, P., Lu, X., Shen, X., Yang, Q., 2014. Electrospinning of poly(butylene-carbonate): Effect of solvents on the properties of the nanofibers film. Int. J. Electrochem. Sci. 9, 8045–8056.

Guarino, V., Causa, F., Taddei, P., di Foggia, M., Ciapetti, G., Martini, D., Fagnano, C., Baldini, N., Ambrosio, L., 2008. Polylactic acid fibre-reinforced polycaprolactone scaffolds for bone tissue engineering. Biomaterials 29, 3662–3670.

Habibovic, P., Sees, T.M., van den Doel, M.A., van Blitterswijk, C.A., de Groot, K., 2006. Osteoinduction by biomaterials—Physicochemical and structural influence. J. Biomed. Mater. Res. 77A, 747–762.

Habraken, W., Habibovic, P., Epple, M., Bohner, M., 2016. Calcium phosphates in biomedical applications: Materials for the future? Mater. Today 19, 69–87.

Haider, A., Haider, S., Kang, I.K., 2015. A comprehensive review summarizing the effect of electrospinning parameters and potential applications of nanofibers in biomedical and biotechnology. Arab. J. Chem. In press.

Han, S.O., Son, W.K., Youk, J.H., Lee, T.S., Park, W.H., 2005. Ultrafine porous fibers electrospun from cellulose triacetate. Mater. Lett. 59, 2998–3001.

Hannink, G., Arts, J.J.C., 2011. Bioresorbability, porosity and mechanical strength of bone substitutes: What is optimal for bone regeneration? Injury 42, S22–S25.

Hart, N.H., Nimphius, S., Rantalainen, T., Ireland, A., Siafarikas, A., Newton, R.U., 2017. Mechanical basis of bone strength: Influence of bone material,

bone structure and muscle action. J. Musculoskelet. Neuronal Interact. 17, 114–139.

Hassan, M.I., Sultana, N., Hamdan, S., 2014. Bioactivity assessment of poly (ε-caprolactone)/ hydroxyapatite electrospun fibers for bone tissue engineering application. J. Nanomater. 2014.

Hatakeyama, T., Quinn, F.X., 1999. Thermogravimetry. In: Thermal Analysis — Fundamentals and Applications to Polymer Science. Wiley, pp. 45–48.

He, C., Jin, X., Ma, P.X., 2014. Calcium phosphate deposition rate, structure and osteoconductivity on electrospun poly(l-lactic acid) matrix using electrodeposition or simulated body fluid incubation. Acta Biomater. 10, 419–427.

He, S., Li, X., Yang, Y., Jia, G., Zou, J., 2012. Correlations of in vitro and in vivo degradation tests on electrospun poly-DL-lactide-poly(ethylene glycol) fibers. J. Appl. Polym. Sci. 125, 2207–2215.

He, W., Ma, Z., Yong, T., Teo, W.E., Ramakrishna, S., 2005. Fabrication of collagen-coated biodegradable polymer nanofiber mesh and its potential for endothelial cells growth. Biomaterials 26, 7606–7615.

Hejazi, F., Mirzadeh, H., 2016. Roll-designed 3D nanofibrous scaffold suitable for the regeneration of load bearing bone defects. Prog. Biomater. 5, 1–13.

Hekmati, A.H., Khenoussi, N., Nouali, H., Patarin, J., Drean, J.Y., 2014. Effect of nanofiber diameter on water absorption properties and pore size of polyamide-6 electrospun nanoweb. Text. Res. J. 84, 2045–2055.

Hench, L.L., 1991. Bioceramics: From concept to clinic. J. Am. Ceram. Soc. 74, 1487–1510.

Hench, L.L., 1998. Bioceramics. J. Am. Ceram. Soc. 81, 1705–1728.

Hench, L.L., Best, S.M., 2013. Ceramics, glasses, and glass-ceramics: Basic principles. In: Ratner, B.D. (Ed.), Biomaterials Science: An Introduction to Materials: Third Edition. Elsevier, pp. 128–151.

Heo, S., Kim, S.-E., Wei, J., Kim, D.H., Hyun, Y., Yun, H., Kim, H.K., Yoon, T.R., 2009. In vitro and animal study of novel nano-hydroxyapatite/poly(epsilon-caprolactone) composite scaffolds fabricated by layer manufacturing process. Tissue Eng. Part A 15, 977–989.

Heydary, H.A., Karamian, E., Poorazizi, E., Heydaripour, J., Khandan, A., 2015. Electrospun of polymer/bioceramic nanocomposite as a new soft tissue for biomedical applications. J. Asian Ceram. Soc. 3, 417–425.

Hohman, M.M., Shin, M., Rutledge, G., Brenner, M.P., 2001. Electrospinning and electrically forced jets. II. Applications. Phys. Fluids 13, 2221–2236.

Horner, C.B., Ico, G., Johnson, J., Zhao, Y., Nam, J., 2016. Microstructure-dependent mechanical properties of electrospun core-shell scaffolds at multi-scale levels. J. Mech. Behav. Biomed. Mater. 59, 207–219.

Hotaling, N.A., Bharti, K., Kriel, H., Simon, C.G., 2015. DiameterJ: A validated open source nanofiber diameter measurement tool. Biomaterials 16, 327–338.

Hsu, C.M., Shivkumar, S., 2004a. N,N-dimethylformamide additions to the solution

for the electrospinning of poly(ε-caprolactone) nanofibers. Macromol. Mater. Eng. 289, 334–340.

Hsu, C.M., Shivkumar, S., 2004b. Nano-sized beads and porous fiber constructs of Poly(ε-caprolactone) produced by electrospinning. J. Mater. Sci. 39, 3003–3013.

Huang, C., Niu, H., Wu, J., Ke, Q., Mo, X., Lin, T., 2012. Needleless electrospinning of polystyrene fibers with an oriented surface line texture. J. Nanomater. 2012, 1–7.

Huang, F., Xu, Y., Peng, B., Su, Y., Jiang, F., Hsieh, Y. Lo, Wei, Q., 2015. Coaxial electrospun cellulose-core fluoropolymer-shell fibrous membrane from recycled cigarette filter as separator for high performance lithium-ion battery. ACS Sustain. Chem. Eng. 3, 932–940.

Huang, J., 2017. Design and development of ceramics and glasses. In: Vishwakarma, A., Karp, J. (Eds.), Biology and Engineering of Stem Cell Niches. Elsevier Inc., pp. 315–329.

Huang, J., Xiong, J., Liu, J., Zhu, W., Chen, J., Duan, L., Zhang, J., Wang, D., 2015. Evaluation of the novel three-dimensional porous poly (L-lactic acid)/nano-hydroxyapatite composite scaffold. Biomed. Mater. Eng. 26, S197–S205.

Huang, J., Xiong, J., Liu, J., Zhu, W., Wang, D., 2013. Investigation of the in vitro degradation of a novel polylactide/ nanohydroxyapatite composite for artificial bone. J. Nanomater. 2013.

Huang, Z.M., Zhang, Y.Z., Kotaki, M., Ramakrishna, S., 2003. A review on polymer nanofibers by electrospinning and their applications in nanocomposites. Compos. Sci. Technol. 63, 2223–2253.

Huang, Z.M., Zhang, Y.Z., Ramakrishna, S., Lim, C.T., 2004. Electrospinning and mechanical characterization of gelatin nanofibers. Polymer. 45, 5361–5368.

Hwang, C.M., Park, Y., Park, J.Y., Lee, K., Sun, K., Khademhosseini, A., Lee, S.H., 2009. Controlled cellular orientation on PLGA microfibers with defined diameters. Biomed. Microdevices 11, 739–746.

Ignjatovic, N., Suljovrujic, E., Budinski-Simendic, J., Krakovsky, I., Uskokovic, D., 2004. Evaluation of hot-pressed hydroxyapatite/poly-L-lactide composite biomaterial characteristics. J. Biomed. Mater. Res. - Part B Appl. Biomater. 71, 284–294.

Inkson, B.J., 2016. Scanning Electron Microscopy (SEM) and Transmission Electron Microscopy (TEM) for materials characterization. In: Huebschen, G., Altpeter, I., Tschuncky, R., Herrmann, H.-G. (Eds.), Materials Characterization Using Nondestructive Evaluation (NDE) Methods. Elsevier Ltd, pp. 17–43.

Islam, M.T., Felfel, R.M., Abou Neel, E.A., Grant, D.M., Ahmed, I., Hossain, K.M.Z., 2017. Bioactive calcium phosphate–based glasses and ceramics and their biomedical applications: A review. J. Tissue Eng. 8, 1–16.

Iyer, K.M., 2013. Anatomy of Bone, Fracture, and Fracture Healing. In: Iyer, K.M. (Ed.), General Principles of Orthopedics and Trauma. Springer, pp. 1–11.

Jaiswal, A.K., Chhabra, H., Soni, V.P., Bellare, J.R., 2013. Enhanced mechanical

strength and biocompatibility of electrospun polycaprolactone-gelatin scaffold with surface deposited nano-hydroxyapatite. Mater. Sci. Eng. C 33, 2376–2385.

Jakobsson, A., Ottosson, M., Zalis, M.C., O'Carroll, D., Johansson, U.E., Johansson, F., 2017. Three-dimensional functional human neuronal networks in uncompressed low-density electrospun fiber scaffolds. Nanomedicine Nanotechnology, Biol. Med. 13, 1563–1573.

Jalili, R., Hosseini, S.A., Morshed, M., 2005. The effects of operating parameters on the morphology of electrospun polyacrilonitrile nanofibres. Iran. Polym. J. 14, 1074–1081.

Ji, W., Yang, F., Van Den Beucken, J.J.J.P., Bian, Z., Fan, M., Chen, Z., Jansen, J.A., 2010. Fibrous scaffolds loaded with protein prepared by blend or coaxial electrospinning. Acta Biomater. 6, 4199–4207.

Johannesdottir, F., Bouxsein, M.L., 2018. Overview of bone structure and strength. In: Thakker, R. V., Michael Whyte, Eisman, J., Igarashi, T. (Eds.), Genetics of Bone Biology and Skeletal Disease. Elsevier Inc., pp. 197–208.

Johnson, J., Niehaus, A., Nichols, S., Lee, D., Koepsel, J., Anderson, D., Lannutti, J., 2009. Electrospun PCL in vitro: a microstructural basis for mechanical property changes. J. Biomater. Sci. Polym. Ed. 20, 467–481.

Joseph, R., McGregor, W.J., Martyn, M.T., Tanner, K.E., Coates, P.D., 2002. Effect of hydroxyapatite morphology/surface area on the rheology and processability of hydroxyapatite filled polyethylene composites. Biomaterials 23, 4295–4302.

Jungst, T., Muerza-Cascante, M.L., Brown, T.D., Standfest, M., Hutmacher, D.W., Groll, J., Dalton, P.D., 2015. Melt electrospinning onto cylinders: Effects of rotational velocity and collector diameter on morphology of tubular structures. Polym. Int. 64, 1086–1095.

Kaerkitcha, N., Chuangchote, S., Hachiya, K., Sagawa, T., 2017. Influence of the viscosity ratio of polyacrylonitrile/poly(methyl methacrylate) solutions on core-shell fibers prepared by coaxial electrospinning. Polym. J. 49, 497–502.

Kai, D., Liow, S.S., Loh, X.J., 2014. Biodegradable polymers for electrospinning: Towards biomedical applications. Mater. Sci. Eng. C 45, 1–12.

Kalra, V., Lee, J.H., Park, J.H., Marquez, M., Joo, Y.L., 2009. Confined assembly of asymmetric block-copolymer nanofibers via multiaxial jet electrospinning. Small 5, 2323–2332.

Karageorgiou, V., Kaplan, D., 2005. Porosity of 3D biomaterial scaffolds and osteogenesis. Biomaterials 26, 5474–5491.

Karak, N., 2012. Biodegradable polymers. In: Vegetable Oil-Based Polymers: Properties, Processing and Applications. Elsevier, pp. 32–53.

Kariduraganavar, M.Y., Kittur, A.A., Kamble, R.R., 2014. Polymer synthesis and processing. In: Kumbar, S., Laurencin, C., Deng, M. (Eds.), Natural and Synthetic Biomedical Polymers. Elsevier Inc., pp. 1–31.

Karim, L., Hussein, A.I., Morgan, E.F., Bouxsein, M.L., 2013. The Mechanical Behavior of Bone, Fourth Edi. ed, Osteoporosis: Fourth Edition. Elsevier.

Katsanevakis, E., Wen, X., Zhang, N., 2012. Creating Electrospun Nanofiber-Based Biomimetic Scaffolds for Bone Regeneration. In: Jayakumar, R., Nair, S. V. (Eds.), Advances in Polymer Science. Springer, pp. 63–100.

Katsogiannis, K.A.G., Vladisavljević, G.T., Georgiadou, S., 2015. Porous electrospun polycaprolactone (PCL) fibres by phase separation. Eur. Polym. J. 69, 284–295.

Kaynak, C., Kaygusuz, I., 2016. Consequences of accelerated weathering in polylactide nanocomposites reinforced with halloysite nanotubes. J. Compos. Mater. 50, 365–375.

Keaveny, T.M., Morgan, E.F., Yeh, O.C., 2004. Bone Mechanics. In: Kutz, M. (Ed.), Standard Handbook of Biomedical Engineering and Design. p. 8.1-8.23.

Kemala, T., Budianto, E., Soegiyono, B., 2012. Preparation and characterization of microspheres based on blend of poly(lactic acid) and poly(ε-caprolactone) with poly(vinyl alcohol) as emulsifier. Arab. J. Chem. 5, 103–108.

Keun Kwon, I., Kidoaki, S., Matsuda, T., 2005. Electrospun nano- to microfiber fabrics made of biodegradable copolyesters: Structural characteristics, mechanical properties and cell adhesion potential. Biomaterials 26, 3929–3939.

Khajavi, R., Abbasipour, M., 2012. Electrospinning as a versatile method for fabricating coreshell, hollow and porous nanofibers. Sci. Iran. 19, 2029–2034.

Khalf, A., Madihally, S. V., 2017. Recent advances in multiaxial electrospinning for drug delivery. Eur. J. Pharm. Biopharm. 112, 1–17.

Khan, W., Muntimadugu, E., Jaffe, M., Domb, A.J., 2014. Implantable Medical Devices. In: Khan, W. (Ed.), Focal Controlled Drug Delivery. Springer, pp. 33–59.

Khatri, Z., Nakashima, R., Mayakrishnan, G., Lee, K.H., Park, Y.H., Wei, K., Kim, I.S., 2013. Preparation and characterization of electrospun poly(ε-caprolactone)-poly(l-lactic acid) nanofiber tubes. J. Mater. Sci. 48, 3659–3664.

Ki, C.S., Park, S.Y., Kim, H.J., Jung, H.M., Woo, K.M., Lee, J.W., Park, Y.H., 2008. Development of 3-D nanofibrous fibroin scaffold with high porosity by electrospinning: Implications for bone regeneration. Biotechnol. Lett. 30, 405–410.

Kim, C.H., Jung, Y.H., Kim, H.Y., Lee, D.R., Dharmaraj, N., Choi, K.E., 2006. Effect of collector temperature on the porous structure of electrospun fibers. Macromol. Res. 14, 59–65.

Kim, H.-M., Himeno, T., Kawashita, M., Kokubo, T., Nakamura, T., 2004. The mechanism of biomineralization of bone-like apatite on synthetic hydroxyapatite: an in vitro assessment. J. R. Soc. Interface 1, 17–22.

Kim, H.M., Himeno, T., Kokubo, T., Nakamura, T., 2005. Process and kinetics of bonelike apatite formation on sintered hydroxyapatite in a simulated body fluid. Biomaterials 26, 4366–4373.

Kim, M.S., Kim, G., 2014. Three-dimensional electrospun polycaprolactone (PCL)/alginate hybrid composite scaffolds. Carbohydr. Polym. 114, 213–221.

Kim, S.H., Nam, Y.S., Lee, T.S., Park, W.H., 2003. Silk fibroin nanofiber. electrospinning, properties, and structure. Polym. J. 35, 185–190.

Kini, U., Nandeesh, B.N., 2012. Physiology of Bone Formation, Remodelling, and Metabolism. In: Fogelman, I. (Ed.), Radionuclide and Hybrid Bone Imaging. Springer, pp. 29–57.

Kiselev, P., Rosell-Llompart, J., 2012. Highly aligned electrospun nanofibers by elimination of the whipping motion. J. Appl. Polym. Sci. 125, 2433–2441.

Klein-Nulend, J., Van Oers, R.F.M., Bakker, A.D., Bacabac, R.G., 2014. Nitric oxide signaling in mechanical adaptation of bone. Osteoporos. Int. 25, 1427–1437.

Kogure, T., 2013. Electron Microscopy. In: Bergaya, F., Lagaly, G. (Eds.), Developments in Clay Science. Elsevier Ltd., pp. 275–317.

Kokubo, T., 1991. Bioactive glass ceramics: properties and applications. Biomaterials 12, 155–163.

Kokubo, T., 1993. A/W glass ceramic: Processing and properties. In: Hench, L.L., Wilson, J. (Eds.), An Introduction to Bioceramics. World Scientific Publishing, pp. 75–89.

Kokubo, T., Kushitani, H., Sakka, S., Kitsugi, T., Yamamuro, T., 1990. Solutions able to reproduce in vivo surface-structure changes in bioactive glass-ceramic A-W3. J. Biomed. Mater. Res. 24, 721–734.

Kokubo, T., Takadama, H., 2006. How useful is SBF in predicting in vivo bone bioactivity? Biomaterials 27, 2907–2915.

Kongkhlang, T., Tashiro, K., Kotaki, M., Chirachanchai, S., 2008. Electrospinning as a new technique to control the crystal morphology and molecular orientation of polyoxymethylene nanofibers. J. Am. Chem. Soc. 130, 15460–15466.

Koombhongse, S., Liu, W., Renker, D.H., 2001. Flat polymer ribbons and other shapes by electrospinning. J. Polym. Sci. Part B Polym. Phys. 39, 2598–2606.

Kostakova, E., Seps, M., Pokorny, P., Lukas, D., 2014. Study of polycaprolactone wet electrospinning process. Express Polym. Lett. 8, 554–564.

Kouhi, M., Prabhakaran, M.P., Shamanian, M., Fathi, M., Morshed, M., Ramakrishna, S., 2015. Electrospun PHBV nanofibers containing HA and bredigite nanoparticles: Fabrication, characterization and evaluation of mechanical properties and bioactivity. Compos. Sci. Technol. 121, 115–122.

Kourkoumelis, N., Balatsoukas, I., Tzaphlidou, M., 2012. Ca/P concentration ratio at different sites of normal and osteoporotic rabbit bones evaluated by Auger and energy dispersive X-ray spectroscopy. J. Biol. Phys. 38, 279–291.

Krishnan, L., Priddy, L.B., Esancy, C., Klosterhoff, B.S., Stevens, H.Y., Tran, L., Guldberg, R.E., 2017. Delivery vehicle effects on bone regeneration and heterotopic ossification induced by high dose BMP-2. Acta Biomater. 49, 101–112.

Krynauw, H., Bruchmüller, L., Bezuidenhout, D., Zilla, P., Franz, T., 2011. Degradation-induced changes of mechanical properties of an electro-spun polyester-urethane scaffold for soft tissue regeneration. J. Biomed. Mater.

Res. - Part B Appl. Biomater. 99 B, 359–368.

Kuboki, Y., Takita, H., Kobayashi, D., Tsuruga, E., Inoue, M., Murata, M., Nagai, N., Dohi, Y., Ohgushi, H., 1998. BMP-induced osteogenesis on the surface of hydroxyapatite with geometrically feasible and nonfeasible structures: Topology of osteogenesis. J. Biomed. Mater. Res. 39, 190–199.

Kumar, P., Vasita, R., 2017. Understanding the relation between structural and mechanical properties of electrospun fiber mesh through uniaxial tensile testing. J. Appl. Polym. Sci. 134.

Kurokawa, N., Endo, F., Maeda, T., Hotta, A., 2017. Electrospinning and surface modification methods for functionalized cell scaffolds. In: Ficai, D., Grumezescu, A.M. (Eds.), Nanostructures for Novel Therapy: Synthesis, Characterization and Applications. Elsevier Inc., pp. 201–225.

Labet, M., Thielemans, W., 2009. Synthesis of polycaprolactone: a review. Chem. Soc. Rev. 38, 3484.

Lam, C.X.F., Savalani, M.M., Teoh, S.-H., Hutmacher, D.W., 2008. Dynamics of in vitro polymer degradation of polycaprolactone-based scaffolds: accelerated versus simulated physiological conditions. Biomed. Mater. 3, 1–15.

Langer, R., Vacanti, J.P., 1993. Tissue Engineering. Science (80-.). 260, 920–926.

Lao, L., Wang, Y., Zhu, Y., Zhang, Y., Gao, C., 2011. Poly(lactide-co-glycolide)/hydroxyapatite nanofibrous scaffolds fabricated by electrospinning for bone tissue engineering. J. Mater. Sci. Mater. Med. 22, 1873–1884.

Laranjeira, M.S., Fernandes, M.H., Monteiro, F.J., 2010. Innovative macroporous granules of nanostructured-hydroxyapatite agglomerates: Bioactivity and osteoblast-like cell behaviour. J. Biomed. Mater. Res. - Part A 95, 891–900.

Larsen, G., Spretz, R., Velarde-Ortiz, R., 2004. Use of coaxial gas jackets to stabilize Taylor cones of volatile solutions and to induce particle-to-fiber transitions. Adv. Mater. 16, 166–169.

Lee, K., Silva, E.A., Mooney, D.J., 2011. Growth factor delivery-based tissue engineering: general approaches and a review of recent developments. J. R. Soc. Interface 8, 153–70.

LeGeros, R.Z., 2008. Calcium phosphate-based osteoinductive materials. Chem. Rev. 108, 4742–4753.

LeGeros, R.Z., LeGeros, J.P., 1984. Phosphate minerals in human tissues. In: Nriagu, J.O., Moore, P.H. (Eds.), Phosphate Minerals. Springer-Verlag Berlin Heidelberg, pp. 351–385.

LeGeros, R.Z., LeGeros, J.P., 2013. Hydroxyapatite. In: Hench, L.L. (Ed.), An Introduction to Bioceramics. Imperial College Press, pp. 229–277.

Leong, W.S., Wu, S.C., Ng, K.W., Tan, L.P., 2016. Electrospun 3D multi-scale fibrous scaffold for enhanced human dermal fibroblast infiltration. Int. J. Bioprinting 2, 81–92.

Li, C., Li, Q., Ni, X., Liu, G., Cheng, W., Han, G., 2017. Coaxial electrospinning and characterization of core-shell structured cellulose nanocrystal reinforced PMMA/PAN composite fibers. Materials. 10, 572–588.

Li, C., Wang, Z.-H., Yu, D.-G., Williams, G.R., 2014. Tunable biphasic drug release from ethyl cellulose nanofibers fabricated using a modified coaxial electrospinning process. Nanoscale Res. Lett. 9, 258–267.

Li, D., Babel, A., Jenekhe, S.A., Xia, Y., 2004a. Nanofibers of conjugated polymers prepared by electrospinning with a two-capillary spinneret. Adv. Mater. 16, 2062–2066.

Li, D., Wang, Y., Xia, Y., 2004b. Electrospinning Nanofibers as Uniaxially Aligned Arrays and Layer-by-Layer Stacked Films. Adv. Mater. 16, 361–366.

Li, D., Wang, Y., Xia, Y., 2004c. Electrospinning nanofibers as uniaxially aligned arrays and layer-by-layer stacked films. Adv. Mater. 16, 361–366.

Li, D., Xia, Y., 2004. Direct fabrication of composite and ceramic hollow nanofibers by electrospinning. Nano Lett. 4, 933–938.

Li, J., Jiang, G., Ding, F., 2008. The Effect of pH on the Polymer Degradation and Drug Release from PLGA-mPEG Microparticles. J. Appl. Polym. Sci. 109, 475–482.

Li, J., Stocum, D.L., 2013. Fracture healing. In: Burr, D.B., Allen, M.R. (Eds.), Basic and Applied Bone Biology. Elsevier Inc., pp. 205–223.

Li, S., McCarthy, S., 1999. Further investigations on the hydrolytic degradation of poly (DL-lactide). Biomaterials 20, 35–44.

Li, Y., Liu, J., de Bruyn, J.R., Wan, W., 2014. Optimization of the electrospinning process for core-shell fiber preparation. J. Biomater. Tissue Eng. 4, 973–980.

Li, Z., Wang, C., 2013. Effects of Working Parameters on Electrospinning. In: One-Dimensional Nanostructures: Electrospinning Technique and Unique Nanofibers. Springer Berlin Heidelberg, Berlin, Heidelberg, pp. 15–28.

Lim, H., Hoag, S.W., 2013. Plasticizer effects on physical–mechanical properties of solvent cast Soluplus® films. AAPS PharmSciTech 14, 903–910.

Lim, L.T., Auras, R., Rubino, M., 2008. Processing technologies for poly(lactic acid). Prog. Polym. Sci. 33, 820–852.

Lin, C.-C., Anseth, K.S., 2013. The Biodegradation of Biodegradable Polymeric Biomaterials. In: Ratner, B.D., Hoffman, A.S., Schoen, F.J., Lemons, J.E. (Eds.), Biomaterials Science. Elsevier, pp. 716–728.

Lin, F., Wang, X., Wang, Y., Yang, Y., Li, Y., 2017. Preparation and biocompatibility of electrospinning PDLLA/β-TCP/collagen for peripheral nerve regeneration. RSC Adv. 7, 41593–41602.

Lin, L.C., Chang, S.J., Kuo, S.M., Niu, G.C.-C., Keng, H.K., Tsai, P.H., 2008. Preparation and evaluation of β-TCP/polylactide microspheres as osteogenesis materials. J. Appl. Polym. Sci. 108, 3210–3217.

Linh, N.T.B., Min, Y.K., Song, H.Y., Lee, B.T., 2010. Fabrication of polyvinyl alcohol/gelatin nanofiber composites and evaluation of their material properties. J. Biomed. Mater. Res. - Part B Appl. Biomater. 95, 184–191.

Liu, H., Hsieh, Y. Lo, 2002. Ultrafine fibrous cellulose membranes from electrospinning of cellulose acetate. J. Polym. Sci. Part B Polym. Phys. 40, 2119–2129.

Liu, H., Webster, T.J., 2007. Bioinspired nanocomposites for orthopedic applications. In: Webster, T.J. (Ed.), Nanotechnology for the Regeneration of Hard and Soft Tissues. World Scientific Publishing, pp. 1–52.

Liu, W., Huang, C., Jin, X., 2015. Electrospinning of grooved polystyrene fibers: effect of solvent systems. Nanoscale Res. Lett. 10, 1–10.

Liu, X., Khor, S., Petinakis, E., Yu, L., Simon, G., Dean, K., Bateman, S., 2010. Effects of hydrophilic fillers on the thermal degradation of poly(lactic acid). Thermochim. Acta 509, 147–151.

Liu, X., Wang, T., Chow, L.C., Yang, M., Mitchell, J.W., 2014. Effects of inorganic fillers on the thermal and mechanical properties of poly(lactic acid). Int. J. Polym. Sci. 2014, 1–8.

Liu, Y., Luo, D., Wang, T., 2016. Hierarchical Structures of Bone and Bioinspired Bone Tissue Engineering. Small 12, 4611–4632.

Liu, Y., Zhang, L., Sun, X.F., Liu, J., Fan, J., Huang, D.W., 2015. Multi-jet electrospinning via auxiliary electrode. Mater. Lett. 141, 153–156.

Loh, Q.L., Choong, C., 2013. Three-dimensional scaffolds for tissue engineering applications: role of porosity and pore size. Tissue Eng. Part B. Rev. 19, 485–502.

Lopes, M.S., Ardini, A.L., Filho, R.M., 2012. Poly (lactic acid) production for tissue engineering applications. Procedia Eng. 42, 1402–1413.

López de Dicastillo, C., Garrido, L., Alvarado, N., Romero, J., Palma, J., Galotto, M., 2017. Improvement of Polylactide Properties through Cellulose Nanocrystals Embedded in Poly(Vinyl Alcohol) Electrospun Nanofibers. Nanomaterials 7, 106–121.

Lotfi, M., Nejib, M., Naceur, M., 2013. Cell adhesion to biomaterials: Concept of biocompatibility. In: Pignatello, R. (Ed.), Advances in Biomaterials Science and Biomedical Applications. IntechOpen, pp. 207–240.

Lowery, J.L., Datta, N., Rutledge, G.C., 2010. Effect of fiber diameter, pore size and seeding method on growth of human dermal fibroblasts in electrospun poly(ε-caprolactone) fibrous mats. Biomaterials 31, 491–504.

Lu, Y., Huang, J., Yu, G., Cardenas, R., Wei, S., Wujcik, E.K., Guo, Z., 2016. Coaxial electrospun fibers: applications in drug delivery and tissue engineering. Wiley Interdiscip. Rev. Nanomedicine Nanobiotechnology 8, 654–677.

Ma, H. Bin, Su, W.X., Tai, Z.X., Sun, D.F., Yan, X. Bin, Liu, B., Xue, Q.J., 2012. Preparation and cytocompatibility of polylactic acid/hydroxyapatite/graphene oxide nanocomposite fibrous membrane. Chinese Sci. Bull. 57, 3051–3058.

Ma, R., Tang, T., 2014. Current strategies to improve the bioactivity of PEEK. Int. J. Mol. Sci. 15, 5426–5445.

Ma, Z., Kotaki, M., Yong, T., He, W., Ramakrishna, S., 2005. Surface engineering of electrospun polyethylene terephthalate (PET) nanofibers towards development of a new material for blood vessel engineering. Biomaterials 26, 2527–2536.

Malherbe, I., Sanderson, R.D., Smit, E., 2010. Reversibly thermochromic microfibres by coaxial electrospinning. Polymer. 51, 5037–5043.

Mallick, S., Tripathi, S., Srivastava, P., 2015. Advancement in scaffolds for bone tissue engineering: A review. IOSR J. Pharm. Biol. Sci. 10, 37–54.

Manoukian, O.S., Ahmad, A., Marin, C., James, R., Mazzocca, A.D., Kumbar, S.G., 2016. Bioactive nanofiber dressings for wound healing. In: Ågren, M.S. (Ed.), Wound Healing Biomaterials Volume 2: Functional Biomaterials. Woodhead Publishing Limited, pp. 451–481.

Mansfield, P.J., Neumann, D.A., 2013. Structure and function of joints. In: Essentials of Kinesiology for the Physical Therapist Assistant. Mosby, pp. 21–33.

Marotti, G., Muglia, M.A., Palumbo, C., 1995. Collagen texture and osteocyte distribution in lamellar bone. Ital. J. Anat. Embryol. 100, 95–102.

Marques, M.R.C., Loebenberg, R., Almukainzi, M., 2011. Simulated biologic fluids with possible application in dissolution testing. Dissolution Technol. 15–28.

Martins, A., Chung, S., Pedro, A.J., Sousa, R.A., Marques, A.P., Reis, R.L., Neves, N.M., 2009. Hierarchical starch-based fibrous scaffold for bone tissue engineering applications. J. Tissue Eng. Regen. Med. 3, 37–42.

Martins, A., Reis, R.L., Neves, N.M., 2008. Electrospinning: processing technique for tissue engineering scaffolding. Int. Mater. Rev. 53, 257–274.

Masoudi Rad, M., Nouri Khorasani, S., Ghasemi-Mobarakeh, L., Prabhakaran, M.P., Foroughi, M.R., Kharaziha, M., Saadatkish, N., Ramakrishna, S., 2017a. Fabrication and characterization of two-layered nanofibrous membrane for guided bone and tissue regeneration application. Mater. Sci. Eng. C 80, 75–87.

Masoudi Rad, M., Nouri Khorasani, S., Ghasemi-Mobarakeh, L., Prabhakaran, M.P., Foroughi, M.R., Kharaziha, M., Saadatkish, N., Ramakrishna, S., 2017b. Fabrication and characterization of two-layered nanofibrous membrane for guided bone and tissue regeneration application. Mater. Sci. Eng. C 80, 75–87.

Mathiowitz, E., Kline, D., Langer, R., 1990. Morphology of polyanhydride microsphere delivery systems. Scanning Microsc. J. 4, 329–340.

Maurus, P.B., Kaeding, C.C., 2004. Bioabsorbable implant material review. Oper. Tech. Sports Med. 12, 158–160.

McCullen, S.D., Stano, K.L., Stevens, D.R., Roberts, W.A., Monteiro-Riviere, N.A., Clarke, L.I., Gorga, R.E., 2007. Development, Optimization, and Characterization of Electrospun Poly(lactic acid) Nanofibers Containing Multi-Walled Carbon Nanotubes. J. Appl. Polym. Sci. 105, 1668–1678.

McCullen, S.D., Zhu, Y., Bernacki, S.H., Narayan, R.J., Pourdeyhimi, B., Gorga, R.E., Loboa, E.G., 2009. Electrospun composite poly(L-lactic acid)/tricalcium phosphate scaffolds induce proliferation and osteogenic differentiation of human adipose-derived stem cells. Biomed. Mater. 4, 035002.

McKinley, T., 2003. Principles of fracture healing. Surg. 21, 209–212.

McManus, M.C., Boland, E.D., Koo, H.P., Barnes, C.P., Pawlowski, K.J., Wnek,

G.E., Simpson, D.G., Bowlin, G.L., 2006. Mechanical properties of electrospun fibrinogen structures. Acta Biomater. 2, 19–28.

Megelski, S., Stephens, J.S., Bruce Chase, D., Rabolt, J.F., 2002. Micro- and nanostructured surface morphology on electrospun polymer fibers. Macromolecules 35, 8456–8466.

Mehdikhani, B., Borhani, G.H., 2014. Densification and mechanical behavior of ß-tricalcium phosphate bioceramics. Int. Lett. Chem. Phys. Astron. 36, 37–49.

Meijer, G.J., De Bruijn, J.D., Koole, R., Van Blitterswijk, C.A., 2007. Cell-based bone tissue engineering. PLoS Med. 4, 0260–0264.

Mellon, S.J., Tanner, K.E., 2012. Bone and its adaptation to mechanical loading: a review. Int. Mater. Rev. 57, 235–255.

Mi, H.-Y., Palumbo, S., Jing, X., Turng, L.-S., Li, W.-J., Peng, X.-F., 2014. Thermoplastic polyurethane/hydroxyapatite electrospun scaffolds for bone tissue engineering: Effects of polymer properties and particle size. J. Biomed. Mater. Res. Part B Appl. Biomater. 102, 1434–1444.

Min, B.M., You, Y., Kim, J.M., Lee, S.J., Park, W.H., 2004. Formation of nanostructured poly(lactic-co-glycolic acid)/chitin matrix and its cellular response to normal human keratinocytes and fibroblasts. Carbohydr. Polym. 57, 285–292.

Mirhadi, B., Mehdikhani, B., Askari, N., 2011. Synthesis of nano-sized ß-tricalcium phosphate via wet precipitation. Process. Appl. Ceram. 5, 193–198.

Mirjalili, M., Zohoori, S., 2016. Review for application of electrospinning and electrospun nanofibers technology in textile industry. J. Nanostructure Chem. 6, 207–213.

Mishra, R.K., Zachariah, A.K., Thomas, S., 2017. Energy-Dispersive X-ray spectroscopy techniques for nanomaterial. In: Thomas, S., Thomas, R., Zachariah, A., Mishra, R. (Eds.), Microscopy Methods in Nanomaterials Characterization. Elsevier Inc., pp. 383–405.

Moghe, A.K., Gupta, B.S., 2008. Co-axial Electrospinning for Nanofiber Structures: Preparation and Applications. Polym. Rev. 55, 353–377.

Mohammadzadehmoghadam, S., Dong, Y., Barbhuiya, S., 2016. Electrospinning: Current Status and Future Trends. In: Fakirov, S. (Ed.), Nano-Size Polymers Preparation, Properties, Applications. Springer, pp. 89–154.

Morgan, E.F., Barnes, G.L., Einhorn, T.A., 2013. The Bone Organ System. Form and Function. In: Marcus, R., Feldman, D., Dempster, D.W., Luckey, M., Cauley, J.A. (Eds.), Osteoporosis: Fourth Edition. Elsevier, pp. 3–20.

Müller, M., 2006. Confocal fluorescence microscopy. In: Introduction to Confocal Fluorescence Microscopy. SPIE, pp. 1–27.

Murugan, R., Ramakrishna, S., 2005. Development of nanocomposites for bone grafting. Compos. Sci. Technol. 65, 2385–2406.

Mustafa, Z.B., 2012. Multiaxial fatigue characterization of self-reinforced polylactic acid-calcium phosphate composite. University of Glasgow.

Nair, L.S., Laurencin, C.T., 2007. Biodegradable polymers as biomaterials. Prog.

Polym. Sci. 32, 762–798.

Naito, Y., Shinoka, T., Duncan, D., Hibino, N., Solomon, D., Cleary, M., Rathore, A., Fein, C., Church, S., Breuer, C., 2011. Vascular tissue engineering: Towards the next generation vascular grafts. Adv. Drug Deliv. Rev. 63, 312–323.

Nakamura, H., 2007. Morphology, function, and differentiation of bone cells. J. Hard Tissue Biol. 16, 15–22.

Nakano, T., 2015. Bone tissue and biomaterial design based on the anisotropic microstructure. In: Niinomi, M., Narushima, T., Masaaki Nakai (Eds.), Advances in Metallic Biomaterials Processing and Applications. Springer, pp. 3–30.

Nam, Y.S., Park, W.H., Ihm, D., Hudson, S.M., 2010. Effect of the degree of deacetylation on the thermal decomposition of chitin and chitosan nanofibers. Carbohydr. Polym. 80, 291–295.

Nejati, E., Mirzadeh, H., Zandi, M., 2008. Synthesis and characterization of nano-hydroxyapatite rods/poly(l-lactide acid) composite scaffolds for bone tissue engineering. Compos. Part A Appl. Sci. Manuf. 39, 1589–1596.

Nerurkar, N.L., Elliott, D.M., Mauck, R.L., 2007. Mechanics of oriented electrospun nanofibrous scaffolds for annulus fibrosus tissue engineering. J. Orthop. Res. 25, 1018–1028.

Nguyen, L.B., Anderson, C.R., 2015. Parametric study on the size and alignment of electrospun PLGA nanofibrous matrices. In: 2015 41st Annual Northeast Biomedical Engineering Conference (NEBEC). pp. 1–2.

Nguyen, T.T.T., Chung, O.H., Park, J.S., 2011. Coaxial electrospun poly(lactic acid)/chitosan (core/shell) composite nanofibers and their antibacterial activity. Carbohydr. Polym. 86, 1799–1806.

Novotna, K., Zajdlova, M., Suchy, T., Hadraba, D., Lopot, F., Zaloudkova, M., Douglas, T.E.L., Munzarova, M., Juklickova, M., Stranska, D., Kubies, D., Schaubroeck, D., Wille, S., Balcaen, L., Jarosova, M., Kozak, H., Kromka, A., Svindrych, Z., Lisa, V., Balik, K., Bacakova, L., 2014. Polylactide nanofibers with hydroxyapatite as growth substrates for osteoblast-like cells. J. Biomed. Mater. Res. - Part A 102, 3918–3930.

Nyberg, E., Holmes, C., Witham, T., Grayson, W.L., 2016. Growth factor-eluting technologies for bone tissue engineering. Drug Deliv. Transl. Res. 6, 184–194.

O'Brien, F.J., 2011. Biomaterials & scaffolds for tissue engineering. Mater. Today 14, 88–95.

Oonishi, H., Hench, L.L., Wilson, J., Sugihara, F., Tsuji, E., Kushitani, S., Iwaki, H., 1999. Comparative bone growth behavior in granules of bioceramic materials of various sizes. J. Biomed. Mater. Res. 44, 31–43.

Oonishi, H., Oomamiuda, H., 2016. Degradation/resorption in Bioactive Ceramics in Orthopaedics. In: Murphy, W., Black, J., Hastings, G. (Eds.), Handbook of Biomaterial Properties. Springer New York, New York, NY, pp. 495–507.

Oranger, A., Colaianni, G., Grano, M., 2014. Bone Cells. Imaging Prosthet. Joints 1, 3–13.

Osterhoff, G., Morgan, E.F., Shefelbine, S.J., Karim, L., McNamara, L.M., Augat, P., 2016. Bone mechanical properties and changes with osteoporosis. Injury 47, S11–S20.

Oyane, A., Kim, H.-M., Furuya, T., Kokubo, T., Miyazaki, T., Nakamura, T., 2003. Preparation and assessment of revised simulated body fluids. J. Biomed. Mater. Res. 65, 188–195.

Pal, S., 2014. Mechanical properties of biological materials. In: Design of Artifi Cial Human Joints & Organs,. Springer Science+Business Media, pp. 23–40.

Palmero, P., 2016. Ceramic-polymer nanocomposites for bone-tissue regeneration. In: Liu, H. (Ed.), Nanocomposites for Musculoskeletal Tissue Regeneration. Elsevier Ltd, pp. 331–367.

Park, C.H., Kim, E.K., Tijing, L.D., Amarjargal, A., Pant, H.R., Kim, C.S., Shon, H.K., 2014. Preparation and characterization of LA/PCL composite fibers containing beta tricalcium phosphate (β-TCP) particles. Ceram. Int. 40, 5049–5054.

Park, J., 2008. Hard tissues: Structure, properties, healing, remodeling, and biocompatibility. In: Bioceramics Properties, Characterizations, and Applications. Springer-Verlag New York, pp. 80–112.

Park, J., Lakes, R.S., 2007a. Polymeric implant materials. In: Biomaterials: An Introduction. Springer, pp. 174–208.

Park, J., Lakes, R.S., 2007b. Composites as biomaterials. In: Biomaterials :An Introduction. Springer Science+Business Media, LLC, pp. 208–226.

Park, J.S., 2010. Electrospinning and its applications. Adv. Nat. Sci. Nanosci. Nanotechnol. 1.

Paşcu, E.I., Cahill, P.A., Stokes, J., McGuinness, G.B., 2016. Towards functional 3D-stacked electrospun composite scaffolds of PHBV, silk fibroin and nanohydroxyapatite: Mechanical properties and surface osteogenic differentiation. J. Biomater. Appl. 30, 1334–1349.

Patel, N.R., Gohil, P.P., 2012. A review on biomaterials: scope, applications & human anatomy significance. Int. J. Emerg. Technol. Adv. Eng. 2, 91–101.

Patlolla, A., Collins, G., Livingston Arinzeh, T., 2010. Solvent-dependent properties of electrospun fibrous composites for bone tissue regeneration. Acta Biomater. 6, 90–101.

Peng, F., Yu, X., Wei, M., 2011. In vitro cell performance on hydroxyapatite particles/poly(L-lactic acid) nanofibrous scaffolds with an excellent particle along nanofiber orientation. Acta Biomater. 7, 2585–2592.

Peng, X., Santulli, A.C., Sutter, E., Wong, S.S., 2012. Fabrication and enhanced photocatalytic activity of inorganic core–shell nanofibers produced by coaxial electrospinning. Chem. Sci. 3, 1262.

Penido, M.G.M.G., Alon, U.S., 2012. Phosphate homeostasis and its role in bone health. Pediatr. Nephrol. 27, 2039–2048.

Pereira, B.P., Thambyah, A., 2005. An Introduction to Biomechanics of Bone. In: Nather, A. (Ed.), Bone Grafts and Bone Subtitutes: Basic Science and Clinical Applications: Basic Science and Clinical Applications. World Scientific

Publishing, pp. 31–59.

Perez, R.A., Kim, H.W., 2015. Core-shell designed scaffolds for drug delivery and tissue engineering. Acta Biomater. 21, 2–19.

Pham, Q.P., Sharma, U., Mikos, A.G., 2006. Electrospun Poly(ε-caprolactone) microfiber and multilayer nanofiber/microfiber scaffolds: Characterization of scaffolds and measurement of cellular infiltration. Biomacromolecules 7, 2796–2805.

Pişkin, E., Işoglu, I.A., Bölgen, N., Vargel, I., Griffiths, S., Çavuşoglu, T., Korkusuz, P., Güzel, E., Cartmell, S., 2009. In vivo performance of simvastatin-loaded electrospun spiral-wound polycaprolactone scaffolds in reconstruction of cranial bone defects in the rat model. J. Biomed. Mater. Res. - Part A 90, 1137–1151.

Polini, A., Pisignano, D., Parodi, M., Quarto, R., Scaglione, S., 2011. Osteoinduction of human mesenchymal stem cells by bioactive composite scaffolds without supplemental osteogenic growth factors. PLoS One 6, 1–8.

Porter, A.E., Buckland, T., Hing, K., Best, S.M., Bonfield, W., 2006. The structure of the bond between bone and porous silicon-substituted hydroxyapatite bioceramic implants. J. Biomed. Mater. Res. Part A 78, 25–33.

Porter, J.R., Ruckh, T.T., Popat, K.C., 2009. Bone tissue engineering: A review in bone biomimetics and drug delivery strategies. Biotechnol. Prog. 25, 1539–1560.

Prabhakaran, M.P., Vatankhah, E., Ramakrishna, S., 2013. Electrospun aligned PHBV/collagen nanofibers as substrates for nerve tissue engineering. Biotechnol. Bioeng. 110, 2775–2784.

Prakasam, M., Locs, J., Salma-Ancane, K., Loca, D., Largeteau, A., Berzina-Cimdina, L., 2015. Fabrication, properties and applications of dense hydroxyapatite: A review. J. Funct. Biomater. 6, 1099–1140.

Pretula, J., Slomkowski, S., Penczek, S., 2016. Polylactides — Methods of synthesis and characterization. Adv. Drug Deliv. Rev. 107, 3–16.

Price, D.M., Hourston, D.J., Dumont, F., 2000. Thermogravimetry of Polymers. In: Meyers, R.A. (Ed.), Encyclopedia of Analytical Chemistry. John Wiley & Sons Ltd, Chichester, pp. 8094–8105.

Purbrick, M., L. Ambrosio, M. Ventre, Netti, P., 2010. Natural composites: structure–property relationships in bone, cartilage, ligament and tendons. In: Ambrosio, L. (Ed.), Biomedical Composites. Woodhead Publishing Limited, pp. 3–24.

Qian, W., Yu, D.G., Li, Y., Liao, Y.Z., Wang, X., Wang, L., 2014. Dual drug release electrospun core-shell nanofibers with tunable dose in the second phase. Int. J. Mol. Sci. 15, 774–786.

Qian, Y., Zhang, Z., Zheng, L., Song, R., Zhao, Y., 2014. Fabrication and characterization of electrospun polycaprolactone blended with chitosan-gelatin complex nanofibrous mats. J. Nanomater. 2014, 1–7.

Qin, X., 2017. Coaxial electrospinning of nanofibers. In: Afshari, M. (Ed.), Electrospun Nanofibers. Woodhead Publishing, pp. 41–71.

Qu, H., Wei, S., Guo, Z., 2013. Coaxial electrospun nanostructures and their applications. J. Mater. Chem. A 1, 11513.

Quarto, R., Mastrogiacomo, M., Cancedda, R., Kutepov, S., Mukhachev, V., Lavroukov, A., Kon, E., Marcacci, M., 2001. Repair of large bone defects with the use of autologous bone marrow stromal cells. N. Engl. J. Med. 344, 385–6.

Rahaman, M.N., Day, D.E., Sonny Bal, B., Fu, Q., Jung, S.B., Bonewald, L.F., Tomsia, A.P., 2011. Bioactive glass in tissue engineering. Acta Biomater. 7, 2355–2373.

Rajzer, I., 2014. Fabrication of bioactive polycaprolactone/hydroxyapatite scaffolds with final bilayer nano-/micro-fibrous structures for tissue engineering application. J. Mater. Sci. 49, 5799–5807.

Rajzer, I., Menaszek, E., Kwiatkowski, R., Chrzanowski, W., 2014. Bioactive nanocomposite PLDL/nano-hydroxyapatite electrospun membranes for bone tissue engineering. J. Mater. Sci. Mater. Med. 25, 1239–1247.

Rakmae, S., Ruksakulpiwat, Y., Sutapun, W., Suppakarn, N., 2011. Physical properties and cytotoxicity of surface-modified bovine bone-based hydroxyapatite/poly(lactic acid) composites. J. Compos. Mater. 45, 1259–1269.

Ramakrishna, S., Mayer, J., Wintermantel, E., Leong, K.W., 2001. Biomedical applications of polymer-composite materials: A review. Compos. Sci. Technol. 61, 1189–1224.

Ramirez, E., Angeles, J., Cervantes, O.R., Jacobo, V., Prado, A.O., 2015. Viscoelastic characterization of bovine trabecular bone samples. Int. J. Mech. Mechatronics Eng. 9, 898–903.

Ranjbar-Mohammadi, M., Prabhakaran, M.P., Bahrami, S.H., Ramakrishna, S., 2016. Gum tragacanth/poly(l-lactic acid) nanofibrous scaffolds for application in regeneration of peripheral nerve damage. Carbohydr. Polym. 140, 104–112.

Ratner, B.D., Hoffman, A.S., Schoen, F.J., Lemons, J.E., 2013. Biomaterials Science: An Evolving, Multidisciplinary Endeavor. In: Biomaterials Science. Elsevier, pp. xxv–xxxix.

Raucci, M.G., Guarino, V., Ambrosio, L., 2012. Biomimetic Strategies for Bone Repair and Regeneration. J. Funct. Biomater. 3, 688–705.

Rehman, I., Smith, R., Hench, L.L., Bonfield, W., 1995. Structual evaluation of human and sheep bone and camparison with synthetic hydroxyapatite by FT-Raman spectrscopy. J. Biomed. Mater. Res. 29, 1287–1294.

Reneker, D.H., Chun, I., 1996. Nanometre diameter fibres of polymer, produced by electrospinning. Nanotechnology 7, 216.

Rennert, R.C., Sorkin, M., Garg, R.K., Gurtner, G.C., 2013. Stem cell recruitment after injury: lessons for regenerative medicine. Regen. Med. J. 7, 833–850.

Revati, R., Majid, M.S.A., Normahira, M., 2015. Biodegradable poly (lactic acid) scaffold for tissue engineering : A brief review. J. Polym. Sci. Technol. 1, 16–24.

Reznik, S.N., Yarin, A.L., Zussman, E., Bercovici, L., 2006. Evolution of a

compound droplet attached to a core-shell nozzle under the action of a strong electric field. Phys. Fluids 18, 0621011.

Rho, J.Y., Kuhn-Spearing, L., Zioupos, P., 1998. Mechanical properties and the hierarchical structure of bone. Med. Eng. Phys. 20, 92–102.

Rho, J.Y., Pharr, G.M., 1999. Effects of drying on the mechanical properties of bovine femur measured by nanoindentation. J. Mater. Sci. Mater. Med. 10, 485–488.

Rivet, C.J., Zhou, K., Gilbert, R.J., Finkelstein, D.I., Forsythe, J.S., 2015. Cell infiltration into a 3D electrospun fiber and hydrogel hybrid scaffold implanted in the brain. Biomatter 5, e1005527.

Rnjak-Kovacina, J., Weiss, A.S., 2011. Increasing the pore size of electrospun scaffolds. Tissue Eng. Part B Rev. 17, 365–372.

Robb, B., Lennox, B., 2011. The electrospinning process, conditions and control. In: Bosworth, L.A., Downes, S. (Eds.), Electrospinning for Tissue Regeneration. Woodhead Publishing Limited, pp. 51–66.

Robling, A.G., Fuchs, R.K., Burr, D.B., 2013. Mechanical Adaptation. In: Burr, D.B., Allen, M.R. (Eds.), Basic and Applied Bone Biology. Elsevier Inc., pp. 175–204.

Rogina, A., 2014. Electrospinning process: Versatile preparation method for biodegradable and natural polymers and biocomposite systems applied in tissue engineering and drug delivery. Appl. Surf. Sci. 296, 221–230.

Romagnoli, C., D'Asta, F., Brandi, M.L., 2013. Drug delivery using composite scaffolds in the context of bone tissue engineering. Clin. Cases Miner. Bone Metab. 10, 155–161.

Rong, Z., Zeng, W., Kuang, Y., Zhang, J., Liu, X., Lu, Y., Cheng, X., 2015. Enhanced bioactivity of osteoblast-like cells on poly(lactic acid)/poly(methyl methacrylate)/nano-hydroxyapatite scaffolds for bone tissue engineering. Fibers Polym. 16, 245–253.

Roseti, L., Parisi, V., Petretta, M., Cavallo, C., Desando, G., Bartolotti, I., Grigolo, B., 2017. Scaffolds for Bone Tissue Engineering: State of the art and new perspectives. Mater. Sci. Eng. C 78, 1246–1262.

Ross, F.P., 2003. Cytokine regulation of osteoclast formation and function. J. Musculoskelet. Neuronal Interact. 3, 282–286.

Royer, A., Viguie, J.C., Heughebaert, M., Heughebaert, J.C., 1993. Stoichiometry of hydroxyapatite: influence on the flexural strength. J. Mater. Sci. Mater. Med. 4, 76–82.

Rutledge, G.C., Lowery, J.L., Pai, C., 2009. Characterization by mercury porosimetry of nonwoven fiber media with deformation. J. Eng. Fiber. Fabr. 4, 1–13.

Sackett, C.K., Narasimhan, B., 2011. Mathematical modeling of polymer erosion: Consequences for drug delivery. Int. J. Pharm. 418, 104–114.

Sadat-Shojai, M., Khorasani, M.T., Jamshidi, A., 2016. A new strategy for fabrication of bone scaffolds using electrospun nano-HAp/PHB fibers and protein hydrogels. Chem. Eng. J. 289, 38–47.

Salgado, A.J., Coutinho, O.P., Reis, R.L., 2004. Bone tissue engineering: State of the art and future trends. Macromol. Biosci. 4, 743–765.

Sampath, U.G.T.M., Ching, Y.C., Chuah, C.H., Sabariah, J.J., Lin, P.C., 2016. Fabrication of porous materials from natural/synthetic biopolymers and their composites. Materials. 9, 1–32.

Sanosh, K.P., Chu, M.C., Balakrishnan, A., Kim, T.N., Cho, S.J., 2010. Sol-gel synthesis of pure nano sized β-tricalcium phosphate crystalline powders. Curr. Appl. Phys. 10, 68–71.

Schimming, R., Schmelzeisen, R., 2004. Tissue-engineered bone for maxillary sinus augmentation. J. Oral Maxillofac. Surg. 62, 724–729.

Schmitt, R., 2014. Scanning Electron Microscope. In: Laperrière, L., Reinhart, G. (Eds.), CIRP Encyclopedia of Production Engineering. Springer Berlin Heidelberg, pp. 1085–1089.

Schoenau, E., Saggese, G., Peter, F., Baroncelli, G.I., Shaw, N.J., Crabtree, N.J., Zadik, Z., Neu, C.M., Noordam, C., Radetti, G., Hochberg, Z., 2004. From bone biology to bone analysis. Horm. Res. 61, 257–269.

Scurlock, J., Andersen, B.R., 2005. Bones and joints. In: Diagnoses in Assyrian and Babylonian Medicine, Ancient Sources, Translations, and Modern Medical Analyses. University of Illinois Press, pp. 247–258.

Semnani, D., 2017. Geometrical characterization of electrospun nanofibers. In: Afshari, M. (Ed.), Electrospun Nanofibers. Woodhead Publishing, pp. 151–180.

Sfeir, C., Ho, L., Doll, B.A., Azari, K., Hollinger, J.O., 2005. Fracture Repair. In: Lieberman, J.R., Friedlaender, G.E. (Eds.), Bone Regeneration and Repair: Biology and Clinical Applications. Humana Press Inc, pp. 21–44.

Shah, A.A., Hasan, F., Hameed, A., Ahmed, S., 2008. Biological degradation of plastics: A comprehensive review. Biotechnol. Adv. 26, 246–265.

Shang, S., Yang, F., Cheng, X., Frank Walboomers, X., Jansen, J.A., 2010. The effect of electrospun fibre alignment on the behaviour of rat periodontal ligament cells. Eur. Cells Mater. 19, 180–192.

Shao, W., He, J., Sang, F., Ding, B., Chen, L., Cui, S., Li, K., Han, Q., Tan, W., 2016. Coaxial electrospun aligned tussah silk fibroin nanostructured fiber scaffolds embedded with hydroxyapatite-tussah silk fibroin nanoparticles for bone tissue engineering. Mater. Sci. Eng. C 58, 342–351.

Sheikh, Z., Javaid, M., Hamdan, N., Hashmi, R., 2015. Bone regeneration using bone morphogenetic proteins and various biomaterial carriers. Materials. 8, 1778–1816.

Shepherd, J.H., Shepherd, D. V., Best, S.M., 2012. Substituted hydroxyapatites for bone repair. J. Mater. Sci. Mater. Med. 23, 2335–2347.

Shuai, C., Yang, B., Peng, S., Li, Z., 2013. Development of composite porous scaffolds based on poly(lactide-co- glycolide)/nano-hydroxyapatite via selective laser sintering. Int. J. Adv. Manuf. Technol. 69, 51–57.

Sill, T., von Recum, H., 2008. Electrospinning: applications in drug delivery and tissue engineering. Biomaterials 29, 1989–2006.

Silva, C.S.R., Luz, G.M., Mano, J.F., JL Gómez Ribelles, Gómez-Tejedor, J., 2014. Poly(epsilon-caprolactone) electrospun scaffolds filled with nanoparticles. Production and optimization according to Taguchi's methodology. J. Macromol. Sci. Part B Phys. 53, 781–799.

Singh, P., Andola, H.C., Rawat, M.S.M., Pant, G.J.N., Purohit, V.K., 2011. Fourier Transform Infrared (FT-IR) Spectroscopy in An-Overview. Res. J. Med. Plants 5, 127–135.

Siqueira, L., Passador, F.R., Costa, M.M., Lobo, A.O., Sousa, E., 2015. Influence of the addition of β-TCP on the morphology, thermal properties and cell viability of poly (lactic acid) fibers obtained by electrospinning. Mater. Sci. Eng. C 52, 135–43.

Širc, J., Hobzová, R., Kostina, N., Munzarová, M., Juklíčková, M., Lhotka, M., Kubinová, Š., Zajícová, A., Michálek, J., 2012. Morphological characterization of nanofibers: Methods and application in practice. J. Nanomater. 2012.

Ślósarczyk, A., E. Stobierska, Paszkiewicz, Z., Gawlicki, M., 1996. Calcium phosphate materials prepared from precipitates with various calcium: Phosphorus molar ratios. J. Am. Ceram. Soc. 79, 2539–2544.

Smith, B.D., Grande, D.A., 2015. The current state of scaffolds for musculoskeletal regenerative applications. Nat. Rev. Rheumatol 11, 213–222.

Sobczak, M., 2012. Ring-opening polymerization of cyclic esters in the presence of choline/SnOct2 catalytic system. Polym. Bull. 68, 2219–2228.

Sombatmankhong, K., Suwantong, O., Waleetorncheepsawat, S., Supaphol, P., 2006. Electrospun fiber mats of poly(3-hydroxybutyrate), poly(3-hydroxybutyrate-co-3-hydroxyvalerate), and their blends. J. Polym. Sci. Part B Polym. Phys. 44, 2923–2933.

Son, W.K., Youk, J.H., Lee, T.S., Park, W.H., 2004. The effects of solution properties and polyelectrolyte on electrospinning of ultrafine poly(ethylene oxide) fibers. Polymer. 45, 2959–2966.

Sonseca, A., Peponi, L., Sahuquillo, O., Kenny, J.M., Giménez, E., 2012. Electrospinning of biodegradable polylactide/hydroxyapatite nanofibers: Study on the morphology, crystallinity structure and thermal stability. Polym. Degrad. Stab. 97, 2052–2059.

Sooksaen, P., Pengsuwan, N., Karawatthanaworrakul, S., Pianpraditkul, S., 2015. Formation of porous apatite layer during in vitro study of hydroxyapatite-AW based glass composites. Adv. Condens. Matter Phys. 2015, 1–9.

Srinivasarao, M., Collings, D., Philips, A., Patel, S., 2001. Three-dimensionally ordered array of air bubbles in a polymer film. Science (80-.). 292, 79.

Srouji, S., Kizhner, T., Suss-Tobi, E., Livne, E., Zussman, E., 2008. 3-D Nanofibrous electrospun multilayered construct is an alternative ECM mimicking scaffold. J. Mater. Sci. Mater. Med. 19, 1249–1255.

Subia, B., Kundu, J., Kundu, S.C., 2010. Biomaterial Scaffold Fabrication Techniques for Potential Tissue Engineering Applications. In: Eberli, D. (Ed.), Tissue Engineering. IntechOpen, pp. 141–159.

Subramaniam, A., Sethuraman, S., 2014. Biomedical Applications of

Nondegradable Polymers. In: Natural and Synthetic Biomedical Polymers. Elsevier Inc., pp. 301–308.

Subramanian, A., Krishnan, U.M., Sethuraman, S., 2011. Fabrication of uniaxially aligned 3D electrospun scaffolds for neural regeneration. Biomed. Mater. 6, 1–10.

Suchanek, W., Yoshimura, M., 1998. Processing and properties of hydroxyapatite-based biomaterials for use as hard tissue replacement implants. J. Mater. Res. 13, 94–117.

Sui, G., Yang, X., Mei, F., Hu, X., Chen, G., Deng, X., Ryu, S., Wang, D.-M., Hou, L.-T., 2007. Poly-L-lactic acid/hydroxyapatite hybrid membrane for bone tissue regeneration. J. Biomed. Mater. Res. A 82A, 445–454.

Sultana, N., 2013a. Scaffolds for Tissue Engineering. In: Biodegradable Polymer-Based Scaffolds for Bone Tissue Engineering. Springer, pp. 1–17.

Sultana, N., 2013b. Fabrication Techniques and Properties of Scaffolds. In: Biodegradable Polymer-Based Scaffolds for Bone Tissue Engineering. Springer, pp. 19–42.

Sun, B., Duan, B., Yuan, X., 2006. Preparation of core/shell PVP/PLA ultrafine fibers by coaxial electrospinning. J. Appl. Polym. Sci. 102, 39–45.

Sun, Z., Zussman, E., Yarin, A.L., Wendorff, J.H., Greiner, A., 2003. Compound core-shell polymer nanofibers by co-electrospinning. Adv. Mater. 15, 1929–1932.

Suwanprateeb, J., Tanner, K.E., Turner, S., Bonfield, W., 1997. Influence of Ringer's solution on creep resistance of hydroxyapatite reinforced polyethylene composites. J. Mater. Sci. Mater. Med. 8, 469–472.

Szcześ, A., Hołysz, L., Chibowski, E., 2017. Synthesis of hydroxyapatite for biomedical applications. Adv. Colloid Interface Sci. 249, 321–330.

Talal, A., Waheed, N., Al-Masri, M., McKay, I.J., Tanner, K.E., Hughes, F.J., 2009. Absorption and release of protein from hydroxyapatite-polylactic acid (HA-PLA) membranes. J. Dent. 37, 820–826.

Tamada, J.A., Langer, R., 1993. Erosion kinetics of hydrolytically degradable polymers. Proc. Natl. Acad. Sci. U. S. A. 90, 552–556.

Tan, S.-H., Inai, R., Kotaki, M., Ramakrishna, S., 2005. Systematic parameter study for ultra-fine fiber fabrication via electrospinning process. Polymer. 46, 6128–66134.

Tanaka, K., Shiga, T., Katayama, T., 2016. Fabrication of hydroxyapatite/PLA composite nanofiber by electrospinning. In: High Performance and Optimum Design of Structures and Materials II. pp. 371–379.

Tang, C.Y., Yang, Z., 2017. Transmission Electron Microscopy (TEM). In: Hilal, N., Ismail, A.F., Matsuura, T., Oatley-Radcliffe, D. (Eds.), Membrane Characterization. Elsevier B.V., pp. 145–159.

Tang, X., Thankappan, S.K., Lee, P., Fard, S.E., Harmon, M.D., Tran, K., Yu, X., 2014. Polymeric biomaterials in tissue engineering and regenerative medicine. In: Kumbar, S., Laurencin, C., Deng, M. (Eds.), Natural and Synthetic Biomedical Polymers. Elsevier Inc., pp. 351–371.

Tang, Y., Chen, L., Zhao, K., Wu, Z., Wang, Y., Tan, Q., 2016. Fabrication of PLGA/HA (core)-collagen/amoxicillin (shell) nanofiber membranes through coaxial electrospinning for guided tissue regeneration. Compos. Sci. Technol. 125, 100–107.

Tanner, K., Downes, R.N., Bonfield, W., 1994. Clinical applications of hydroxyapatite reinforced materials, British Ceramic Transactions.

Tanner, K.E., 2009. Composites based on degradable polymers. In: Wuisman, P.I.J.M., Smit, T.H. (Eds.), Degradable Polymers for Skeletal Implants. Nova Science Publishers, pp. 74–93.

Tanner, K.E., 2010a. Bioactive composites for bone tissue engineering. Proc. Inst. Mech. Eng. Part H J. Eng. Med. 224, 1359–1372.

Tanner, K.E., 2010b. Hard tissue applications of biocomposites. Biomed. Compos. 44–58.

Tanner, K.E., 2010c. Bioactive ceramic-reinforced composites for bone augmentation. J. R. Soc. Interface 7, S541–S557.

Tao, C., Zhang, Y., Li, B., Chen, L., 2017. Hierarchical micro/submicrometer-scale structured scaffolds prepared *via* coaxial electrospinning for bone regeneration. J. Mater. Chem. B 5, 9219–9228.

Taraballi, F., Pandolfi, L., Powell, S., Cabrera, F.J., Torres, A., Minardi, S., Tasciotti, E., 2015. Strategic Approaches to Growth Factors Delivery for Regenerative Medicine. In: Panseri, S., Taraballi, F., Cunha, C. (Eds.), Biomimetic Approaches for Tissue Healing. OMICS Group International.

Tarus, B., Fadel, N., Al-Oufy, A., El-Messiry, M., 2016. Effect of polymer concentration on the morphology and mechanical characteristics of electrospun cellulose acetate and poly (vinyl chloride) nanofiber mats. Alexandria Eng. J. 55, 2975–2984.

Taylor, D., 2011. What we can't learn from nature. Mater. Sci. Eng. C 31, 1160–1163.

Teo, W.E., Ramakrishna, S., 2006. A review on electrospinning design and nanofibre assemblies. Nanotechnology 17, R89–R106.

Tetteh, G., Khan, A.S., Delaine-Smith, R.M., Reilly, G.C., Rehman, I.U., 2014. Electrospun polyurethane/hydroxyapatite bioactive scaffolds for bone tissue engineering: The role of solvent and hydroxyapatite particles. J. Mech. Behav. Biomed. Mater. 39, 95–110.

Tham, W.L., Chow, W.S., Ishak, Z.A.M., 2010. Simulated body fluid and water absorption effects on poly(methyl methacrylate)/hydroxyapatite denture base composites. Express Polym. Lett. 4, 517–528.

Thomas, P.C., Thomas, S.P., George, G., Thomas, S., Kuruvilla, J., 2011. Impact of filler geometry and surface chemistry on the degree of reinforcement and thermal stability of nitrile rubber nanocomposites. J. Polym. Res. 18, 2367–2378.

Thomas, V., Zhang, X., Vohra, Y.K., 2009. A biomimetic tubular scaffold with spatially designed nanofibers of Protein/PDS® bio-blends. Biotechnol. Bioeng. 104, 1025–1033.

Tokiwa, Y., Calabia, B.P., Ugwu, C.U., Aiba, S., 2009. Biodegradability of plastics. Int. J. Mol. Sci. 10, 3722–3742.

Tong, H.W., Wang, M., Li, Z.Y., Lu, W.W., 2010. Electrospinning, characterization and in vitro biological evaluation of nanocomposite fibers containing carbonated hydroxyapatite nanoparticles. Biomed. Mater. 5, 054111–05123.

Tong, H.W., Zhang, X., Wang, M., 2012. A new nanofiber fabrication technique based on coaxial electrospinning. Mater. Lett. 66, 257–260.

Tozzi, G., De Mori, A., Oliveira, A., Roldo, M., 2016. Composite hydrogels for bone regeneration. Materials. 9, 1–24.

Treiser, M., Abramson, S., Langer, R., Kohn, J., 2013. Degradable and Resorbable Biomaterials. In: D. Ratner, Hoffman, A.S., Schoen, F.J., Lemons, J.E. (Eds.), Biomaterials Science. Elsevier, pp. 179–195.

Tsuji, H., 2009. Poly(lactide)s and their copolymers: Physical properties and hydrolytic degradation. In: Wuisman, P.I.J.M., Smit, T.H. (Eds.), Degradable Polymers for Skeletal Implants. Nova Science Publishers, pp. 41–71.

Tur, K., 2009. Biomaterials and tissue engineering for regenerative repair of articular cartilage defects. Arch. Rheumatol. 24, 206–217.

Tyagi, P., Catledge, S.A., Stanishevsky, A., Thomas, V., Vohra, Y.K., 2009. Nanomechanical properties of electrospun composite scaffolds based on polycaprolactone and hydroxyapatite. J. Nanosci. Nanotechnol. 9, 4839–4845.

Tzaphlidou, M., Zaichick, V., 2003. Calcium, phosphorus, calcium – phosphorus ratio in rib bone of healthy humans. Biol. Trace Elem. Res. 93, 63–74.

Uma Maheshwari, S., Samuel, V.K., Nagiah, N., 2014. Fabrication and evaluation of (PVA/HAp/PCL) bilayer composites as potential scaffolds for bone tissue regeneration application. Ceram. Int. 40, 8469–8477.

Unnithan, A.R., Arathyram, R.S., Kim, C.S., 2015. Nanotechnology Applications for Tissue Engineering. In: S. Thomas, Y. Grohens, N.N. (Ed.), Nanotechnology Applications for Tissue Engineering. Elsevier Inc., pp. 45–56.

Urist, M., Lietze, A., Dawson, E., 1984. Bone regeneration under the influence of a bone morphogenetic protein (BMP) beta tricalcium phosphate (TCP) composite in skull trephine defects in dogs. Clin. Orthop. Relat. Res. 187, 277–280.

Vacanti, J.P., Vacanti, C.A., 2013. The History and Scope of Tissue Engineering, Fourth Edi. ed, Principles of Tissue Engineering: Fourth Edition. Elsevier.

Vaseashta, A., 2007. Controlled formation of multiple Taylor cones in electrospinning process. Appl. Phys. Lett. 90, 23–26.

Vaz, C.M., van Tuijl, S., Bouten, C.V.C., Baaijens, F.P.T., 2005. Design of scaffolds for blood vessel tissue engineering using a multi-layering electrospinning technique. Acta Biomater. 1, 575–582.

Velasco, M.A., Narvaez-Tovar, C.A., Garzon-Alvarado, D.A., 2015. Design, materials, and mechanobiology of biodegradable scaffolds for bone tissue engineering. Biomed Res. Int. 2015, 1–21.

Venugopal, J., Zhang, Y.Z., Ramakrishna, S., 2005. Electrospun nanofibres:

Biomedical applications. Proc. Inst. Mech. Eng. Part N J. Nanoeng. Nanosyst. 218, 35–45.

Venugopal, J.R., Low, S., Choon, A.T., Kumar, A.B., Ramakrishna, S., 2008. Nanobioengineered electrospun composite nanofibers and osteoblasts for bone regeneration. Artif. Organs 32, 388–397.

Vert, M., Li, S., Garreau, H., 1992. New insights on the degradation of bioresorbable polymeric devices based on lactic and glycolic acids. Clin. Mater. 10, 3–8.

Von Burkersroda, F., Schedl, L., Göpferich, A., 2002. Why degradable polymers undergo surface erosion or bulk erosion. Biomaterials 23, 4221–4231.

Vuluga, Z., Potarniche, C., Albu, M.G., Trandafir, V., Iordachescu, D., Vasile, E., 2012. Collagen - Modified Layered Silicate Biomaterials for Regenerative Medicine of Bone Tissue. In: Hutagalung, S. (Ed.), Materials Science and Technology. InTech, pp. 125–148.

Vysloužilová, L., Buzgo, M., Pokorný, P., Chvojka, J., Míčková, A., Rampichová, M., Kula, J., Pejchar, K., Bílek, M., Lukáš, D., Amler, E., 2017. Needleless coaxial electrospinning: A novel approach to mass production of coaxial nanofibers. Int. J. Pharm. 516, 293–300.

W. J. Morton, 1902. Method of dispersing fluids. 705691.

Walther, T., 2017. Transmission electron microscopy of nanostructures. In: Thomas, S., Thomas, R., Zachariah, A.K., Mishra, R.K. (Eds.), Microscopy Methods in Nanomaterials Characterization. Elsevier Inc., pp. 105–134.

Wang, J., Zhou, P., Obata, A., Jones, J.R., Kasuga, T., 2015. Preparation of cotton-wool-like poly(lactic acid)-based composites consisting of core-shell-type fibers. Materials. 8, 7979–7987.

Wang, L., Ryan, A.J., 2011. Introduction to electrospinning. In: Bosworth, L.A., Downes, S. (Eds.), Electrospinning for Tissue Regeneration. Woodhead Publishing Limited, pp. 3–33.

Wang, M., Cai, Y., Zhao, B., Zhu, P., 2017. Time-resolved study of nanomorphology and nanomechanic change of early-stage mineralized electrospun poly(lactic acid) fiber by scanning electron microscopy, Raman spectroscopy and atomic force microscopy. Nanomaterials 7, 1–11.

Wang, S.G., Jiang, X., Chen, P.C., Yu, A.G., Huang, X.J., 2012. Preparation of coaxial-electrospun poly[bis(p-methylphenoxy)]phosphazene nanofiber membrane for enzyme immobilization. Int. J. Mol. Sci. 13, 14136–14148.

Wang, X.Y., Zuo, Y., Huang, D., Hou, X.D., Li, Y.B., 2010. Comparative study on inorganic composition and crystallographic properties of cortical and cancellous bone. Biomed. Environ. Sci. 23, 473–480.

Wannatong, L., Sirivat, A., Supaphol, P., 2004. Effects of solvents on electrospun polymeric fibers: Preliminary study on polystyrene. Polym. Int. 53, 1851–1859.

Watson, J.T., 2015. Biology and enhancement of skeletal repair. In: Browner, B., Jupiter, J., Krettek, C., Anderson, P. (Eds.), Skeletal Trauma: Basic Science, Management, and Reconstruction. Saunders, pp. 69–95.

Wei, Q., Xia, X., 2012. Types and processing of structured functional nanofibers:

Core-shell, aligned, porous and gradient nanofibers. In: Wei, Q. (Ed.), Functional Nanofibers and Their Applications. Woodhead Publishing Limited, pp. 22–37.

Wei, Q., Xu, F., Xu, X., Geng, X., Ye, L., Zhang, A., Feng, Z., 2016. The multifunctional wound dressing with core–shell structured fibers prepared by coaxial electrospinning. Front. Mater. Sci. 10, 113–121.

Wei, X., Xia, Z., Wong, S.C., Baji, A., 2009. Modelling of mechanical properties of electrospun nanofibre network. Int. J. Exp. Comput. Biomech. 1, 45.

Whelan, T., 1994. Polymer Technology Dictionary. Chapman & Hall, London.

Wilson, E.E., Awonusi, A., Morris, M.D., Kohn, D.H., Tecklenburg, M.M.J., Beck, L.W., 2006. Three structural roles for water in bone observed by solid-state NMR. Biophys. J. 90, 3722–3731.

Wong, S.C., Baji, A., Leng, S., 2008. Effect of fiber diameter on tensile properties of electrospun poly(ε-caprolactone). Polymer. 49, 4713–4722.

Woodard, H., 1962. The elementary composition of human cortical bone. Health Phys. 8, 513–517.

Woodward, S.C., Brewer, P.S., Moatamed, F., Schindler, A., Pitt, C.G., 1985. The intracellular degradation of poly(ε-caprolactone). J. Biomed. Mater. Res. 19, 437–444.

Wozney, J.M., Rosen, V., Byrne, M., Celeste, A.J., Moutsatsos, I., Wang, E.A., 1990. Growth factors influencing bone development. J. Cell Sci. Suppl. 13, 149–156.

Wraighte, P.J., Scammell, B.E., 2006. Principles of fracture healing. Surg. 24, 198–207.

Xu, B., Rollo, B., Stamp, L.A., Zhang, D., Fang, X., Newgreen, D.F., Chen, Q., 2013. Non-linear elasticity of core/shell spun PGS/PLLA fibres and their effect on cell proliferation. Biomaterials 34, 6306–6317.

Xu, X., Chen, X., Ma, P., Wang, X., Jing, X., 2008. The release behavior of doxorubicin hydrochloride from medicated fibers prepared by emulsion-electrospinning. Eur. J. Pharm. Biopharm. 70, 165–170.

Yamamuro, T., 2004. Bioceramics. In: Poitout, D.G. (Ed.), Biomechanics and Biomaterials in Orthopedics. Springer-Verlag London, pp. 22–33.

Yang, S., Madbouly, S.A., Schrader, J.A., Srinivasan, G., Grewell, D., McCabe, K.G., Kessler, M.R., Graves, W.R., 2015. Characterization and biodegradation behavior of bio-based poly(lactic acid) and soy protein blends for sustainable horticultural applications. Green Chem. 17, 380–393.

Yang, Y., Li, X., Cui, W., Zhou, S., Tan, R., Wang, C., 2008. Structural stability and release profiles of proteins from core-shell poly (DL-lactide) ultrafine fibers prepared by emulsion electrospinning. J. Biomed. Mater. Res. - Part A 86, 374–385.

Yao, Q., Cosme, J.G.L., Xu, T., Miszuk, J.M., Picciani, P.H.S., Fong, H., Sun, H., 2017. Three dimensional electrospun PCL/PLA blend nano fibrous scaffolds with significantly improved stem cells osteogenic differentiation and cranial bone formation. Biomaterials 115, 115–127.

Yarin, A.L., Koombhongse, S., Reneker, D.H., 2001. Bending instability in electrospinning of nanofibers. J. Appl. Phys. 89, 3018–3026.

Yin, X., Stott, M.J., Rubio, A., 2003. α - and ß -tricalcium phosphate: A density functional study Xilin. Phys. Rev. B 68, 1–8.

Yokoyama, Y., Hattori, S., Yoshikawa, C., Yasuda, Y., Koyama, H., Takato, T., Kobayashi, H., 2009. Novel wet electrospinning system for fabrication of spongiform nanofiber 3-dimensional fabric. Mater. Lett. 63, 754–756.

Yördem, O.S., Papila, M., Menceloğlu, Y.Z., 2008. Effects of electrospinning parameters on polyacrylonitrile nanofiber diameter: An investigation by response surface methodology. Mater. Des. 29, 34–44.

Yoruç, A.B.H., Cem, B.Ş., 2012. Biomaterials. In: Kara, S. (Ed.), A Roadmap of Biomedical Engineers and Milestones. InTech, pp. 67–114.

Yoshimoto, H., Shin, Y.M., Terai, H., Vacanti, J.P., 2003. A biodegradable nanofiber scaffold by electrospinning and its potential for bone tissue engineering. Biomaterials 24, 2077–2082.

You, Y., Min, B.M., Lee, S.J., Lee, T.S., Park, W.H., 2005. In vitro degradation behavior of electrospun polyglycolide, polylactide, and poly(lactide-co-glycolide). J. Appl. Polym. Sci. 95, 193–200.

Yousefi, A., James, P., Akbarzadeh, R., Subramanian, A., Flavin, C., Oudadesse, H., 2016. Prospect of Stem Cells in Bone Tissue Engineering : A Review. Stem Cells Int. 2016, 1–13.

Yu, D.G., Zhu, L.M., Branford-White, C.J., Yang, J.H., Wang, X., Li, Y., Qian, W., 2011. Solid dispersions in the form of electrospun core-sheath nanofibers. Int. J. Nanomedicine 6, 3271–3280.

Yu, H.J., Fridrikh, S. V., Rutledge, G.C., 2004. Production of submicrometer diameter fibers by two-fluid electrospinning. Adv. Mater. 16, 1562–1566.

Yu, S., Hariram, K.P., Kumar, R., Cheang, P., Aik, K.K., 2005. In vitro apatite formation and its growth kinetics on hydroxyapatite/ polyetheretherketone biocomposites. Biomaterials 26, 2343–2352.

Zafar, M., Najeeb, S., Khurshid, Z., Vazirzadeh, M., Zohaib, S., Najeeb, B., Sefat, F., 2016. Potential of electrospun nanofibers for biomedical and dental applications. Materials. 9, 1–21.

Zafar, M.T., Maiti, S.N., Ghosh, A.K., 2016. Effect of surface treatments of jute fibers on the microstructural and mechanical responses of poly(lactic acid)/jute fiber biocomposites. RSC Adv. 6, 73373–73382.

Zaichick, V., Tzaphlidou, M., 2002. Determination of calcium, phosphorus, and the calcium/phosphorus ratio in cortical bone from the human femoral neck by neutron activation analysis. Appl. Radiat. Isot. 56, 781–786.

Zander, N.E., 2013. Hierarchically structured electrospun fibers. Polymers. 5, 19–44.

Zhang, C., Yuan, X., Wu, L., Han, Y., Sheng, J., 2005. Study on morphology of electrospun poly(vinyl alcohol) mats. Eur. Polym. J. 41, 423–432.

Zhang, H., Fu, Q.-W., Sun, T.-W., Chen, F., Qi, C., Wu, J., Cai, Z.-Y., Qian, Q.-R., Zhu, Y.-J., 2015. Amorphous calcium phosphate, hydroxyapatite and poly(d,l-lactic acid) composite nanofibers: Electrospinning preparation, mineralization and in vivo bone defect repair. Colloids Surfaces B Biointerfaces 136, 27–36.

Zhang, H., Zhao, C., Zhao, Y., Tang, G., Yuan, X., 2010. Electrospinning of ultrafine core/shell fibers for biomedical applications. Sci. China Chem. 53, 1246–1254.

Zhang, X., Meng, S., Huang, Y., Xu, M., He, Y., Lin, H., Han, J., Chai, Y., Wei, Y., Deng, X., 2015. Electrospun gelatin / ß -TCP composite nanofibers enhance osteogenic differentiation of BMSCs and in vivo bone formation by activating Ca+2-sensing receptor signaling. Stem Cells Int. 2015, 1–13.

Zhang, X., Peng, X., Zhang, S.W., 2017. Synthetic biodegradable medical polymers: Polymer blends, Science and Principles of Biodegradable and Bioresorbable Medical Polymers. Elsevier Ltd.

Zhang, Y., Hao, L., Savalani, M.M., Harris, R.A., Di Silvio, L., Tanner, K.E., 2009. In vitro biocompatibility of hydroxyapatite-reinforced polymeric composites manufactured by selective laser sintering. J. Biomed. Mater. Res. - Part A 91, 1018–1027.

Zhang, Y., Huang, Z.-M., Xu, X., Lim, C.T., Ramakrishna, S., 2004. Preparation of core-shell structured PCL-r-gelatin bi-component nanofibers by coaxial electrospinning. Chem. Mater. 16, 3406–3409.

Zhang, Y., Tanner, K.E., 2003. Impact behavior of hydroxyapatite reinforced polyethylene composites. J. Mater. Sci. Mater. Med. 14, 63–68.

Zhang, Y., Tanner, K.E., 2008. Effect of filler surface morphology on the impact behaviour of hydroxyapatite reinforced high density polyethylene composites. J. Mater. Sci. Mater. Med. 19, 761–766.

Zhang, Y., Venugopal, J.R., El-Turki, A., Ramakrishna, S., Su, B., Lim, C.T., 2008. Electrospun biomimetic nanocomposite nanofibers of hydroxyapatite/chitosan for bone tissue engineering. Biomaterials 29, 4314–4322.

Zhang, Y.Z., Wang, X., Feng, Y., Li, J., Lim, C.T., Ramakrishna, S., 2006. Coaxial electrospinning of (fluorescein isothiocyanate-conjugated bovine serum albumin)-encapsulated poly(ε-caprolactone) nanofibers for sustained release. Biomacromolecules 7, 1049–1057.

Zhou, F.L., Gong, R.H., Porat, I., 2009. Mass production of nanofibre assemblies by electrostatic spinning. Polym. Int. 58, 331–342.

Zhou, P., Wang, J., Macon, A.B., Obata, A., Jones, J.R., Kasuga, T., 2017. Tailoring the delivery of therapeutic ions from bioactive scaffolds while inhibiting their apatite nucleation: a coaxial electrospinning strategy for soft tissue regeneration. RSC Adv. 7, 3992–3999.

Zhou, Y., Li, S., Yuan, B., Men, B., Ren, M., 2018. Fabrication of Core–Shell Collagen/HAP Fibers via Coaxial Electrospinning Using Nontoxic Solvent. Sci. Adv. Mater. 10, 18–23.

Zong, X., Kim, K., Fang, D., Ran, S., Hsiao, B.S., Chu, B., 2002. Structure and

process relationship of electrospun bioabsorbable nanofiber membranes. Polymer. 43, 4403–4412.

Appendix A

A.1 Statistical analysis for Chapter 4

Table A.1 Statistical analysis for 15% PLA samples degradation in distilled water comparing the non-filled with each of the fillers at 10 or 20% and between the fillers at 10 or 20% filler content. n.s. = non-significant, * = $p < 0.05$, ** = $p < 0.01$, *** = $p < 0.001$

Day	Non-filled vs. HA1		Non-filled vs. HA2		Non-filled vs. TCP		HA1 vs HA2		HA1 vs TCP		HA2 vs TCP	
	10%	20%	10%	20%	10%	20%	10%	20%	10%	20%	10%	20%
1	n.s.	n.s.	n.s.	n.s.	n.s.	n.s.	n.s.	n.s.	n.s.	n.s.	n.s.	n.s.
3	n.s.	n.s.	n.s.	n.s.	n.s.	*	***	n.s.	*	**	***	*
5	n.s.	n.s.	n.s.	n.s.	n.s.	n.s.	n.s.	*	*	***	**	***
7	n.s.	n.s.	*	n.s.	n.s.	*	***	*	n.s.	**	**	***
14	n.s.	*	n.s.	n.s.	**	***	**	*	**	***	***	***

Table A.2 Statistical analysis for 20% PLA samples degradation in distilled water comparing the non-filled with each of the fillers at 10 or 20% and between the fillers at 10 or 20% filler content. n.s. = non-significant, * = $p < 0.05$, ** = $p < 0.01$, *** = $p < 0.001$

Day	Non-filled vs. HA1		Non-filled vs. HA2		Non-filled vs. TCP		HA1 vs HA2		HA1 vs TCP		HA2 vs TCP	
	10%	20%	10%	20%	10%	20%	10%	20%	10%	20%	10%	20%
1	n.s.	n.s.	n.s.	n.s.	n.s.	n.s.	n.s.	n.s.	n.s.	n.s.	n.s.	n.s.
3	n.s.	n.s.	n.s.	n.s.	n.s.	n.s.	n.s.	n.s.	n.s.	n.s.	n.s.	n.s.
5	n.s.	n.s.	n.s.	n.s.	*	n.s.	**	n.s.	**	*	n.s.	n.s.
7	n.s.	**	**	**	*	n.s.	**	n.s.	**	n.s.	n.s.	*
14	*	n.s.	n.s.	n.s.	n.s.	**	n.s.	n.s.	*	n.s.	n.s.	*

Table A.3 Statistical analysis for 15% PLA samples degradation in SBF comparing the non-filled with each of the fillers at 10 or 20% and between the fillers at 10 or 20% filler content. n.s. = non-significant, * = $p < 0.05$, ** = $p < 0.01$, *** = $p < 0.001$

Day	Non-filled vs. HA1		Non-filled vs. HA2		Non-filled vs. TCP		HA1 vs HA2		HA1 vs TCP		HA2 vs TCP	
	10%	20%	10%	20%	10%	20%	10%	20%	10%	20%	10%	20%
1	n.s.	n.s.	n.s.	n.s.	n.s.	n.s.	n.s.	n.s.	n.s.	n.s.	n.s.	n.s.
3	n.s.	n.s.	n.s.	n.s.	n.s.	n.s.	n.s.	n.s.	n.s.	n.s.	n.s.	n.s.
5	n.s.	n.s.	n.s.	n.s.	n.s.	n.s.	n.s.	n.s.	n.s.	*	**	n.s.
7	*	*	**	**	*	**	n.s.	n.s.	n.s.	n.s.	n.s.	n.s.
14	*	n.s.	*	n.s.	n.s.	**	n.s.	n.s.	n.s.	n.s.	n.s.	*

Table A.4 Statistical analysis for 20% PLA samples degradation in SBF comparing the non-filled with each of the fillers at 10 or 20% and between the fillers at 10 or 20% filler content. n.s. = non-significant, * = $p < 0.05$, ** = $p < 0.01$, *** = $p < 0.001$

Day	Non-filled vs. HA1		Non-filled vs. HA2		Non-filled vs. TCP		HA1 vs HA2		HA1 vs TCP		HA2 vs TCP	
	10%	20%	10%	20%	10%	20%	10%	20%	10%	20%	10%	20%
1	n.s.	n.s.	n.s.	n.s.	n.s.	n.s.	n.s.	n.s.	n.s.	n.s.	n.s.	n.s.
3	n.s.	n.s.	n.s.	n.s.	n.s.	n.s.	n.s.	n.s.	n.s.	n.s.	n.s.	n.s.
5	n.s.	n.s.	n.s.	n.s.	n.s.	n.s.	n.s.	n.s.	n.s.	n.s.	n.s.	n.s.
7	n.s.	n.s.	n.s.	n.s.	n.s.	n.s.	n.s.	n.s.	n.s.	n.s.	n.s.	n.s.
14	n.s.	n.s.	n.s.	*	n.s.	n.s.	n.s.	n.s.	n.s.	n.s.	n.s.	n.s.

Table A.5 Statistical analysis for 15% PLA samples degradation in distilled water comparing weight loss of 15% PLA samples at different time points. n.s. = non-significant, * = $p < 0.05$, ** = $p < 0.01$, *** = $p < 0.001$

Degradation time/days	14	7	5	3
1	n.s.	n.s.	n.s.	n.s.
	***	***	***	n.s.
	***	***	***	n.s.
	*	n.s.	*	n.s.
	n.s.	n.s.	n.s.	n.s.
	***	*	**	n.s.
	***	**	*	n.s.
3	n.s.	n.s.	n.s.	
	***	**	*	
	***	**	n.s.	
	***	***	***	
	n.s.	n.s.	n.s.	
	**	n.s.	n.s.	
	***	**	n.s.	
5	n.s.	n.s.		
	**	*		
	***	**		
	n.s.	*		
	n.s.	n.s.		
	**	*		
	***	*		
7	n.s.			
	n.s.			
	*			
	*			
	n.s.			
	*			
	***			

Non-filled
10 HA1
20 HA1
10 HA2
20 HA2
10 TCP
20 TCP

Table A.6 Statistical analysis for 20% PLA samples degradation in distilled water comparing weight loss of 20% PLA samples at different time points. n.s. = non-significant, * = $p < 0.05$, ** = $p < 0.01$, *** = $p < 0.001$

Degradation time/days	14	7	5	3
1	**	**	n.s.	n.s.
	***	***	***	*
	**	***	***	*
	***	**	*	n.s.
	***	*	**	n.s.
	*	n.s.	n.s.	n.s.
	***	**	**	n.s.
3	*	*	n.s.	
	**	**	*	
	*	n.s.	n.s.	
	***	*	n.s.	
	**	n.s.	n.s.	
	**	*	n.s.	
	***	*	*	
5	n.s.	n.s.		
	*	n.s.		
	*	n.s.		
	**	n.s.		
	*	n.s.		
	**	*		
	**	n.s.		
7	n.s.			
	n.s.			
	*			
	**			
	*			
	*			
	**			

Non-filled
10 HA1
20 HA1
10 HA2
20 HA2
10 TCP
20 TCP

Table A.7 Statistical analysis for 15% PLA samples degradation in SBF comparing weight loss of 15% PLA samples at different time points. n.s. = non-significant, * = $p < 0.05$, ** = $p < 0.01$, *** = $p < 0.001$

Degradation time/days	14	7	5	3
1	n.s.	n.s.	n.s.	n.s.
	n.s.	n.s.	n.s.	n.s.
	n.s.	n.s.	n.s.	n.s.
	n.s.	*	n.s.	n.s.
	n.s.	**	n.s.	n.s.
	n.s.	n.s.	n.s.	n.s.
	***	**	n.s.	**
3	n.s.	n.s.	n.s.	
	n.s.	n.s.	n.s.	
	n.s.	n.s.	n.s.	
	n.s.	n.s.	n.s.	
	n.s.	**	n.s.	
	n.s	n.s.	n.s.	
	n.s.	*	n.s.	
5	n.s.	n.s.		
	n.s.	n.s.		
	n.s.	n.s.		
	n.s.	*		
	n.s.	***		
	n.s.	n.s.		
	n.s.	n.s.		
7	n.s.			
	n.s.			
	n.s.			
	**			
	*			
	n.s.			
	n.s.			

Non-filled
10 HA1
20 HA1
10 HA2
20 HA2
10 TCP
20 TCP

Since p values for two-factor ANOVA test for the 20% PLA samples in SBF were higher than 0.05, no comparison were made for each PLA/filler composition among degradation days.

Table A.8 Levels of significance for Young's moduli and UTS values of 15% PLA samples before degradation comparing the non-filled and each of the fillers at 10 or 20% and between the fillers at 10 or 20% filler content. n.s. = non-significant, * = $p < 0.05$, ** = $p < 0.01$, *** = $p < 0.001$

	Non-filled vs. HA1		Non-filled vs. HA2		Non-filled vs. TCP		HA1 vs HA2		HA1 vs TCP		HA2 vs TCP	
	10%	20%	10%	20%	10%	20%	10%	20%	10%	20%	10%	20%
E (MPa)	n.s.	*	n.s.	n.s.	*	***	*	n.s.	n.s.	**	**	**
UTS (MPa)	n.s.	*	n.s.	*	*	**	**	n.s.	*	n.s.	***	**

Table A.9 Levels of significance for Young's moduli and UTS values of 20% PLA samples before degradation comparing the non-filled and each of the fillers at 10 or 20% and between the fillers at 10 or 20% filler content. n.s. = non-significant, * = $p < 0.05$, ** = $p < 0.01$, *** = $p < 0.001$

	Non-filled vs. HA1		Non-filled vs. HA2		Non-filled vs. TCP		HA1 vs HA2		HA1 vs TCP		HA2 vs TCP	
	10%	20%	10%	20%	10%	20%	10%	20%	10%	20%	10%	20%
E (MPa)	n.s.	*	n.s.	n.s.	n.s.	**	*	n.s.	n.s.	***	*	***
UTS (MPa)	n.s.	n.s.	n.s.	n.s.	n.s.	**	n.s.	n.s.	n.s.	**	*	***

A.2 Statistical analysis for Chapter 5

Table A.10 Statistical analysis for 15% PLA samples water uptake comparing the non-filled with each of the fillers at 10 or 20% and between the fillers at 10 or 20% filler content. n.s. = non-significant, * = p < 0.05, ** = p < 0.01, *** = p< 0.001

Day	Non-filled vs. HA1		Non-filled vs. HA2		HA1 vs HA2		10% vs. 20% HA1	10% vs. 20% HA2
	10%	20%	10%	20%	10%	20%		
1	**	***	n.s.	**	*	**	n.s.	n.s.
2	**	***	*	**	n.s.	*	n.s.	n.s.
4	***	***	**	**	n.s.	n.s.	n.s.	n.s.
7	*	*	n.s.	n.s.	n.s.	**	n.s.	n.s.
14	**	*	n.s.	*	n.s.	n.s.	n.s.	n.s.
21	**	**	n.s.	*	*	n.s.	n.s.	n.s.
28	***	***	*	*	*	*	n.s.	n.s.

Table A.11 Statistical analysis for 20% PLA samples water uptake comparing the non-filled with each of the fillers at 10 or 20% and between the fillers at 10 or 20% filler content. n.s. = non-significant, * = p < 0.05, ** = p < 0.01, *** = p< 0.001

Day	Non-filled vs. HA1		Non-filled vs. HA2		HA1 vs HA2		10% vs. 20% HA1	10% vs. 20% HA2
	10%	20%	10%	20%	10%	20%		
1	n.s.	n.s.	n.s.	n.s.	n.s.	n.s.	n.s.	n.s.
2	n.s.	n.s.	n.s.	n.s.	n.s.	n.s.	n.s.	n.s.
4	n.s.	n.s.	n.s.	n.s.	n.s.	n.s.	n.s.	n.s.
7	n.s.	n.s.	n.s.	n.s.	n.s.	n.s.	n.s.	n.s.
14	*	**	n.s.	**	n.s.	n.s.	n.s.	n.s.
21	*	**	n.s.	n.s.	*	**	**	n.s.
28	**	***	n.s.	n.s.	**	***	n.s.	n.s.

Table A.12 Statistical analysis for 15% PLA samples weight loss comparing the non-filled with each of the fillers at 10 or 20% and between the fillers at 10 or 20% filler content. n.s. = non-significant, * = $p < 0.05$, ** = $p < 0.01$, *** = $p < 0.001$

Day	Non-filled vs. HA1		Non-filled vs. HA2		HA1 vs HA2		10% vs. 20% HA1	10% vs. 20% HA2
	10%	20%	10%	20%	10%	20%		
1	n.s.	n.s.	n.s.	n.s.	n.s.	n.s.	n.s.	n.s.
2	n.s.	n.s.	n.s.	n.s.	n.s.	n.s.	n.s.	n.s.
4	n.s.	n.s.	n.s.	n.s.	n.s.	n.s.	n.s.	n.s.
7	n.s.	n.s.	n.s.	n.s.	n.s.	n.s.	n.s.	n.s.
14	*	**	n.s.	n.s.	n.s.	**	n.s.	n.s.
21	*	**	n.s.	*	n.s.	**	n.s.	n.s.
28	**	***	*	*	n.s.	**	*	n.s.

Table A.13 Statistical analysis for 20% PLA samples weight loss comparing the non-filled with each of the fillers at 10 or 20% and between the fillers at 10 or 20% filler content. n.s. = non-significant, * = $p < 0.05$, ** = $p < 0.01$, *** = $p < 0.001$

Day	Non-filled vs. HA1		Non-filled vs. HA2		HA1 vs HA2		10% vs. 20% HA1	10% vs. 20% HA2
	10%	20%	10%	20%	10%	20%		
1	n.s.	n.s.	n.s.	n.s.	n.s.	n.s.	n.s.	n.s.
2	n.s.	n.s.	n.s.	n.s.	n.s.	n.s.	n.s.	n.s.
4	n.s.	n.s.	n.s.	n.s.	n.s.	n.s.	n.s.	n.s.
7	n.s.	n.s.	n.s.	n.s.	n.s.	n.s.	n.s.	n.s.
14	n.s.	n.s.	n.s.	n.s.	n.s.	n.s.	n.s.	n.s.
21	n.s.	n.s.	n.s.	n.s.	n.s.	n.s.	n.s.	n.s.
28	**	***	*	**	n.s.	***	***	n.s.

Table A.14 Levels of significance for Young's moduli and UTS values of 15% PLA samples after immersion in SBF comparing the non-filled and each of the fillers at 10 or 20% and between the fillers at 10 or 20% filler content. n.s. = non-significant, * = p < 0.05, ** = p < 0.01, *** = p< 0.001

	Non-filled vs. HA1		Non-filled vs. HA2		HA1 vs HA2		10% vs 20% HA1	10% vs 20% HA2
	10%	20%	10%	20%	10%	20%		
E (MPa)	***	***	***	*	*	**	*	n.s.
UTS (MPa)	***	***	n.s.	n.s.	**	n.s.	n.s.	n.s.

Table A.15 Levels of significance for Young's moduli and UTS values of 20% PLA samples after immersion in SBF comparing the non-filled and each of the fillers at 10 or 20% and between the fillers at 10 or 20% filler content. n.s. = non-significant, * = p < 0.05, ** = p < 0.01, *** = p< 0.001

	Non-filled vs. HA1		Non-filled vs. HA2		HA1 vs HA2		10% vs 20% HA1	10% vs 20% HA2
	10%	20%	10%	20%	10%	20%		
E (MPa)	**	***	n.s.	n.s.	n.s.	**	n.s.	n.s.
UTS (MPa)	*	*	n.s.	n.s.	n.s.	n.s.	n.s.	n.s.

A.3 Statistical analysis for Chapter 6

Table A.16 Levels of significance for Young's moduli, UTS and elongation values of coaxial electrospun scaffolds comparing the control samples with HA-containing samples and between 2:3 and 3:3 core: shell flow rate ratios. n.s. = non-significant, * = $p < 0.05$, ** = $p < 0.01$, *** = $p < 0.001$

	Coaxial CTRL vs. HA		Coaxial CTRL (3:3) vs. (3:2) flow rate ratio	Coaxial HA (3:3) vs. (3:2) flow rate ratio	Coaxial HA (3:3) vs. 20%PCL (2:1 chloroform: acetone)	**Coaxial HA (3:3) vs. 15 20 HA2 (2:1 chloroform: acetone)**
	Core :shell flow rate 2:3	Core :shell flow rate 3:3				
E (MPa)	*	*	*	***	***	***
UTS (MPa)	*	***	n.s.	***	n.s.	***
Elongation (%)	***	***	n.s.	***	***	***

A.4 Statistical analysis for Chapter 7

Table A.17 Statistical analysis for coaxial scaffolds water uptake and weight loss comparing control scaffolds with HA-containing coaxial scaffolds and between scaffolds immersed in PBS or in SBF. n.s. = non-significant, * = $p < 0.05$, ** = $p < 0.01$, *** = $p < 0.001$

Time (week)	Water uptake in PBS vs. SBF		Weight loss in PBS vs. SBF		CTRL VS HA in PBS		CTRL VS HA in SBF	
	CTRL	HA	CTRL	HA	Weight loss	Water uptake	Weight loss	Water uptake
4	n.s.	n.s.	***	n.s.	n.s.	n.s.	n.s.	n.s.
8	**	*	**	n.s.	n.s.	n.s.	n.s.	n.s.
12	*	**	***	n.s.	n.s.	n.s.	**	n.s.

Table A.18 Statistical analysis for control and HA-containing coaxial scaffolds water uptake in PBS or SBF at different time points. n.s. = non-significant, * = p < 0.05, ** = p < 0.01, *** = p< 0.001

Immersion time (weeks)	12	8
4	n.s.	n.s.
	n.s	n.s.
	*	***
	n.s.	n.s.
8	n.s.	
	n.s.	
	n.s.	
	n.s.	

CTRL PBS
CTRL SBF
HA PBS
HA SBF

Table A.19 Statistical analysis for control and HA-containing coaxial scaffolds weight loss in PBS or SBF at different time points. n.s. = non-significant, * = p < 0.05, ** = p < 0.01, *** = p< 0.001

Immersion time (weeks)	12	8
4	**	n.s.
	***	*
	**	n.s.
	n.s.	n.s.
8	n.s.	
	n.s.	
	n.s.	
	n.s.	

CTRL PBS
CTRL SBF
HA PBS
HA SBF

Table A.20 Levels of significance for Young's moduli, UTS and elongation values of coaxial control and HA-containing scaffolds after immersion in either PBS or SBF. n.s. = non-significant, * = $p < 0.05$, ** = $p < 0.01$, *** = $p < 0.001$

Time (week)	E (MPa) PBS vs. SBF		UTS (MPa) PBS vs. SBF		Elongation (%) PBS vs. SBF	
	CTRL	HA	CTRL	HA	CTRL	HA
4	n.s.	n.s.	n.s.	n.s.	n.s.	n.s.
8	n.s.	n.s.	n.s.	n.s.	n.s.	n.s.
12	n.s.	n.s.	n.s.	n.s.	n.s.	n.s.

Table A.21 Statistical analysis for the reduction in Young's modulus values of control and HA-containing coaxial scaffolds immersed in PBS or SBF at different time points. n.s. = non-significant, * = $p < 0.05$, ** = $p < 0.01$, *** = $p < 0.001$

Immersion time (weeks)	12	8	4
0	*	n.s.	n.s.
	n.s.	n.s.	n.s.
	**	**	n.s.
	**	*	*
4	n.s.	n.s.	
	n.s.	n.s.	
	n.s.	*	
	n.s.	n.s.	
8	n.s.		
	n.s.		
	n.s.		
	n.s.		

CTRL PBS
CTRL SBF
HA PBS
HA SBF

Table A.22 Statistical analysis for the reduction in tensile strength values of control and HA-containing coaxial scaffolds immersed in PBS or SBF at different time points. n.s. = non-significant, * = p < 0.05, ** = p < 0.01, *** = p< 0.001

Immersion time (weeks)	12	8	4
0	n.s.	n.s.	n.s.
	n.s.	n.s.	n.s.
	***	**	**
	***	**	*
4	n.s.	n.s.	
	n.s.	n.s.	
	n.s.	n.s.	
	n.s.	n.s.	
8	n.s.		
	n.s.		
	n.s.		
	***		

CTRL PBS
CTRL SBF
HA PBS
HA SBF

Table A.23 Statistical analysis for the reduction in elongation values of control and HA-containing coaxial scaffolds immersed in PBS or SBF at different time points. n.s. = non-significant, * = p < 0.05, ** = p < 0.01, *** = p< 0.001

Immersion time (weeks)	12	8	4
0	n.s.	n.s.	n.s.
	*	*	n.s.
	n.s.	n.s.	n.s.
	n.s.	n.s.	n.s.
4	n.s.	n.s.	
	n.s.	n.s.	
	n.s.	n.s.	
	n.s.	n.s.	
8	n.s.		
	n.s.		
	n.s.		
	n.s.		

CTRL PBS
CTRL SBF
HA PBS
HA SBF

Appendix B

B.1 List of publications

Conferences abstracts:

1- WBC 2016 (Montreal-Canada): Poster presentation entitled: “Effect of filler type on mechanical and biological properties of electrospun PLA used for bone tissue applications”- whole poster attached.

2- UKSB 2016 (London-UK): Oral presentation entitled: “Effect of filler type on mechanical and biological properties of electrospun PLA used for bone tissue applications”.

3- ESB 2017 (Athens-Greece): Poster presentation entitled: “Characterization of Electrospun PLA/HA Fibres: Effect of Filler Concentration and Surface Area”.

4- ESB 2017 (Athens-Greece): Poster presentation entitled: “Degradation of Electrospun PLA/HA Fibres: Effect of Filler Concentration and Surface Area”.

5- UKSB 2017 (Loughborough- UK): Accepted for poster presentation entitled: “Electrospinning of core/shell PCL/PLA-HA fibres for bone tissue engineering”.

Effect of filler type on mechanical and biological properties of electrospun PLA used for bone tissue applications

Muna M. Kareem and K.E. Tanner

Biomedical Engineering Division, School of Engineering, University of Glasgow, Glasgow, G12 8QQ, UK

Introduction

Electrospinning is used widely to produce bone tissue engineering scaffolds as the electrospun fibres have similar diameters to natural extracellular matrix (ECM) fibrils and can serve as an effective substrate for cell growth [1]. Electrospun scaffolds for bone tissue engineering can be made from biodegradable polymers with the addition of calcium phosphate ceramics to optimise their degradation rate, osteoconductivity and mechanical properties [2].

Results

Electrospinning

Pure PLA solutions with no filler were spun into randomly oriented, smooth fibers with no beads present (Fig. 1a), however, introducing 10 and 20% of HA1 and HA2 into those solutions resulted in non-uniform fibers with enlarged diameters (Fig. 1b and c). Incorporation of β-TCP into 15% and 20% PLA samples caused clusters formation along the fibers which increased in size with increasing TCP content (Fig. 1d). The average diameter of the electrospun fibers analyzed using ImageJ are shown in Table 1.

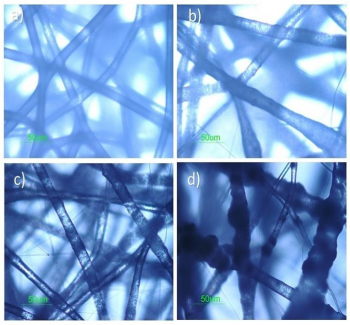

Figure 1 Microscope images of electrospun fibres: (a) PLA with no filler; (b) PLA/HA1; (c) PLA/HA2; and (d) PLA/TCP (all marker bars = 50μm)

Table 1 Average Fibre Diameters

Filler percentage	Average fibre diameters (μm)	
	15% PLA	20% PLA
0 %	12.02 ± 0.64	13.60 ± 0.92
10% HA1	21.24 ± 4.32	21.00 ± 6.51
20% HA1	23.29 ± 6.23	20.01 ± 6.40
10% HA2	18.88 ± 6.72	18.72 ± 3.55
20% HA2	19.28 ± 4.24	17.24 ± 5.51
10% TCP	19.74 ± 1.97	18.83 ± 4.01
20% TCP	20.15 ± 8.40	19.26 ± 2.53

Degradation results

- Pure 15% PLA scaffolds exhibited weight increases during the first 5 days, followed by progressive weight reduction (Fig. 2a), while for the 20% PLA scaffolds the weight increase continued throughout the 2 weeks of degradation (Fig. 2b). The weight gain of the samples could be resulted from water absorption which is the first event in polymer degradation.
- Incorporation of HA1 and HA2 into 15% PLA led to generally higher mineral deposition in SBF represented by weight increase during the first week of immersion then degradation started on week 2 on immersion, but with increasing PLA concentration to 20%, degradation seemed to be more dominant than mineralization. HA2 showed higher weight increase in 15% PLA samples than HA1, while in 20% PLA samples, samples weight values for both fillers were relatively similar.
- Mineral deposition of samples containing 10% TCP during the first week was lower than those containing HA1 and HA2, while the overall behavior of 20% TCP samples indicated higher degradability than all other samples, especially on the second week of immersion.

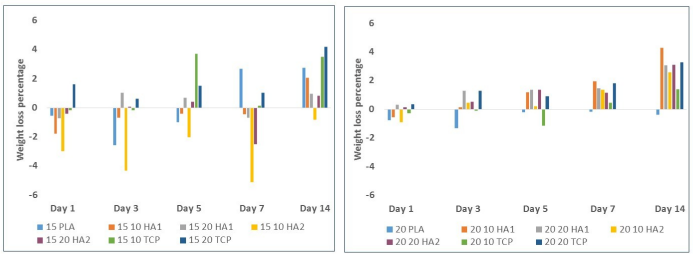

Figure 2 Net weight change of samples containing a) 15% PLA and b) 20%PLA before and after degradation

References:

1. Bhardwaj, N., Kundu, S.C., 2010. Electrospinning: A fascinating fiber fabrication technique. Biotechnol. Adv. **28**, 325–347

2. Braghirolli, D.I., Steffens, D., Pranke, P., 2014. Electrospinning for regenerative medicine: A review of the main topics. Drug Discov. Today **19**, 743–753

Materials and Methods

Electrospun fibres were produced using PLA (3001D, NatureWorks, USA) and 3 fillers: spray dried hydroxyapatite (HA P218R, d_{50}= 4.02μm, specific surface area = 13.536m^2 g^{-1}), sintered hydroxyapatite (HA P220S, d_{50}= 3.59μm, specific surface area = 0.965m^2 g^{-1}) and tricalcium phosphate (β-TCP, d_{50}= 3.44μm) (all Plasma Biotal Ltd, UK). Being spray dried, HA1 was formed of acicular agglomerates of nanoscale needles, while sintered HA2 had smooth surfaces and the particles were solid. The PLA was dissolved in chloroform at 15 or 20 wt/vol% and the filler added to give 10 or 20 vol% in the final composite material. The samples were electrospun at 13.7 kV and 1ml hr^{-1} flow rate, onto a microscope slide and allowed to dry. Fibre diameter was measured using a Nomarski microscope (Nikon Instruments Europe B.V, Netherland) and ImageJ software (NIH, USA).

Samples were immersed in either simulated body fluid (SBF) or distilled water in order to evaluate bioactivity and to measure the degradation rate for up to 14 days. Degradation solutions were changed every 7 days. Tensile test samples were cut to 10mm by 60mm to provide a 40mm test gauge length and tested at 1 mm s^{-1} (reduce sized ISO 13934). Young's modulus, ultimate tensile strength and strain at failure were calculated before and after 14 days degradation.

Results

Mechanical Properties

- Figures 4 and 5 indicate that the addition of increasing amounts of HA1 and HA2 to 15% PLA samples generally decreased stiffness and ultimate strength. However, for samples made from 20% PLA, their addition led to higher Young's modulus and did not effect the strength substantially. Incorporation of β-TCP significantly decreased the mechanical properties of both 15% and 20% PLA samples which might resulted from cluster formation, causing breakage in the continuity of the resulted fibre chain and made the samples more fragile.
- After degradation in SBF, the UTS of all samples were significantly reduced to almost half of the values before degradation, while many samples have preserved their tensile strength values or reduced slightly during distilled water degradation (Fig. 3).
- On the other hand, Young's modulus values were also decreased by different amounts after degradation in both media for all samples Ffig.4).
- It could also be seen that by increasing the filler percentage in the composite, the mechanical properties were dropping faster during degradation.

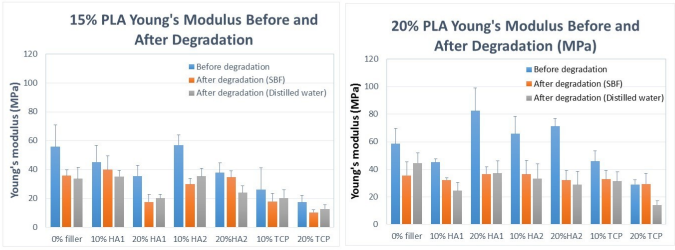

Figure 3 Young's modulus of samples containing a)15% PLA and b) 20%PLA before and after degradation

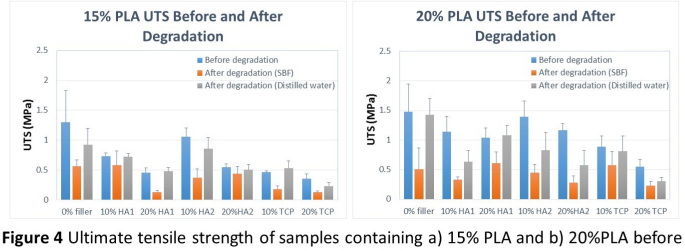

Figure 4 Ultimate tensile strength of samples containing a) 15% PLA and b) 20%PLA before and after degradation

Conclusions:

- PLA/TCP samples degraded faster than those containing HA1 or HA2 due to higher solubility of TCP, while samples containing HA1 and HA2 exhibited higher bioactivity.
- Increase fillers content in electrospun PLA scaffolds leads to significant reduction in their mechanical properties
- Considerable amounts of calcium phosphate can be added to PLA while still being able to produce useful scaffolds.

Acknowledgment:

MMK is supported by a PhD studentship from the Iraqi Ministry of Higher Education and Scientific Research (reference S 1648).

Effect of filler type on mechanical and biological properties of electrospun PLA used for bone tissue applications

Muna M. Kareem, K. E. Tanner

Biomedical Engineering Division, School of Engineering, University of Glasgow

Corresponding author: m.kareem.2@research.gla.ac.uk – PhD student (2nd year)

Introduction

Electrospinning is used widely to produce bone tissue engineering scaffolds as the electrospun fibres have similar diameters to natural extracellular matrix (ECM) fibrils and can serve as an effective substrate for cell growth [1]. Electrospun scaffolds for bone tissue engineering can be made from biodegradable polymers with the addition of calcium phosphate ceramics to enhance their degradation rate, osteoconductivity and mechanical properties [2].

Materials and Methods

Electrospun fibres were produced using PLA (3001D, NatureWorks, USA) and 3 fillers: spray dried hydroxyapatite (HA P218R, d_{50}= 4.02 µm), sintered hydroxyapatite (HA P220S, d_{50}= 3.59 µm) and tricalcium phosphate (β-TCP, d_{50}= 3.44 µm) (all Plasma Biotal Ltd, UK). The PLA was dissolved in chloroform at 15 and 20wt/vol% and the filler added to give 10 or 20 vol% in the final material. The samples were electrospun at 13.7 kV onto a microscope slide and allowed to dry. Fibre diameter was measured using a Nomarski microscope and ImageJ software. Samples were immersed in either simulated body fluid (SBF) or distilled water in order to evaluate bioactivity and to measure the degradation rate for up to 14 days. Degradation solutions were changed every 7 days. Tensile test samples were cut to 10mm by 40mm gauge length and tested at 1 mm s^{-1}(reduce sized ISO 13934). Young's modulus, ultimate tensile strength and strain at failure were calculated before and after 14 days degradation.

Results and Discussion

Pure PLA solutions with no filler were spun into randomly oriented, smooth fibres with no beads present, however, introducing 10 and 20% of HA1 and HA2 into those solutions resulted in non-uniform fibers with enlarged diameters. Incorporation of β-TCP into 15% and 20% PLA samples caused clusters formation along the fibres which increased in size with increasing TCP content. The addition of increasing amounts of HA1 and HA2 to 15% PLA samples generally decreased stiffness and ultimate strength. However, for samples made from 20% PLA, their addition led to higher Young's modulus and did not affect the strength substantially. Incorporation of β-TCP significantly decreased the mechanical properties of both 15% and 20% PLA samples which might resulted from cluster formation, causing breakage in the continuity of the resulted fibre chain and made the samples more fragile. After degradation in SBF, the UTS of all samples were significantly reduced to almost half of the values before degradation, while many samples have preserved their tensile strength values or reduced slightly during distilled water degradation On the other hand, Young's modulus values were also decreased by different amounts after degradation in both media for all samples.

	15% PLA				20% PLA			
	Young's Modulus (Before degradation) /MPa	Young's Modulus (After degradation in SBF) /MPa	UTS (Before degradation) /MPa	UTS (After degradation in SBF) /MPa	Young's Modulus (Before degradation) /MPa	Young's Modulus (After degradation in SBF) /MPa	UTS (Before degradation) /MPa	UTS (After degradation in SBF) /MPa
0% filler	55.78±15.02	35.74±4.09	1.300±0.527	0.570±0.098	58.55±11.15	35.51 ± 9.81	1.428±0.470	0.510 ± 0.355
10% HA1	39.25± 9.47	39.77±9.57	0.735±0.052	0.581±0.238	45.13±2.56	32.18 ± 1.74	1.137±0.260	0.329 ± 0.046
20% HA1	31.85±3.26	17.55±5.35	0.460±0.074	0.133±0.025	82.32±16.56	36.64 ± 5.19	1.041±0.166	0.608 ± 0.187
10% HA2	57.03±7.00	29.77±4.02	1.059±0.147	0.376±0.147	65.65±12.61	36.39 ± 9.92	1.394±0.264	0.446 ± 0.138
20%HA2	37.73±6.81	34.61±4.43	0.546±0.061	0.440±0.125	71.23±5.57	32.08 ± 7.26	1.165±0.112	0.284 ± 0.114
10% TCP	26.10±15.08	17.96±5.40	0.465±0.180	0.183±0.057	45.85±7.51	32.78 ± 6.53	0.890±0.174	0.578 ± 0.225
20% TCP	17.33±4.86	10.33±1.67	0.361±0.074	0.132±0.018	28.92±3.41	18.82± 8.85	0.552±0.118	0.228 ± 0.071

References

1. Bhardwaj, N., and Kundu S. Biotechnology Advances 28: 325–347, 2010.

2. Braghirolli, D., Daniela S., and P. Drug Discovery Today 19: 743–753, 2014.

Characterizations of Electrospun PLA/HA Fibres: Effect of Filler Concentration and Surface Area

Muna M. Kareem, K. E. Tanner

Biomedical Engineering Division/School of Engineering, University of Glasgow, UK
m.kareem.2@research.gla.ac.uk

INTRODUCTION

Electrospinning is a simple, versatile and cost effective technique to produce micro to nanoscale diameter fibres through the application of a high static voltage to a viscous polymer solution [1]. For bone tissue engineering, polymeric scaffolds are usually reinforced with bioceramics, including hydroxyapatite, to provide cells with a native environment which mimicks the extracellular matrix and to increase the mechanical properties of the scaffold [2, 3]. This study investigated the effect of increasing hydroxyapatite concentration and specific surface area on the morphology and mechanical properties of electrospun PLA fibres.

EXPERIMENTAL METHODS

Electrospinning was used to produce scaffolds based on PLA (3001D, NatureWorks, USA) reinforced with either a spray dried hydroxyapatite (HA1) in the form of agglomerates of nanoscale needles (P218R, d_{50}=4.02µm, specific surface area=13.536m^2g^{-1}), or a solid, previously sintered hydroxyapatite (HA2) with smooth surfaces (P220S, d_{50}=3.59µm, specific surface area= 0.965m^2g^{-1}) (Plasma Biotal Ltd, UK). Two PLA concentrations were used in the chloroform (15 or 20 wt/vol%) with the HA added to give final compositions of 10 or 20 vol%. A flow rate of 1ml hr^{-1} was used at 13.7 kV to spin onto a microscope slide. Non-filled PLA was used as a control.

Morphology of the resulted fibres was observed using scanning electron microscope (JOEL JSM-6400 SEM) at an accelerated voltage of 10 kV and fibre diameters were calculated using ImageJ software (NIH, USA).

Tensile test samples were cut to 10mm by 60mm to provide a 40mm test gauge length and tested at 1 mm s^{-1} (reduced size ISO 13934). For each PLA/HA combination, 5 samples were tested and the average values of Young's modulus (E) and ultimate tensile strength (UTS) were calculated.

RESULTS AND DISCUSSION

Fibre diameter analysis (Figure 1) showed that adding HA1 and HA2 have led significant increases in the fibre diameters of both 15% and 20% PLA scaffold ($p \leq 0.05$), however, the differences between both fibres containing HA1 and fibres containing HA2 was not significant. In contrast, the porosity of electrospun scaffolds was not affected by the addition of either HA and ranged from 87% to 92%. Mechanical testing (Table 2) showed that the addition of increasing amounts of HA1 and HA2 to 15% PLA samples generally decreased stiffness and ultimate strength. However, for samples made from 20% PLA, their addition led to higher Young's modulus but did not affect the strength substantially. Scaffolds with HA1 exhibited higher Young's moduli than those containing HA2, while the differences in the UTS values were generally minor.

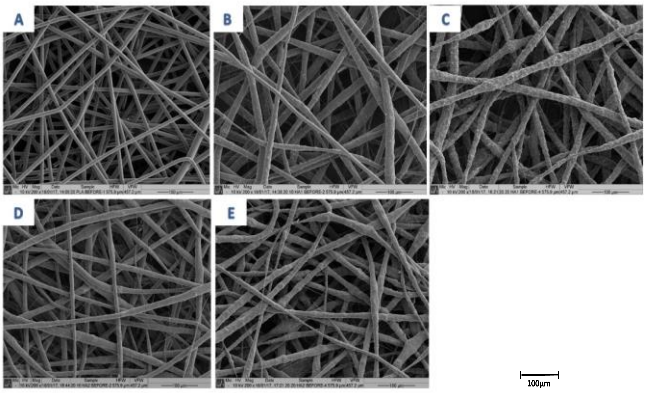

Figure 1 SEM images for electrospun 20%PLA with (A) no filler, (B) 10%HA1, (C) 20%HA1, (D) 10% HA2, and (E) 20% HA2 (marker bars= 100µm)

Table 1 Mechanical properties of electrospun 15% and 20% PLA scaffolds

	15% PLA		20% PLA	
Filler content	**E /MPa**	**UTS /MPa**	**E /MPa**	**UTS /MPa**
0% HA	55.78±15.02	1.300±0.527	58.55±11.15	1.428±0.470
10% HA1	39.25± 9.47	0.735±0.052	45.13±2.56	1.137±0.260
20% HA1	31.85±3.26	0.460±0.074	82.32±16.56	1.041±0.166
10% HA2	57.03±7.00	1.059±0.147	65.65±12.61	1.394±0.264
20% HA2	37.73±6.81	0.546±0.061	71.23±5.57	1.165±0.112

CONCLUSIONS

The higher concentration of PLA gave higher mechanical properties. Surprisingly, increasing HA content decreased the stiffness of the scaffolds, but at 20% PLA increased the strength. Generally HA2 gave higher stiffness and strength.

REFERENCES

1. Drew C. *et al.,* J. Macromol. Sci. Part A 40, 1415–1422, 2003.
2. Haider A. *et al.,* Arab. J. Chem., in press, 2015.
3. Tetteh, G. *et al.,* J. Mech. Behav. Biomed. Mater. 39: 95–110, 2014.

ACKNOWLEDGMENTS

MMK is supported by a PhD student scholarship from the Iraqi Ministry of Higher Education and Scientific Research (reference no. S1648).

Degradation of Electrospun PLA/HA Fibres: Effect of Filler Concentration and Surface Area

Muna M. Kareem[1], K. E. Tanner[1], Margaret Smith[2]

[1]Biomedical Engineering Division, School of Engineering, University of Glasgow, UK
[2]Centre for Textile Conservation and Technical Art History, School of Culture and Creative Arts, University of Glasgow, UK
m.kareem.2@research.gla.ac.uk

INTRODUCTION

Polylactic acid (PLA) has gained increasing interest for biomedical applications, including tissue engineering, due to its degradability, biocompatibility and high mechanical strength [1]. However, PLA leads to low cell adhesion due to its hydrophobic nature and inflammatory reactions can start from by-products of the lactic acid degradation. Thus, calcium phosphate (CaP) particles are incorporated into PLA scaffolds to buffer the local pH decrease produced by degradation and to improve cell adhesion and osteoconductivity [2]. This study examines the effect of hydroxyapatite (HA) concentration and specific surface area on the bioactivity and degradation rate of electrospun PLA scaffolds.

EXPERIMENTAL METHODS

Electrospun fibres were produced using PLA (3001D, NatureWorks, USA) and 2 types of HA: HA1 spray dried hydroxyapatite (P218R, d_{50}=4.02µm, specific surface area=13.536m^2g^{-1}), HA2 sintered hydroxyapatite (P220S, d_{50}=3.59µm, specific surface area=0.965m^2g^{-1}) (Plasma Biotal Ltd, UK). Being spray dried, HA1 was formed of acicular agglomerates of nanoscale needles, while the previously sintered HA2 particles were solid with smooth surfaces. The PLA was dissolved in chloroform at 15 or 20 wt/vol% and HA added to give 10 or 20 vol% in the final composite. The samples were electrospun at 13.7 kV and 1ml hr^{-1} flow rate, onto a microscope slide and allowed to dry. After removal from the slide, degradation samples were cut.

Samples were immersed in simulated body fluid (SBF) for up to 28 days in order to evaluate bioactivity and degradation rate. The solutions were changed every 7 days. HA content in the PLA and apatite deposition on the scaffold surfaces were measured by thermogravimetric analysis (TGA) using a TGA Q500 TA Instrument under nitrogen atmosphere heating from 10 to 500°C at a rate of 20 °C min^{-1}.

Bioactivity and degradation of the electrospun fibres were characterised by Fourier Transformation Infrared (FTIR) spectrometer (PerkinElmer, USA) after 14 and 28 days. FTIR spectra were recorded in absorbance mode across the 4000–400cm^{-1} wavenumber range at a resolution of 8cm^{-1} with 16 scans performed per spectra. Weight loss and water uptake percentages of the fibres were also calculated at different intervals after immersion in SBF.

RESULTS AND DISCUSSION

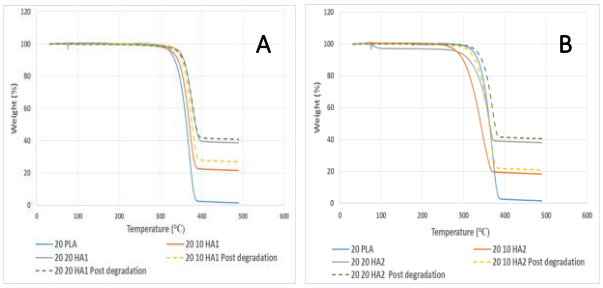

Figure 1 TGA results of electrospun 20% PLA fibres before and after 28 days degradation with: (A) HA1, and (B) HA2, dotted lines are post degradation.

TGA graphs (Figure 1) show increases in the apatite content of 20% PLA samples containing both types of HA after 28 days which indicates formation of new apatite layer on the fibres, while for samples containing 15%PLA, it generally remain the same. HA1 based composites showed greater thermal stability than those containing HA2. This result was confirmed by weight loss calculations, which revealed slower degradation rates for samples containing HA compared to non-filled PLA scaffolds.

FTIR results showed significant increase in the intensity of (468, 560, 602, 630, and 1022 cm^{-1}) peaks between samples containing 10% and 20% of both HAs which belong to the OH^{-1} and $PO4^{-3}$ bands of HA, while no notable changes appeared on the scaffolds after 28 days of degradation.

CONCLUSIONS

Introducing HA into electrospun PLA scaffolds led to slower degradation and higher *in vitro* bioactivity compared to neat PLA scaffolds. On the other hand, no significant changes appeared in the *in vitro* behaviour between the two types of HA.

REFERENCES

1. Tajbakhsh S. & Hajiali F., Int. J. Res. Appl. 4:165–174, 2016.
2. Zhou H. *et al.,* J. Mater. Sci. Mater. Med. 22:1183–1193, 2011.

ACKNOWLEDGMENTS

MMK is supported by a PhD student scholarship from the Iraqi Ministry of Higher Education and Scientific Research (reference no. S1648).

ELECTROSPINNING OF CORE/SHELL PCL/ PLA-HA FIBRES FOR BONE TISSUE ENGINEERING

Muna M. Kareem, K. E. Tanner
Biomedical Engineering Division, School of Engineering, University of Glasgow
Corresponding author: m.kareem.2@research.gla.ac.uk – PhD student (3rd year)

Submitted for either/ both
POSTER ☒
ORAL ☒

Introduction

Recently, modifications have been made in the basic electrospinning process to improve the quality and the functionality of the resulting fibres. Co-axial electrospinning has gained attention for tissue engineering applications, where two different polymers or composites are delivered independently through a co-axial emitter and drawn to produce core-sheath fibrous structures that are capable of encapsulating bioactive agents and drugs within the core layer [1]. This study investigates bioactive scaffolds for bone tissue engineering made of core/ shell fibres via coaxial electrospinning.

Materials and Methods

Co-axial electrospun fibres were fabricated using PCL (Mw=80,000, Sigma-Aldrich, UK), PLA (3001D, NatureWorks, USA) and hydroxyapatite (P220S, d_{50}=3.59µm, specific surface area=0.965$m^2 g^{-1}$, Plasma Biotal Ltd, UK). To prepare the core solution, PCL was dissolved in a mixture of chloroform/acetone (2:1) at 40°C at concentration of 20% (wt/v), while the shell solution were prepared by dissolving PLA in chloroform/acetone (2:1) at room temperature to make 15% (wt/v) PLA solution. HA was then added to the PLA solution to give 10% (v/v) in the final composite. The solutions were fed into two 5 mL plastic syringes driven by a programmable syringe pump modules (Spraybase, Ireland) and connected to a co-axial needle (16 G inner diameter, 11 G outer diameter). Samples were spun on microscope slides using 13.7 kV voltage and flow rate of 3 mL/hr for both solutions. Samples were immersed in simulated body fluid (SBF) for up to 16 weeks in order to evaluate bioactivity and degradation. SEM, fluorescent microscopy and tensile tests were performed to determine fibres diameter, the presence of core and shell, and mechanical properties before and after degradation.

Results and Discussion

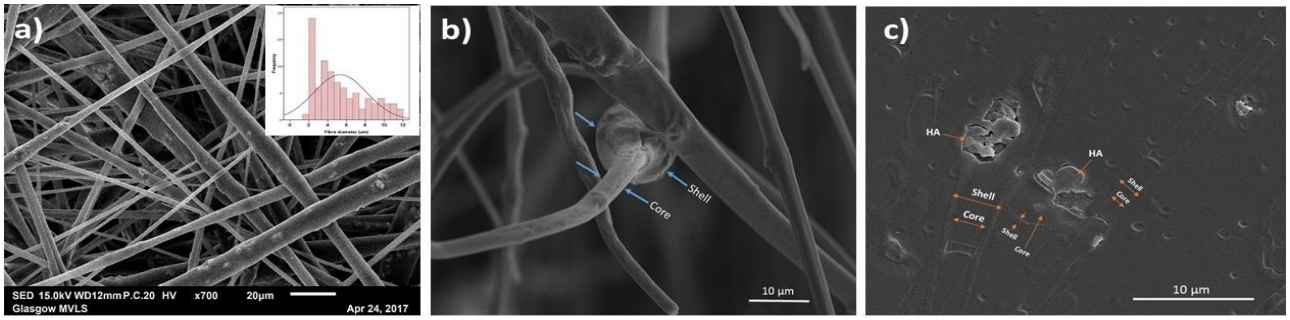

Figure 1: SEM images of core/shell PCL-PLA/HA fibres: a, b) fibres morphology and diameter distribution, and c) ultramicrotome section of the fibres. Marker bars a) 20µm, b) and c) 10µm.

SEM images of co-electrospun scaffolds exhibited non-woven, highly porous structure without any 'beads-on-a-string' morphology along the fibres (Figure 1a). Incorporation of HA led to rough fibre surfaces and enlarged fibre diameters. It was also confirmed that composites were co-electrospun into core/sheath structures with PCL as cores and PLA-HA as shells (Figure 1b and c). Mechanical properties of the PCL-PLA/HA coaxial scaffolds were approximately 31 MPa for tensile modulus, 0.68 MPa for ultimate stress and 30% for strain at failure compared to 59 MPa, 0.26 MPa and 13% respectively for PLA-HA scaffolds. This indicate that the inclusion of PCL as a core component have enhanced both strength and ductility of the scaffolds. The reduction in Young's modulus could be resulted from the non-uniform distribution of the core along the fibres.

Conclusions

PCL/PLA-HA core/shell scaffolds were fabricated using coaxial electrospinning. The resulted composites can serve as a potential scaffold for bone tissue due their osteoinductive and mechanical properties.

References

1. Elahi F et al. Bioeng. Biomed. Sci. J. 3:1-14, 2013.

Acknowledgments

MMK is supported by a PhD student scholarship from the Iraqi Ministry of Higher Education and Scientific Research (reference no. S1648).